

**TOWARD THE SERVICE-LIFE DESIGN OF CEMENTITIOUS  
MATERIALS IN FREEZE-THAW ENVIRONMENTS: NOVEL  
MODELS, SPECIFICATIONS, AND EVALUATION METHODS**

A Dissertation  
Presented to  
The Academic Faculty

by

Scott Howard Smith

In Partial Fulfillment  
of the Requirements for the Degree  
Doctor of Philosophy in the  
School of Civil and Environmental Engineering

Georgia Institute of Technology  
December 2019

**COPYRIGHT © 2019 BY SCOTT HOWARD SMITH**

**TOWARD THE SERVICE-LIFE DESIGN OF CEMENTITIOUS  
MATERIALS IN FREEZE-THAW ENVIRONMENTS: NOVEL  
MODELS, SPECIFICATIONS, AND EVALUATION METHODS**

Approved by:

Dr. Kimberly E. Kurtis, Advisor  
School of Civil and Environmental  
Engineering  
*Georgia Institute of Technology*

Dr. Matthieu Vandamme  
Laboratoire Navier  
*Ecole des Pont ParisTech*

Dr. Iris Tien  
School of Civil and Environmental  
Engineering  
*Georgia Institute of Technology*

Dr. William J. Weiss  
*Civil and Construction Engineering*  
*Oregon State University*

Dr. Surya Kalidindi  
School of Mechanical Engineering  
*Georgia Institute of Technology*

Date Approved: October 8, 2019

For posterity.

## ACKNOWLEDGEMENTS

Since entering higher education, I've found myself continually humbled at how major and minor characters in my life have influenced my education. Without the support of the U.S. Department of Energy and the U.S. Embassy of France in the United States attending graduate school and completing the work presented within this dissertation would not have been financially possible. For that, I am immensely grateful. To my primary advisors, Dr. Kimberly E. Kurtis and Dr. Matthieu Vandamme, thank you for teaching me how to ask questions and pursue their answers with the resources at hand. Graduate school has been one of the most transformative experiences of my life and I have you two to thank. To my family and friends, thanks for being a support network that has always caught me when I've tried to fly too close to the sun. To my broader academic community and research groups at Georgia Tech and Ecole des Ponts, you've taught me what it means to be a member in a significant way. Finally, to the countless number of baristas that have fueled this voyage, you deserve a morning off.

# TABLE OF CONTENTS

<b>ACKNOWLEDGEMENTS</b>	<b>iv</b>
<b>LIST OF TABLES</b>	<b>viii</b>
<b>LIST OF FIGURES</b>	<b>x</b>
<b>LIST OF EQUATIONS</b>	<b>xix</b>
<b>CHAPTER 1. Introduction</b>	<b>1</b>
1.1 Introduction and Motivation	1
1.2 The Current State of Freeze-Thaw Design and Assessment	3
1.3 A New Approach: Connecting Engineering Sciences to Freeze-Thaw Design	5
1.4 Thesis Organization	8
<b>CHAPTER 2. Seminal Efforts, Knowledge Gaps, and Technical Needs</b>	<b>10</b>
2.1 Introduction: Critical Review of Seminal Literature	10
2.2 Research Basis for Modern Material Characterization and Design Specification	11
2.3 Observable Failure Limit-States for Freeze-Thaw	14
2.4 Current Frameworks for Saturation, Freezing, and Characterization	18
2.5 Proposed Work: Knowledge Gaps and Technical Needs	22
2.5.1 Identified Knowledge Gaps	23
2.5.2 Identified Technical Needs	25
<b>CHAPTER 3. Mechanism for the Long-Term Saturation Rate of Air-Entrained Cementitious Materials</b>	<b>27</b>
3.1 Introduction	27
3.2 Literature Review	30
3.2.1 Theoretical Modelling	31
3.2.2 Experimental Results	36
3.3 Void-Scale: Single-Void Dissolution Kinetics (SVDK) Model	42
3.3.1 SVDK System Definition and Mechanisms	45
3.3.2 SVDK Model Formulation and Assumptions	52
3.3.3 SVDK Model Results and Discussion	58
3.3.4 SVDK Model Conclusions	73
3.4 Specimen-Scale: Multi-Void Dissolution Kinetics (MVDK) Model	75
3.4.1 MVDK System Definition and Mechanisms	77
3.4.2 MVDK Model Formulation and Assumptions	79
3.4.3 MVDK Model Results and Discussion	84
3.4.4 MVDK Model Conclusions	93

<b>CHAPTER 4. Critical Saturation of Air-Entrained Cementitious Materials</b>	<b>96</b>
<b>4.1 Introduction</b>	<b>96</b>
<b>4.2 Literature Review</b>	<b>99</b>
4.2.1 Water-filling Regimes of Entrained and Entrapped Air Void Systems	100
4.2.2 Existing Models for the Influence of Freezing on Cementitious Materials	102
<b>4.3 System Definition and Mechanisms</b>	<b>106</b>
<b>4.4 Limit State Model Formulation and Assumptions</b>	<b>114</b>
<b>4.5 Model Results and Discussion</b>	<b>118</b>
<b>4.6 Conclusions</b>	<b>127</b>
<b>CHAPTER 5. Relative Influence of Design Parameters and Performance Prediction</b>	<b>130</b>
<b>5.1 Introduction and Review</b>	<b>130</b>
<b>5.2 Formulation and Theory:</b>	<b>132</b>
5.2.1 General Formulation and System of Study	132
5.2.2 Powers' Hydraulic Pressure Theory	133
5.2.3 Air Void Systems	135
5.2.4 Intrinsic Properties: Porosity and Permeability	137
<b>5.3 Final Limit-State Formulation and Solution Method</b>	<b>138</b>
<b>5.4 Experimental Database of ASTM C666 Results</b>	<b>139</b>
5.4.1 Freeze-thaw Data	139
5.4.2 Random Variable Distributions and International Exposure Categories	141
<b>5.5 Results and Experimental Comparison</b>	<b>145</b>
5.5.1 Exposure Category Assessments	145
5.5.2 Importance and Sensitivity Study	146
5.5.3 Experimental Comparison and Validation	150
<b>5.6 Conclusions</b>	<b>155</b>
<b>CHAPTER 6. A Data Science Approach for Process-Structure-Property Linkages in Hydrating Cement Pastes</b>	<b>157</b>
<b>6.1 Introduction</b>	<b>157</b>
<b>6.2 Literature Review</b>	<b>161</b>
6.2.1 Hierarchical Material Informatics:	161
6.2.2 Cement Hydration and Challenges for Phase Segmentation from CT images:	164
<b>6.3 Database Development of Hydrating Cement Pastes</b>	<b>168</b>
6.3.1 NIST's Visible Cement Database Development and Segmentation	169
6.3.2 VCCTL Cement Database Development and Segmentation	175
<b>6.4 Materials Informatics Framework</b>	<b>177</b>
6.4.1 Spatial Statistics	178
6.4.2 Principal Component Analysis	183
6.4.3 Machine Learning and Diffusivity Determination	187
6.4.4 Process-Structure, Structure-Property, PSP Linkages	191
6.4.5 Extension of Results to the SVDK Model	194
<b>6.5 Conclusions</b>	<b>196</b>

<b>CHAPTER 7. Unifications and Modernization of the American Concrete Institute’s Freeze-Thaw Design Specifications</b>	<b>198</b>
<b>7.1 Introduction, Contracted Efforts, General Methodology</b>	<b>198</b>
<b>7.2 Literature Review</b>	<b>200</b>
7.2.1 Summary of Freeze-Thaw Exposure Categories, Specifications, and Recommendations	200
7.2.2 Background and Critical Review of Freeze-Thaw ACI Provisions	206
<b>7.3 Database Development and Durability Analysis</b>	<b>208</b>
<b>7.4 Suggested Modifications to ACI Code</b>	<b>213</b>
<b>CHAPTER 8. Contributions, Applications , Remaining Knowledge Gaps, and Future Work</b>	<b>222</b>
<b>8.1 Contributions and Applications</b>	<b>222</b>
8.1.1 Engineering Sciences	222
8.1.2 Data, Modelling, and Analytics	224
8.1.3 Durability Specifications	225
<b>8.2 Opportunities for Material Design</b>	<b>226</b>
<b>8.3 Remaining Knowledge Gaps and Future Work</b>	<b>228</b>
8.3.1 Engineering Sciences	228
8.3.2 Data, Modeling, and Analytics	230
8.3.3 Specifications and Evaluation Methods	231

## LIST OF TABLES

Table 3-1 - Definition of terms for the Epstein-Plesset Equation found in Equation 3-1.	32
Table 3-2 - Required inputs for SVDK and Equation 3-1 to results displayed in Figure 3-14a/b.	61
Table 3-3 - SVDK model inputs for cementitious material systems.	62
Table 4-1 - Symbol definition and values retained as constant for analysis and results in Section 4.5 for Limit-state function, Equation 4-6.	116
Table 5-1 - Summary of international design provisions for concrete exposed to FT [7,8,92,93].	144
Table 5-2 - Probability of failure values for various freezing rates.	146
Table 5-3 - Standard Importance Vector.	147
Table 5-4 - Scaled Importance Vectors.	149
Table 5-5 - LS function model parameter $\beta$ sensitivities.	150
Table 6-1 - Various experiments made on CCRL cement 133 for different w/c and total hydration time in [123].	171
Table 6-2 - GPR model parameters for fit squared exponential kernel functions.	193
Table 7-1 - Minimum design strengths and maximum water to cementitious materials ratio based on freeze-thaw exposure category from different ACI documents (1,4-6)...	201
Table 7-2 - Air content limits based on freeze-thaw exposure category from different ACI documents [7,8].	204
Table 7-3 - Allowable cementitious replacement percentages for ACI 318 F3 and ACI 201 F3a exposure categories [7,8].	205
Table 7-4 - Unified exposure category descriptions for FT attack.	218
Table 7-5 - Unified design recommendations for FT performance.	219
Table 7-6 - Unified minimum total air content recommendations for FT performance.	220
Table 7-7 - Complementary durability assessment test methods recommended for mixture pre-qualification or post-assessment for critical concrete placements.	221



## LIST OF FIGURES

Figure 1-1 - Multi-component research methodology.....	2
Figure 1-2 - Aggregated experimental outcomes for $S_{cr}$ determination in cementitious materials [17–19]. .....	6
Figure 1-3 - Idealized bi-linear saturation behavior of air-entrained cementitious materials immersed in water from experimental findings from [18,20,22–25] where a fine and coarse air void distribution have low and high mean air void sizes, respectively. ....	7
Figure 2-1 - Powers’ hydraulic pressure system [13,31]. .....	12
Figure 2-2 - Original FT-induced expansion plots developed by P. Klieger [11]. .....	14
Figure 2-3 - Original plots from [32] that display the influence of the value of spacing factor, $L$ , on the strain response of cement pastes due to freezing where strained was measured only longitudinally.....	15
Figure 2-4 - Original critical saturation plots developed by MacInnis and Beaudoin[16]. Percentage (%) values on lines represent the total material saturation.....	17
Figure 2-5 - Idealized saturation curve of air-entrained cementitious materials and the nick saturation point which corresponds to water-saturated capillary pores and air-filled voids [19]. .....	19
Figure 2-6 - Result of poromechanical model developed in [38] where strain is in the longitudinal direction of specimens taken from [32]. .....	21
Figure 2-7 - 5 research thrusts proposed in Sections 2.5.1 and 2.5.2 and evaluated in Chapters 3 to 7. ....	23
Figure 3-1 - Visual connection of various scales which influence the saturation behavior of air entrained cementitious materials. ....	28
Figure 3-2 - General mechanisms developed by G. Fagerlund in [29] for how air voids in cement pastes become water-saturated. ....	33
Figure 3-3 - Results from work of Eriksson et al [44]. .....	35
Figure 3-4 - Concatenated sorption findings from [18]. .....	37
Figure 3-5 - a). $\mu$ CT specimen b). filled vs. non-filled analysis for air voids within the first 6mm of the specimen [50]. .....	39

Figure 3-6 - a). proxy system examples, b). example of dissolution of isobutanol in water as a function of time [49].	40
Figure 3-7 - a). Outcomes of fit-power laws to a large class of proxy-systems [49,54,56,57], b). Exponent of power-law fits for solutions to the Epstein-Plesset model for initial bubble radius of 15 $\mu$ m.	41
Figure 3-8: Experimental validation of the Epstein-Plesset equation [54] where triangles represent an air bubble on a micro-pipette tip and squares represent an air bubbles resting on a flat wall.	42
Figure 3-9 - a). Idealized air-entrained cementitious material system that is fully immersed in water and single air void-shell system, at the moment when it is immersed b). standard bi-linear saturation curve for air-entrained cementitious materials [18] and idealized saturation behavior of the air-void shell system which is initialized by the compression of gaseous air and its resulting dissolution into the surround saturated capillary porosity [29].	44
Figure 3-10 - Spherical void-shell system and representation of the gas liquid interface which, for a given contact angle, $\theta$ , can be parametrized by the radius of the interface, $R_{gl}$ .	46
Figure 3-11 - Contour plot of normalized mass of air initially trapped, as a function of contact angle, $\theta$ , and initial radius of the gas-liquid interface, $R_{gl}(t=0)$ with associated visualization of corresponding initial system geometries. All calculations are made for $R_v = 10\mu$ m.	50
Figure 3-12 - Simplification of problem to 1D.	54
Figure 3-13 - a). comparison of SVDK model to Epstein-Plesset solution (i.e., Equation 3-1) and experimental data of Duncan 2004 [54], b). evolution of air-liquid interface as predicted by the SVDK model.	60
Figure 3-14 - Influence of advection on time to complete dissolution displayed by a). radius of air-liquid interface. b). Evolution of liquid pressure at $r = R_v$ for when advection is neglected (i.e., not solved for) and considered, respectively. Model inputs: $m_t = 1$ , $\theta = 0$ , $D_g^s = 5 \times 10^{-12} \text{ m}^2/\text{s}$ , $\kappa = 10^{-20} \text{ m}^2$ .	64
Figure 3-15 - Influence of intrinsic permeability on time to complete dissolution of the trapped air. Model inputs: $m_t = 1$ , $\theta = 0^\circ$ , $D_g^s = 5 \times 10^{-12} \text{ m}^2 \cdot \text{s}^{-1}$ , $L = 1 \text{ mm}$ .	65
Figure 3-16 - Influence of diffusivity of dissolved air in saturated hydrated cement paste on trapped air dissolution kinetics. Model inputs: $m_t = 1$ , $\theta = 0^\circ$ .	65
Figure 3-17 - Time to full dissolution, $t_f$ , contours of a large domain of normalized trapped mass, $m_t$ , and a). contact angles, $\theta$ , where $R_v = 10\mu$ m, $D_g^s = 5 \times 10^{-12} \text{ m}^2/\text{s}$ , $\kappa = 10^{-20} \text{ m}^2$ , and $L = 1 \text{ mm}$ , b). intrinsic permeability, $\kappa$ , where $\theta = 0^\circ$ , $R_v = 10\mu$ m, $D_g^s = 5 \times 10^{-12}$	

$12 \text{ m}^2/\text{s}$ , and $L = 1\text{mm}$ , c). diffusivity, $D_g^s$ , where $\theta = 0^\circ$ , $R_V = 10\mu\text{m}$ , $\kappa = 10^{-20} \text{ m}^2$ , and $L = 1\text{mm}$ , and d). air void radius, $R_V$ , where $\theta = 0^\circ$ , $D_g^s = 5 \times 10^{-12} \text{ m}^2/\text{s}$ , $\kappa = 10^{-20} \text{ m}^2$ , $L = 1\text{mm}$ . .....	67
Figure 3-18 - Examples of gas-liquid surface evolution for normalized trapped mass, $m_t$ , of 0.5 and various contact angles: a). $0^\circ$ , b). $25^\circ$ , c). $50^\circ$ , d). $75^\circ$ . Inputs: $R_V = 10\mu\text{m}$ , $D_g^s = 5 \times 10^{-12} \text{ m}^2/\text{s}$ , and $\kappa = 10^{-20} \text{ m}^2$ . .....	68
Figure 3-19 - Influence of spherical air void radius, $R_V$ , and porous solid shell thickness, $L$ , on time to full dissolution for $m_t = 1$ , $\theta = 0^\circ$ , $D_g^s = 5 \times 10^{-12} \text{ m}^2/\text{s}$ , and $\kappa = 10^{-20} \text{ m}^2$ . .....	69
Figure 3-20 - a). Power law evaluation for a system with $\theta = 0^\circ$ , where $R_V = 10\mu\text{m}$ and $m_t = 1$ , for when convection is neglected (i.e., not solved for) and considered, b). contour plot of power-law exponents (i.e. values of $C$ ) as a function of contact angle for when advection is considered. ....	70
Figure 3-21 - Comparison plot of SVDK model results with experimental conclusion from [50]. Model Inputs: $m_t=1$ , $\theta = 0^\circ$ , $D_g^s = 1.5 \times 10^{-12} \text{ m}^2/\text{s}$ , and $\kappa = 10^{-20} \text{ m}^2$ . .....	72
Figure 3-22 - Assessment of initial liquid and gas pressures at $r = R_V$ on dissolution kinetics of trapped air. Model inputs: $m_t=1$ , $\theta = 0^\circ$ , $D_g^1 = 5 \times 10^{-12} \text{ m}^2/\text{s}$ , and $\kappa = 10^{-20} \text{ m}^2$ , $L = 1\text{mm}$ . .....	73
Figure 3-23 - Graphical connection between SVDK, MVDK, and macro-scale phenomena. ....	76
Figure 3-24 - Idealized air-entrained cementitious material system used as the basis for the formulation present in Section 3.4.2. a). cubic system where voids are placed as computational nodes, b). differential element surrounding a node in which a void is placed. ....	78
Figure 3-25 - Example of MVDK model system. All spherical voids in this system have a $R_V = 10\mu\text{m}$ but have been scaled for ease of visualization. ....	79
Figure 3-26 - 2D representation of MVDK assessment for Equation 3-21. ....	81
Figure 3-27 - Comparison of SVDK and MVDK model solutions for various initial void radii. Inputs: $m_t = 1$ , $\theta = 0$ , $D_g^s = 5 \times 10^{-12} \text{ cm}^2/\text{s}$ . ....	85
Figure 3-28 - Influence of normalized depth to the surface on normalized time to full dissolution where $t_0$ is the time to full dissolution for each respective system when the air void is placed in the center of the system, similar to Figure 3-27, and $L$ is the size of the entire cubic lattice. ....	86

Figure 3-29 - Influence of volume fraction a). 0.5% and b). 4% on the dissolution kinetic of trapped air voids where a). has 275 voids and b). has 2060 voids. Inputs: $R_v = 10\mu\text{m}$ , $m_t = 1$ , $\theta = 0$ , $D_g^s = 5 \times 10^{-12} \text{ cm}^2/\text{s}$ , $L = 0.0006\text{m}$ .	87
Figure 3-30 - Influence of volume fraction on air void saturation and corresponding asymptotic approximations of the MVDK cubic systems. Inputs: $R_v = 10\mu\text{m}$ , $m_t = 1$ , $\theta = 0$ , $D_g^s = 5 \times 10^{-12} \text{ cm}^2/\text{s}$ .	88
Figure 3-31 - Comparison of experimental findings from [50], a). air void size distribution found within the first 6mm of the $\mu\text{CT}$ specimen prepared and evaluated in [50], b). estimations of respective saturation behavior using Equation 3-26 for each air void size class, c). comparison of experimental and numerical air void saturations for each evaluated size class, d). homogenization of saturation approximations made in b). and comparison to 60 day air void saturation experimentally determined in [50]. Inputs: $m_t = 1$ , $\theta = 0$ , $D_g^s = 5 \times 10^{-13} \text{ cm}^2/\text{s}$ .	90
Figure 3-32 - a). Comparison of MVDK model with experimental air void saturation curves from [18] and influence of $D_g^s$ on air void saturation evolution, b). study on the influence of coarse and fine air void distributions obtained from [50] on air void saturation evolution.	92
Figure 3-33 - Evaluate of smallest-to-large filling assumption on the mean gas over pressure within the spherical voids and the system saturation to monodisperse MVDK systems with small volume fractions, $v_f$ .	93
Figure 4-1 - a). Generalized model used to predict $S_{cr}$ , b). influence of various filling regimes on nearest-neighbor distance evolution as a function of air void saturation, c). evolution in surrounding hardened paste shell due to air void saturation, d). damage likelihood as a function of saturation and filling regime.	98
Figure 4-2 - Generalized filling regimes evaluated.	101
Figure 4-3 - Relationship between air void saturation and time due to long-term ponding [29], b). influence of air void saturation on spacing factor [25], c). influence of spacing factor on tensile response of air-entrained cement pastes due to temperature depression [32]. Image taken from [19].	102
Figure 4-4 - Influence of degree of saturation on strain response of mortar [19].	105
Figure 4-5 - a). CDF of air void size distribution [50] approximated by a lognormal distribution, b). Outcome of RSSA outcomes – system contains ~9900 non-overlapping voids.	107
Figure 4-6 - a). 2D schematic of NND determination in a polydisperse air void solid system, b). histogram of NND distances for the air void system described and detailed in Figure 4-5.	108

Figure 4-7 - a). 2D schematic of how NND ‘swells’ as a function of saturation, b). corresponding nearest-neighbor distance histogram values as a function of air void system saturation under a smallest-to-largest filling regime. Note that b). contains Figure 4-6b and uses the air void system information and cubic system size as displayed in Figure 4-5. .... 111

Figure 4-8 - Influence of air void saturation on nearest-neighbor distance growth as a function of filling Regimes #1-3..... 113

Figure 4-9 - a). 2D example of half NNDs and surviving and failing regions of cubic system, b). limit-state visualization for Equation 4-6. .... 117

Figure 4-10 - Initial outcome for likelihood of damage initiation given the detail system inputs and the air void size distribution shown in Figure 4-5a obtained from [50].120

Figure 4-11 - Estimations of likelihood of failure for filling regimes, a). smallest-to-largest, b). concurrent sinks, and c). SVDK behavior, using the same air void size distribution from Figure 4-5 and the system parameters shown in Figure 4-10. .... 121

Figure 4-12 - Evolution in NND as a function of total air void content,  $v_f$ , and a). air void saturation and b). system saturation..... 122

Figure 4-13 - Influence of cubic system size on LSF results for various filling regimes. Same material parameters as for Figure 4-10 where the air void volume fraction is 5%. .... 123

Figure 4-14 - Influence of a). degree of cement hydration and b). water-to-cement ratio for the same air void size distribution from Figure 4-5. Smallest-to-largest filling regime. .... 124

Figure 4-15 - Influence of compressive strength on failure likelihood. Smallest-to-largest filling regime..... 125

Figure 4-16 - Influence of a). distribution mean and b). distribution standard deviation on model outcomes for the smallest-to-largest filling regimes..... 126

Figure 4-17 - Influence of a). distribution mean and b). distribution standard deviation on NND for the smallest-to-largest filling regimes. .... 127

Figure 5-1 - Limit-state function schematic where the LS function hyper-plane separates the survival and failure regions..... 132

Figure 5-2 - The system of study contains a spherical air void with radius,  $r_b$ , and hardened paste shell of thickness,  $L$ . .... 133

Figure 5-3 - Comparison plot of Powers’ spacing factors for an arbitrary radius of 0.15 mm (0.006in)..... 136

Figure 5-4 - Analytic evaluation of the developed LS function where the compressive strength is assumed as 27.6MPa (4ksi), over a domain of A and <b>Lh</b> . .....	139
Figure 5-5 - Cumulative ASTM C666 test results for concretes with w/c ranging from 0.35 to 0.55. ....	141
Figure 5-6 - Probability of failure assessment for variable means of A and <b>Lh</b> within allowable range specified by ACI provision 201.16-2R.....	148
Figure 5-7 - Cumulative FT data overlaid on the $P_f$ contour for average values from the FT database. ....	152
Figure 5-8 - Cumulative analysis of developed LS function to predict performance by experimental assessment. ....	152
Figure 5-9 - Comparison of design variables <b>Lh</b> , A, and $f_c$ to $P_f$ for cumulative FT dataset [106–110] .....	153
Figure 5-10 - Exponential function development for probabilistic design of air-entrained concrete. ....	154
Figure 6-1 - Generalized framework for PSP linkage development displayed within this chapter.....	160
Figure 6-2 - Evolution in various hydration products and porosity as a function of time [130]......	165
Figure 6-3 - Evolution of grey-scaled seem images from [131] that with a black, grey, white color bar which can general distinguish present phases of water-filled pores, hydration products, and anhydrous cement, respectively. ....	166
Figure 6-4 - Threshold methodology used in [127] to distinguish between porosity, hydration products, and anhydrous cement grains.....	167
Figure 6-5 - Slice of CCRL cement 133 with a w/c of 0.35 at 16 total hours of hydration [123]......	168
Figure 6-6 - 2D color image of cement 133 exposed to synchrotron light source in Grenoble, France. Image magnification is 500x with dimensions 256 $\mu$ m by 200 $\mu$ m. Red is $C_3S$ , aqua is $C_2S$ , green is $C_3A$ , yellow is $C_4AF$ , pale green is gypsum, white is free lime, dark blue is potassium sulfate, magenta is the magnesium-calcium phase, and orange is an aluminosilicate (kaolin) phase [123]......	169
Figure 6-7 - 300x300pixel image of a 0.30 w/c cement paste at 162 of total hydration time from [123]. ....	170

Figure 6-8 - Global Otsu’s multi-threshold segmentation methodology following [66,121,128] to distinguish between water-filled pores, hydration products, and anhydrous products. ....	172
Figure 6-9 - Example outcome of global segmentation methodology where a). is the original grey-scaled image and b). is the same tri-phase segmented area. ....	173
Figure 6-10 - Example problem with global and local multi-thresholding approach (i.e., cyan hydration products are found well-within the yellow cement grains). Note that the image color bar is the same as that provided in Figure 6-9b. ....	173
Figure 6-11 - Improved segmentation outcomes using an updated phases-detection algorithm for cement paste with a w/c of 0.35.....	174
Figure 6-12 - Example compaction or sample imperfection found a cement paste with a w/c of 0.30 at 162 total hours of hydration. ....	175
Figure 6-13 - Example a). CemHyd3D output where each pixel/voxel represents a different phase and b). segmentation of the CemHyd3D image where white is water/ pores, cyan is anhydrous cement grains, and blue is hydration products.....	176
Figure 6-14 - Generalized outcome of CemHyd3D database that has been segmented porosity, hydration products, and cement grains. ....	177
Figure 6-15 - General workflow for 2-point statistics evaluations for the Visible Cement and CemHyd3D segmented databases. ....	179
Figure 6-16 - Cross correlations a). $f^1_2$ - H <sub>2</sub> O-filled pores and hydration products, b). $f^1_3$ - H <sub>2</sub> O-filled pores and cement grains, and c). $f^2_3$ – hydration products and cement grains.....	179
Figure 6-17 - 3D representation of autocorrelation outcomes for the CemHyd3D database. ....	180
Figure 6-18 - Cut evaluation of various w/c cement pastes at a total hydration time of 72 hours using autocorrelations of a). water-porosity, b). hydration product, and c). cement grain phases where r has units of voxel length (i.e., ~ 1micron).....	181
Figure 6-19 - Evolution in phase volume fraction evolution as a function of total hydration time in hours for w/c of a). 0.25, b). 0.40, and c). 0.55. ....	182
Figure 6-20 - Evolution in volume fractions a). water-porosity, b). hydration products, and c). cement grains as a function of total hydration time in hours for a w/c cement paste of 0.45. ....	183
Figure 6-21 - Scree plot of first five principal components (i.e., eigenvalues) of the data matrix which contains 2-point statistic information for each microstructure class.	184

Figure 6-22 - 3D visualization of primary principal components to distinguish between process parameters a). w/c and b). total hydration time.....	185
Figure 6-23 - Visualization of w/c and total hydration time to form trends between a). PC1, b). PC2, c). PC3, and d). PC4 for all 349 microstructures.....	186
Figure 6-24 - Basis vector plot for statistical assessment of the 349 microstructures and various principal components. ....	187
Figure 6-25 - Summary of theory for gaussian process models for applications in machine learning [139,140].....	188
Figure 6-26 - Outcomes of objective function determination: a). value and b). minimization. ....	189
Figure 6-27 - a). Network model of pores and CSH and b). Nernst-Einstein relation used to predict the diffusivity of the 349 CemHyd3D microstructures [122,141].....	190
Figure 6-28 - Average (effective) relative diffusivity as a function of a). PC scores and b). process parameters of the cement paste microstructures. ....	191
Figure 6-29 - a). GP model outcome and b). parity plot of known PC1 versus Predicted PC1 using the GP model and an 80-20 train-test split. ....	192
Figure 6-30 - a). and c). represent the fit GP model surface (i.e., process-structure linkage) for PC scores 2 and 3 whereas b). and d). represent the parity plots for each PC score. ....	192
Figure 6-31 - Parity plots for a). PC scores to diffusivity and d). process parameter top diffusivity GP models. ....	194
Figure 6-32 - Influence of process parameters on a). mean effective diffusivity and b). average diffusivity. ....	195
Figure 6-33 - Influence of process parameters on time to full dissolution using the SVDK model.....	195
Figure 7-1 - Comparison plot for water-to-cement ratio and a). 28-day compressive strength b). total air content c). total air content in paste fraction and d). spacing factor to ensure FT performance [108–110,145–147].....	210
Figure 7-2 - Comparison plot for 28-day compressive strength and a). total air content b). total air content in paste fraction and c). spacing factor to ensure FT performance [108–110,145–147].....	211
Figure 7-3 - Comparison plot for various measurements to ensure FT performance: a). total air content and total air content in the paste fraction; b). total air content and spacing	

factor; c). total air content in the paste fraction and spacing factor [108–110,145–147].  
..... 212

Figure 7-4 - Influence of specific surface and total air content on spacing factor,  $L$ . .... 217

Figure 8-1 - Summary of opportunities for material design based upon research outcomes  
in Chapters 3-6. .... 227

## LIST OF EQUATIONS

Equation 2-1 - Powers' maximal hydraulic pressure at radial distance $L$ . .....	12
Equation 3-1 - Epstein-Plesset Model [54,55]. .....	31
Equation 3-2 - Volumetric Intersection of two spheres [68]. .....	47
Equation 3-3 - Lineal distance, $d$ , found in Equation 3-2 between spheres $R_v$ and $R_{gl}(t)$ [68]. .....	47
Equation 3-4 - Determination of initial mass of trapped gas at time, $t = 0$ . .....	48
Equation 3-5 - Determination of initial gas-liquid interface radius, $R_{glt} = 0$ . .....	49
Equation 3-6 - Maximal value of trapped mass which can be represented by Equation 3-4 and 3-5. ....	50
Equation 3-7 - Free energy summation for initial configuration assessment. ....	51
Equation 3-8 - Gas free energy. ....	51
Equation 3-9 - Gas-liquid surface free energy. ....	52
Equation 3-10 - Liquid volume free energy. ....	52
Equation 3-11 - Comparison of diffusive fluxes at $r = R_v$ . ....	53
Equation 3-12 - Mass conservation of liquid, $l$ . ....	55
Equation 3-13 - Mass conservation of dissolved gas, $g$ . ....	55
Equation 3-14 - Result of incompressibility assumption. ....	55
Equation 3-15 - Governing transport equation for dissolve gas in the liquid saturation porous shell. ....	55
Equation 3-16 - Dissolved gas concentration, $C_g$ , at $r = R_v$ at all times. ....	56
Equation 3-17 - Liquid pressure concentration, $P_l$ , at $r = R_v$ at all times. ....	57
Equation 3-18 - Rate of change of gas mass in spherical air void due to advection and diffusion .....	57
Equation 3-19 - Rate of change of liquid mass in spherical air void due to advection and diffusion. ....	57

Equation 3-20 - Final representation for the rate of change of liquid mass in the void....	58
Equation 3-21 - Governing MDVK equation for transport of dissolved gas.....	80
Equation 3-22 - Differential equation for mass of air in a differential element containing a spherical air void.....	80
Equation 3-23 - Equation to calculate $R_{gl}(t+dt)$ .....	82
Equation 3-24 - Volumetric homogenization for average saturation of a polydisperse air void system. ....	83
Equation 3-25 - Smallest-to-largest calculation methodology for mean gas pressure in [44]. ....	84
Equation 3-26 - Analytical expression for air void saturation behavior for MVDK model. ....	88
Equation 4-1 - Nearest neighbor distance calculation. ....	108
Equation 4-2 - Determination of air void system saturation for the smallest-to-largest filling regime. ....	110
Equation 4-3 - Volume of water to enter air voids for a given air void system saturation, $S_a$ . ....	110
Equation 4-4 - Powers' equation for capillary porosity in cement pastes as a function of cement hydration and water-to-cement ratio. ....	114
Equation 4-5 - Determination of macro-system saturation, $S$ , from the capillary porosity, air void saturation and air void volume fraction.....	114
Equation 4-6 - Limit-state function for hydraulic pressure evaluation in RSAA system. ....	115
Equation 4-7 - Intrinsic permeability estimation for cement paste as a function of the capillary porosity, $C_p$ , developed in an experimental fit from [13]. ....	116
Equation 5-1 - General limit-state model formulation.....	132
Equation 5-2 - Powers' maximal pressure.....	134
Equation 5-3 - Powers' spacing factor for cementitious materials will values of $(F_p/A)$ less than 4.342 [13,41]. ....	136
Equation 5-4 - Powers' spacing factor for cementitious materials will values of $(F_p/A)$ greater than or equal to 4.342 [13,41]. ....	136

Equation 5-5 - LF model written as a function of compressive strength,  $f_c$ , spacing factor,  $Lh$ , and total air content,  $A$ . ..... 138

Equation 5-6 - Probability of failure fit as a function of spacing factor. .... 154

## SUMMARY

In order to design the service life of cementitious materials in freeze thaw environments, advancements in the engineering sciences, analytics, on-site evaluation techniques, and durability specifications must be connected in a consistent and coherent manner. Using the phenomenon of critical saturation ( $S_{cr}$ ) – which corresponds to the damage initiation of cementitious materials when exposed to freezing – questions and hypotheses are developed to advance the field’s understanding of how cementitious materials become progressively water-filled and the underlying physics and material parameters that govern long-term freeze-thaw durability. Two models, termed single- and multi-void dissolution kinetics (SVDK and MVDK), are derived to build upon the current knowledge of how single and polydisperse air-void systems in water-immersed cementitious material become saturated. A novel limit-state function is also derived to evaluate the hypothesis that the universal value of  $S_{cr}$  (~85%) for cementitious materials can be explained by the evolution in mean distance between non-water-filled air voids as the material saturates. The results of the derived model are invariant of total air content, material strength, and material permeability - agreeing with experimental efforts to date. The same model is then probabilistically evaluated using first-order reliability methods to determine the influence of controllable concrete design parameters and the ability of international design specifications to ensure long-term freeze-thaw performance. Recognizing that the previously derived models are dependent upon common material parameters, a data-science approach for process-structure-property (PSP) linkages is developed for hydrating cement paste and a case study is made to show how the diffusivity of a cement paste can be accurately predicted as a function of its water-to-cement ratio and

total hydration time through rigorous statistical evaluation of the cement paste's microstructure. Using the case study, it is shown how quantitative PSP linkages can be introduced to physics-based models and the influence of simple process parameters may be connected to phenomena which have major relevance for service-life, such as the total time to full dissolution of air voids which progresses the material toward  $S_{cr}$ . Lastly, discrepancies and contradictions between various American Concrete Institute committees are critically reviewed and compared to a database of long-term freeze-thaw tests on concrete. Evidence-based recommendations are made to unify and modernize the current requirements to ensure the freeze-thaw durability of concrete in the 21<sup>st</sup> century.

# CHAPTER 1. INTRODUCTION

## 1.1 Introduction and Motivation

The service-life of a material is understood as its predicted life expectancy based on previous knowledge of how it has performed in the real world [1]. In contrast, the design-life of a material is defined as its forecasted life expectancy and is assessed by engineering calculations that consider loading conditions or specific environments [1]. The service-life design of a material then implies the reduction or removal in the difference between the real and theoretically predicted life expectancies. Progressing the ability to design the service-life of cementitious materials (i.e., concretes, mortars, and pastes) has significant implications for the economy, sustainability, and resiliency for future civil infrastructure but requires a more profound knowledge of the material system, the governing physics of phenomena that lead to degradation in different service environments, and an understanding of the constraints of the concrete specification and construction industries. For the purposes of the work presented, the deleterious effects of freeze-thaw (FT) and cyclic FT environments on cementitious materials that are becoming increasingly liquid saturated is exclusively considered.

In effort to advance the field toward service-life design, it is first necessary to connect the state-of-the-art in research, design requirements established by international specification boards, and on-site assessments techniques. By combining physics-based models, updated design requirements, and novel evaluation methods, salient features of cementitious materials that govern FT service-life can be identified, required for specification by engineers, and then evaluated in the field. The methodology shown in

Figure 1-1 and research proposed herein presents a new paradigm for cementitious materials to meet 21<sup>st</sup> century civil engineering needs in FT environments. As a result, the presented research includes contributions ranging from the fundamental sciences of cementitious to highly-tortuous porous materials. More specifically, the conducted efforts begin with questions related to the mechanism for long-term saturation that leads to an increased likelihood of FT failure and concludes with suggested modifications to current international design specifications used by engineers to ensure the FT durability of placed concrete.

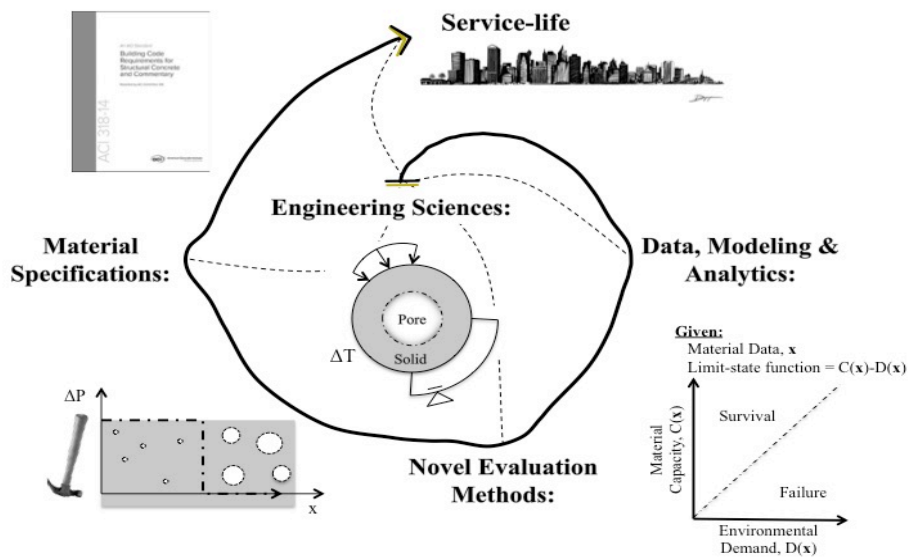


**Figure 1-1 - Multi-component research methodology.**

The technical organization of the work follows Figure 1-1. Beginning with the engineering sciences, the field centrally concerned with the physical and mathematical representation of phenomena important to engineered system, the effects of thermal, hydraulic, and mechanical exposures are considered on cementitious materials – as

idealized by the spherical pore-solid system – to understand the governing physics and effects of FT. Using the physics-based models of FT effects on cementitious materials, analytics techniques are then used to predict the likelihood of failure, as displayed by the limit-state plot in the bottom-right image in Figure 1-1, given material parameters and compared with existing experimental data.

With knowledge of which material parameters (e.g., air porosity volume and size distribution, values of diffusivity, etc.) influence FT resistance most significantly, novel concrete construction technology can be developed and evaluated to ensure that placed concrete has the appropriate material parameters to ensure FT resistance. Lastly, by connecting the engineering sciences, analytics, and novel evaluation methods, international material specifications can be modernized to reflect the state-of-the-art in the field - improving on the current state of FT design and assessment and resulting in the service-life design of cementitious materials.

## **1.2 The Current State of Freeze-Thaw Design and Assessment**

Although the freeze-thaw (FT) durability of cementitious materials has been extensively studied [2], FT-related failures are still frequently reported [3–5] and occur before the desired service-life of the structure. An often-reported problem amongst these failures relates to quality control and the lack of on-site evaluation methods that assess key-parameters of non-hardened cementitious materials that ensure FT resistance [3,4]. With respect to a recent FT-related failure of a concrete pavement section apart of US highway M-6, Executive Commissioner of the Michigan Concrete Association, Dan DeGraff, stated, “it wasn’t a testing problem, we were measuring something that didn’t tell us the whole

story [3],” in response to quality assurance assessments of fresh concrete taken on-site. In that project, unreliable on-site evaluation methods resulted in a total of \$10.5 million in repair for a \$22 million stretch of pavement [3] – nearly 50% of the initial cost - and motivates the need for advancement of on-site evaluate techniques to ensure the FT resistance of cementitious materials. Additionally, changes in mean Artic temperatures are expected to result in an increase in severe winter weather events in North America [6], posing a future challenge for the long-term durability of infrastructure systems.

Complicating matters, current design requirements, guidelines, and specifications established by American Concrete Institute (ACI) committees for FT durability are not consistent [7–9], providing unclear durability specification requirements to design professionals. Furthermore, the design specifications established by ACI Committee 201, the ACI Durability of Concrete Committee, are based upon experimental findings from tests conducted in the early 1950s [10–12]. Despite that the studies are founded on sound principles, advancements in modern cements, admixtures, construction practices, and new understanding of the governing phenomena of FT on cementitious materials call into question the relevance of these results to modern materials and construction requirements.

The design and assessment of cementitious materials to be FT resistant has been stymied by standard test methods that do not assess all of the salient features of the material. Currently, standard practice and specifications only require a total air content value in the material [10–12] when the size distribution and relative spacing of the entrained and entrapped air voids strongly correlate with FT durability [13]. The standard method used in the industry [14] to assess the size distribution and spacing of the air void system is time consuming, costly, and can only be done in a hardened state – leading to infrequent use.

Additionally, specifications [8,9] do not mention that there are additional evaluation or validation methods that can be carried to ensure a concrete placement is FT resistant.

Lastly, another central and current challenge is that design specifications and requirements for FT durability lack a basis in a physical limit-state that defines when FT failure will begin. As a result, the lack of identification of which process parameters, structural forms, or final properties of cementitious materials results in FT resilient concrete makes it very challenging to design the service-life of the material. Other areas of concrete durability, such as chloride-initiated corrosion of steel-reinforcement - as initially proposed in [15] - have clear limit-states which allow for material parameters to be designed into the cementitious material to ensure an absolute minimal service-life by considering the most-extreme environmental exposure.

### **1.3 A New Approach: Connecting Engineering Sciences to Freeze-Thaw Design**

Historically, cementitious materials have been designed for FT durability by the selection of a needed compressive strength, water-to-cement ratio (w/c), and total air content that limits expansion [11,12] and likelihood of scaling [10] upon freezing. Despite that expansion and scaling are related to the response of cementitious materials to FT exposure, they do not exhibit a clear failure limit-state and are dependent upon various materials and environmental exposure parameters (e.g., entrained air void spacing and water saturation). Decades of research has developed techniques to minimize freeze-thaw damage, but a consistent design, specification, and evaluation methodology has yet to be developed, suggesting a new approach is needed.

In 1968, a FT failure limit-state, termed ‘critical saturation’ ( $S_{cr}$ ) [16], was identified in cementitious systems and found to be between 80% and 90%. In 1973, this range was reconfirmed and further defined as the water saturation state at which exposure to freezing results in a measurable reduction in modulus [17]. Figure 1-2 displays collective outcomes from the literature of this FT limit-state [17,18] and shows that concrete and mortars across a large range of air-content and even reinforcing fiber inclusion result in a critical saturation of ~85%. Interestingly, it is found that below this value of water saturation cementitious materials can be exposed to cyclic FT without reduction in measured modulus [17].

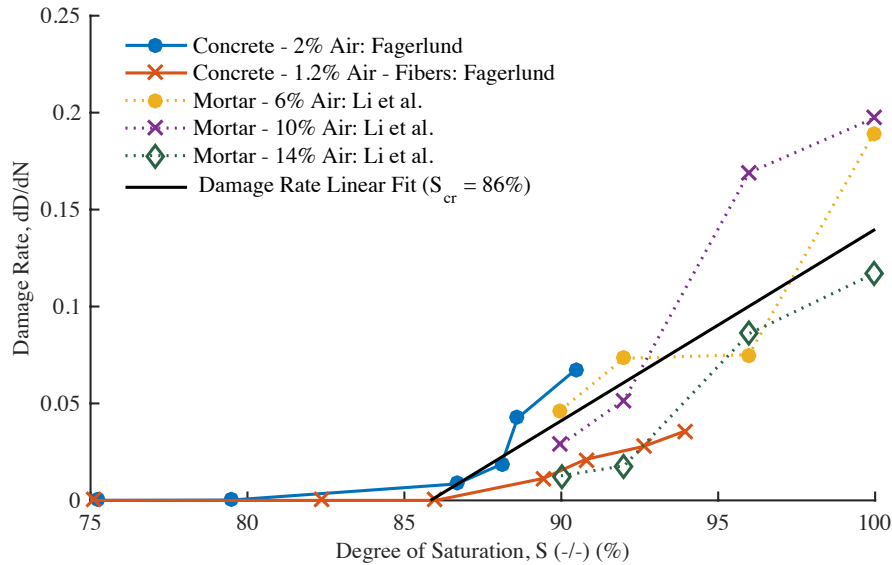


**Figure 1-2 - Aggregated experimental outcomes for  $S_{cr}$  determination in cementitious materials [17–19].**

The existence of  $S_{cr}$  in cementitious materials affords the opportunity for FT service-life design by engineering the material with parameters that yield a hardened structure with a sufficiently large time to  $S_{cr}$  [20,21]. Figure 1-3 shows an idealized saturation curve of air-entrained cementitious materials immersed or ponded under water, which are known to be bi-linear when conditioned at low values of relative humidity as

displayed in [18,22], and various parameters that have been shown to effect the overall time to critical saturation, such as total air content and air void size distribution [23]. Seeing as how the time axis is reported on the  $\frac{1}{2}$  power in Figure 1-3, it is clear that understanding the physical parameters which correspond to the long-term saturation rate, characterized by  $S_2$ , is essential to service-life design. In effort to utilize this limit-state phenomenon as the basis to approach service-life design of cementitious materials in FT environments, it is necessary to improve the theoretical understanding of  $S_{cr}$ , advance on-site assessment techniques, and unify and update current design requirements established by ACI. The proposed approach effectively links the state-of-the-art in the research field, construction, and material administration to progress the field.

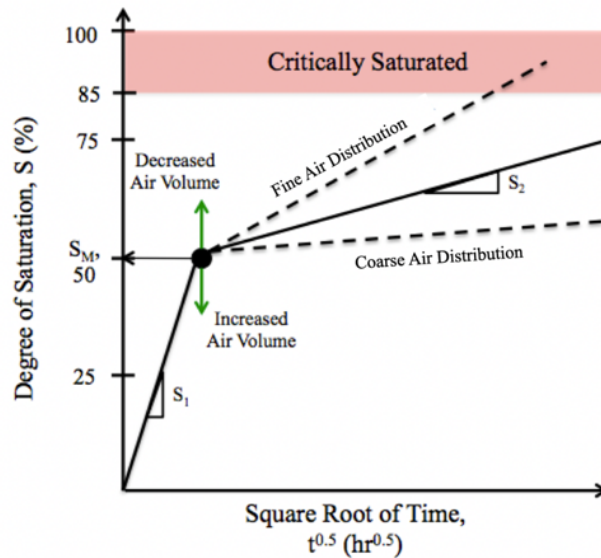


**Figure 1-3 - Idealized bi-linear saturation behavior of air-entrained cementitious materials immersed in water from experimental findings from [18,20,22–25] where a fine and coarse air void distribution have low and high mean air void sizes, respectively.**

## 1.4 Thesis Organization

Aligning with Figure 1-1, a critical review of seminal literature related to how freeze-thaw environments influence cementitious materials is detailed in Chapter 2. Within this chapter, the literature findings are presented in a manner to identify knowledge gaps and technical needs that should be resolved to progress the field toward the capacity to design the service-life of cementitious materials in freeze-thaw environments. Section 2.4 clearly defines fundamental questions, hypotheses, and suggested frameworks which are evaluated in Chapters 3 to 7. Due to the fact that it takes a certain amount of time for cementitious materials to become critically saturated, shown as  $S_2$  in Figure 1-3, Chapter 3 thoroughly reviews, formulates, and analyzes an increasingly physical model to predict how air-voids become water-filled over time.

With improved understanding of how air voids become saturated, Chapter 4 then evaluates a hypothesis that the general value of critical saturation (i.e. 85%) is seen across a broad range of cementitious material due to the increase in mean distance between non-water-filled air voids which corresponds to large increases in internal pressures and increased likelihoods of failure during a freezing event. Chapter 5 probabilistic evaluates the derived limit-state model used to predict the critical saturation of air-entrained cementitious materials, identifying how material and environmental parameters found within the model relatively influence the model outcome while also evaluating the ability for American, Canadian, and British freeze-thaw design specifications to ensure long-term durability.

Recognizing that Chapters 3 through 5 are centrally dependent on the knowledge of the engineering properties of hydrated cement pastes (i.e., the diffusivity and intrinsic permeability), in Chapter 6 a materials informatics framework is applied to generate a full process-structure-property (PSP) linkage using a data science approach - connecting the water-to-cement ratio (w/c) and total hydration time to diffusivity. Leveraging the PSP linkage, it is then shown how the data-driven linkages can be coupled with the air void saturation models presented in Chapter 3 to evaluate how changes in w/c and total hydration time influence time to full saturation of air voids. Chapter 7 rigorously evaluates the current discrepancies and methods used for specification of freeze-thaw durable concrete by respective ACI Committees and proposes how the existing documents can be unified, modernized, and improved based upon the state-of-the-art. Lastly, Chapter 8 summarizes the contributions made in Chapters 3 to 7 and identifies remaining knowledge gaps and future work to further progress the field.

## CHAPTER 2. SEMINAL EFFORTS, KNOWLEDGE GAPS, AND TECHNICAL NEEDS

### 2.1 Introduction: Critical Review of Seminal Literature

In 1992, an annotated bibliography with more than 550 citations related to the theory and effects of FT on cementitious and other porous and brittle materials was published by the U.S. Strategic Highway Commission [2]. Since, numerous reviews and strategic initiatives to improve the design of cementitious materials for FT resistance have been developed [26–28]. Due to the volume of work carried out on the topic, a complete review of the entire field is outside the scope of this section. Detailed literature reviews for respective topics in which technical contributions are made are found within the second sections of Chapters 3 through 7. Rather, a critical assessment of seminal efforts is detailed in a manner that showcases how critical saturation ( $S_{cr}$ ) can serve as a limit-state metric for FT service-life design as theorized in [29].

Although previously discussed, a limit-state is defined as a condition in which a structure or a material no longer meets a desired or safe design criteria [30]. As shown in Figure 1-2, the  $S_{cr}$  of a cementitious material is the saturation condition in which exposure to freezing or FT cycling results in a measurable loss in modulus. The time it takes for a cementitious material to come critically saturated when immersed in water agrees with previous limit-states defined by other well-developed fields of cementitious durability study, such that the time to critical chloride concentration at the depth of rebar which will result in corrosion initiation [15]. The use of  $S_{cr}$  as a service-life design metric results in

the most-conservative estimate of the material's service-life (i.e., it is an absolute minimum) developed for the most-extreme environmental exposure conditions (e.g., complete immersion in liquid water). The review conducted herein is organized into sections related to current design requirements, experimentally displayed failure limit-states, and modern physics-based models and material characterization methods. The following sections are aimed at displaying and discussing the most important findings to investigate why a universal value of critical saturation is seen for cementitious materials and how this phenomenon can be leveraged in design for durability. Section 2.5 serves to clearly detail knowledge gaps and technical needs from this condensed review and contains research hypotheses, technical approaches, and expected outcomes investigated and evaluated in Chapters 3 to 7.

## **2.2 Research Basis for Modern Material Characterization and Design Specification**

As mentioned in Section 1.2, the current FT durability requirements and specifications [7–9] established by respective ACI committees are largely reflective of seminal efforts of T.C. Powers [13] and P. Klieger [10–12]. In 1949, T.C. Powers established the hydraulic pressure theory which states that the pressures exerted on the hardened cement paste during a freezing event occur due to the forced migration of water through the paste's porosity as ice forms in large capillary voids [13]. Powers' work resulted in Equation 2-1 that predicts the hydraulic pressure,  $P$ , at a distance  $L$  from the air void, where  $\eta$  is the viscosity of the water,  $S_{cp}$  is the water saturation of the capillary porosity,  $K$  is the permeability of the hardened cement paste,  $R$  is the freezing rate,  $U$  is the amount of freezable water present,  $r_b$  is the size of the air void, and  $L$  is the shell

thickness. Figure 2-1 shows the idealized material system used in Powers' original derivation.

**Equation 2-1 - Powers' maximal hydraulic pressure at radial distance L.**

$$P = \frac{\eta}{3} \left( 1.09 - \frac{1}{S_{cp}} \right) \frac{UR}{K} \left( \frac{L^3}{r_b} + \frac{3L^2}{2} \right)$$

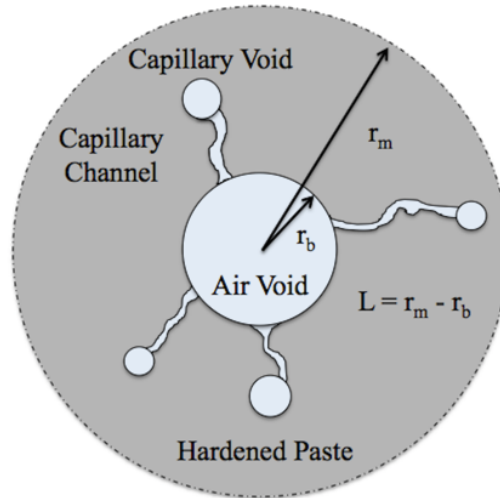


**Figure 2-1 - Powers' hydraulic pressure system [13,31].**

Based on Equation 2-1, Powers' identified values of  $L$  that would result in FT resistant concrete and developed the experimental theory to determine the mean half-distance between air voids, termed spacing factor,  $\bar{L}$ , which approximates  $L$ . It is important to note that Powers'  $\bar{L}$  still serves as the industry standard for assessing the pore structure of hardened cementitious materials [14] and has been shown to be the most-reliable predictor of FT resistance [31]. Despite this,  $\bar{L}$  is not specified, or required, by any ACI committee to-date due to the challenges detailed in Section 1.2. Advancements in FT theory

and characterization methods - detailed in Sections 2.4, 4.2, and 5.2 - have shown that Power's hydraulic pressure theory and spacing factor equations do not consider the effects of ice crystallization pressures or the polydispersity of the entrained air void system. This implies that the prevailing theories still utilized in the industry to characterize air-entrained cementitious materials do not consider critical physical aspects of the FT phenomenon or respective material system.

Similar to how the research basis for ASTM C457 can be traced directly to [13], the current material specifications established by ACI 201, the ACI Durability of Concrete Committee, can be linked to the efforts of P. Klieger throughout the 1950s [10–12]. To date, a required compressive strength value, water-to-cement ratio (w/c), and total air content are specified by all ACI committees for FT durability. The values set for the compressive strength and w/c for ACI 201 are taken from a 'required curing time' study conducted in 1957 [10] where scaling and mass loss after exposure to ponding and FT were used as performance metrics. Similarly, the total air content values specified by ACI 201 are based on two studies [11,12] that evaluated the required air content as a function of nominal maximum aggregate size (NMAS) to minimize expansion after 300 cycles of FT. Figure 2-2 displays the original plots obtained from [11].

Although the work in [10–12] is founded upon sound experimental science and technique, the metrics used to evaluate the cementitious materials only reduce the likelihood that FT damage will occur under accelerated lab testing (i.e., scaling, mass loss, or expansion). This implies that the current specifications and requirements can only reduce the extent of FT damage a cementitious material will undergo. Additionally, the phenomenology used to limit the FT-induced damage does not provide a way to a predict

or measure a minimal service-life (i.e., the metrics are not selected to control the time to critical saturation). Pending the improved understanding of how cementitious materials saturate over time and why a critical degree of saturation is observed, the minimal total service-life of a cementitious material can be determined and engineered into the material system.

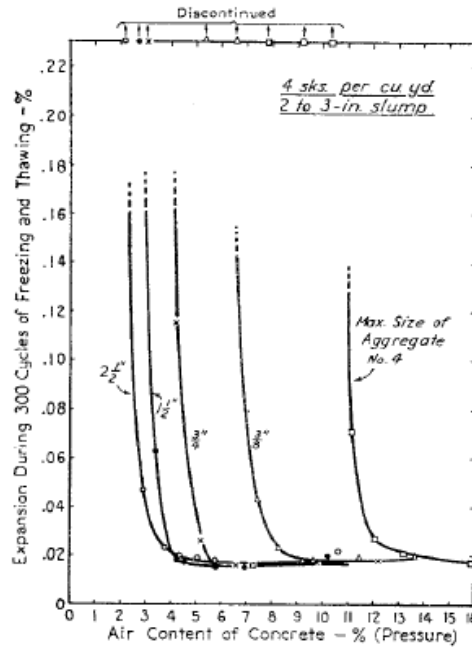


**Figure 2-2 - Original FT-induced expansion plots developed by P. Klieger [11].**

### 2.3 Observable Failure Limit-States for Freeze-Thaw

Shortly after identifying the importance of the spacing between entrained air voids for FT resistance in cementitious materials, Powers and Helmuth [32] displayed that as the spacing factor increases from 0.012in (0.3mm) to 0.025in (0.64mm) the freezing-induced strain changes from compressive strain to tensile strain. Figure 2-3 shows the original results of cement pastes containing different entrained air-void systems with spacing factor,  $\bar{L}$ , values which range from 0.0075in (0.19mm) to 0.1in (2.54mm). Due to the weak

tensile capacity of cementitious materials, this finding suggests that the spacing factor can identify if a specimen will begin to deteriorate under FT cycling. It is important to note that the exact saturation state for these experiments for the cementitious materials was not reported, but the specimens were cured for anywhere from 3 weeks to 3 months - suggesting that the degree of saturation was sufficiently high [32]. Although numerous experimental factors are not clearly discussed or reported with Figure 2-3, the findings helped establish the recommended 0.01in (0.25mm) spacing factor minimum discussed in [7].

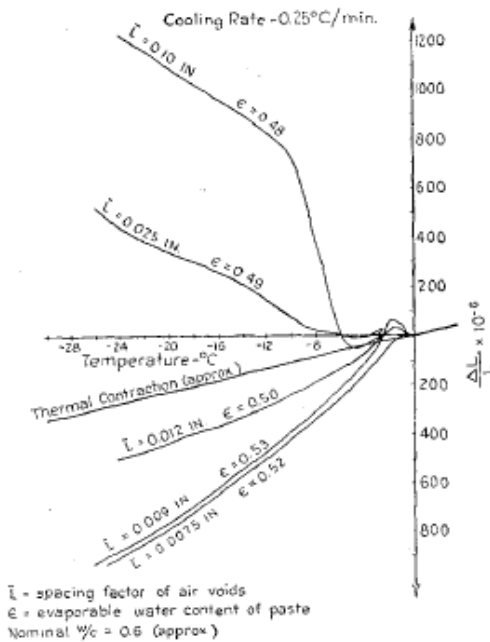


**Figure 2-3 - Original plots from [32] that display the influence of the value of spacing factor,  $\bar{L}$ , on the strain response of cement pastes due to freezing where strained was measured only longitudinally.**

Critical saturation ( $S_{cr}$ ), similar to the findings shown in Figure 2-3, was discovered through a series of experiments in [16] which displayed that as the saturation degree of various air-entrained mortars increased a bifurcation of longitudinal strain occurs (i.e., for

sufficiently low saturations the strain becomes increasingly compressive and for sufficiently high saturations – at and above the  $S_{cr}$  – the strain becomes increasingly tensile). Figure 2-4 displays the outcomes of the original experimental work by MacInnis and Beaudoin in 1968 [16], complementing outcomes of more recent experiments [17,18] shown in Figure 1-2. In Figure 2-4, it is seen that mortars with degrees of saturation of 86% and below display continuously compressive strain behavior when exposed to freezing temperature-depression. For degrees of saturation larger than 86%, the strain response becomes exponentially compressive. To date, the  $S_{cr}$  of cementitious materials has been accepted to be 85% [21,33]. Recognizing that a significant amount of time is need to for water-immersed air-entrained cementitious materials to high value of saturation, the work presented in [18,21,33] has also displayed how  $S_{cr}$  can be connected to a total time to critical saturation ( $t_{cr}$ ) using scalar properties (i.e., the value of secondary saturation,  $S_2$ , displayed in Figure 1-3) of air-entrained mortars obtained from long-term sorption tests.

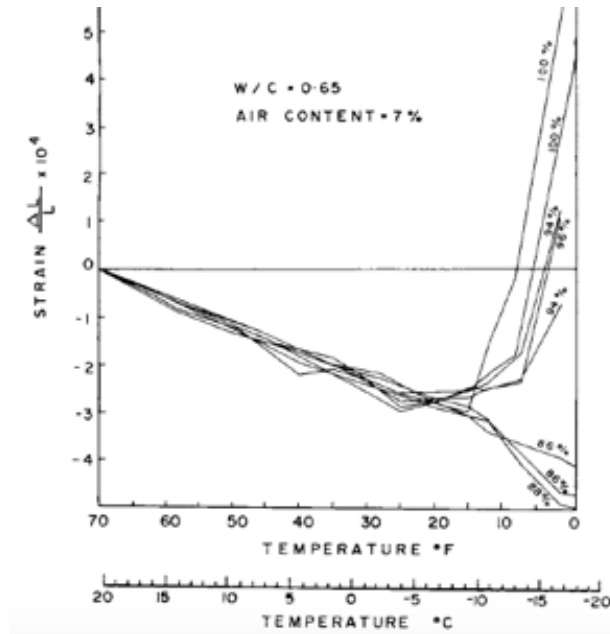


**Figure 2-4 - Original critical saturation plots developed by MacInnis and Beaudoin[16]. Percentage (%) values on lines represent the total material saturation.**

It is important to note that  $S_{cr}$  has already been incorporated into service-life forecasting models [33,34] – the connection between the long-term saturation rate can clearly be used to predict a minimal total service-life. Nonetheless, numerous fundamental questions have yet to be investigated regarding what parameters influence or govern its value [19]. To date, the vast majority of the research on  $S_{cr}$  and  $t_{cr}$  has been experimental, assessing the influence of variables such as total air content, w/c, and sequential air meter (SAM) number [18,20,35]. Significant gaps still remain with respect to the mechanisms in which air-entrained cementitious materials saturate over long time periods of fluid exposure and how that results in an increased likelihood of FT failure in a consistent, physics-based framework. Nonetheless, the coupled work of Powers and Helmuth and MacInnis and Beaudoin suggests that changes in salient microstructural features (i.e., the mean half-spacing between voids that are still not saturated) due to the saturation of

cementitious materials could govern  $S_{cr}$  and to-date this has not been evaluated in a modern framework with state-of-the-art models.

## 2.4 Current Frameworks for Saturation, Freezing, and Characterization

Prior to leveraging  $S_{cr}$  as a limit-state metric for service-life design, it is first necessary to understand what properties of the material govern the value of the phenomenon and how cementitious materials become water saturated. Based on Figure 1-2, it is clear that the value of  $S_{cr}$  is independent of the total air content and found in both mortars and concretes. As suggested in Section 2.3, by connecting the work conducted in [16,32] a connection between the spacing factor, or some representation of the spacing between the entrained air voids, and the degree of saturation might influence the value of  $S_{cr}$ . In effort to understand this phenomenon holistically, the practical first step is to understand the underlying physics behind the saturation of the material, what parameters govern its long-term rate, and what effects a certain level of saturation has on the mechanical response of the cementitious material when frozen.

As briefly discussed in Section 1.3, air-entrained cementitious materials have two distinct saturation regimes when fully immersed in a fluid or liquid water. For specimens conditioned at low values of relative humidity these two regimes can be treated as linear on a square root of time plot. The first saturation rate,  $S_1$ , is dominated by small, interconnected capillary pores, which range in size from 10nm to hundreds of nanometers [36]. These pores fill first due to high suction potential, understood by the Young-Laplace equation, resulting in fast imbibition [19]. The second saturation rate,  $S_2$ , has been theorized to occur through the dissolution and diffusion of trapped gaseous air in the

entrained and entrapped air voids [18], which range in size from tens of microns to multiple millimeters [36]. The intersection of the two saturation regimes is referred to as the matrix saturation point,  $S_M$ , where all of the capillary pores are assumed to be completely liquid-water saturated while the air voids remain empty or gas-filled as shown in Figure 2-5 [19,29].

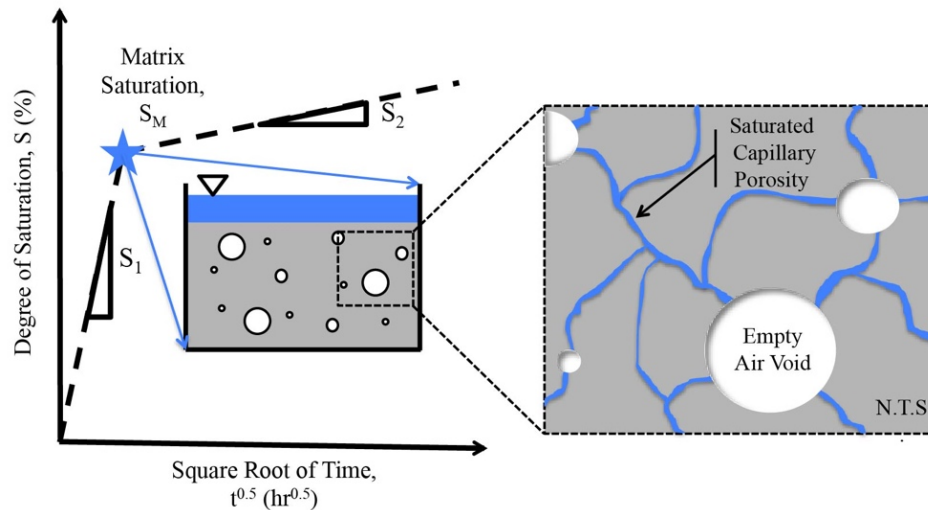


**Figure 2-5 - Idealized saturation curve of air-entrained cementitious materials and the nick saturation point which corresponds to water-saturated capillary pores and air-filled voids [19].**

In 1993, G. Fagerlund theorized three ways in which the air-voids could become water saturated [29], in attempt to predict the long-term saturation rate,  $S_2$ . The three models presented in [29] evaluate the: 1. rapid dissolution of compressed air in an air void into the surrounding water-saturated porous cement paste, 2. Diffusion of dissolved air from a smaller to a larger air void, and 3. Diffusion of dissolved air to a free surface of ponded water. Section 3.2 contains a full review of Fagerlund's models. From the second model, Fagerlund concluded that it was thermodynamically favorable for air voids to fill in order of increasing size (i.e., from smallest-to-largest), but did not consider a

representative 3D system with a polydisperse air void system and the general formulation neglected the coupled influence of dissolution, diffusion, and advection. Additionally, based on insights from the original models in [29], it was displayed that the water saturation of the air voids could lead to an increase in the mean half-distance of between the non-saturated air voids system [25], increasing the likelihood of failure if exposed to freezing as shown in Figure 2-3.

The mechanical response of air-entrained cementitious materials can be directly evaluated using a poromechanical formulation [37–39] and probabilistic limit-state functions [31] that capture the governing physics of freezing in porous media. In 2008, Coussy and Monteiro extended poromechanical theory to assess the multi-phase (i.e., liquid, ice, solid) nature of freezing in air-entrained cementitious materials [37]. Initial outcomes predicted that the hydraulic and crystallization pressures can result in tensile pressures in excess of 10 MPa – well above the tensile capacity of cementitious materials. In 2011, Zeng et al. [38] validated the poromechanical model for air-entrained and non-air-entrained hardened cement pastes specimens by predicting longitudinal strain as a function of temperature depression. Figure 2-6 displays outcomes of the model where experimental data was taken from [32] and shows that spacing factor,  $\bar{L}$ , separates tensile and compressive strain regimes for well-saturated, air-entrained cement pastes exposed to constant temperature depression below freezing. Section 4.2 will clearly detail the current theory for these models. Lastly, in 2016, Mayercsik et al. used the poromechanical model to evaluate the influence of different size distributions of entrained air voids on FT performance and displayed that an improved description of the mean distance between entrained air voids is necessary to accurately predict FT failure in concrete [40].

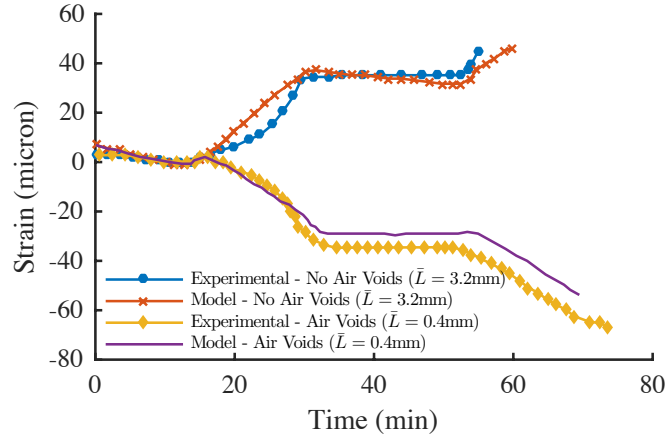


**Figure 2-6 - Result of poromechanical model developed in [38] where strain is in the longitudinal direction of specimens taken from [32].**

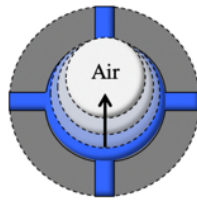
As shown in [39], improved characterization of air void systems is necessary to improve the prediction and overall design of cementitious materials for FT resistance. In the original derivation, Powers states that the spacing factor,  $\bar{L}$ , is a gross over-estimation of the real air void spacing [13]. As developed in [40] and evaluated in [39],  $\bar{M}$ , which is based upon nearest-neighbor calculations, was found to have an improved correlation with FT performance assessed by the ASTM C666 Durability Factor [41]. In addition to developing improved characterization methods for air-entrained cementitious materials, it is also necessary to automate previous experiments that are time-consuming and costly. In 2015, Fonseca and Scherer [42] developed an automated methodology to evaluate the size distribution of entrained and entrapped voids in cementitious materials using a flatbed scanner, standard preparation techniques established in ASTM C457, and an open source MATLAB suite. While [40,42,43] have significantly improved the state-of-the-art, validated and reliable on-site evaluation techniques of air-entrained cementitious materials are also necessary to translate theory to practice in a manner that can be required by international specification organizations.

## **2.5 Proposed Work: Knowledge Gaps and Technical Needs**

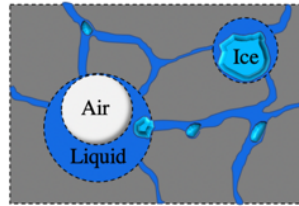
In effort to advance the state-of-the-art in research, on-site assessment techniques, and specifications, knowledge gaps and technical needs are identified and used as the basis for the conducted research presented herein. The knowledge gaps identified in Section 2.5.1 are related to current uncertainties or inconsistencies related to fundamental mechanisms and the physics needed to predict  $S_{cr}$ . Technical needs, detailed in Section 2.5.2, identify necessary advancements in on- and off-site characterization tools for cementitious materials and updated specifications. By filling in the identified knowledge gaps and removing critical technical needs, the state-of-the-art in research can be leveraged to direct the field towards service-life design of cementitious materials in FT environments. Figure 2-7 shows a general framework for the 5 respective research thrusts.

### **Knowledge Gaps:**

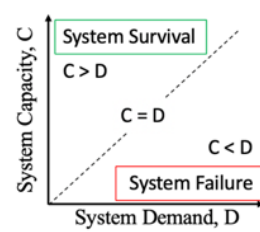
A). Understand air-void saturation.



B). Predict  $S_{cr}$  when material is freezing.

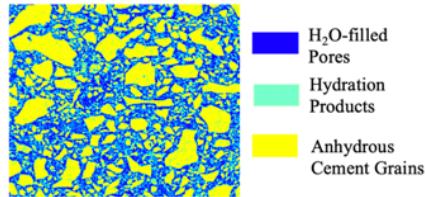


C). Evaluate material and environmental influence.



### **Technical Needs:**

D). Predict material property evolution.



E). Recommend modern ACI specifications.

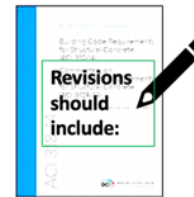


**Figure 2-7 - 5 research thrusts proposed in Sections 2.5.1 and 2.5.2 and evaluated in Chapters 3 to 7.**

## 2.5.1 *Identified Knowledge Gaps*

### 2.5.1.1 Long-Term Saturation Mechanisms

As detailed in Section 2.4, the underlying physics driving the long-term water saturation of air-entrained cementitious materials on the pore-scale has to yet be satisfactorily detailed. Based on [26], it is clear that the size and spatial distribution of the air voids has a significant effect on long-term saturation, but a physics-based model on the air-void scale that couples the dissolution of trapped air in the air void and its resulting diffusion and advection through the capillary matrix of a cementitious material leading to increasing saturation remains unanswered. Recently, Eriksson et al. [44], developed a multi-phase model to explain the macroscopic hygro-thermal-mechanical nature of saturating cementitious materials, but fundamental questions still remain regarding how

pore or air-void scale phenomena should influence macro-scale saturation rates. The first critical step toward using  $S_{cr}$  as a service-life metric depends on the accurate modeling of pore-scale phenomena and scaling the problem appropriately to eventually predict the time to  $S_{cr}$  and understanding the parameters that most significantly influence it. Within Chapter 3 two models are developed. The first, termed the single-void dissolution kinetics (SVDK) model, develops and describes the kinetics of air void saturation at the single air void scale. The second model, termed the multi-void dissolution kinetics (MVDK) model, leverages the SVDK model but in a cubic sample with a polydisperse air void system.

#### 2.5.1.2 Critical Saturation Mechanism

The second major knowledge gap is the current lack of a validated physics-based model that predicts the  $S_{cr}$  value for a broad range of cementitious materials. In short, a clear mechanism for what governs the magnitude of  $S_{cr}$  has yet to be displayed. Due to the fact that water expands approximately 9% when frozen, understanding why failure begins to occur in cementitious materials saturated at and above 85% requires a better understanding of the physics of saturation and freezing in cementitious media. As detailed in the experimental outcomes from [16,32] shown in Section 2.2 and [17,29,45] it is expected that there is a relationship between the likelihood of failure initiation, the mean spacing of the air voids, and the saturation state. To address this problem, a novel, physics-based limit-state model is derived to predict the likelihood of failure at various levels of water saturation of a 3D polydisperse air void system that simulates long-term saturation (i.e., the saturation of entrapped and entrained air voids). Additionally, the saturation modeling results will be used to inform how air voids become water-filled complementing

and expanding on other proposed air-void filling theories present in the literature [25,29,44].

### 2.5.1.3 Relative Influence of Design Parameters and Performance Prediction

In terms of design, it is essential to understand the relative influence that design parameters have on FT performance and  $S_{cr}$ . Additionally, it is necessary to understand how common material parameters that are currently specified by ACI committees for FT durability and those that are easily evaluated on an active construction sites correlate with FT durability and resistance. By using a limit-state formulation developed for the modeling the magnitude of  $S_{cr}$ , a first-order reliability method (FORM) is leveraged to predict the likelihood of failure for a large database of concretes using parameters that are standard to the industry (i.e., w/c ratio, compressive strength, total air content, and spacing factor) and compared to those same concrete's ASTM C666 Durability Factor [41] for means of validation. The FORM assessment also results in importance vectors which detail how unit changes in model inputs and parameters influence the probability of failure. This information can then be used to assess whether the current ACI durability standards are specifying the most salient parameters and how specifications could be changed to ensure durability.

## 2.5.2 *Identified Technical Needs*

### 2.5.2.1 A Data Science Approach for Process-Structure-Property Linkages of Hydrating Cement Pastes

The first identified technical need is a well-established and data-driven approach for process-structure-property (PSP) linkages for cementitious materials. The study and prediction of the long-term and critical saturation mechanisms respectively depend on material properties of the material (i.e., diffusivity, intrinsic permeability, tensile strength, etc.). Therefore, it follows that being able to predict the final properties of a cementitious material is essential to design and service-life prediction. For the purposes of this approach, it is displayed how the diffusivity property of cement paste can be predicted as a function of total hydration time and w/c ratio for a standard Portland Cement using a Material Informatics framework.

#### 2.5.2.2 Unification and Modernization of ACI Freeze-Thaw Durability Specifications

The final technical need is centered on the unification and modernization of ACI freeze-thaw durability specifications. As previously detailed, the current specifications are neither consistent across the three major committees 201, 318, and 350, and their current status does not reflect the state-of-the-art in translated research science. In addition to evaluating the current standards ability to ensure freeze-thaw performance – as measured by the ASTM C666 Durability Factor - the existing legal precedent and contractor requirements are reviewed to provide realistic recommendations for design engineers to specify and contractors to construct.

# CHAPTER 3. MECHANISM FOR THE LONG-TERM SATURATION RATE OF AIR-ENTRAINED CEMENTITIOUS MATERIALS

## 3.1 Introduction

In recent years, the critical saturation ( $S_{cr}$ ) of cementitious materials has gained significant attention [18,19,21,33,46] due to its ability to predict when freeze-thaw-induced damage will initiate [16–18,45]. The time it takes for fully water-immersed concrete specimens to reach  $S_{cr}$ , referred to as time to critical saturation ( $t_{cr}$ ), has recently been incorporated in AASHTO PP84 [47] to ensure a minimal service life in freezing-and-thawing environments. Beginning in [33] and extended in [18,21], it was recognized that experimentally obtained long-term saturation rate values can be used to estimate  $t_{cr}$  assuming an experimental  $S_{cr}$  value of 85% [16–18]. The long-term saturation of air-entrained cementitious materials, idealized as a heterogenous porous solid with dispersed spherical voids as shown at the specimen-scale of Figure 3-1, refers to the slow and time-dependent process in which air-entrained cementitious material move from its matrix saturation,  $S_m$ , to its critical saturation  $S_{cr}$  [29]. Although significant progress has been made experimentally in understanding how  $S_{cr}$  can be leveraged as a service-life assessment tool, the fundamental mechanism by which air voids in cementitious materials become slowly water-filled needs to be better understood theoretically.

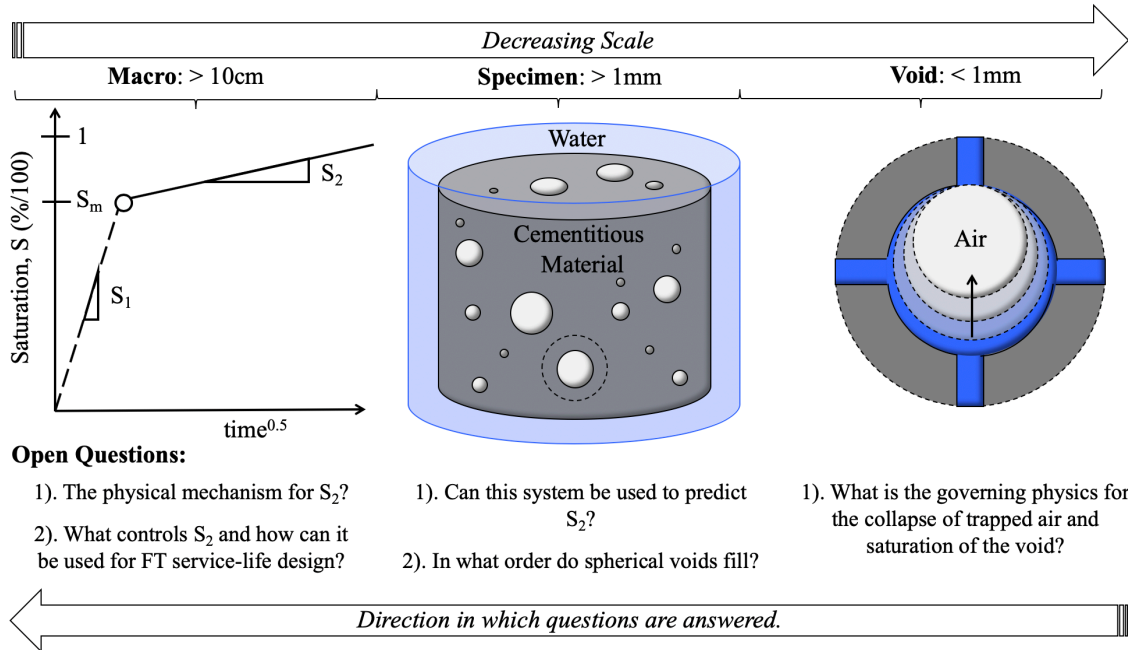


**Figure 3-1 - Visual connection of various scales which influence the saturation behavior of air entrained cementitious materials.**

The long-term saturation rate,  $S_2$ , is hypothesized to occur due to the dissolution and diffusion of compressed air in the entrapped and entrained air voids [18,29], as shown at the void scale of Figure 3-1. Once the material reaches its matrix saturation (i.e., when the capillary porosity of the cement matrix is saturated with liquid water), trapped air is compressed by the Laplace pressure resulting from surface tension effects which induces dissolution of the compressed air into the fluid within or in the vicinity of the air void [29,48]. This dissolved air slowly diffuses outward while liquid water flows toward the air void, resulting in a slowly increasing saturation of the air void and the complete dissolution of the initially trapped air [48]. However, despite previous efforts, the coupled mechanism of dissolution, diffusion, and advection that lead to the saturation of a single air void, or as group of air voids (i.e., a realistic 3D system), has yet to be clearly expressed in a single, physics-based model [19]. For the purposes of the efforts presented within this chapter, the

theoretical water-filling mechanisms for a single air void surrounded by a cement paste shell will be developed in Section 3.3 followed by a polydisperse system of air voids in a cube of paste in Section 3.4.

The first model, presented in Section 3.3, focuses exclusively on the dissolution kinetics for a single spherical air void, termed the Single Void Dissolution Kinetics (SVDK) model. The second model, presented in Section 3.4, then leverages the SVDK formulation to assess the macro- or specimen-scale long-term saturation behavior of air entrained cementitious materials that are fully immersed in liquid water. The latter model is termed the Multi-Void Dissolution Kinetics (MVDK) model. Ultimately, the aim of the work presented within this chapter is to provide the theoretical foundation to predict and understand which parameters significantly influence the time to critical saturation which can be used as a conservative service-life estimation by design engineers.

In effort to ensure that the governing physics of how air voids become increasingly water-filled is captured, theoretical and experimental efforts made in various fields, ranging from macro-scale investigations of water-immersed mortars [22] to micro-fluidic studies on the dissolution of trapped gas bubbles [49], are critically reviewed. The review will first assess macro-scale phenomena and progressively move in the direction towards the void scale – as the long-term saturation of cementitious materials occurs due to the slow saturation of large porosity [29,50] (i.e., spherical air voids which range on the order from  $10\mu\text{m}$  to  $1\text{mm}$  in radius and are interconnected by irregular capillary pores which are orders of magnitude smaller [36]). Additionally, fundamental questions are identified which are central to understanding the governing dynamics of time-to-full-dissolution of air within a single spherical air void as shown in Figure 3-1.

It is important to note that the following work has been found to have a broad range of application and contribution. The dissolution of trapped gaseous air has major relevance and significance in fields ranging from carbon capture [51] to drug delivery [52] and bioremediation [53]. Due to this, the formulations presented in the SVDK and MVDK are written in a very general form to allow for translation across academic and intellectual fields of interest. With respect to the findings and results, they are presented for cementitious material systems immersed in liquid water to promote continuity within the document and are compared to: validated models of simple systems [54,55] (i.e., a gas bubble suspended in an infinite amount of liquid), micro-fluidic studies [49,54,56,57], and to findings of imaging studies [50] which provide a temporal sense of when near-surface air voids of a given size should become completely saturated.

### **3.2 Literature Review**

The literature review provided for the formulation of the SVDK and MVDK models is divided into theoretical and experimental sections. Theoretical Section 3.2.1 details the seminal contributions that serve as the technical basis for the formulation of the SVDK and MVDK models. Additionally, previous studies are reviewed and used as a means of comparison for how the presented work advances the state-of-the-art in predicting the long-term saturation rate of air entrained cementitious materials. Experimental Section 3.2.2 is organized into two sections. The first section treats specimen-scale phenomena, where the behavior of cementitious materials immersed in a fluid is studied using a variety of experimental techniques. The second section evaluates known void-scale phenomena, where micro-fluidic models are used to provide insight into the phenomenology that would occur within a saturating air void.

### 3.2.1 Theoretical Modelling

In 1950, Epstein and Plesset [55] developed a model for the evolution over time of a single bubble of gas suspended in a liquid solution. They displayed that by considering mass-balance at the bubble-liquid interface the reduction, growth, or stability of the bubble could be explained. In summary, their derivation was formed around the equivalence of mass-fluxes at the gas-liquid interface where thermodynamic equilibrium must be maintained. Equation 3-1 displays their final partial differential equation and Table 3-1 defines its terms. A detailed derivation can be found in [54]. Additionally, multiple forms of the original Epstein-Plesset equations can be obtained when neglecting temporal and surface-tension effects, as shown in [54,58]. From Equation 3-1, it can be directly seen that the term  $f$ , which represents the ratio of the initial dissolved gas concentration in the surrounding infinite fluid to the saturated concentration, will dictate whether the bubble with radius,  $R$ , will grow or shrink. With respect to gas bubbles that have surrounding liquids that are not saturated with dissolved gas species (i.e., a value of  $f \leq 1$ ), the model predicts that a gas bubble with initial radius  $R_0$  will completely dissolve due to an internal pressure (given by the Laplace equation) larger than that of the surrounding fluid, which drives the dissolution of gaseous species, understood by Henry's Law, followed by Fickian transport.

**Equation 3-1 - Epstein-Plesset Model [54,55].**

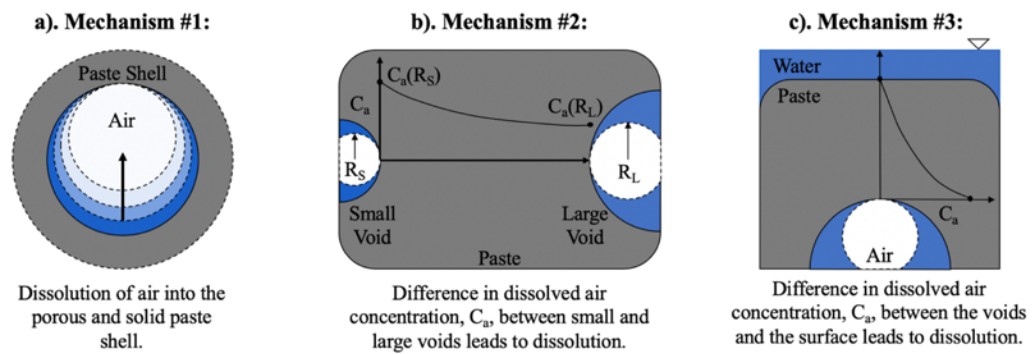
$$\frac{dR}{dt} = -Dk_HGT \frac{1 - f + \frac{2M_w\sigma}{\rho GTR}}{1 + \frac{4M_w\sigma}{3\rho GTR}} \left[ \frac{1}{R} + \frac{1}{\sqrt{\pi Dt}} \right]$$

**Table 3-1 - Definition of terms for the Epstein-Plesset Equation found in Equation 3-1.**

<b>Term:</b>	<b>Definition:</b>
R	Bubble radius (m)
T	Time (s)
D	Diffusivity of dissolved gas in surround liquid (m <sup>2</sup> /s)
k <sub>H</sub>	Henry's constant (kg/m/Pa)
G	Universal Gas Constant (m <sup>3</sup> Pa/mol/K)
T	Temperature (K)
f	Ratio of initial concentration to saturated concentration (-)
M <sub>w</sub>	Molecular weight of the gas (kg/mol)
σ	Surface tension of the air-water interface (N/m)
ρ	Density of the gas at atmospheric pressure and the initial temperature (kg/m <sup>3</sup> )

Recognizing the applicability of the work in [55] to the long-term saturation of air-entrained cementitious materials in [29], G. Fagerlund proposed three ways in which air voids in cementitious materials could become fully water-saturated. To initiate the dissolution-driven system, Fagerlund assumed that air is trapped in the voids due to the fast

imbibition of water into the capillary porosity, characterized by saturation rate  $S_1$  in the bilinear saturation curve shown in Figure 3-1. Once the gaseous air is trapped in the void it is then compressed to satisfy Laplace effects – given by the size of the void and taking the water in the surrounding capillary pores to be at atmospheric pressure. As a result, the system is a spherical air bubble that is surrounded by a porous paste shell in which the capillary porosity is completely water-saturated, as shown in Figure 3-2a.



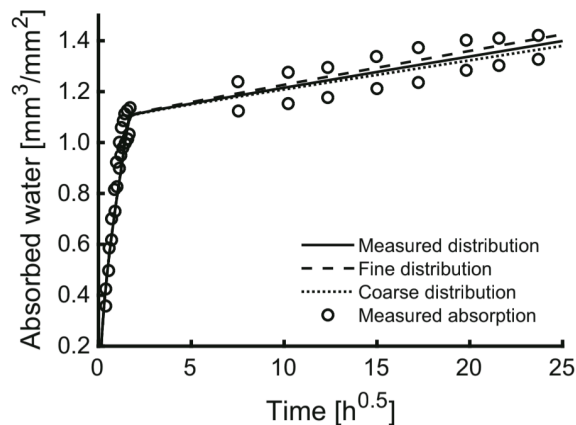
**Figure 3-2 - General mechanisms developed by G. Fagerlund in [29] for how air voids in cement pastes become water-saturated.**

Figure 3-2 shows a general schematic of the models discussed in [29]. The first mechanism suggested that the compressed air will rapidly diffuse into the paste shell if enough water exists in the surrounding capillary pores and that the water is not already saturated with dissolved air. Although this mechanism considers the influence of the initial state of the surrounding capillary water, similar to the term  $f$  in Equation 3-1, it provides no insight into how water enters the void or the time-dependent mass conservation of air and water in the total system. In the second model, shown in Figure 3-2b, it was suggested that the dissolved air diffuses from small to progressively larger air voids that are nearby, in the spirit of Ostwald ripening. Seeing as how the concentration at the gaseous air-liquid interface is proportional to the inverse of the compressed air bubble size, a concentration

gradient of dissolved air would exist between a small and large air void, as shown in Mechanism #2 in Figure 3-2b, and result in diffusive flow of dissolved air through the water-saturated paste. In the third model, Fagerlund proposed that the saturation of air-entrained cementitious materials depends on the diffusion of the dissolved air within the voids to the surface of the specimen where the concentration of dissolved air is low (assuming that the entire specimen is immersed in water) – see Mechanism #3 in Figure 3-2c. In [29], it was additionally displayed how to leverage Mechanism #2 to predict the concurrent filling of a system of air voids and the resulting long-term saturation.

While the work in [29] suggested how air voids could fill with water (i.e., into surrounding porosity, into one another, and to the surface), clear systems of equations, state equations, and boundary conditions were not developed to aid in the fundamental understanding of how air voids become progressively saturated. Moving from the air-void scale to the specimen-scale, numerous efforts have been put forth to explain the fast initial imbibition of a surrounding fluid into cementitious materials, characterized by saturation rate  $S_1$  [59–61]. For the purposes of this work, understanding the slow secondary saturation rate,  $S_2$ , is of greater interest. In 2018, Eriksson et al. [44] derived a multi-phase (i.e., solid, liquid, gas) transport and mechanics model to assess the entire saturation curve for air-entrained cementitious materials. Until the idealized specimen arrived at its value of matrix saturation,  $S_m$ , the model follows a similar imbibition study found in [61]. Once a representative elementary volume (REV) in the analysis arrives at its matrix saturation  $S_m$ , Eriksson et al. assumes that the air voids, which are homogenized within a REV, are filled with compressed air. The compression, as in Fagerlund’s work, results in dissolution of air and diffusion of dissolved air through the system and leads to a slow increase of water

saturation. The results of the model were found to agree very well with experimental results taken from [25] and suggested that air void systems with more coarse, or broad, air void size distributions saturate more slowly as shown in Figure 3-3. Additionally, it is important to note that in the work of Eriksson et al. the air voids within an REV are assumed to fill in order of increasing size from [29].



**Figure 3-3 - Results from work of Eriksson et al [44].**

A multitude of other models exist which aim to predict the time to critical saturation of air-entrained cementitious materials but use experimental data as the basis for which to do so. In [21,33,35] the time to critical saturation is predicted using the value of secondary saturation rate, which is related to the secondary sorptivity, following the work presented in [18]. This method is reliable and can be done to validate that specific concrete or mortar mixtures have a desired minimal service-life. The approach has been adopted by AASHTO [47]. Additionally, based on the assumptions presented and found in [17,29,44], recent efforts have shown how a simple geometric model can be used to predict the evolution in Powers' spacing factor [13,41] between remaining air-filled voids, as more and more air voids become water-saturated [25]. The presented efforts have provided significant insight

and advancement with respect to how air-entrained cementitious materials may become increasingly saturated. Nonetheless, numerous gaps remain with respect to governing mechanisms at the air void-scale. The central intention of the SVDK model, found in Section 3.3, is to then build on what has been presented in a complementary manner in effort to provide fundamental insight into the water-saturation mechanism for single air voids that occur below the REV scale for models similar to [44]. Section 3.4 then builds upon knowledge of how single air void saturate derived from the SVDK and leverages it in a cubic porous solid system with a polydisperse air void system, termed the MVDK model.

### 3.2.2 *Experimental Results*

#### 3.2.2.1 Specimen-Scale Phenomena

In 2012, based on a series of highly controlled sorption tests, Li et al. [18] displayed that the secondary saturation rates,  $S_2$ , as shown in Figure 3-4, were approximately equivalent irrespective of the total air content or the relative humidity at which the mortar specimens were conditioned at prior to conducting ASTM C1585-04 – the standard sorption experiment. This finding served as the justification for a series of models, similar to those found in [33,34], that predicted the time to critical saturation [21,35]. Figure 3-4 displays the concatenated findings from [18] and shows the similarity in secondary saturation rate  $S_2$  for the respective sorption tests.

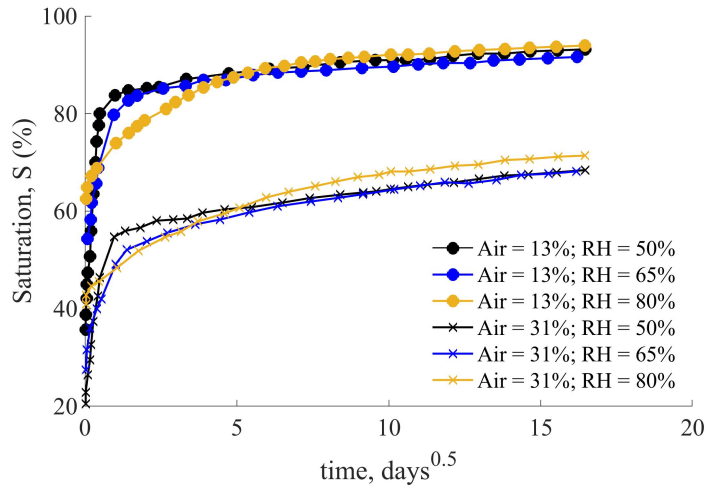


**Figure 3-4 - Concatenated sorption findings from [18].**

Figure 3-4 shows that as the relative humidity at which the samples were conditioned prior to conducting sorption testing increases the matrix saturation point (identified as a kink in the saturation versus square-root-of-time curve) is not clearly identifiable. In [62], using neutron radiography, it was displayed that after 12 hours of fluid exposure, air-entrained and non-air-entrained mortars remained below their matrix saturation point from depths of 5mm to 25mm within the specimen. Additionally, at twelve hours of testing it was found that the degree of saturation for all of the specimens were within 5% of the matrix saturation, but not above it at any point, irrespective of the degree of cement hydration. This finding suggests that the initial saturation regime is exclusively driven by capillary action leading to a saturation state at which the capillary pores are fully liquid-saturated and the air voids remain filled with gaseous air. It follows then that for long-term fluid exposure the entrained and entrapped air voids will begin to saturate and make the material progress toward a critically saturated state as shown at the void scale of Figure 3-1.

In 2017, Moradllo and Ley [50] published a series of 8.8 $\mu\text{m}/\text{voxel}$   $\mu\text{CT}$  results obtained by ponding a potassium iodide solution on top of a cement paste for up to 60 days. Although the paste was not air-entrained, a distribution of spherical voids was found in the hardened specimen and a final analysis was done with respect to their final saturation state. In [50] the cylindrical specimen, size distribution of air voids within the first 6mm of the sample, and which voids became saturated and remained air-filled were displayed as shown in Figure 3-5. It is important to note that the first 6mm was selected because of a homogeneous concentration in potassium iodide solution within that region (i.e., it was uniformly solution-saturated). Based on their results, it is clear that the air voids, which ranged from 20 $\mu\text{m}$  to 500 $\mu\text{m}$  in radius, did not fill solely as a function of increasing size. This finding suggests that further efforts are needed to investigate the nature of how air voids become saturated by considering the effect of the relative location of the air voids with respect to one another and their respective distance to a free surface of the specimen.

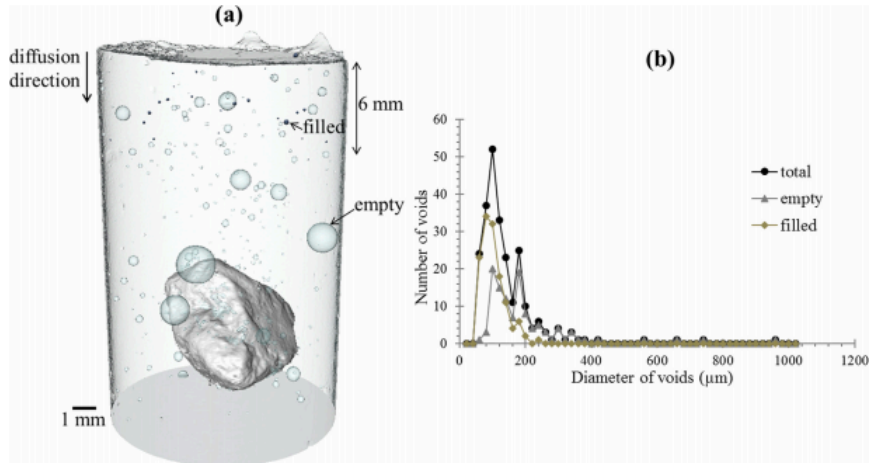
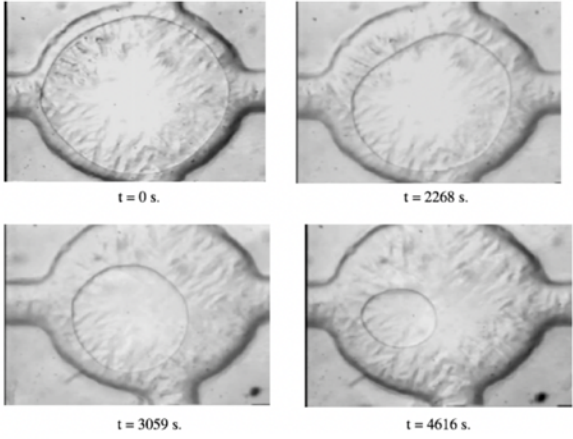
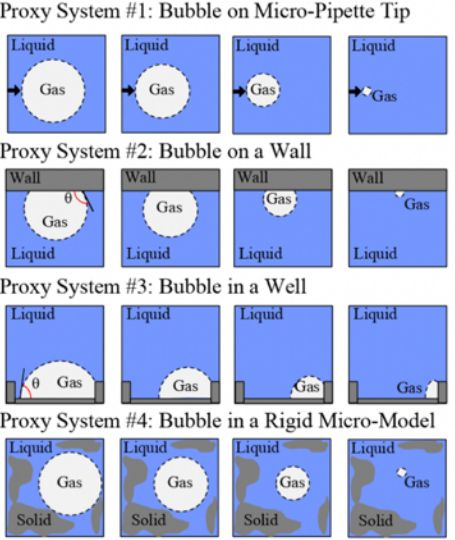


**Figure 3-5 - a).  $\mu$ CT specimen b). filled vs. non-filled analysis for air voids within the first 6mm of the specimen [50].**

### 3.2.2.2 Pore-Scale Phenomena

As detailed in Section 3.2.1, an experimental investigation capturing the saturation dynamics of a single air void in a cementitious material has yet to be conducted. A great deal of understanding can be gained by studying proxy systems, as idealized in Figure 3-6a, of trapped air or immobile bubbles undergoing a temporal process of dissolution, diffusion, and advection that leads to complete liquid saturation. Proxy system 1, idealized from the work conducted in [54,58], provides a simplistic gas-liquid system and was used as a basis to evaluate Epstein and Plesset's original model presented in Section 3.2.1. Proxy systems 2 and 3, in which a gas bubble is resting underneath a flat plate [54,57] or within a well [63] have also been extensively studied experimentally and numerically. Lastly, proxy system 4 provides the closest 2D approximation of how a highly tortuous micro-model can be idealized and used to study the in-place dissolution dynamics of trapped gases [49,56,64]. A series of images capturing the dissolution of a trapped isobutanol bubble within a silica micro-model is shown in Figure 3-6b.

Temporal Evolution of Proxy Systems →



a). b).

**Figure 3-6 - a). proxy system examples, b). example of dissolution of isobutanol in water as a function of time [49].**

In addition to gaining a qualitative understanding of how compressed gases dissolve in gas-saturated liquids, it is well-established [65] that the temporal evolution of droplets and bubbles often follow a universal power-law scaling (i.e., that the radius evolves as a power-law of the difference between the time-to-full-dissolution and the actual time, see Figure 3-7a). As displayed in [65,66], for steady-state and diffusion-controlled conditions, the radius and time of liquid droplets have such  $\frac{1}{2}$  power law relationship. Referring to Equation 3-1, when the temporal term and surface tension are neglected and  $f$  is unity, it can be shown that the size reduction of a gas bubble surrounded by an infinite amount of fluid follows such a  $\frac{1}{2}$  power law. However, when these assumptions are not made, the exponent of the power-law relationship can significantly vary. Figure 3-7a displays a concatenated group of experiments representing proxy systems 1 to 4, for which time-to-full-dissolution was fit so that power-law relationships were obtained. Based on these

analyses, it can be seen that the determined exponents of the power-law relationship, found in the legend and denoted by C, range from 0.33 to 0.86. Figure 3-7b displays the determined exponents of the power-laws for solutions to the Epstein-Plesset equation for various values of f and surface tension. From Figure 3-7b it can be seen that the exponent of the power-law ranges from 0.36 to 0.52 for the Epstein-Plesset model. For proxy systems 1-3, the exponents found for the radius-time relationship agree well. The exponents found for proxy system 4 are generally higher, which is attributed to the influence of dealing with a non-3D system.

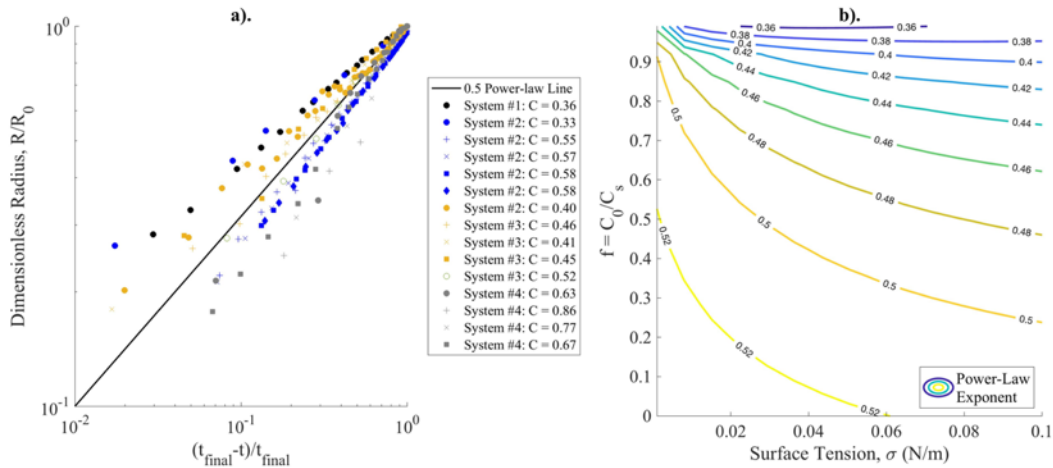


**Figure 3-7 - a). Outcomes of fit-power laws to a large class of proxy-systems [49,54,56,57], b). Exponent of power-law fits for solutions to the Epstein-Plesset model for initial bubble radius of  $15\mu\text{m}$ .**

It is also important to note that the Epstein-Plesset model has been experimentally validated. In 2004 and 2006, Duncan and Needham [54,67] displayed the ability of the model presented in [55] to predict the size reduction of gas bubbles placed on the tip of a micro-pipette or against a flat, impermeable wall – see Figure 3-8. Original results for the validation can be found in [54]. Additionally, the exponent of the power-law relationship

between the radius and time history was found to be 0.37 and 0.33, for the bubble on the micro-pipette and resting on a flat wall, respectively. Based on the reduction in exponent, the presence of the wall causes the radius of the bubble to reduce in size slower than if it was suspended in an infinite liquid, which is a state of isotropic diffusion. Although the presented proxy systems are significantly more ideal than what can be expected in air-entrained cementitious materials, their analysis still provides profound insight into the qualitative and quantitative nature of how trapped gases reduce in size as a function of their surroundings.

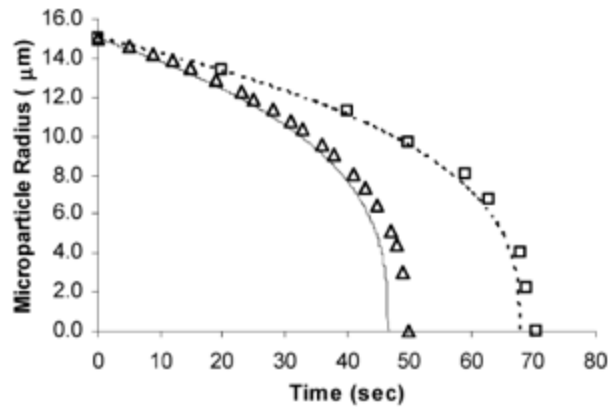


**Figure 3-8: Experimental validation of the Epstein-Plesset equation [54] where triangles represent an air bubble on a micro-pipette tip and squares represent an air bubbles resting on a flat wall.**

### 3.3 Void-Scale: Single-Void Dissolution Kinetics (SVDK) Model

By considering the following pore-scale and specimen-scale findings presented in Section 3.2.2 in a consistent framework, it is clear that many open questions still exist. Regarding the long-term saturation phenomenon, a central question that remains is: by what physics-based mechanism do the spherical air voids become water-, or liquid-, saturated? Section 3.3 is oriented around deriving a model which advances current answers

to this void-scale question. Pending an improved understanding of the pore-scale phenomenology, it is also of interest to see how its behavior compares to the Epstein-Plesset model detailed in Section 3.2.1 and the proxy systems displayed in Section 3.2.2.2.

As displayed in Figure 3-9a, the macro-system of interest is a porous cementitious paste in which spherical air voids can be found - analogous to the  $\mu$ CT specimen assessed in [50]. For the purposes of the ensuing section, the macro-system is considered to be fully immersed in water and when a spherical region is taken around a single air void, the capillary pores connect the air voids to the surface of the specimen and one another. Figure 3-9b, building on Figure 3-9a, then shows that the following work is interested in understanding how the secondary saturation rate occurs due to the saturation of single spherical air voids. The pore-scale image below the saturation curve in Figure 3-9b qualitatively displays how compressed air is expected to behave once the void-scale system has reached the matrix saturation,  $S_m$ . The evolution of the air-liquid interface was informed by experimental outcomes that captured the dissolution of trapped gas in infinite liquid or micro-models - displayed in Figure 3-6b – which serve as proxy systems of study for air-entrained cementitious materials.

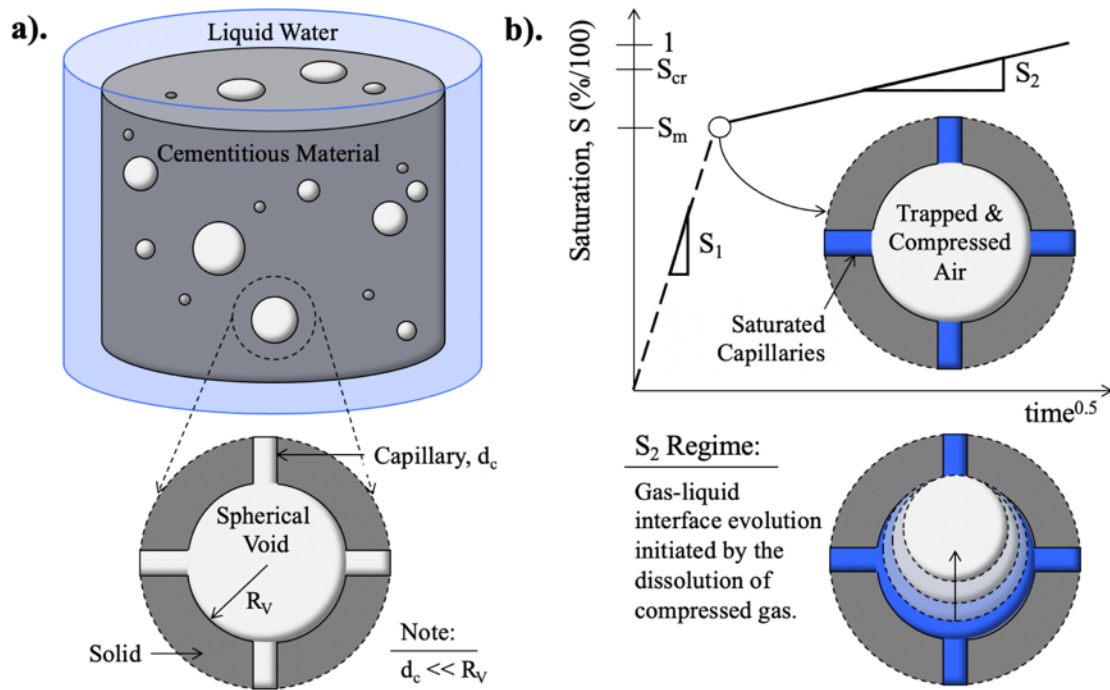


**Figure 3-9 - a). Idealized air-entrained cementitious material system that is fully immersed in water and single air void-shell system, at the moment when it is immersed b). standard bi-linear saturation curve for air-entrained cementitious materials [18] and idealized saturation behavior of the air-void shell system which is initialized by the compression of gaseous air and its resulting dissolution into the surround saturated capillary porosity [29].**

From now on within this section, an individual air void surrounded by a spherical shell of saturated cement paste is considered. The modeling of the progressive saturation of this air void will lead to what we call the single-void dissolution kinetics (SVDK) model. Within Sections 3.3.1 to 3.3.3 the single-void dissolution kinetics (SVDK) model is derived to provide insight into how air voids in cementitious materials, and other analogous porous media, become saturated over time. Section 3.3.1 defines a system which can be mathematically evaluated and how the gaseous air-liquid interface can be represented at any level of air-void saturation. Within this section, specific attention is given to how the system can be initiated at time  $t = 0$  and the implications that the initial geometry will have

on the long-term dissolution kinetics. Section 3.3.2 contains the model formulation and presents assumptions. Detail is given to how the assumptions can be expected to influence the model outcomes with corresponding justifications. Section 3.3.3 provides the results and an extended discussion of the model outcomes. Lastly, Section 3.3.4 contains conclusions, implications of the model outcomes for the broader field of cementitious-material durability research, and opportunities for future work for void-scale modeling.

### *3.3.1 SVDK System Definition and Mechanisms*

The initial step to developing and understanding the dissolution of compressed gas within a single air void, and its resulting saturation, is idealizing the system, and in particular its geometry, so that it can be mathematically represented. Figure 3-10 shows the bilinear saturation regime common for air-entrained cementitious materials where saturation rate  $S_2$  characterizes the dissolution-driven regime. As detailed, it is of interest to understand this long-term saturation phenomenon at the void-scale as the matrix saturation represents the saturation state at which all of the capillary pores are filled with liquid water and the larger spherical voids contain trapped gaseous air.

The contact angle of the liquid at the surface of the air void is denoted  $\theta$  and is assumed to remain constant over time. From the fluid-immersed macro-scale system, a spherical region of interest is defined around a single air void. The air bubble in the air void is considered to rest at the top of the air void because of gravity. Equation 3-2 displays the mathematical representation of the volume of the gaseous air region,  $V_g$ , trapped within the spherical void, which is the volume of intersection of two spheres of radius  $R_v$  (which is the radius of the air void) and  $R_{gl}$  (which is the radius of curvature of the air-liquid

interface) [68]. Following this equation, for a given contact angle  $\theta$  of the liquid-air-solid interface, there is a unique relationship between the liquid saturation of the air void with radius  $R_v$  and the radius of the gas-liquid interface,  $R_{gl}$  (see Figure 3-10). It is important to note that because  $V_g$  will evolve as a function of time during the saturation process, the radius  $R_{gl}$  will also vary temporally, which governs the Laplace pressure in the air bubble. Lastly,  $d$ , the lineal distance between the centers of the spheres of radius  $R_v$  and  $R_{gl}(t)$  is written in Equation 3-3. The volume of the liquid can then be directly calculated as the difference in the volume of the spherical void, given by  $(4/3)\pi(R_v)^3$ , and  $V_g$ .

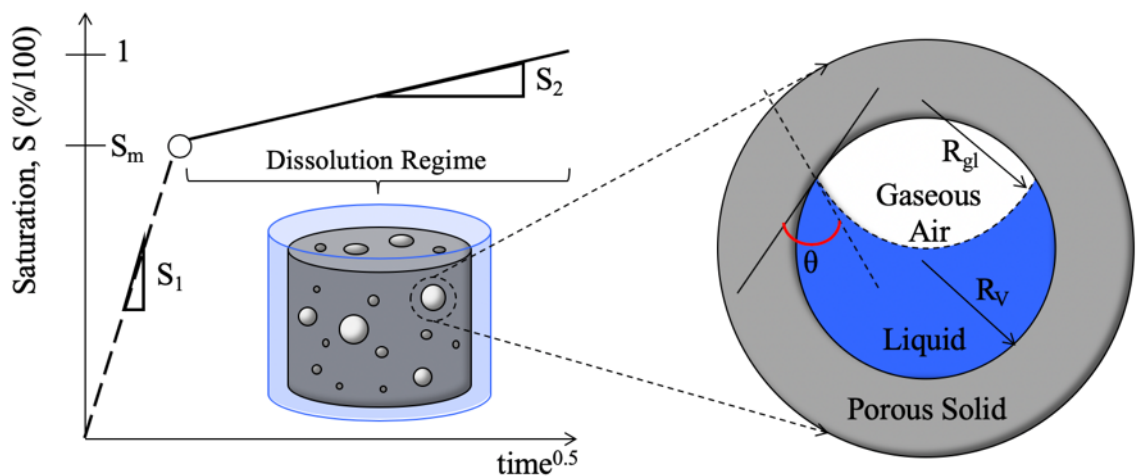


**Figure 3-10 - Spherical void-shell system and representation of the gas liquid interface which, for a given contact angle,  $\theta$ , can be parametrized by the radius of the interface,  $R_{gl}$ .**

**Equation 3-2 - Volumetric Intersection of two spheres [68].**

$$V_g(R_v, R_{gl}(t), \theta, d) = \frac{\pi}{12d} (R_v + R_{gl}(t) - d)^2 (d^2 + 2dR_{gl}(t) - 3R_{gl}(t)^2 + 2dR_v + 6R_{gl}(t)R_v - 3R_v^2)$$

**Equation 3-3 - Lineal distance, d, found in Equation 3-2 between spheres  $R_v$  and  $R_{gl}(t)$  [68].**

$$d(R_v, R_{gl}(t), \theta) = (R_v^2 + R_{gl}(t)^2 - 2R_v R_{gl}(t) \cos \theta)^{1/2}$$

The porous solid shell surrounding the spherical void shown in Figure 3-10 is considered to be saturated at all times and the capillary pores are no longer displayed since they are orders of magnitude smaller than the voids [36]. The stipulation that the capillary pores are always completely liquid-saturated implies that saturation states below  $S_m$  are not considered in the SVDK model. Because the initial imbibition of liquid through the surrounding capillary pores is assumed to be complete, it is uncertain if all of the original air in the void remains present or if more, or less, air is present than was present in the void's volume before immersion, when air was still at atmospheric pressure. For example, it is possible that, during the imbibition process, some of the air initially present in the capillary pores was forced into the spherical voids. Conversely, it is also possible that, during the imbibition process, part of the air initially in the air void could have escaped outward. Consequently, in this study, a large domain of initial gaseous air mass trapped in the air void is considered.

To define the initial geometry of the system at time  $t = 0$  (corresponding to the moment when all capillary porosity is saturated), for a given contact angle  $\theta$  of the liquid

on the solid, two parameters of the void-scale system need to be defined: the mass of the trapped gas in the void, and the initial pressure at time  $t = 0$  of the liquid,  $P_l$ , or of the gas,  $P_g$ . A normalized trapped mass of gas,  $m_t$ , is introduced where the mass used for normalization is that of air (considered as an ideal gas) at atmospheric pressure filling the spherical air void. The mass of gas trapped in the void,  $m_g$ , can then be calculated by Equation 3-4. Definitions for other terms presented in Equation 3-4 can be found in Table 3-1. To determine the initial geometry for a given normalized mass,  $m_g(t=0)$ , of trapped air, Equation 3-5 is numerically solved where  $R_{gl}(t=0)$  is the only unknown, as  $\theta$  is prescribed. Additionally, as is done in [29], it is assumed that at time  $t = 0$  the liquid pressure,  $P_l$ , is at atmospheric pressure,  $P_{atm}$ , so the pressure of the trapped gas (whose volume is given by  $V_g(R_v, R_{gl}(t = 0), \theta, d)$ ), is  $P_{atm}$  plus the Laplace pressure - which is inversely proportional to the radius of the gas-liquid interface,  $R_{gl}(t = 0)$ . It is important to note that other assumptions could have been made: for instance, it could have been assumed that the pressure of the trapped gas at time  $t = 0$  is equal to  $P_{atm}$ . This assumption on initial pressure, and its implications on the dissolution dynamics of the trapped gas, will be discussed within Section 3.3.4.

**Equation 3-4 - Determination of initial mass of trapped gas at time,  $t = 0$ .**

$$m_a(t = 0) = m_t \frac{P_{atm} \frac{4}{3} \pi R_v^3 M_w}{GT}$$

**Equation 3-5 - Determination of initial gas-liquid interface radius,  $R_{gl}(t = 0)$ .**

$$m_a(t = 0) - \frac{\left(P_{atm} + \frac{2\sigma}{R_{gl}(t = 0)}\right) V_g(R_v, R_{gl}(t = 0), \theta, d) M_w}{GT} = 0$$

Figure 3-11 displays a contour plot of initial normalized masses,  $m_i$ , of trapped gas, as a function of the contact angle,  $\theta$ , and of the radius of curvature,  $R_{gl}(t=0)$ , of the gas-liquid interface. Figure 3-11's contour plot can be understood as a 'look-up' chart for initial system geometries based on the previously presented assumptions. Next to the contour plot are a series of 6 different initial geometries, identified by letters A - F. Figure 3-11 shows that, for a given non-zero contact angle,  $\theta$ , if the trapped mass of air is larger than a critical value, there exists no solution to Equations 3-4 and 3-5: such states cannot exist physically under the assumption of liquid water at atmospheric pressure. For instance, for  $\theta > 32^\circ$  and a normalized trapped mass,  $m_i$ , of 1, Figure 3-11 shows that there are no initial geometries.

No contour plot can be drawn for trapped masses greater than the value given by Equation 3-6, which, in the present case of spherical voids with a radius of  $10\mu\text{m}$ , corresponds to a normalized trapped mass of 1.13. If a larger mass of air is initially trapped in the air voids, i.e. if, at time  $t = 0$ , air in the capillaries pores was pushed into the spherical void during the fast liquid water imbibition process, the air void would be completely filled with gaseous air and the gas-liquid interface would be located inside the capillary pores rather than inside the air void. In such case, the geometry of the gas-liquid interface would no longer be governed by Equations 3-4 and 3-5. It is possible that air would dissolve and diffuse until the pressure of the air (which would still occupy the full air void) reaches atmospheric pressure, at which point thermodynamic equilibrium would be reached and

the radius of curvature of the gas-liquid interface, still located in the capillary pores, would be infinite: the air void would remain full of air and would never fill with liquid, even when left indefinitely under water.

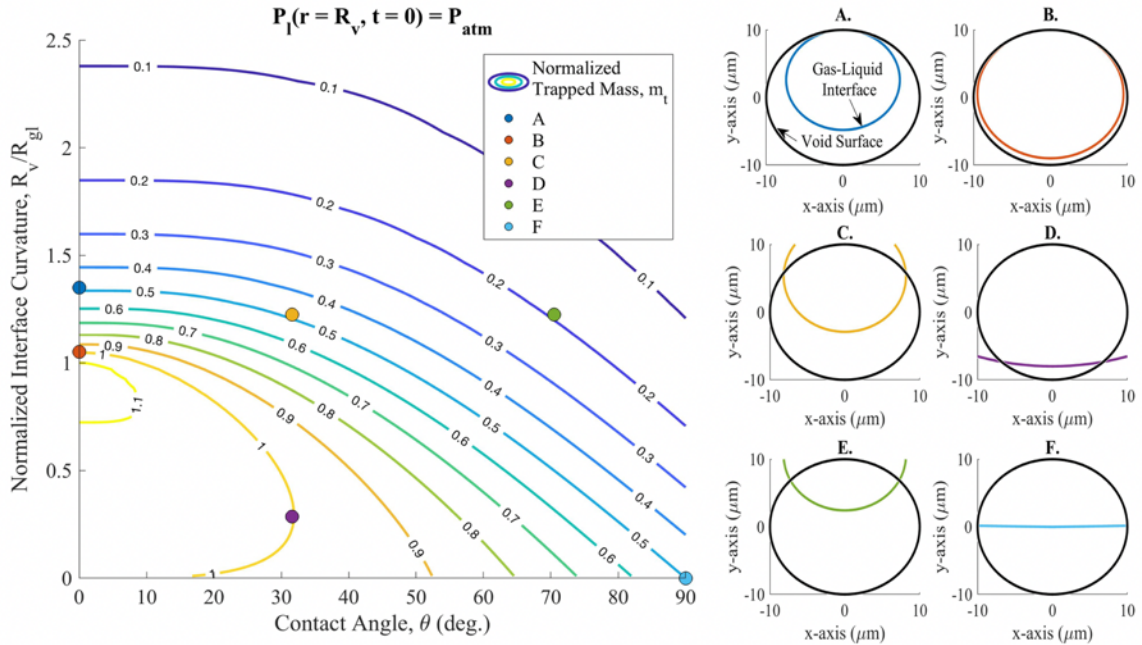


**Figure 3-11 - Contour plot of normalized mass of air initially trapped, as a function of contact angle,  $\theta$ , and initial radius of the gas-liquid interface,  $R_{gl}(t=0)$  with associated visualization of corresponding initial system geometries. All calculations are made for  $R_v = 10\mu\text{m}$ .**

**Equation 3-6 - Maximal value of trapped mass which can be represented by Equation 3-4 and 3-5.**

$$m_t^{max} = \frac{P_{atm} + \frac{2\sigma}{R_v}}{P_{atm}}$$

Figure 3-11 also shows that there exist combinations of contact angle  $\theta$  and normalized initial trapped mass  $m_t$  for which more than one potential initial geometry exists

(for example for  $m_t = 1$  and  $\theta = 25$  degrees, for which there are two potential values of  $R_{gl}(t=0)$ ). In this case, for subsequent calculations, we considered that the system adopted the configuration with the lower free energy, where the free energy,  $E_{sum}$ , of an initial geometry is calculated based on Equation 3-7. Note that, if the other configuration (with high free energy) is adopted as the initial configuration, the model would predict that air would dissolve until the radius of curvature of the gas-liquid interface would be infinite. Starting from this other configuration, one would hence find out that the air void would remain at least partially filled with air and would never become full saturated with a liquid, even when left indefinitely under water. Equations 3-8 through 3-10 display how the gas,  $E_g$ , surface,  $E_{surf}$ , and bulk liquid,  $E_{vol}$ , free energies are respectively calculated, where in Equation 3-9  $\sigma$  is the gaseous air – liquid interfacial surface tension,  $\gamma_{gas}^{solid}$  is the gaseous air – solid paste interfacial surface tension, and  $\gamma_{liquid}^{solid}$  is the liquid – solid paste surface tension.

**Equation 3-7 - Free energy summation for initial configuration assessment.**

$$\begin{aligned}
 E_{sum}(R_{gl}(t = 0), \theta) \\
 &= E_{gas}(R_{gl}(t = 0)) + E_{surf}(R_{gl}(t = 0), \theta) \\
 &\quad + E_{vol}(R_{gl}(t = 0), \theta)
 \end{aligned}$$

**Equation 3-8 - Gas free energy.**

$$E_{gas}(R_{gl}(t = 0)) = \frac{4\pi}{3} R_v^3 P_{atm} \ln \left( 1 + \frac{2\sigma}{R_{gl}(t = 0) P_{atm}} \right)$$

**Equation 3-9 - Gas-liquid surface free energy.**

$$\begin{aligned} E_{surf}(R_{gl}(t = 0), \theta, d) &= E_{gas}^{liquid} + E_{gas}^{solid} + E_{liquid}^{solid} \\ &= 2\pi\sigma R_{gl}(t = 0)^2 \left( 1 - \cos \left( \theta \sin^{-1} \left( \frac{R_v}{d} \right) \right) \right) \\ &\quad + 2\pi\gamma_{gas}^{solid} R_v^2 \left( 1 - \cos \left( \theta \sin^{-1} \left( \frac{R_{gl}(t = 0)}{d} \right) \right) \right) \\ &\quad + 2\pi\gamma_{liquid}^{solid} R_v^2 \cos \left( \theta \sin^{-1} \left( \frac{R_{gl}(t = 0)}{d} \right) \right) \end{aligned}$$

**Equation 3-10 - Liquid volume free energy.**

$$E_{vol}(R_{gl}(t = 0), \theta) = P_{atm} V_g(R_v, R_{gl}(t), \theta, d)$$

Finally, it is important to note that due to the fact that the capillary pores are orders of magnitude smaller than the spherical voids, the trapped gaseous air cannot ‘escape’ under the form of tiny gas bubbles by rising through the saturated capillary porosity, as can be directed evaluated from a calculation of the breakthrough pressure presented in [69]. The only way for the air to escape outward and for the air void to become saturated is through dissolution and diffusion, which are modeled in the next section.

**3.3.2 SVDK Model Formulation and Assumptions**

For the purpose of modeling the saturation of the void-shell system presented in Figure 3-10b, it is of principal interest to understand the transport of the liquid water within the porous solid shell into the spherical void and the resulting dissolution dynamics of the trapped gas. As detailed in the review of the model presented by Epstein and Plesset, the

liquid also contains dissolved gas which fluxes into the fluid to maintain thermodynamic equilibrium at the gas-liquid interface.

By writing the continuity of the diffusive mass fluxes of dissolved air in the liquid at the surface of the air void (i.e., within the void and within the saturated porous solid shell), we show with Equation 3-11 that the gradient of concentration of dissolved gas (this concentration is denoted as  $C_g$ ) is orders of magnitude smaller in the liquid in the air void than in the porous shell. Indeed, the diffusivity of air in liquid water,  $D_g^l$ , has a value of  $10^{-8}$  cm<sup>2</sup>/s [54] whereas the diffusivity of dissolved air in saturated hydrated cement paste,  $D_g^s$ , is on the order from  $10^{-10}$  to  $10^{-13}$  cm<sup>2</sup>/s [70]. Based on this result, we assume that the concentration of dissolved gas,  $C_g$ , is homogeneous in the liquid within the air void and must satisfy thermodynamic equilibrium of the gas-liquid interface. Thanks to this assumption, the concentration of dissolved gas,  $C_g$ , is the same everywhere around the surface of the spherical void (i.e. at  $r = R_v$ ).

**Equation 3-11 - Comparison of diffusive fluxes at  $r = R_v$ .**

$$\frac{\partial C_g}{\partial r} \Big|_{r=R_v^-} / \frac{\partial C_g}{\partial r} \Big|_{r=R_v^+} = \frac{D_g^s}{D_g^l} \ll 1$$

As a result, the 3D system of interest can be simplified into a 1D system (see Figure 3-12), where the concentration of dissolved gas in the liquid saturated porous shell will be evaluated as a function of time in the shell (of thickness L), i.e. from  $r = R_v$  to  $r = R_v + L$ . As a consequence of the evolution of the size and mass of the trapped gaseous air within the spherical void during the saturation process, the concentration  $C_g$  of dissolved gas at

the surface of the air void (i.e. at  $r=R_V$ ) will need to be properly integrated into the system of equations to be solved.

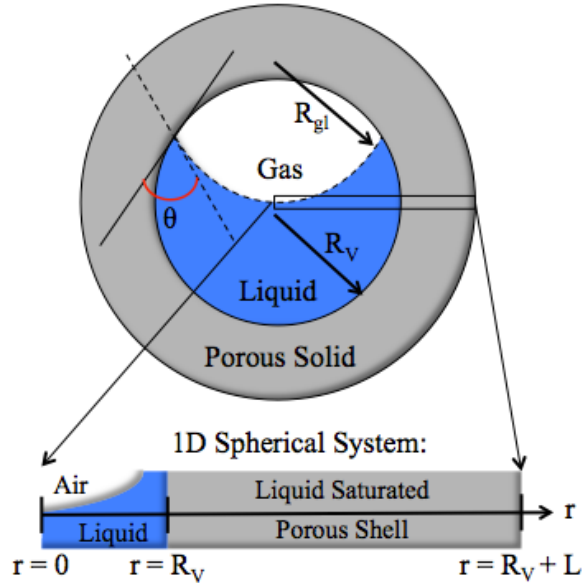


**Figure 3-12 - Simplification of problem to 1D.**

By conserving all phases present in the porous shell (i.e. liquid water and dissolved gas), the mass conservation of liquid water,  $l$ , and dissolved gaseous air,  $g$ , can be written by the advection-diffusion equation following [71]. Equation 3-12 shows the advection-diffusion equation for the liquid,  $l$ , where  $\rho_l$  is the liquid density,  $\kappa$  is the intrinsic permeability of the porous solid shell,  $\phi_0$  is the porosity of the shell,  $\eta$  is the dynamic viscosity of the liquid, and  $P_l$  is the liquid pressure. Equation 3-13 displays the advection-diffusion equation for the dissolved air within the liquid in the porous solid shell where  $C_g$  is the concentration of dissolved gas in the liquid. In Equations 3-12 and 3-13, the material parameters (i.e.,  $\kappa$ ,  $\phi_0$ ,  $\eta$ , and  $D_g^s$ , whose meaning is given in Table 3-3) in the porous shell are taken as homogeneous in space and constant over time. Additionally, it is assumed that the liquid flow is incompressible and that the density of the liquid,  $\rho_l$ , is not a function of

the dissolved gas concentration [72], implying that this density,  $\rho_l$ , is assumed constant. As shown in Equation 3-14, the incompressible flow condition of the liquid in the porous solid shell results in  $r^2 \partial P_l / \partial r$  being constant from  $r = R_v$  to  $r = R_v + L$ . The final governing equation for the mass transport of the dissolved gas in the liquid saturated porous shell is written as Equation 3-15, where  $r^2 \partial P_l / \partial r$  is homogeneous in space but varies over time.

**Equation 3-12 - Mass conservation of liquid, l.**

$$\frac{\partial \rho_l}{\partial t} - \rho_l \frac{\kappa}{\varphi_0 \eta} \frac{1}{r^2} \frac{\partial}{\partial r} \left( r^2 \frac{\partial P_l}{\partial r} \right) = 0$$

**Equation 3-13 - Mass conservation of dissolved gas, g.**

$$\frac{\partial C_g}{\partial t} - \frac{\kappa}{\varphi_0 \eta} \frac{1}{r^2} \frac{\partial}{\partial r} \left( r^2 \frac{\partial P_l}{\partial r} C_g \right) - \frac{D_g^s}{\varphi_0} \frac{1}{r^2} \frac{\partial}{\partial r} \left( r^2 \frac{\partial C_g}{\partial r} \right) = 0$$

**Equation 3-14 - Result of incompressibility assumption.**

$$r^2 \frac{\partial P_l}{\partial r} = \text{cons} = (P_l(r = R_v + L, t) - P_l(r = R_v, t)) \frac{1}{\frac{1}{R_v} - \frac{1}{R_v + L}}$$

**Equation 3-15 - Governing transport equation for dissolve gas in the liquid saturation porous shell.**

$$\frac{\partial C_g}{\partial t} - \frac{\kappa R_v (R_v + L)}{\varphi_0 \eta} \frac{(P_l(r = R_v + L) - P_l(r = R_v, t))}{r^2 L} \frac{\partial C_g}{\partial r} - \frac{D_g^s}{\varphi_0} \frac{1}{r^2} \frac{\partial}{\partial r} \left( r^2 \frac{\partial C_g}{\partial r} \right) = 0$$

To solve Equation 3-15, the boundary conditions for the liquid pressure,  $P_l$ , and dissolved gas concentration,  $C_g$ , must be known. At  $r = R_v + L$ , the liquid pressure is taken equal to the atmospheric pressure,  $P_{atm}$ , and the concentration in dissolved gas is considered to be equal to that in water in equilibrium with air at atmospheric pressure, such that, with Henry's law, the concentration of dissolved gas,  $C_g$ , at  $r = R_v + L$ , is given by the product,  $k_H P_{atm}$  [29,55], where  $k_H$  is Henry's constant for air. To understand how  $C_g$  and  $P_l$  vary at  $r = R_v$ , they are written as a function of the mass of the gas,  $m_g(t)$ , and the mass of the liquid,  $m_l(t)$ , within the spherical void. To do so, it is assumed that the mass of dissolved gas in the liquid within the spherical void is negligible based upon [72] - implying that the mass of gas is exclusively given by the trapped volume defined by  $R_{gl}(t)$ , which, for a given contact angle  $\theta$ , is a function of  $m_l(t)$ . Based on this assumption, the concentration of the dissolved gas at  $r = R_v$  can be expressed for all times by combining Henry's Law and the Ideal Gas law as displayed in Equation 3-16. Additionally, the liquid pressure at  $r = R_v$  can also be expressed, as shown in Equation 3-17, by combining Henry's law, the ideal gas law, and Laplace equation. Although the system is treated as isothermal, Equation 3-16 suggests that increased in liquid temperature will result in a linear increase in the dissolve gas concentration at  $r = R_v$  and will also corresponding to mass flux of dissolved gas species into the liquid within the porous shell, increasing the time to full saturation of a given air void.

**Equation 3-16 - Dissolved gas concentration,  $C_g$ , at  $r = R_v$  at all times.**

$$C_g(r = R_v, t) = C_g(m_g(t), m_l(t)) = \frac{k_H m_g(t) G T}{M_w \left( \frac{4\pi}{3} R_v^3 - \frac{m_l(t)}{\rho_l} \right)}$$

**Equation 3-17 - Liquid pressure concentration,  $P_l$ , at  $r = R_v$  at all times.**

$$P_l(r = R_v, t) = P_l(m_g(t), m_l(t)) = \frac{m_g(t)GT}{M_w \left( \frac{4\pi}{3} R_v^3 - \frac{m_l(t)}{\rho_l} \right)} - \frac{2\sigma}{R_{gl}(m_l(t))}$$

To have a solvable system of equations,  $m_g(t)$  and  $m_l(t)$ , the masses of gaseous air and of liquid water within the spherical void, can be determined by evaluating the respective mass fluxes through the spherical void surface. Equation 3-18 calculates the rate of change of the mass of gaseous air in the spherical void by summing the advective and diffusive mass fluxes through the spherical void surface. Equation 3-19 is written in a similar form to calculate the rate of change of liquid in the spherical void. In Equation 3-19, the term,  $C_l$ , denotes the concentration of liquid in the pore solution and thus is equal to the difference between the liquid density,  $\rho_l$ , and the dissolved gas concentration,  $C_g$ , at  $r = R_v$  at any time. When replacing  $C_l$  with this difference, Equation 3-19 becomes Equation 3-20.

**Equation 3-18 - Rate of change of gas mass in spherical air void due to advection and diffusion**

$$\frac{\partial m_g}{\partial t} = 4\pi R_v^2 \left( D_g^s \frac{\partial C_g}{\partial r} \Big|_{r=R_v^+} + \frac{\kappa}{\eta} C_g \frac{\partial P_l}{\partial r} \Big|_{r=R_v^+} \right)$$

**Equation 3-19 - Rate of change of liquid mass in spherical air void due to advection and diffusion.**

$$\frac{\partial m_l}{\partial t} = 4\pi R_v^2 \left( D_g^s \frac{\partial C_l}{\partial r} \Big|_{r=R_v^+} + \frac{\kappa}{\eta} C_l \frac{\partial P_l}{\partial r} \Big|_{r=R_v^+} \right)$$

**Equation 3-20 - Final representation for the rate of change of liquid mass in the void.**

$$\frac{\partial m_l}{\partial t} = 4\pi R_v^2 \left( -D_g^s \frac{\partial C_g}{\partial r} \Big|_{r=R_v^+} + \frac{\kappa}{\eta} (\rho_l - C_g) \frac{\partial P_l}{\partial r} \Big|_{r=R_v^+} \right)$$

As a result, Equations 3-15 to 3-17, 3-19, and 3-20 represent a complete system of equations. This system can then be solved, given the initial condition  $m_t$ , and the previously defined boundary conditions for  $C_g$  and  $P_l$  at  $r = R_v + L$ , thus making it possible to understand the dissolution kinetics of trapped gaseous air due to coupled-transport of fluid and dissolved gas by advection and diffusion. It is important to note that the gradients of liquid pressure  $P_l$  in equations 3-18 and 3-20 also appear in Equation 3-14. It can be seen that if the liquid pressure within the spherical void is imposed to be equal to the atmospheric pressure at all times at the surface of the air void then a purely diffusive-driven dissolution model for the trapped gaseous air is obtained.

### 3.3.3 *SVDK Model Results and Discussion*

#### 3.3.3.1 Comparison with the Epstein-Plesset Model

As motivated in the review and detailed in the SVDK model formulation, understanding how the air voids become liquid filled and how various modes of mass transport (i.e., diffusion and advection) influence the dissolution dynamics and resulting saturation of the spherical void is of central importance to fundamentally understanding the long-term saturation of air-entrained cementitious materials and other materials with similar multi-scale pore structures. Prior to displaying and discussing these phenomena for cementitious materials and other analogous porous media, it is first of interest to evaluate

the SVDK model in the context of the Epstein-Plesset model. Although the formulations are notably different and departures can be expected due to the presented assumptions, if the porous solid shell surrounding the spherical air void is treated as liquid water and the initial amount of trapped air,  $m_t$ , is equal to 1 and the contact angle,  $\theta$ , is zero, then systems at time  $t = 0$  are analogous.

Figure 3-13a displays results for the Epstein-Plesset model and the SVDK model when the porous solid is treated as liquid water and when advection is neglected (i.e., the liquid pressure at  $r = R_V$  is considered equal to  $P_{atm}$  for all times), for an initial air bubble with a radius of  $15\mu\text{m}$ . Table 3-2 displays the necessary input values for the respective models. It can clearly be seen that the initial linear portion of the two models agree well in terms of rate. Once the radius of the trapped gas reduced below  $12\mu\text{m}$ , the models and experimental behavior of the trapped air becomes increasingly non-linear. Ultimately, because the SVDK model assumes that the concentration of the dissolved gaseous air in the liquid is homogeneous within a sphere of radius of  $15\mu\text{m}$  (which is a reasonable assumption for tortuous porous media as shown in Equation 3-11, but not a reasonable assumption for a bubble surrounded solely by liquid water) and satisfies thermodynamic equilibrium of the liquid-air interface, the SVDK model logically predicts a collapse of the air bubble being faster than that given by the Epstein-Plesset model. Otherwise, in terms of comparison, the SVDK model agrees very well with the Epstein-Plesset model in terms of order of magnitude but eventually predicts –as could be expected– a smaller (by about 22%) time to full dissolution. Figure 3-13b displays the evolution of the air-liquid interface with the SVDK model, which is qualitatively very comparable to Figure 3-10b.

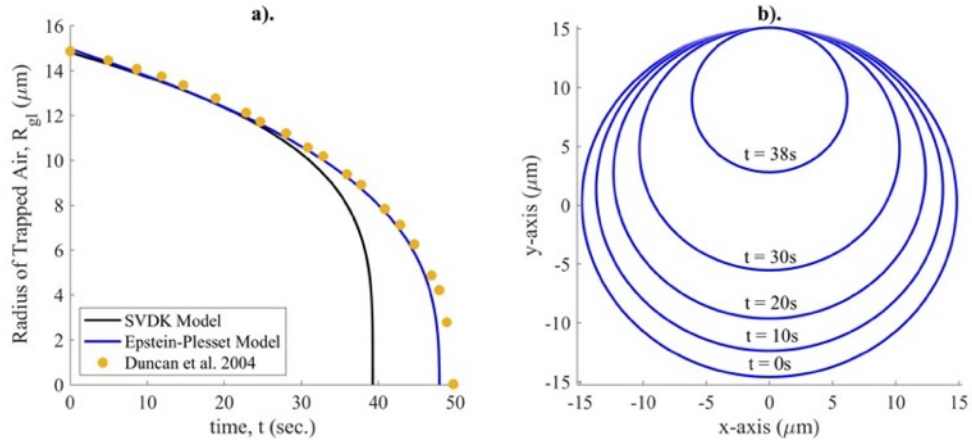


**Figure 3-13 - a). comparison of SVDK model to Epstein-Plesset solution (i.e., Equation 3-1) and experimental data of Duncan 2004 [54], b). evolution of air-liquid interface as predicted by the SVDK model.**

**Table 3-2 - Required inputs for SVDK and Equation 3-1 to results displayed in Figure 3-14a/b.**

<b>Symbol</b>	<b>Definition</b>	<b>Value</b>
T	Temperature	295.15 K
$M_w$	Molecular mass of air	28.97 g/mol
G	Universal Gas Constant	$m^3 \cdot Pa / (mol \cdot K)$
f	Ratio of initial concentration to saturated concentration	1
$\sigma$	Air-water surface tension with a surfactant used in [54]	40 mN/m [54]
$D^1$	Diffusivity of air in water	$1.8 \cdot 10^{-9} m^2/s$ [54]
$\rho$	Density of air	$1.225 kg/m^3$
$k_H$	Henry's law of for air in water	$1.9 \cdot 10^{-7} kg / (m^3 \cdot Pa)$ [54]

1. In this evaluation  $D_g^s$  is equivalent to the D defined and given in this table.

### 3.3.3.2 Discussion of the Role of Advection

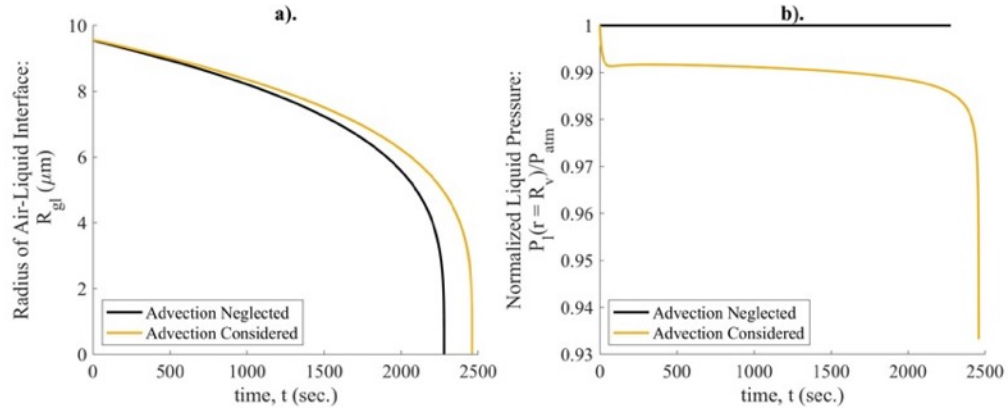
For the purposes of the remaining results section, the findings of the SVDK model will be reported for material values expected for well-hydrated cement pastes and the kinetics of the trapped air geometry are compared to behavior seen for the proxy systems presented in Section 3.2.2.2. Additionally, the system is assumed to be at room

temperature. Table 3-3 displays specific values, or ranges of values, that are taken for the SVDK model inputs that are not held constant or already given in Table 3-2. In terms of organization, Figures 3-14 and 3-15 display the influence of advection and the order of magnitude of the intrinsic permeability,  $\kappa$ , while the diffusivity of the dissolved gas in the liquid saturated porous shell is taken as the mean value of the range presented Table 3-3 (i.e., a value of  $5 \times 10^{-12} \text{ m}^2/\text{s}$ ). The size of the spherical air void is also taken as  $R_v = 10 \mu\text{m}$ , representing the absolute lower bound for entrained air voids in cementitious materials [36] and  $L$  is set to 1mm.

**Table 3-3 - SVDK model inputs for cementitious material systems.**

Symbol	Definition	Value
$D_g^s$	Diffusivity of dissolved air in saturated hydrated cement paste	$10^{-10} - 10^{-13} \text{ m}^2/\text{s}$ [73]
$\kappa$	Intrinsic permeability of hydrated cement paste	$10^{-18} \text{ to } 10^{-22} \text{ m}^2$ [74]
$\eta$	Dynamic viscosity of water	$8.9 \times 10^{-4} \text{ Pa}\cdot\text{s}$
$\phi_0$	Porosity of cement paste	$0.20 - 0.30 \text{ (\%/100)}$ [74]
$\sigma$	Air-water surface tension	$70 \text{ mN/m}$ [54]
$\rho_l$	Density of water	$997 \text{ kg/m}^3$

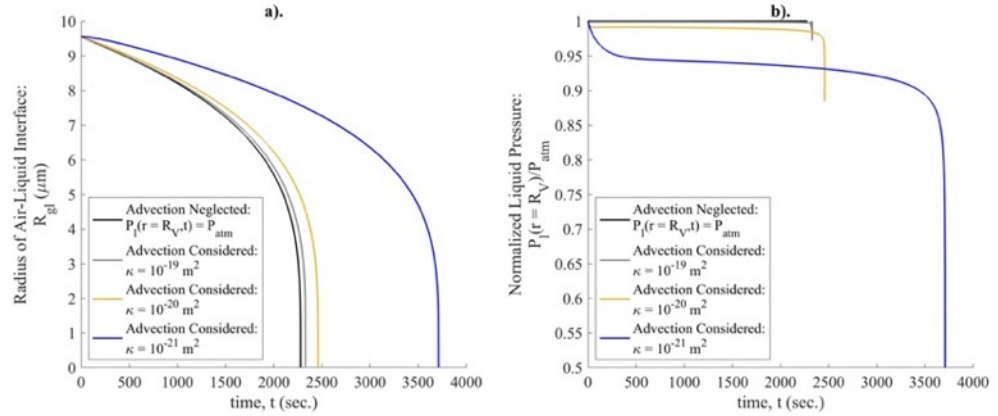
More specifically, in Figure 3-14, the influence of the liquid pressure,  $P_l$ , boundary condition is evaluated and  $\kappa$  is set to  $10^{-19} \text{ m}^2$ . As detailed in the formulation, the influence of advection on the transport of the dissolved air can be not solved for when  $P_l$  is required to be equivalent to  $P_{\text{atm}}$  at  $r = R_v$  and within the liquid in the void. Figure 3-14a displays the change in radius of the trapped air when  $m_t = 1$  and  $\theta = 0$ . The findings in Figure 10a display that when advection is considered the total time to dissolution increases by approximately 15%. Upon reviewing Figure 3-14b, which displays the evolution in the liquid pressure at  $r = R_v$ , it can be seen that when advection is considered, the liquid pressure at the surface of the air void drops below the atmospheric pressure. The reduction in the liquid pressure at  $r = R_v$  results in a pressure gradient that pulls liquid into the air void and slows the diffusion of the dissolved gas through the porous solid shell (because it slows the increase of pressure in the gas bubble), causing a longer time to full dissolution of the trapped air.



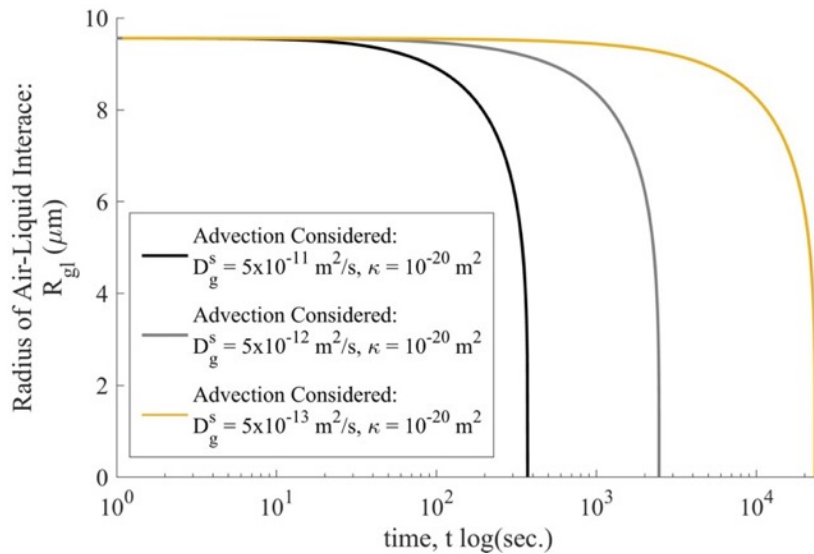
**Figure 3-14 - Influence of advection on time to complete dissolution displayed by a). radius of air-liquid interface. b). Evolution of liquid pressure at  $r = R_V$  for when advection is neglected (i.e., not solved for) and considered, respectively. Model inputs:  $m_t = 1$ ,  $\theta = 0$ ,  $D_g^s = 5 \times 10^{-12} \text{ m}^2/\text{s}$ ,  $\kappa = 10^{-20} \text{ m}^2$ .**

Figure 3-15a displays the influence of the value of intrinsic permeability,  $\kappa$ , on the dissolution kinetics of the same trapped air. Interestingly, as  $\kappa$  approaches the maximum value for cementitious materials as shown in Table 3-3, it begins to approximate the solution in which advection is neglected (i.e., not solved for) whereas when  $\kappa$  approaches the minimum usual value for cementitious materials the time to dissolution significantly increases. This phenomenon can be understood by considering the implications of the results presented in Figure 3-15b. When the value of  $\kappa$  is large, the pressure gradient quickly reduces because the liquid can quickly flow into the spherical void. When  $\kappa$  is high, a pressure gradient, as seen for smaller values of  $\kappa$ , between  $r = R_V$  and  $r = R_V + L$  cannot be sustained and is mostly diffusion-driven. This finding is in line with the drying asymptotics of quite permeable porous media as developed in [75] (i.e., the initial gas pressure gradient cannot be sustained due to the rapid rate of advective transport through the material as compared to the slow transport of gas due to diffusion). Figure 3-16 displays

the influence of the order of magnitude of the diffusivity of dissolved air in liquid-saturated cement paste on the dissolution kinetics when advection is considered.



**Figure 3-15 - Influence of intrinsic permeability on time to complete dissolution of the trapped air. Model inputs:  $m_t = 1$ ,  $\theta = 0^\circ$ ,  $D_g^s = 5 \times 10^{-12} \text{ m}^2 \cdot \text{s}^{-1}$ ,  $L = 1 \text{ mm}$ .**



**Figure 3-16 - Influence of diffusivity of dissolved air in saturated hydrated cement paste on trapped air dissolution kinetics. Model inputs:  $m_t = 1$ ,  $\theta = 0^\circ$ .**

### 3.3.3.3 Results on Time to Full Dissolution and Dissolution Kinetics

From the previously displayed outcomes and results, the influence in initially trapped mass of air,  $m_t$ , and the contact angle,  $\theta$ , can be evaluated. Figure 3-17a displays a contour plot for time to full dissolution, when advection is considered, as a function of  $m_t$  and  $\theta$  for a spherical void of radius  $10\mu\text{m}$  and where the diffusivity  $D_g^s$  of dissolved air in the shell is equal to  $5 \times 10^{-12} \text{ m}^2/\text{s}$  and the permeability  $\kappa$  is equal to  $10^{-20} \text{ m}^2$ . It can be clearly seen that the amount of trapped air significantly influences the total time to full dissolution whereas the effect of the contact angle to the time to full dissolution becomes notably pronounced when above a value of 20 degrees. Corresponding with Section 3.3.1, on Figure 3-17a we delimitate regions that are not physically possible under the assumption of a liquid pressure equal to the atmospheric pressure in the initial state (in blue) and regions for which multiple initial geometries are possible (in pink). In this latter case, we chose the initial geometry with the lowest free energy (see Equation 3-7) to calculate the time to full dissolution. Figures 3-17b to 3-17d evaluate other material and system inputs: values of intrinsic permeability, the diffusivity of dissolved air in saturated cement paste, and the air void size. Figure 3-18 displays examples of evolutions for various contact angles and Figure 3-19 displays the influence of the thickness,  $L$ , of surrounding cement paste shell and the spherical air void radius,  $R_v$ , on time to full dissolution,  $t_f$ , of the trapped gaseous air.

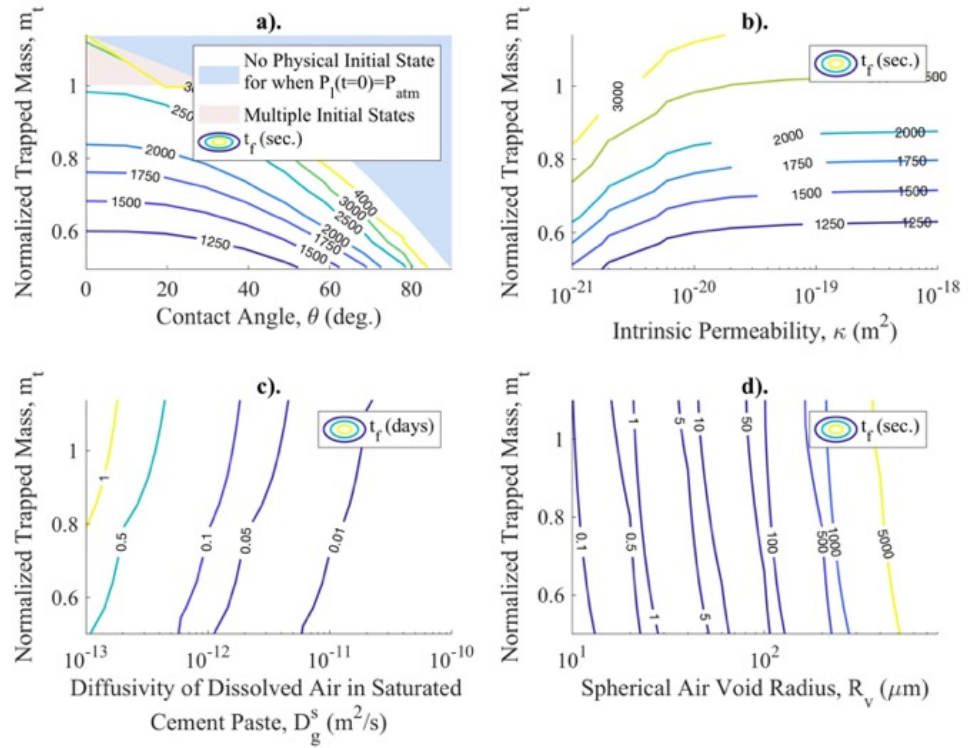


**Figure 3-17 - Time to full dissolution,  $t_f$ , contours of a large domain of normalized trapped mass,  $m_t$ , and a). contact angles,  $\theta$ , where  $R_v = 10\mu m$ ,  $D_g^s = 5 \times 10^{-12} m^2/s$ ,  $\kappa = 10^{-20} m^2$ , and  $L = 1mm$ , b). intrinsic permeability,  $\kappa$ , where  $\theta = 0^\circ$ ,  $R_v = 10\mu m$ ,  $D_g^s = 5 \times 10^{-12} m^2/s$ , and  $L = 1mm$ , c). diffusivity,  $D_g^s$ , where  $\theta = 0^\circ$ ,  $R_v = 10\mu m$ ,  $\kappa = 10^{-20} m^2$ , and  $L = 1mm$ , and d). air void radius,  $R_v$ , where  $\theta = 0^\circ$ ,  $D_g^s = 5 \times 10^{-12} m^2/s$ ,  $\kappa = 10^{-20} m^2$ ,  $L = 1mm$ .**

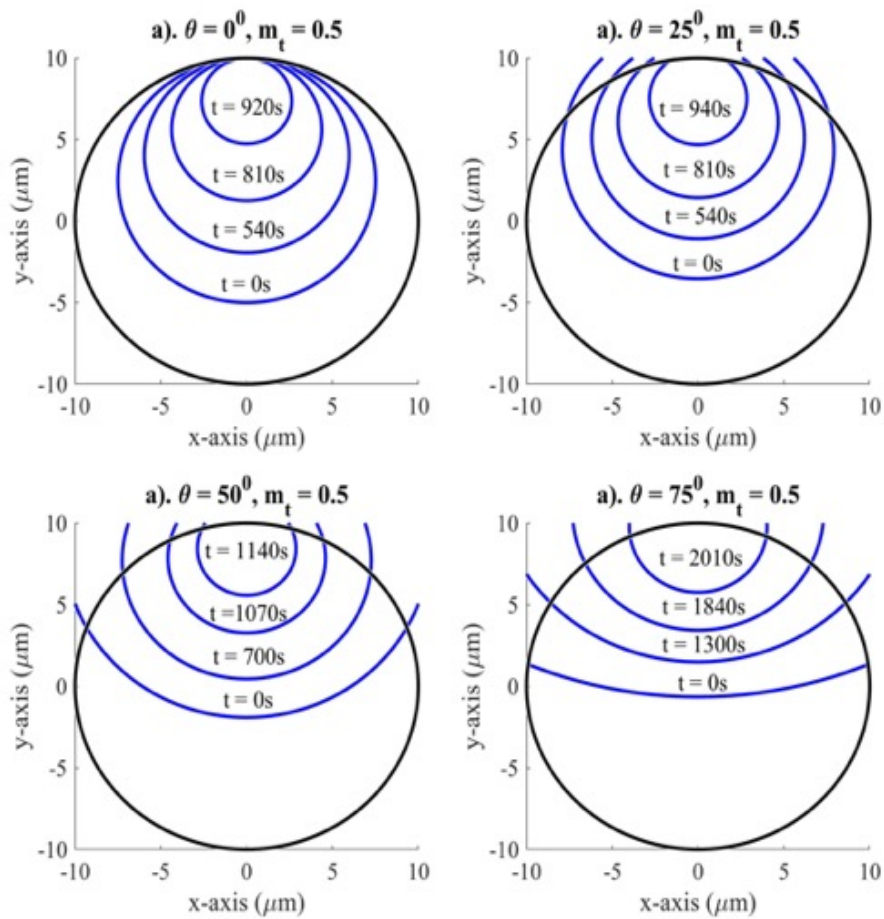


**Figure 3-18 - Examples of gas-liquid surface evolution for normalized trapped mass,  $m_t$ , of 0.5 and various contact angles: a).  $0^\circ$ , b).  $25^\circ$ , c).  $50^\circ$ , d).  $75^\circ$ . Inputs:  $R_V = 10\mu\text{m}$ ,  $D_g^s = 5 \times 10^{-12} \text{ m}^2/\text{s}$ , and  $\kappa = 10^{-20} \text{ m}^2$ .**

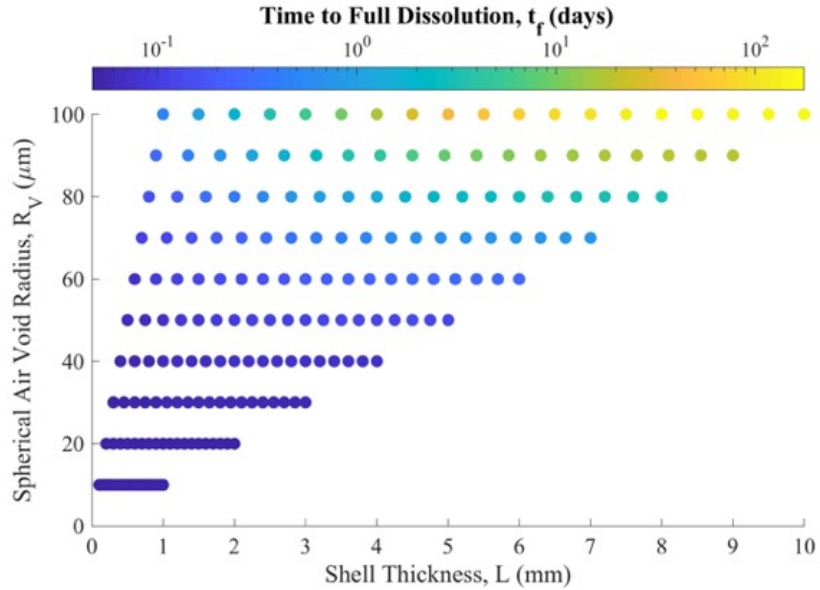


**Figure 3-19 - Influence of spherical air void radius,  $R_v$ , and porous solid shell thickness,  $L$ , on time to full dissolution for  $m_t = 1$ ,  $\theta = 0^\circ$ ,  $D_g^s = 5 \times 10^{-12} \text{ m}^2/\text{s}$ , and  $\kappa = 10^{-20} \text{ m}^2$ .**

#### 3.3.3.4 Comparison with Experimental Data

As discussed and displayed in Section 3.2.2.2 and Figure 3-7, fitting power law relationships to the temporal size reduction of the trapped air can provide significant insight into the governing physics of the model. For the following findings the fit relation is given by  $R_{gl}(t) = A(B-t)^C$ , where  $A$  is a constant,  $B$  represents the time to full dissolution, and  $C$  is the exponent of the power-law relation [65,66]. As displayed in Figure 3-20a, for systems with a zero contact angle (i.e.  $\theta=0^\circ$ ), the determined power (i.e., value of  $C$ ) is  $\sim 0.25$ , independent of whether advection is considered or neglected, and is found to be mostly independent of the initial trapped mass  $m_t$ . As a means of comparison, the Epstein-Plesset and experimental results for similar systems give a power-law fit of  $\sim 0.33$ . The lower value found by the SVDK model is expected and its explanation coincides with that given for the difference in solutions to the SVDK and Epstein-Plesset model shown in Figure 3-13 (i.e.,

the concentration of dissolved gas in the liquid within the air void is homogeneous and required to satisfy thermodynamic equilibrium of the air-liquid interface which increases the rate of dissolution as compared to [55] leading to a lower value of exponent in a power-law relation). Figure 3-20b displays a contour plot of fitted exponents of the power-law relation for various values of  $m_t$  and  $\theta$ . As expected, the power-law strongly depends on the value of  $\theta$ , which can be understood by the influence of Laplace pressure applied to the system (i.e., for a larger value of  $\theta$  larger values of  $R_{gl}$  are obtained, reducing the Laplace-driven dissolution effects of the trapped air).

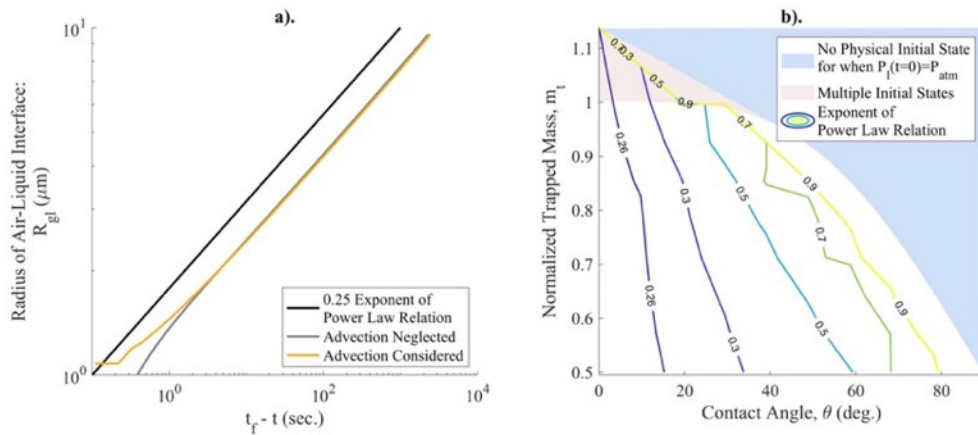


**Figure 3-20 - a). Power law evaluation for a system with  $\theta = 0^\circ$ , where  $R_v = 10\mu\text{m}$  and  $m_t = 1$ , for when convection is neglected (i.e., not solved for) and considered, b). contour plot of power-law exponents (i.e. values of  $C$ ) as a function of contact angle for when advection is considered.**

Having evaluated the general outcomes of the model and its comparison to proxy systems, it is also of interest to understand how it relates to the experimental data that is available relating to the long-term saturation of air void in cementitious materials. As initially presented in Section 3.2.2.1, Moradillo and Ley conducted a series of long-term ponding experiments [50] on cement pastes with a similar pore structure used to formulate

the model presented herein. A primary conclusion was that after 60 days of ponding and within the first 6mm of the sample (i.e., depth from the ponded surface) air voids with radii less than 100 $\mu\text{m}$  were found to be saturated whereas larger air voids remained air-filled. Figure 3-21 displays that for acceptable values of  $D_g^s$  and  $\kappa$ , it can be directly shown that air voids smaller than 100 $\mu\text{m}$  in radius will be completely saturated, while voids larger than 100 $\mu\text{m}$  will remain partially air-filled. Similar to the comparison made to the Epstein-Plesset model presented in Figure 3-13, this finding does not directly validate the model but improves the likelihood that it is capturing the governing physics of the phenomena, seeing as how it agrees very well within that same order-of-magnitude of each comparison.

Also, it is important to note that if air-voids are well-spaced and do not influence the dissolution kinetics of one-another, Figure 3-21 suggests that the air voids roughly fill in order of increasing size, as postulated in [29]. This calculation neglected interactions between air voids. In real systems, interactions may happen: small air voids, subjected to larger Laplace pressures, should empty into larger air voids, akin to Oswald ripening. Therefore, in real materials, interactions may make the air voids fill in order of increasing size in a still more pronounced manner.

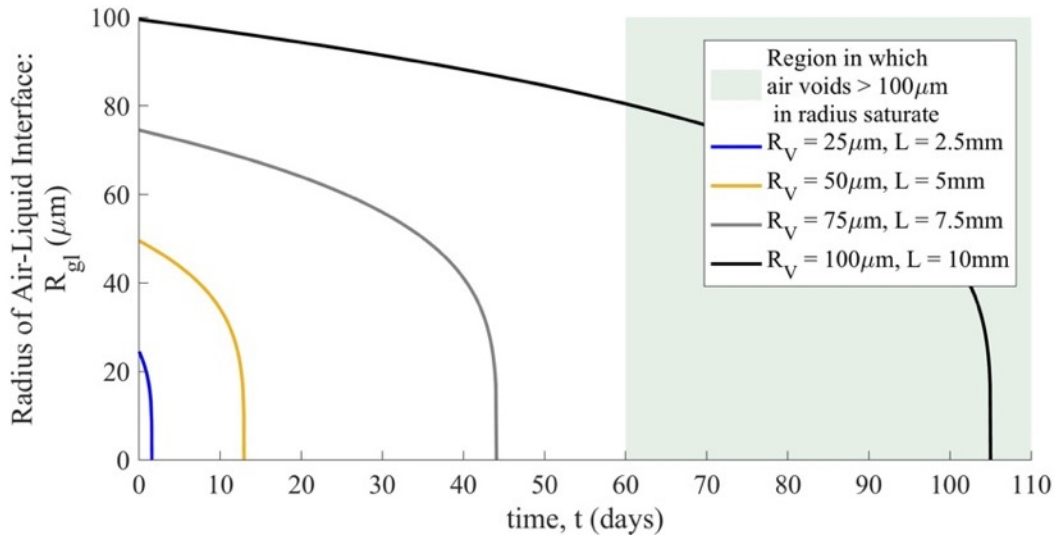


**Figure 3-21 - Comparison plot of SVDK model results with experimental conclusion from [50]. Model Inputs:  $m_t=1$ ,  $\theta = 0^\circ$ ,  $D_g^s = 1.5 \times 10^{-12} \text{ m}^2/\text{s}$ , and  $\kappa = 10^{-20} \text{ m}^2$ .**

### 3.3.3.5 Discussion on the Impact of Initial Pressure Assumptions

As mentioned in the formulation section, the previously presented results have assumed that at time  $t = 0$  the liquid pressure  $P_l$  at  $r = R_v$ , and within the spherical void, is equal to  $P_{\text{atm}}$  and the gas pressure is then given by the Laplace Equation. It could also be reasonably assumed that the gas pressure is equal to the atmospheric pressure  $P_{\text{atm}}$ . Figure 3-22a displays the outcomes of setting the gas pressure initially equal to  $P_{\text{atm}}$  on the evolution of the radius of the air-liquid interface and Figure 3-22b displays the evolution in liquid pressure at  $r = R_v$ . It is clear that the assumption does not significantly influence the outcome due to the fact that the liquid pressure gradient in the system quickly equilibrates, resulting in very similar dissolution kinetics of the trapped gaseous air.

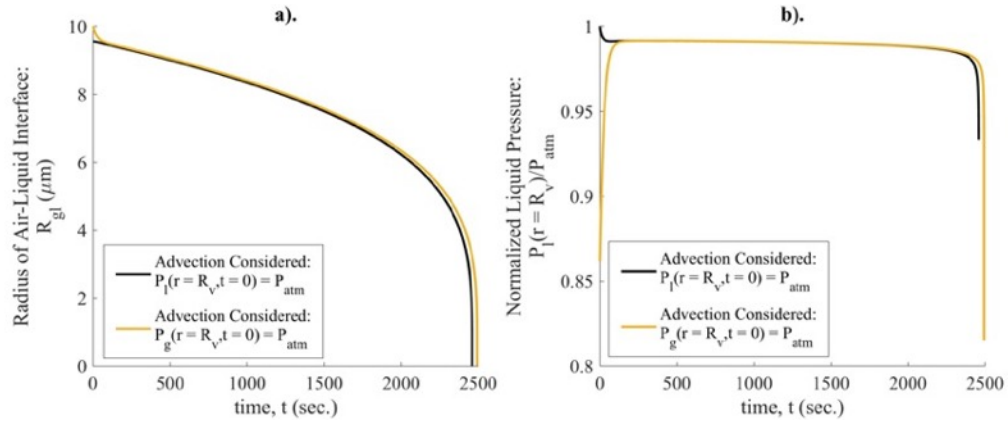


**Figure 3-22 - Assessment of initial liquid and gas pressures at  $r = R_v$  on dissolution kinetics of trapped air. Model inputs:  $m_t=1$ ,  $\theta = 0^\circ$ ,  $D_g^l = 5 \times 10^{-12} \text{ m}^2/\text{s}$ , and  $\kappa = 10^{-20} \text{ m}^2$ ,  $L = 1 \text{ mm}$ .**

With the SVDK model, the time to full dissolution of spherical voids that end up being fully saturated with liquid was examined. However, based on our theoretical considerations, it is possible that, depending on the configuration of the gas-liquid interfaces right after capillary imbibition, some air voids never fill fully with liquid, even if left indefinitely under water.

### 3.3.4 SVDK Model Conclusions

As displayed in the previous section, the formulated SVDK model advances the current state-of-the-art in the field, reviewed in Section 3.2, by clearly detailing how single air voids become liquid-saturated due to dissolution, diffusion, and advection of the trapped gaseous air. The SVDK model results were compared to previous efforts [54,55,67] for simple systems (i.e. as spherical gas bubble surrounded by an infinite amount of liquid) as shown in Figure 3-13 and found to agree well in terms of solution form and the order of magnitude of time to full dissolution. As noted, the departures in the results can be readily explained due to assumptions present in the model that are applicable to porous media with

highly tortuous capillary porosity. Additionally, the SVDK model results were compared to experimental findings presented in [50] and found to agree very well. Outcomes of this comparison were also used to evaluate a postulation made by G. Fagerlund in [29] that the voids in cementitious material fill in order of increasing size – likely this is the case when considering a polydisperse air void system (i.e., small air voids preferentially diffuse into larger voids).

Along with the comparisons made to previous efforts, it was displayed how the SVDK model can evaluate the dissolution kinetics of trapped gases over a very large domain of trapped masses of air and contact angles in addition to the influence of when advection is considered and neglected. Notably, it was found that as the intrinsic permeability of the porous paste shell increased the SVDK model begins to approximate the solution when advection is not solved for (i.e., when the dissolution of the dissolved air in the porous shell is exclusively limited by diffusion). This finding, alongside the influence of the contact angle and value of the diffusivity on time to full dissolution, is significant as it provides novel insight into how such a system might behave and could be manipulated for design purposes. For example, using the outcomes of this model, the diffusivity and intrinsic permeability can be designed into the material through selection of appropriate values of water/cement (w/c) ratio and a minimal curing time, in the case of cementitious materials, and reliably provide a desired time to critical saturation. Also, by impacting the time to full dissolution, the contact angle between the pore solution and the solid surfaces could influence the freeze-thaw resistance, which might explain why hydrophobic agents can impact freeze-thaw durability of concrete [76]. Lastly, the phenomenon of trapping more air than the spherical void can accommodate – effectively forcing air into the

surrounding capillary pores- was discussed as a feasible way in which air voids could remain indefinitely air filled.

Although the SVDK model has resulted in numerous insights into the slow saturation of air void in cementitious materials, its direct validation is still necessary. To do so, small specimens of air-entrained cement pastes could be prepared and evaluated using high resolution nanoCT as they saturate over time. The efforts and results found in a similar experiment [50] have provided insight into the global saturation of a sample, but it is necessary to study only a selection of air voids at finer time steps and resolution below  $8.8\mu\text{m}/\text{voxel}$  in effort to see the evolution of the air-liquid interface. Additionally, it could be envisioned that a microfluidic device could be constructed as in [49] to provide similar insight and is left as future work.

### **3.4 Specimen-Scale: Multi-Void Dissolution Kinetics (MVDK) Model**

As mentioned in Sections 3.2.1 and 3.2.2.2, previous specimen-scale theoretical [21,25,29,44] and experimental [18,22,50] assessments of the long-term saturation kinetics of air-entrained cementitious materials, and other like materials, have left numerous fundamental questions open for investigation. Within this section, a multi-void dissolution kinetics model (MVDK) – building on the SVDK model presented in Section 3.3 – will be formulated and assessed. As displayed in Figure 3-23, the principal intent of the investigation is to display how the now understood pore-scale governs the long-term saturation rate of cementitious materials. The MVDK model will also be able to directly evaluate the influence of the air void interaction in a disperse void system and the influence of depth to the free surface. The ultimate goal of the MVDK model is to complement and

improve assumptions present in previously developed multi-phase saturation models, as found in [44], by providing insight into the governing physics which happens below the REV scale for most continuum-scale evaluations of saturating cementitious materials.

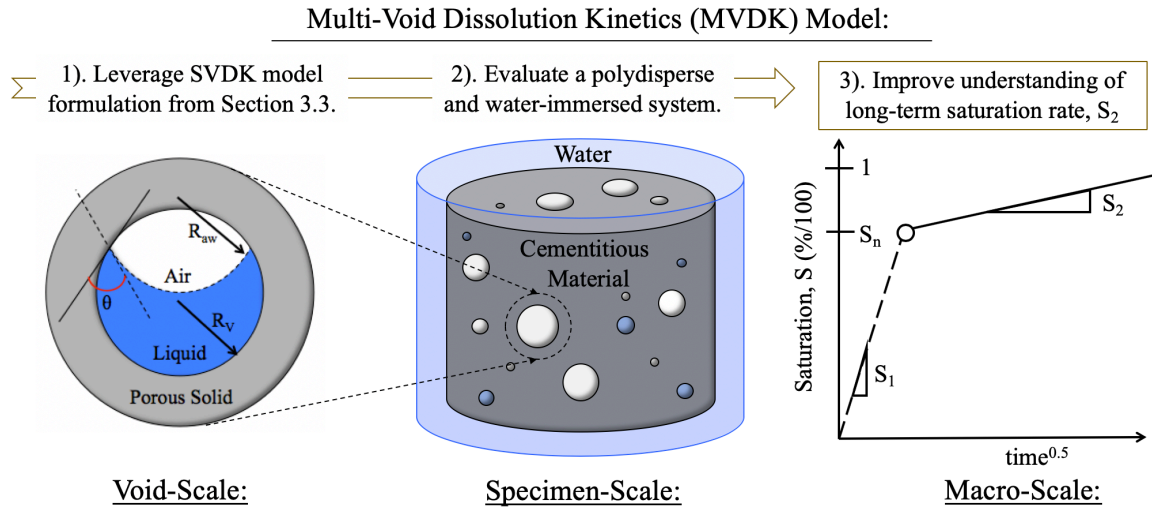


**Figure 3-23 - Graphical connection between SVDK, MVDK, and macro-scale phenomena.**

More specifically, the MVDK model will be able to display in which order the air voids saturate, rigorously evaluating various filling-regime postulations found in the literature [25,29], Ostwald's ripening due to phenomena related to Mechanism #2 presented in Figure 3-2, and should display that a void near the surface of the specimen should become liquid saturated faster than one in the center of the specimen. Lastly, the model will be compared to various experimental outcomes [50] as a means of validation and show that the secondary saturation rate can be readily predicted for standard size distributions of air voids in cementitious materials and material property values. As a result, the MVDK model can be used to inform design and improve the prediction of time to

critical saturation of air-entrained cementitious materials based upon the governing physics of pore-scale phenomenon developed in Section 3.3.

#### *3.4.1 MVDK System Definition and Mechanisms*

In effort to move from the void-scale to the specimen-scale, as displayed in Figure 2-23, it is necessary to develop a simplified system which can be easily mathematically evaluated, no different than that done for the SVDK formulation presented in Section 3.3.1. Figure 3-24a shows a cubic system that will be discretized and air voids will be placed at respective computational nodes. Figure 3-24b displays how the cubic area surrounding the computational node will be treated similarly to the SVDK model, allowing for the pore-scale to directly be placed into the specimen-scale model. Also, it is important to note that as displayed in Figure 3-23, the MVDK model system is assumed to be fully liquid immersed. Similar to the SVDK model, it is assumed that the porous solid, or cementitious material, which surrounds the spherical air voids is completely liquid saturated (i.e., the system is at its matrix saturation) at time  $t = 0$ .

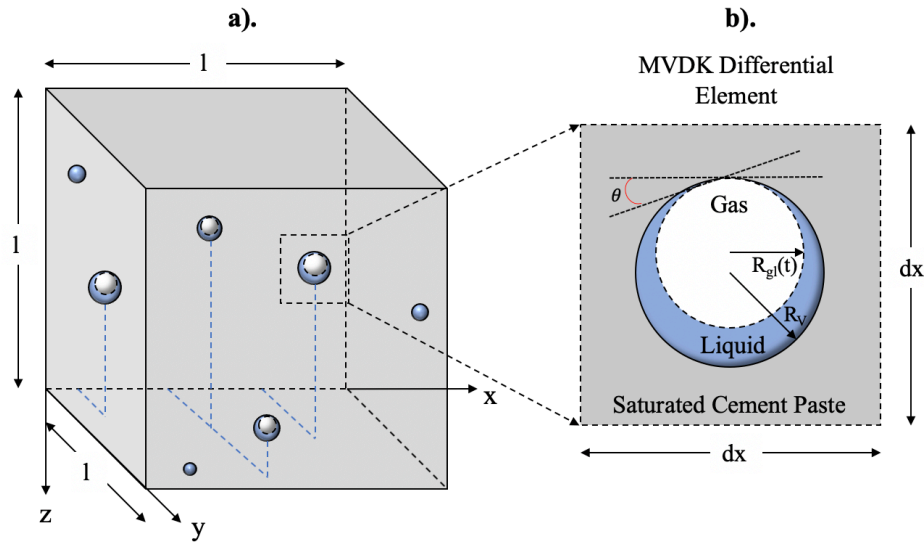


**Figure 3-24 - Idealized air-entrained cementitious material system used as the basis for the formulation present in Section 3.4.2. a). cubic system where voids are placed as computational nodes, b). differential element surrounding a node in which a void is placed.**

The necessary inputs for the MVDK model include the spherical void size distribution, the total volume of air voids in the cubic sample, the respective contact angles,  $\theta$ , and normalized values of trapped mass,  $m_t$ , for each void. With respect to the initial geometry of the compressed air in a given air void, the same formulation and corresponding mechanisms are used for the computational element in the MVDK model, displayed in Figure 3-24b, as in the SVDK model – reference Section 3.3.1. With respect to placing the voids at a respective computational node, a random number generator is used to select available values of  $x$ ,  $y$ , and  $z$  and coupled with an algorithm that ensures that the voids do not interpenetrate. Additionally, it is stipulated that air voids cannot be placed along or overlap the free surface. Figure 3-25 displays an example of the cubic MVDK model where each length is 0.6mm and clearly denotes the interior nodes, surface nodes, and randomly placed spherical voids. It is important to note that in order for the model to have the most

physical meaning possible, the radius of the largest air void placed in the cubic system must be less than one-half the differential element size,  $dx$ . When this condition is not met, the spherical void occupies volume in the neighboring elements and conflicts with the model formulation presented in Section 3.4.2.

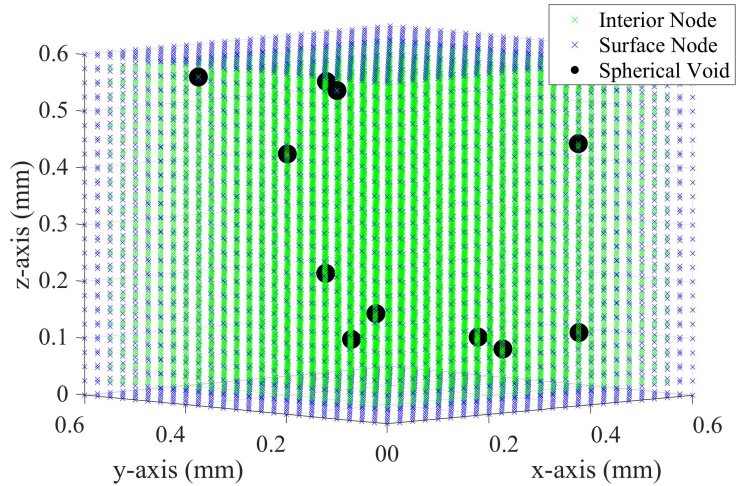


**Figure 3-25 - Example of MVDK model system. All spherical voids in this system have a  $R_v = 10\mu\text{m}$  but have been scaled for ease of visualization.**

### 3.4.2 MVDK Model Formulation and Assumptions

Due the similarity in solutions given by the SVDK model for when advection was or was not considered, the MVDK model considers the liquid pressure to be  $P_{\text{atm}}$  everywhere at all time. It is important to note that it is only a reasonable assumption for mean values of intrinsic permeability,  $\kappa$ , and diffusivity of dissolved air in saturated cement paste,  $D_g^s$ , as shown in the results presented in Figure 3-15. Additionally, by only considering the diffusion-driven transport of the dissolved gas, the minimal time to full saturation of the cubic MVDK system will be obtained. Based on this, it can be assumed that the rate of saturation of the MVDK system will be slightly faster than for a system in

which advection is considered or the liquid pressure is a function of space and time. As a result, the formulation to solve the MVDK system is simpler than the SVDK model as only the concentration of dissolved gas,  $C_g$ , needs to be solved at each node in addition to the mass of the remaining air at the nodes in which spherical air voids are present. Equation 3-21 displays Fick's second law, the governing diffusion equation, that is solved for the entire system at each time step. Similar to the SVDK model, it is assumed that the cubic system is rigid, its porosity is constant, and the entire system is isothermal. Equation 3-22 displays how the mass of air,  $m_a$ , within the differential element is calculated by considering the flux of dissolved air on the respective faces of the differential elements in which air voids are found – visualized in Figure 3-26.

**Equation 3-21 - Governing MDVK equation for transport of dissolved gas.**

$$\frac{\partial C_g}{\partial t} = D_g^s \nabla^2 C_g = D_g^s \left( \frac{\partial^2 C_g}{\partial x^2} + \frac{\partial^2 C_g}{\partial y^2} + \frac{\partial^2 C_g}{\partial z^2} \right)$$

**Equation 3-22 - Differential equation for mass of air in a differential element containing a spherical air void.**

$$\frac{\partial m_a}{\partial t} = dx^2 D_g^s \nabla C_g$$

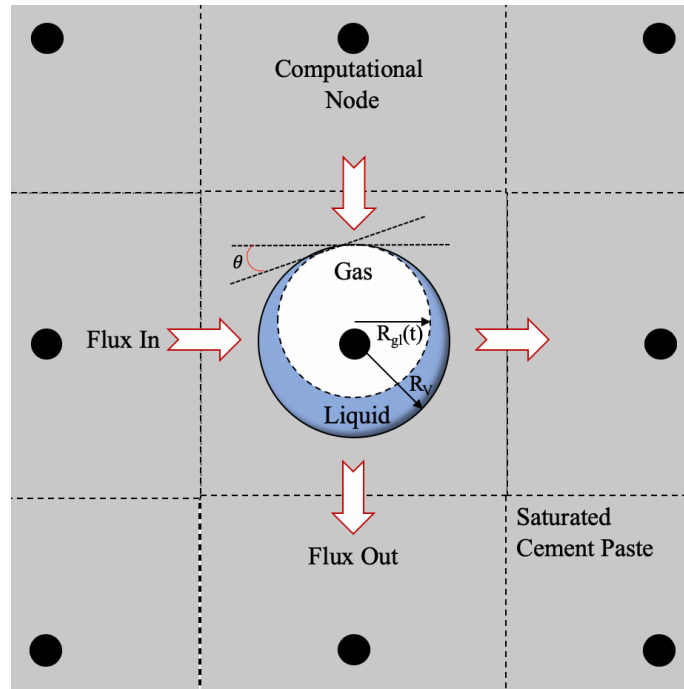


**Figure 3-26 - 2D representation of MVDK assessment for Equation 3-21.**

Once  $m_a(t+dt)$  is known the next value of the radius of the air-liquid interface,  $R_{gl}(t+dt)$ , can be calculated by solving Equation 3-23. With  $R_{gl}(t+dt)$  obtained, it is used to establish the new dissolved air concentration at the same node. To calculate  $R_{gl}(t+dt)$ , it is assumed that the concentration of the dissolved air concentration is homogenous everywhere in the element and given by the concentration which maintains thermodynamic equilibrium at the air-liquid interface (i.e., Henry's Law and the Laplace equation). Due to this assumption, it is expected that the time to full dissolution for a single air void will be shorter than that determined by the SVDK model, but still closely comparable in terms of solution form and well within the same order of magnitude. The other assumptions present in the determination of the new radius of the air-liquid align with the SVDK model (i.e., the concentration of dissolved gas in the liquid within the void is assumed constant and the trapped gas is treated as ideal).

**Equation 3-23 - Equation to calculate  $R_{gl}(t+dt)$ .**

$$m_a(t + dt) - \left( P_{atm} + \frac{2\sigma}{R_{gl}(t + dt)} \right) \left( \varphi_0 dx^3 k_H + \frac{4\pi}{3} R_V^3 (-\varphi_0 k_H + 1) \right. \\ \left. + V_g(R_V, R_{gl}(t + dt), \theta, d) \left( -1 + \frac{M_w}{GT} \right) \right) = 0$$

As presented in the previous section, for a realistic system the spatial step,  $dx$ , must be greater than the diameter of the largest air void in the system. For polydisperse air void systems – as displayed in Figure 3-5b and in [36,40] – the preceding formulation presents a problem. That problem is centered on the approximation of the dissolved gas concentration gradients (e.g., if a small air void is placed in a large representative elementary volume the developed formulation will result in an instantaneous dissolution). It is important to note that as displayed in the SVDK model, such instantaneous dissolution somewhat accurate (i.e., for spherical voids of 10 $\mu$ m and 100 $\mu$ m, the times for full dissolution differ by 3 orders of magnitude, which coincide with the initial volume and mass difference). Additionally, it could be physically possible to have very small spherical voids within a single element. Despite these challenges, for the purposes of the results presented herein, monodisperse air void systems will be analyzed to ensure that the underlying dissolution dynamics of the trapped air is captured. For each monodisperse system, the influence of depth to the surface will be characterized on time to full-dissolution in addition to calculating the temporal evolution in the air void system saturation,  $S_a$ , and mean internal gas pressure of all of the air voids. The latter two parameters are of central interest to evaluate assumptions made in previous models found

in [17,25,29,44] and will be evaluated based on the total volume fraction of air voids within the MVDK models.

Leveraging the evaluations made on the monodisperse systems, as shown in Figure 3-25, the outcomes of a polydisperse system will be made using an volumetric homogenization approach of approximated solutions to the MVDK model. The homogenization is done by assuming that each size class,  $i$ , of air voids in the monodisperse system occupies a known volume fraction,  $v_f^i$ , within a size distribution of spherical voids. At any time,  $t$ , the average saturation,  $S_a^{avg}$ , of a polydisperse air void system can then be approximated by Equation 3-24 where  $S_a^i$  is the saturation of a given size class of air voids. The mean compressed gas pressure in saturation MVDK systems will be evaluated and compared to previous approximations made in [44] that assume the air voids fill in order of increasing size. Equation 3-25 gives the mean compressed gas pressure,  $P_g^{avg}$ , used in [44] to calculate concentration of dissolved air within a REV containing representative distribution of air void sizes.  $V_a$  in Equation 3-25 is the volume of air given by the distribution of spherical air voids and the total air void volume fraction in the cementitious material.  $R_v^{sat}$  is the largest size class of air void that is fully liquid saturated. Additionally, the implications of this assumption on a REV scale within a continuum model will be discussed.

**Equation 3-24 - Volumetric homogenization for average saturation of a polydisperse air void system.**

$$S_a^{avg}(t) = \sum_{t=0}^{\infty} \sum_{i=1}^n v_f^i S_a^i(R_v, t, D_g^s, v_f^i)$$

**Equation 3-25 - Smallest-to-largest calculation methodology for mean gas pressure in [44].**

$$P_g^{avg}(R_V^{sat}) = \frac{2\sigma \int_{R_V^{sat}}^{\infty} \frac{1}{R_V} \frac{dV_a}{dR_V} dR_V}{\int_{R_V^{sat}}^{\infty} \frac{dV_a}{dR_V} dR_V}$$

### 3.4.3 MVDK Model Results and Discussion

In order to ensure the presented MVDK formulation agrees with and reflects the findings of the SVDK model, a single void was placed at the center of the cubic computational system and the dissolution kinetics were evaluated. Figure 3-27 displays the MVDK and SVDK solutions agree very well. Additionally, as detailed in the formulation, it is found that the MVDK model slightly under approximates the SVDK solution. This finding, as previously noted, results from the assumption that concentration of dissolved gas everywhere in the element has the same value as that required for thermodynamic equilibrium at the gas-liquid interface, where the gas is air and the liquid is a combination of dissolved air and pure water. In addition to ensuring that the MVDK model captures the void-scale behavior, the results presented in Figure 3-28 allow for the determination of what size of model system would be appropriate for a monodisperse analysis. Figures 3-28a and 3-28b, display how the influence of depth from the surface for a single air void in the cubic system influences its total time to full dissolution as the size of the lattice is appropriately scaled. Based on the results presented in Figure 3-28b, when an air void is placed a normalized distance of 0.05 away from a free surface, and there is no influence of any other air voids, the total time to dissolution decreases 10% to 15% with respect to when the air void is placed far from the surface. The small difference can be directly explained

by the fact only one face of the void-containing element is in contact with a fixed surface concentration.

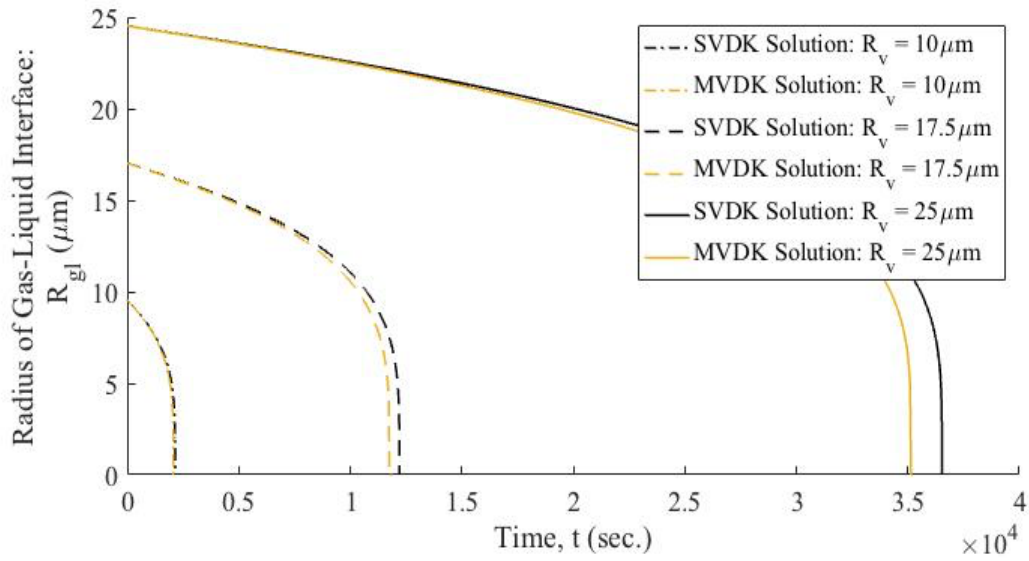


**Figure 3-27 - Comparison of SVDK and MVDK model solutions for various initial void radii. Inputs:  $m_t = 1$ ,  $\theta = 0$ ,  $D_g^s = 5 \times 10^{-12} \text{ cm}^2/\text{s}$ .**

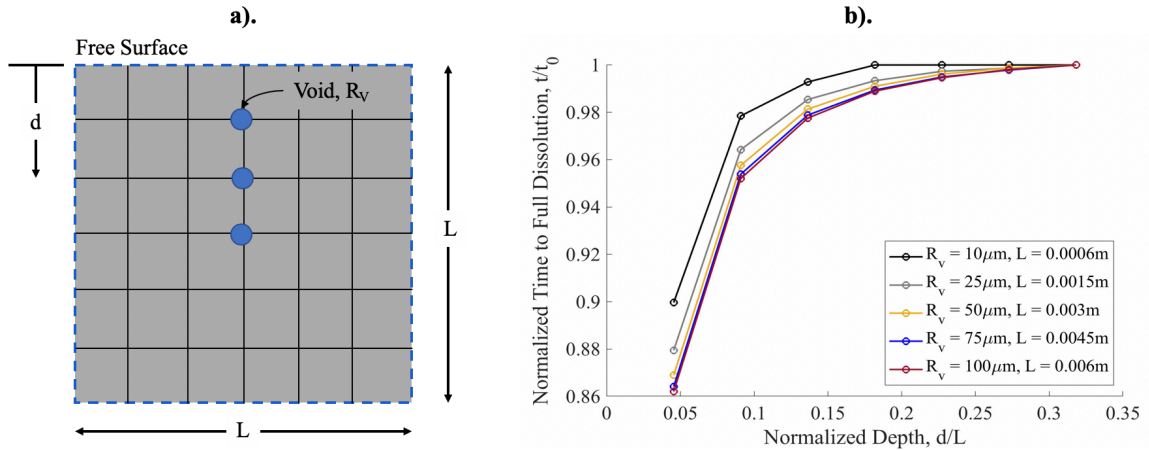


**Figure 3-28 - Influence of normalized depth to the surface on normalized time to full dissolution where  $t_0$  is the time to full dissolution for each respective system when the air void is placed in the center of the system, similar to Figure 3-27, and  $L$  is the size of the entire cubic lattice.**

To capture the influence of void-void interaction, a series of monodisperse cubic systems were evaluated. Figure 3-29a and 3-29b display the gas-liquid interface kinetics for cubic systems in which the volume fraction of air voids are 0.5% and 4%, respectively, and all of the voids have a radius of  $10\mu\text{m}$ . Figure 3-29a clearly displays that even for a system with a small total air content, the time to complete dissolution is significantly increased by a factor of 3 (i.e., from Figure 3-27 it takes 2500s for a  $10\mu\text{m}$  air void to become fully saturated whereas in Figure 3-29a the same size air voids are not yet completely water-filled at 7500s). Figure 3-29b further displays the reduction in spherical void saturation rate while clearly capturing the ripening effect of air voids. It is important to note that similar to the SVDK model, when the radius of the gas-liquid interface is larger than the void radius and the contact angle is zero, the void is completely gas-filled and the surrounding capillary porosity is slightly gas-filled and the over-pressure results in its

dissolution and reduction. Additionally, despite the ripening of trapped air in various voids, for long-times all of the trapped gas will dissolve.

Figure 3-30 shows the evolution in air void saturation as a function of time and the influence of volume fraction of spherical air voids in the cubic system. Additionally, Figure 3-30 includes corresponding analytical asymptotic approximations of the air void saturation kinetics given by Equation 3-26 which approximates the saturation kinetics of monodisperse air voids systems, capturing the interaction between the air voids and with the surface. It can clearly be seen that as the void fraction,  $v_f$ , increases, the approximation becomes increasingly accurate, but agrees very well in terms of general form and order of magnitude – the primary concern for predicting the behavior of a polydisperse air void system.

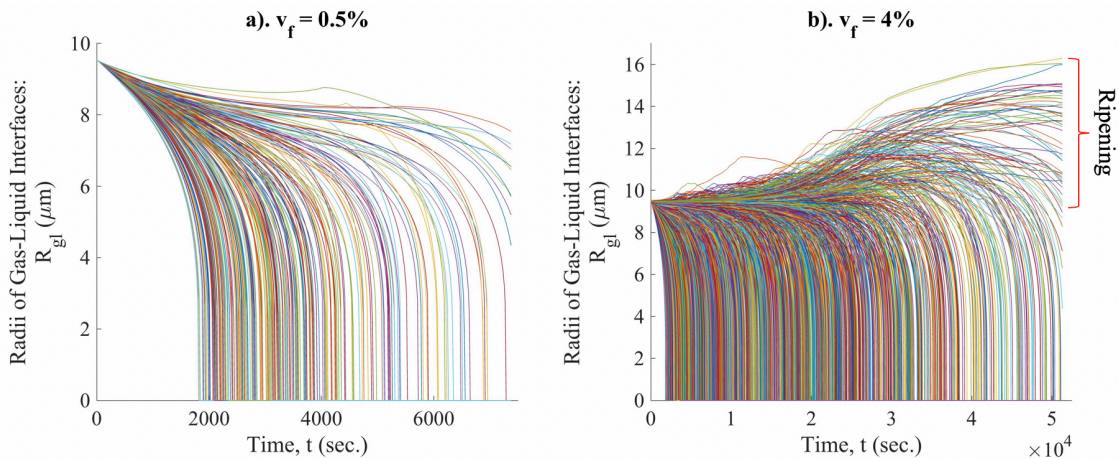


**Figure 3-29 - Influence of volume fraction a). 0.5% and b). 4% on the dissolution kinetic of trapped air voids where a). has 275 voids and b). has 2060 voids. Inputs:  $R_v = 10\mu\text{m}$ ,  $m_t = 1$ ,  $\theta = 0$ ,  $D_g^s = 5 \times 10^{-12} \text{ cm}^2/\text{s}$ ,  $L = 0.0006\text{m}$ .**

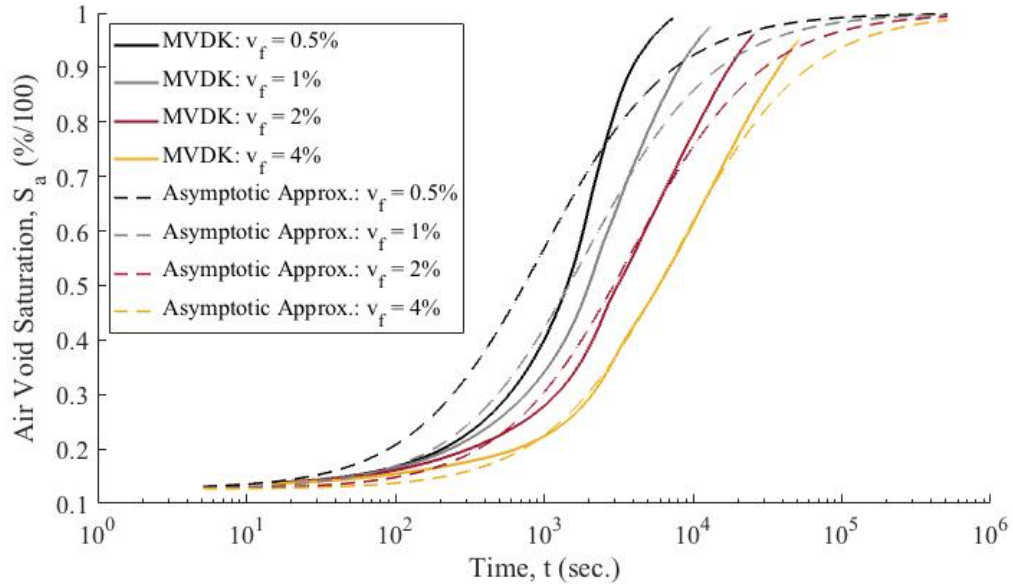


**Figure 3-30 - Influence of volume fraction on air void saturation and corresponding asymptotic approximations of the MVDK cubic systems. Inputs:  $R_v = 10\mu\text{m}$ ,  $m_t = 1$ ,  $\theta = 0$ ,  $D_g^s = 5 \times 10^{-12} \text{ cm}^2/\text{s}$ .**

**Equation 3-26 - Analytical expression for air void saturation behavior for MVDK model.**

$$S_a^{apx}(t, v_f) = \left( \frac{R_{gl}(t=0)}{R_v} \right)^3 \left( \frac{t}{t + v_f e^{1 \frac{L^2}{D_g^s}}} \right) + \left( 1 - \left( \frac{R_{gl}(t=0)}{R_v} \right)^3 \right)$$

As discussed in Section 3.2.2.2, in 2017 Moradillo and Ley experimentally displayed how air voids saturate in cement pastes when ponded under a potassium iodide solution [50]. Figure 3-31a displays the spherical void size distribution that was found in the first 6mm of the cylindrical sample. Using the reported size classes for the air void size distribution shown in Figure 3-31a, the saturation kinetics of monodisperse MVDK systems for each size class was determined using Equation 3-26 as displayed in Figure 3-31b. In addition to reporting the void sizes, the total number of voids of a given size that were

completely saturated at 60 days was determined in [50] and used to calculate the experimental air void size class saturation,  $S_a^i$ , and the total air void system saturation,  $S_a^{avg}$ , as shown in Figures 3-31c and 3-31d.

Using the approximated saturations for each air void size class shown in Figure 3-31b, the saturation for each class,  $S_a^i$ , at 60 days was determined and reported in Figure 3-31c. The approximated MVDK model values shown for each size class in Figure 3-31c is calculated by the product of the approximated saturation of a given air void size class at 60 days by the volume fraction of each air void size class for the entire air void system. The experimental and numerical estimations of the degree of saturation of each size class agree very well and depart only for the largest air void size classes. The saturation of the total air void system,  $S_a^{avg}$ , was determined by using the volumetric homogenization approach detailed in the preceding formulation. Figure 3-31d displays the results of the homogenization and its comparison to the experimental saturation degree of the air voids at 60 days.

It is important to note that the following findings were obtained by assuming that for each air void the normalized trapped mass,  $m_t$ , and the contact angle,  $\theta$ , were 1 and 0, respectively. Additionally, it was found that MVDK approximations and homogenization gave the best results when a diffusivity of the dissolved air in the saturated cement paste,  $D_g^s$ , was taken to be  $5e-13$  m<sup>2</sup>/s, which is well within the range of experimental values as shown in Table 3-3. Overall, the findings in Figure 3-31 display that the approximated MVDK model solutions, and their volumetric homogenization, can accurately predict the evolution of the saturation on the pore- and specimen-scales. The accuracy of these

prediction using the approximate MVDK solution (i.e. Equation 3-26) is attributed to the fact that the size of the air void is largely what governs its dissolution kinetics.

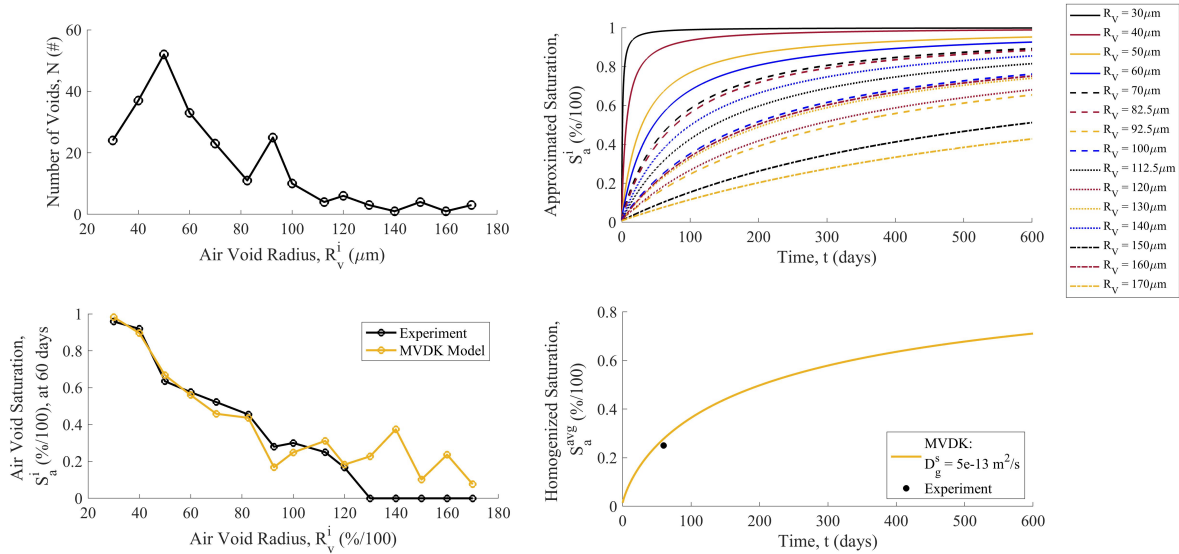


**Figure 3-31 - Comparison of experimental findings from [50], a). air void size distribution found within the first 6mm of the  $\mu$ CT specimen prepared and evaluated in [50], b). estimations of respective saturation behavior using Equation 3-26 for each air void size class, c). comparison of experimental and numerical air void saturations for each evaluated size class, d). homogenization of saturation approximations made in b). and comparison to 60 day air void saturation experimentally determined in [50]. Inputs:  $m_t = 1$ ,  $\theta = 0$ ,  $D_g^s = 5 \times 10^{-13} \text{ cm}^2/\text{s}$ .**

Using the entire spherical void size distribution from [50], it was of interest to see if the approximated MVDK model by Equation 3-26 can predict experimental secondary saturation curves determined in [18] and displayed in Figure 3-4 of Section 3.2.2.1. Figure 3-32a displays the ability of the approximated MVDK model to approximate the evolution in air void saturation as a function of the diffusivity of dissolved gas in the surrounding saturated cementitious media,  $D_g^s$ . The air void saturations for the mortars specimens are found by identifying the nick point from each curve present in Figure 3-4 and appropriately scaling by the known total air void content for each specimen. Figure 3-32b displays a

similar comparison where the air void size distribution is made finer or coarser by while holding  $D_g^s$  constant. It is important to note that the fine and coarse distribution are made by shifting the mean radial air void distribution values by  $25\mu\text{m}$  in a positive and negative directions, respectively. For the coarse adjustment, the result is a system in which the total volume of air voids is overwhelmingly made from air voids greater than  $100\mu\text{m}$  in radius, in line with the definitions presented and used in [25,44]. Clearly, both comparisons agree very well.

In Figure 3-32a, the factor of five increase and decrease in  $D_g^s$  bounds the experimental air void saturation curves while also displaying the influence of the diffusivity material property on the MVDK model. In Figure 3-32b, the fine and coarse distributions similarly capture the rate of air void saturation for the mortar systems evaluated in [18] while displaying that air void system with coarse distributions saturate more slowly, which falls in line with the findings in [44] and agrees with the results and intuition provided by the SVDK model (i.e., larger air void should take a longer time to saturate due to a smaller dissolved gas concentration gradients and higher air volumes). It is worthy to note that the secondary saturation, characterized by  $S_2$  in Figure 3-23, would be found in Figure 3-32a and 3-32b by fitting linear approximations to the experimental and model curves, but it is important to note that upon closer consideration these curves behave in an asymptotically.

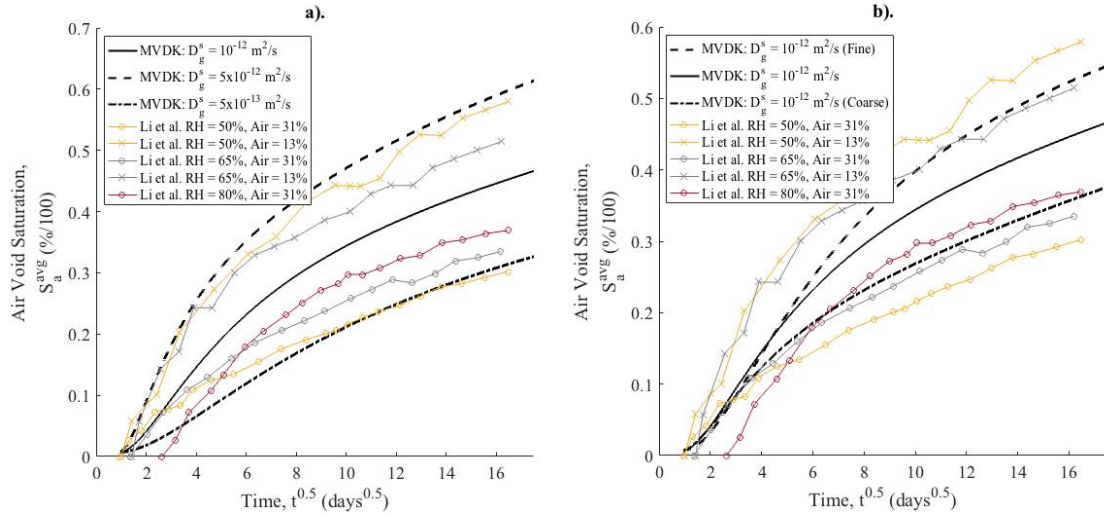


**Figure 3-32 - a). Comparison of MVDK model with experimental air void saturation curves from [18] and influence of  $D_g^s$  on air void saturation evolution, b). study on the influence of coarse and fine air void distributions obtained from [50] on air void saturation evolution.**

In [44], it was assumed that the mean gas pressure, which is used to determine the liquid saturation of the air voids within a REV, can be calculated by assuming that the air voids fill from smallest to largest. Using the void size distribution in Figure 3-30a, the evolution in the mean compressed gas pressure and corresponding air void system saturation is determined by Equation 3-24. Figure 3-33 displays the mean gas pressure based upon the assumption that the voids fill from smallest-to-largest (in black). Additionally, Figure 3-33 displays the gas pressure and saturation relationship for monodisperse MVDK systems with small volume fractions and various void sizes,  $R_V$ . The difference between the outcomes suggests that the mean gas pressure is highly sensitive to how the air voids become filled. Despite the difference in the form of the evolution, it is important to note that the mean pressures given by Equation 3-24 are near the same magnitude of the mean gas pressure given by the monodisperse MVDK model outcomes and both converge to the atmospheric pressure as the air void saturation goes to unity.

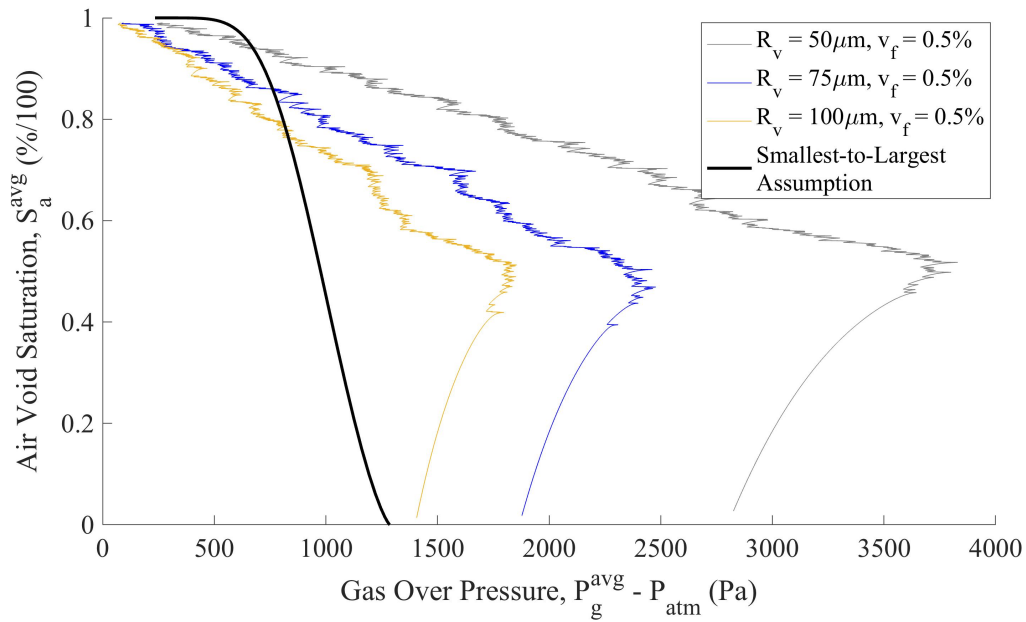


**Figure 3-33 - Evaluate of smallest-to-large filling assumption on the mean gas over pressure within the spherical voids and the system saturation to monodisperse MVDK systems with small volume fractions,  $v_f$ .**

#### 3.4.4 MVDK Model Conclusions

As detailed in the review within this chapter and in the introduction of Section 3.4, numerous fundamental questions regarding the mechanisms for long-term saturation, characterized by slope  $S_2$ , that specimen- and lab-scale experiments display were unanswered. The multi-void dissolution kinetics (MVDK) model formulated and evaluated how the pore-scale saturation phenomenon governs the long-term saturation of monodisperse systems, which can then be approximated and homogenized to understand the saturation kinetics of polydisperse air void systems in cementitious materials. In order to display continuity between the SVDK and MVDK models, it was shown that MVDK formulation can predict the same dissolution and resulting saturation kinetics as the SVDK model. Following this, the influence of depth to a free surface was evaluated and displayed

to reduce the total time to full dissolution for a single air void by 10% to 15%, as shown in Figure 3-29b, when the bubble was placed a normalized distance of 0.05 away from a free surface. Additionally, it was found that as a single void reached one third of the side length, the time to full dissolution was equivalent to that given by the SVDK model or when a single void was placed at the center of the cubic system as analyzed in Figure 3-27.

Following the SVDK and depth analysis, monodisperse air void systems were evaluated using the presented MVDK formulation and the influence of total void volume fraction was displayed. Figures 3-29a, 3-29b, and 3-30 displayed that as the volume fraction increases the dissolution kinetics of the monodisperse system slows due to void-void interactions and can result in Oswald's ripening. As displayed in Figure 3-30, the influence of volume fraction on the saturation evolution of the monodisperse can be accurately modeled using the asymptotic approximation developed and displayed in Equation 3-25. It was then shown by using a volumetric homogenization approach that the saturation of the air void size classes and the specimen from [50] could be accurately predicted using the approximated MVDK behaviors. Lastly, with respect to the long-term saturation, it was displayed that the homogenized and approximated MVDK model solutions could be used to predict the air void saturation evolution as a function of time for a set of 5 different specimens from [18] in addition to displaying the influence of the diffusivity property and air void size distribution on the results.

As a result, the MVDK formulation and approximate model can clearly establish a connection between the void-scale filling and the specimen-scale saturation while predicting correct rates of long-term saturation to cementitious materials. While numerous insights have been provided by this model, as previously concluded, additional work is

needed to further generalize the MVDK model to consider the influence of liquid pressure and improve the state equation which relates the mass of trapped gas and concentration of dissolved gas within a differential volume containing a spherical void. Additionally, the overall computational efficiency of the MVDK model could be improved by moving from the use of the current representative volume element (RVE) to a statistical volume element (SVE), which can provide equivalent information of how a system of air void saturate when homogenized [77,78]. The necessary length-scale for the SVE can be identified by ensuring the spatial correlations with between the RVE and SVE scales are identical [77,78].

Additionally, the experimental comparisons made herein are not entirely satisfactory. A full set of  $\mu$ CT data similar to [50] where the saturating spherical air voids are reported at a more frequent time step would serve as a more valid form of assessment. However, the comparison in Figure 3-32 suggests that the governing physics has been captured by the homogenized and approximated MVDK model solutions and that for expected values of diffusivity and common ranges of air void size distributions the long-term saturation rate of air-entrained cementitious materials can be predicted. Ultimately, the MVDK model can aid not only in the prediction of the time to critical saturation of an air-entrained cementitious material but also in its design.

## CHAPTER 4. CRITICAL SATURATION OF AIR-ENTRAINED CEMENTITIOUS MATERIALS

### 4.1 Introduction

In 1968 [16], the existence of a critical water saturation ( $S_{cr}$ ) where specimens transitioned from experiencing compressive to tensile strains upon temperature depression below freezing was displayed. Additional studies [17,18,45] confirmed the findings in [16], showing that air-entrained concretes and mortars over a large range of air content have a universal  $S_{cr}$  value of ~85%. Due to the fact that the same value of critical saturation has been experimentally obtained across such a broad range of cementitious materials – see Figure 1-2 -  $S_{cr}$  can adeptly serve as an indicator for damage initiation and therefore as a service-life and durability metric [20,21,33,35] when coupled with the understanding of how the air voids become liquid water filled over time - the central topic of Chapter 3. In 2018, AASHTO updated provision PP84 [47] and incorporated a time to  $S_{cr}$  ( $t_{cr}$ ) assessment to ensure a minimum 30-year service-life for concrete pavement mixtures, highlighting the utility of the  $S_{cr}$  phenomena to industry.

Although the  $S_{cr}$  phenomenon has been known for decades [16], a single model that incorporates and evaluates the critical parameters seen in experimental and numerical evaluations (e.g., air void size distribution, various air void saturation regimes, etc.) has yet to be developed to describe this phenomenon. The model presented within this chapter is aimed at predicting the likelihood of damage initiation in air-entrained cementitious materials as a function of the air void system and total material saturation. Similar to the

MVDK model, when the air void saturation is at 0% the macro-scale system is assumed to be at the matrix saturation,  $S_m$ . Figure 4-1 displays a general schematic of how the model is formulated and expected to inform how cementitious materials with entrained and entrapped air begin to become damaged as a function of increasing liquid saturation past their matrix saturation,  $S_m$ . The presented model complements recent experimental efforts aimed at determining which material and environmental parameters influence cementitious material's value of  $S_{cr}$  [18,22,25,35,50] in addition to investigating an experimentally supported hypothesis that the  $S_{cr}$  value is linked to the evolution in spacing between non-water-filled air voids as summarized in Section 2.5.1.2 and supported by the literature review in Section 2.3. Outcomes of this work can be used to further inform design specifications and requirements for cementitious materials in freeze-thaw prone environments and aid in the identification of future research efforts to tailor the  $S_{cr}$  and  $t_{cr}$  of a cementitious material to a needed application.

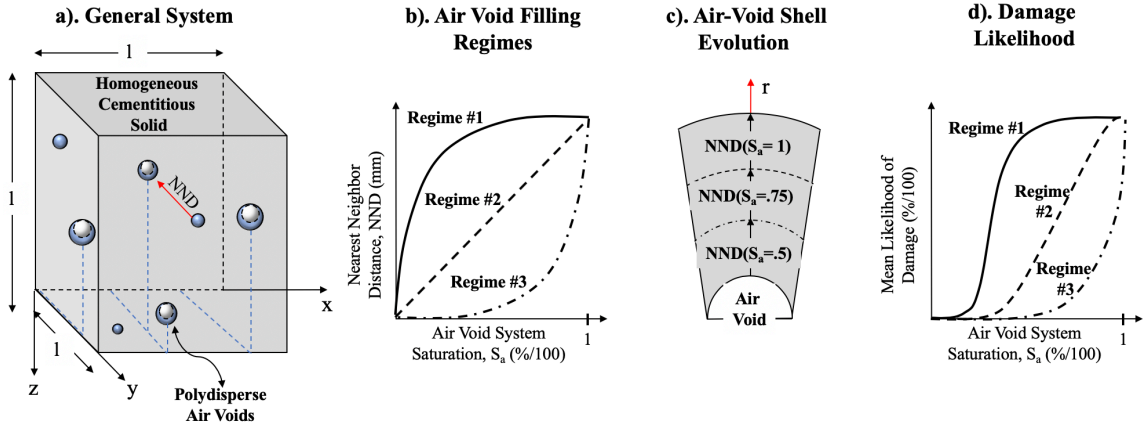


**Figure 4-1 - a). Generalized model used to predict  $S_{cr}$ , b). influence of various filling regimes on nearest-neighbor distance evolution as a function of air void saturation, c). evolution in surrounding hardened paste shell due to air void saturation, d). damage likelihood as a function of saturation and filling regime.**

As shown in Figure 4-1a, a similar cubic system to that used in the development of the multi-void dissolution kinetics (MVDK) model, presented in Section 3.4, can be utilized to physically represent a polydisperse entrapped and entrained air void system in a homogenous and porous cement paste matrix. Using this system, the influence of air void volume fraction and size distribution can be directly evaluated. Figure 4-1b shows how various air void filling regimes (i.e. air void saturation regimes), reviewed in Section 4.2.1, could influence the evolution in the void-void nearest-neighbor distance (NND). The NND can be understood as a more general and descriptive representation of the spacing of the void system as compared to Power's spacing factor derived and developed in [13]. Figure 4-1c then displays the physical implications for evolution in the nearest-neighbor distance (i.e., it results in an increased spherical paste volume around non-saturated air voids). The increase in the neighbor distance and surrounding volume has been shown to have deleterious effects on cementitious materials using theoretical models and in experimental evaluations, discussed in Section 4.2 and highlighted in Section 2.3.

As shown in Figure 4-1d, the final outcome of the model formulated in Sections 4.3 and 4.4 are likelihood of damage initiation curves as a function of air void- or macro-system saturation. Similar to the SVDK and MVDK models, parameter studies are carried out to evaluate the influence of system inputs and material parameters (i.e., volume fraction of voids, intrinsic permeability, air void distribution parameters, strength of the material, etc.). Ultimately, the aim of the work presented within this chapter is to rigorously evaluate if the systematic saturation of the entrained and entrapped air voids which corresponds to an increase in NND between non-saturated leads to the critical saturation of cementitious materials across a broad domain of cementitious material systems. With the presented hypothesis evaluated, improved confidence of the governing mechanism for the  $S_{cr}$  phenomenon can be gained and the derived model can be leveraged to identify physical parameters which govern its value - as experiment has shown it is independent of total air content and cementitious material type (i.e., concrete, mortar, or paste).

## **4.2 Literature Review**

Dissimilar to Chapter 3, the literature review within this section concurrently highlights the relevant theoretical and experimental efforts made to rigorously evaluate the hypothesis proposed in the preceding section and Chapter 2 (i.e., that the universal value of  $S_{cr} = 85\%$  - in cementitious materials occurs due to the saturation of entrapped and entrained voids which increases the likelihood of failure initiation upon freezing). The review begins in Section 4.2.1 by analyzing various water-filling regimes of entrained and entrapped air void systems - connecting previous experimental work to results displayed in Sections 3.3 and 3.4 for the SVDK and MVDK models, respectively. Section 4.2.2 then

summarizes existing physics-based models that evaluate the mechanical influence of freezing on an air-entrained cementitious materials.

#### *4.2.1 Water-filling Regimes of Entrained and Entrapped Air Void Systems*

In order to predict the  $S_{cr}$  of air-entrained cementitious materials, an understanding of how these materials become saturated is necessary and has been extensively investigated in Chapter 3. As  $S_{cr}$  occurs past the matrix saturation of most air-entrained specimens, the influence of the air void volume, size distribution, and filling regime is of particular interest. Additionally, as detailed in Section 2.3, there is a clear relationship between the spacing factor and freezing-induced strain behavior of cementitious materials which are well-saturated – reference Figures 2.3, 2.4, and 2.6.

In [44], it was assumed that air voids become water-filled in a representative elementary volume from smallest-to-largest, consistent with a thermodynamically favored theory proposed in [29] and investigated in the results portion of Sections 3.3 and 3.4. It is important to note that the results of the SVDK model, presented in Section 3.3, confirmed that the smallest-to-largest filling regime is likely only if the air void system is well-spaced (i.e., the dissolution of the compressed air in the voids does not interact with and slow the dissolution of the other air voids nearby). Despite this, based upon the imaging work completed in [50] and the results of the MVDK model, presented in Section 3.4, it is clear that air voids do not systematically fill from smallest-to-largest but is retained in the study due to its simplicity and potential to serve as an upper-bound for NND evolution as a function of air void system saturation.

Other filling regimes have been proposed and are collectively categorized into 3 groups: smallest-to-largest [29,44], equal water contribution [29,39], and proportional their single-void dissolution kinetics as detailed in Section 3.3. Figure 4-2 displays how these regimes can be understood as a function of their size distribution for an equivalent value of air void saturation. The first regime, smallest-to-largest, was previously described. Regime #2, Figure 4-2b, suggests that the air voids are simply free ‘sinks’ and their size have no influence on the likelihood of water to enter them. Regime #3, Figure 4-2c, suggests that the air voids of a given size class are saturated according to their single void dissolution kinetics – similar to the analysis conducted in Figure 3-21 – to capture the non-temporal behavior of air void filling.

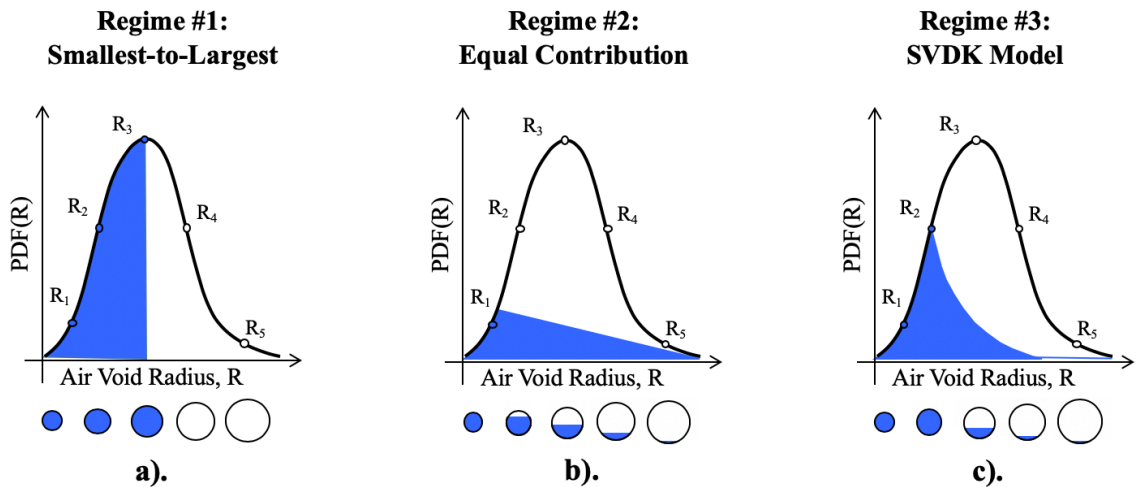


**Figure 4-2 - Generalized filling regimes evaluated.**

It is important to note that the regimes in which entrapped and entrained air void saturate over time has not yet been evaluated. To date, the imaging work conducted in [50] – see Figure 3-8b - is the field’s sole evaluation of how air voids within a cement paste become saturated over longtime periods. The three filling regimes reviewed and proposed

herein are intended to cover a large domain of physical possibilities and then evaluate a given regimes influence on the likelihood of failure initiation as the air voids become progressively water filled. Figure 4-3 serves to re-articulate how air-void saturation is connected to increasingly tensile behavior, which leads to damage through the increase of mean spacing between non-saturated, or water fill, entrained and entrapped air voids.

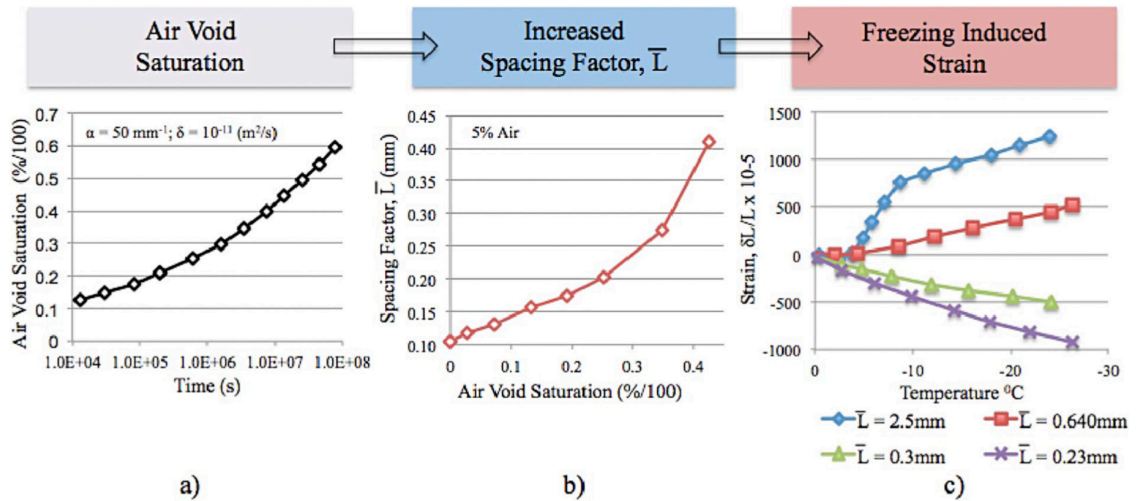


**Figure 4-3 - Relationship between air void saturation and time due to long-term ponding [29], b). influence of air void saturation on spacing factor [25], c). influence of spacing factor on tensile response of air-entrained cement pastes due to temperature depression [32]. Image taken from [19].**

#### 4.2.2 Existing Models for the Influence of Freezing on Cementitious Materials

The freezing-and-thawing of concrete is a fully coupled thermo-hydro-mechanical phenomenon. Most models are formulated as a combination of momentum, mass, and entropy balance [37–39]. It is important to note that a single model that predicts critical degree of saturation from the mechanical response of cementitious materials has also not yet to be developed. As shown in Figure 4-3c, the strain response of air entrained cement pastes changes from compressive to tensile when the spacing factor increases from 300  $\mu\text{m}$

to 640  $\mu\text{m}$  [32], a phenomenon that has been replicated using the poromechanical model [38]. Following the findings from [39], once FT-induced pressures become positive, tensile strains are induced and brittle materials are increasingly likely to become damaged. A full treatment of poromechanical theory and thermo-hydro-mechanical modeling is outside the scope of this section and readers are referred to a succinct, yet encompassing review of the fundamental physics behind freezing in cementitious materials presented by Valenza and Scherer in [79,80]. Instead, historic and seminal contributions made to the current state-of-the-art are reviewed to further the ability to predict the critical degree of saturation phenomenon.

In 1949, Powers published his hydraulic pressure theory [13] which approximated the maximal pressure exerted on the solid phase of a hardened cement paste shell surrounding an entrained air void due to the forced movement of non-frozen water by ice growing in large capillary voids – as detailed in Equation and Figure 2-1. Powers' theory, although lacking multiple first principles of FT phenomena understood today developed the framework around which advanced models have been derived and showed that microstructural features, such as the spacing factor and permeability of the hardened matrix influence the FT response [13]. Based on Powers' original theory, the maximal pressure exerted on a shell surrounding a non-filled air void is proportional to the cubic power of the spacing factor and the inverse of the non-water-saturated void radius. This suggests that it is essential to understand how the mean size and spacing of the air void system evolves to predict the mechanical effect of the saturation state on a representative region, or sufficiently thin section, of an air-entrained specimen. To date, the mechanics of FT in concrete are best understood by poromechanical theory [37–39].

In 2008, Coussy and Monteiro extended the poromechanical theory [37] to specifically address the multi-phase nature of FT phenomena and further elucidate how entrained air voids improve FT resistance of concrete. It was shown that the combination of hydraulic and crystallization pressure can result in tensile forces on the solid phase in excess of 10 MPa [37]. It was also demonstrated that entrained air voids serve as cryopumps and ice-growth reservoirs, drawing unfrozen water in the capillary pore space to the air voids where nucleation and growth of ice is favorable. In terms of validating the poromechanical model, in 2012 Zeng et al. showed that the theory can effectively predict historical strain versus temperature curves obtained by Powers and Helmuth in 1953 [32,38]. The results of the model developed by Zeng et al. are shown in Figure 2-6 and demonstrate the ability for the poromechanical model to predict strain development in air-entrained and non-air-entrained hardened cement pastes as a function of time with a known thermal exposure.

The major outcome of the poromechanical model is the establishment of the microstructural features of the concrete, such as the spacing factor and matrix permeability, that control the mechanical response of the material. In 2016, Mayercsik et al. further explained the relationship between the quality of air void systems and mechanical response to FT using a novel spacing factor based on nearest-surface functions [39]. The spacing factor is known to increase as a function of saturation based upon the work conducted in [25,81] and results in increased tensile strains on the solid matrix [32] resulting in damage. Relationships between strain development and the degree of saturation have also been explored. Figure 4-4 illustrates the behavior of mortars with different degrees of saturation (S) during freeze-thaw. The fully saturated mortar (S=100%) shows significant expansion

during freezing, while the partially saturated mortar (S=17%) displays contraction during freezing. These findings show the importance of the degree of saturation in determining the performance of cementitious materials under FT conditions.

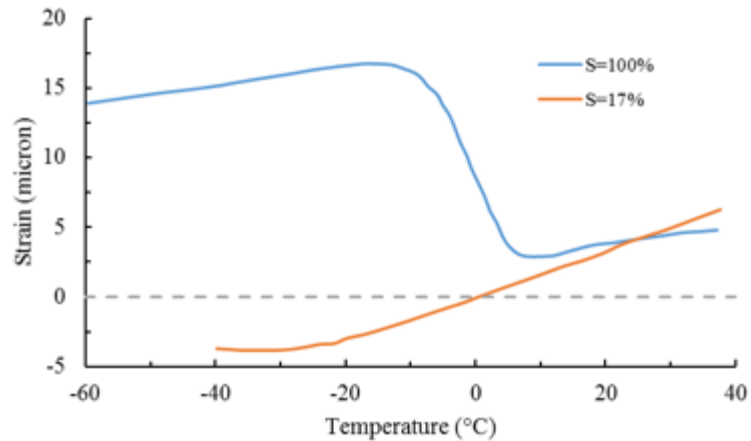


**Figure 4-4 - Influence of degree of saturation on strain response of mortar [19].**

While the poromechanical theory has provided a basis to predict the mechanical response of a material, numerous other models have been developed that provide insights into the freezing process and how it is influenced by chemical species present in the pore solution. In 2017, Esmaeli et al. developed a 1D model that considers the influence of ionic species coming from deicing salts present in pore solution [82]. This model illustrates the freezing point depression due to pore size, nucleation, and ionic species in the pore solution. As the salt concentration increases, the freezing temperature decreases due to ionic concentration and the heat flow decreases as the volume of ice that forms decreases [82]. The results of the model and accompanying experiments conducted by Farnam et al. in 2014 [83] agree well and show that the influence of the capillary pores are more significant during melting than freezing due to the prevalence of large amounts of air voids

whose freezing-point depression is negligible and provide favorable ice nucleation sites in comparison to the capillary pores.

### 4.3 System Definition and Mechanisms

For the purposes of the model presented within this chapter, the entrained/entrapped air voids and surrounding matrix are computationally modeled by randomly placing non-overlapping spheres in a cubic system with a side-length,  $l$ . The air void information is obtained from a cumulative distribution function (CDF) of the radii of the air voids and total air content information. Based on previous studies [25,50], the air void radii CDF's used to populate the cubic system are either assumed to be lognormal or are directly acquired from previous  $\mu$ CT analyses. As shown in Figure 4-5a, the radii CDF of the entrained air void system is discretized  $n$  times and the number of air voids for each size class is calculated to achieve the desired volume fraction (i.e. total air content).

Using a random sequential absorption algorithm (RSAA) [84–86], the air voids are randomly placed in the cubic system from largest to smallest, resulting in the air void – matrix system shown in Figure 4-5b. The RSAA was used in comparison to other methodologies, such as metropolis arrangement [87], because the volume fraction of the air void system is well below the jamming limit [85] (i.e., where it becomes highly-computationally inefficient for the algorithm to find available space for an air void). For modeling highly porous media, such as pervious concrete, the use of a different addition and spacing algorithm would be necessary in order to allow particles to interpenetrate or overlap. Additionally, it is important to note that the randomly dispersed system displayed in Figure 4-5b differs from that used in the MVDK model found in Section 3.4. Here, the

voids are placed randomly anywhere in the cubic space such that they do not overlap, whereas in the MVDK cubic model the air voids were placed at discretized computational nodes to solve the detailed governing equations.

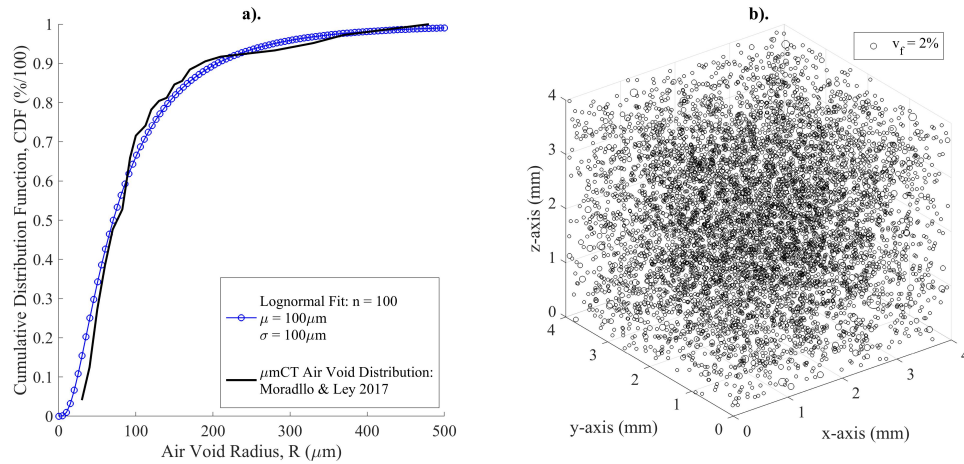


**Figure 4-5 - a). CDF of air void size distribution [50] approximated by a lognormal distribution, b). Outcome of RSSA outcomes – system contains ~9900 non-overlapping voids.**

Following the dispersion of the discrete air voids, nearest neighbor distance (NND) calculations are made for each air void in the cubic system [86,88]. For the purpose of this calculation, see Equation 4-1, the NND is defined as the smallest distance calculated between the centers of air void ‘i’ located at coordinates  $(x_i, y_i, z_i)$  and any other air void ‘j’ in the system located at coordinates  $(x_j, y_j, z_j)$  where their respective radii,  $R_i$  and  $R_j$ , have been subtracted. This definition intentionally departs from the traditional definition of NNDs [86] (i.e., the minimal radial distance from one point to another point in 2 or 3 dimensions (D)) allowing for the direct measurement of the solid cement paste surrounding each air void. Figure 4-6a displays an example nearest neighbor evaluation from a 2D plane in the cubic system, where the green arrow depicts the NND for the central air void. Figure

4-6b shows a histogram of the NND's for the polydisperse system displayed in Figure 4-5b. The presented NND histogram in Figure 4-6b presents the nearest void-void distances when their material system is at the matrix saturation point, implying the air voids are completely air-filled but the surrounding capillary porosity is saturated.

**Equation 4-1 - Nearest neighbor distance calculation.**

$$NND_i = \left( (x_j - x_i)^2 + (y_j - y_i)^2 + (z_j - z_i)^2 \right)^{1/2} - R_j - R_i$$

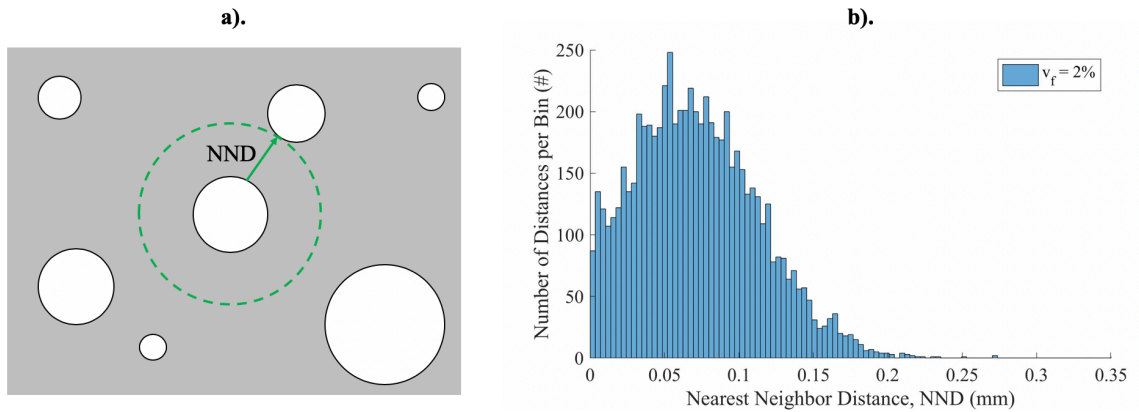


**Figure 4-6 - a). 2D schematic of NND determination in a polydisperse air void solid system, b). histogram of NND distances for the air void system described and detailed in Figure 4-5.**

Suggested originally in [25], the saturation of the air void system is hypothesized to lead to the increased spacing of the remaining air-filled voids. In the literature, various regimes have been proposed on how the air voids become water-filled, as detailed in Section 4.2.1. The first regime occurs from smallest to largest [29]. The second regime occurs concurrently where water enters each air void without considerations of air void

size. The third regime hypothesizes that the air voids fill in accordance with the previously derived SVDK model in Section 3.3. It is important to note that when an air void has a saturation greater than or equal to 91.7%, it is assumed to be completely water-filled with respect to the NND calculation. This was done as air voids with this level of water-saturation will become completely ice-filled upon freezing and can no longer serve as cryo-suction pumps or expansion reservoirs in accordance with the theory developed in [37] and evaluated in [39].

The first filling regime, smallest-to-largest, is the simplest to implement into the RSAA algorithm to populate the cubic system. Due to the fact that the distribution of the air void size distribution is already discretized  $n$  times, the air void saturation of the system,  $S_a^{S-L}$  can be directly determined by Equation 4-2, where  $m$  is the discretization index which increases to  $n$ ,  $N_i$  is the number of air voids of size class  $i$ , and  $R_i$  is the radius for air void class  $i$ . For each discretized step, the air voids of size class  $m$  and less are removed from cubic system and the NNDs of the remaining air voids are re-calculated. The second two filling regimes (i.e., concurrently-filling sinks and as a function of the SVDK behavior), require that the volume of water,  $V_w(S_a)$ , which saturates the air void system first be calculated, as shown in Equation 4-3. In Equation 4-3,  $S_a$  is the air void system saturation which ranges from 0 to 1, where  $l$  is a size of the RSAA cubic system, and  $v_f$  is the volume fraction of air voids.

**Equation 4-2 - Determination of air void system saturation for the smallest-to-largest filling regime.**

$$S_a^{S-L} = \frac{\sum_{i=1}^m N_i R_i^3}{\sum_{i=1}^n N_i R_i^3}$$

**Equation 4-3 - Volume of water to enter air voids for a given air void system saturation,  $S_a$ .**

$$V_w(S_a) = S_a l^3 v_f$$

For the second filling regime, the amount of water that should be equally distributed amongst the air voids is  $V_w(S_a)$  divided by the number of air void size classes,  $n$ . When the calculated water volume is larger than that of a given air void size class, the voids are fully saturated, removed from the cubic system, and the remaining water volume is equally divided amongst the other non-saturated voids. For the third filling regime, the amount of water that fills air voids of a given size class will follow the solutions to the SVDK model presented in Section 3.3.

It is important to note that the influence of air void depth (i.e., distance from the air void center to specimen surface) is not considered in any of the presented regimes. An inherent assumption of all of the models is that the specimen is sufficiently small such that there are no water saturation gradients in the capillary porosity, which allows for the air in the voids to diffuse to a free surface. Figure 4-7a, building on Figure 4-6a, displays how the NND can be understood to increase or ‘swell’ as a function air void saturation. Figure 4-7b then displays the evolution in NND histogram for the smallest to largest filling regime for various air void saturation steps and the same material system presented Figure 4-5.

Clearly, the air voids filling has significant implications for the evolution in mean spacing between the non-saturated voids - as measured by the NND. Additionally, seeing as how this system is randomly developed, in the following analyses, multiple polydisperse air void system are simulated to gain a statistical sense of how the RSAA system will behave under the three filling regimes.

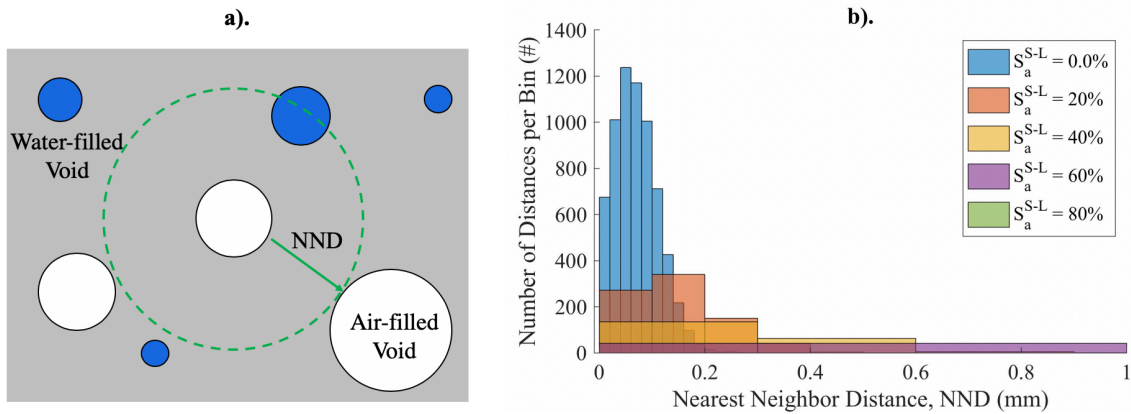


**Figure 4-7 - a). 2D schematic of how NND ‘swells’ as a function of saturation, b). corresponding nearest-neighbor distance histogram values as a function of air void system saturation under a smallest-to-largest filling regime. Note that b). contains Figure 4-6b and uses the air void system information and cubic system size as displayed in Figure 4-5.**

Using the presented regimes and multiple cubic systems, the evolution in NND as a function of filling regime can be directly evaluated. Figure 4-8 displays how the mean NND increases as a function of air void saturation and various regimes for the same air void system detailed in Figure 4-5 where the error bars represent one standard deviation from the mean NND obtained from 5 randomly generated polydisperse air void systems. The NND’s for the first filling regime, smallest-to-largest, increases fastest as a function of the air void system saturation. This falls in line with general intuition (i.e., the initial spacing should largely be dictated by the small air voids and as they become water-filled

the mean distance of air voids in the system should increase). Additionally, it is important to note that the technique used here and displayed in Figure 4-8 departs significantly as compared to previous geometric models [25] that have used Powers' spacing factor to predict the evolution in void-void spacing due to saturation. Additionally, the various trends displayed in Figure 4-8 are likely dependent upon the volume fraction of air content and air void size distribution. For the purposes of this section the methods used to evaluate the defined system of interest are only generally evaluated. Section 4.5 will evaluate the influence of these parameters on the void-void spacing outcomes and also the predicted likelihood of damage initiation based upon a model formulated in Section 4.4. Additionally, as previously mentioned, if any air void size class had a degree of saturation greater than 91.7%, it was treated as fully water-filled with respect to the NND determination.

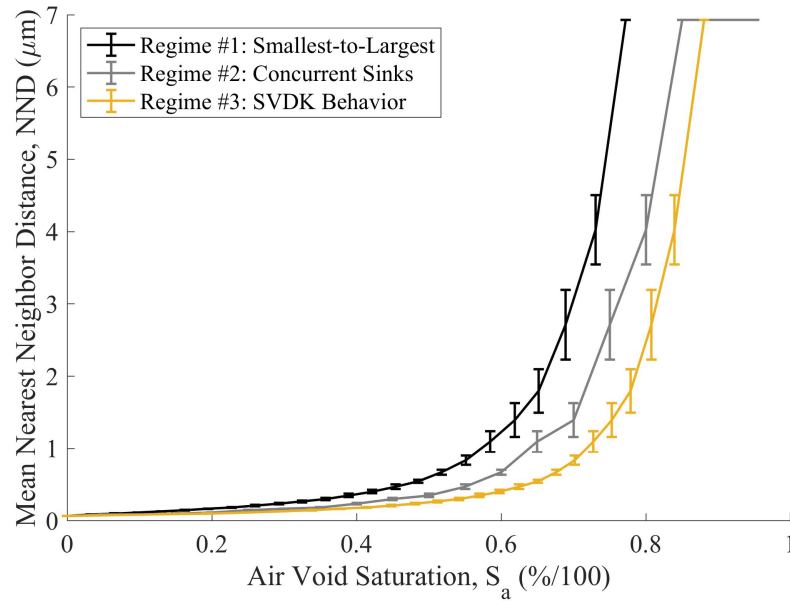


**Figure 4-8 - Influence of air void saturation on nearest-neighbor distance growth as a function of filling Regimes #1-3.**

As suggested by Figure 4-1a, the random spherical air void systems are assumed to be dispersed in a homogeneous and porous cementitious material. For the purposes of the work in this chapter, the material is assumed to be cement paste. To this point, critical saturation ( $S_{cr}$ ) has been discussed with respect to the entire material system, but the preceding air void analyses presented in Figure 4-8 or within Figure 3-31c/d have treated the air void system saturation. In order to move from one type of saturation to the other, knowledge of the porosity surrounding and interconnecting the air voids to one another, and to the specimen surface, needs to be reliably estimated. Seeing as how the material surrounding the air void system is idealized as cement paste, Powers' hydration models can be conveniently applied. Equation 4-4 displays the Powers' equation used to estimate the capillary porosity,  $C_p$ , in the air voids, where  $w_c$  is the water-to-cement ratio,  $SG_C$  is the cement specific gravity, and  $\alpha$  is the degree of cement hydration [36]. Assuming that

the capillary porosity is completely water filled the cubic system, the saturation,  $S$ , can be calculated by Equation 4-5.

**Equation 4-4 - Powers' equation for capillary porosity in cement pastes as a function of cement hydration and water-to-cement ratio.**

$$C_p = 1 - \left( 1 - \frac{wc}{wc - \frac{1}{SG_c}} \right) ((1 - \alpha) + 1.52\alpha + 0.6\alpha + 0.2\alpha)$$

**Equation 4-5 - Determination of macro-system saturation,  $S$ , from the capillary porosity, air void saturation and air void volume fraction.**

$$S = \frac{C_p + S_a v_f}{C_p + v_f}$$

#### 4.4 Limit State Model Formulation and Assumptions

By calculating half of the NND for each air void in the polydisperse air void system as a function of air void saturation,  $S_a$ , the spherical region that will undergo pressures due to freezing around the remaining air-filled voids is captured. By coupling Powers' hydraulic pressure theory presented as Equation 2-1 in Section 2.2 with an estimate of the tensile strength of cement pastes [13] as a function of their compressive strength,  $f_c$ , a limit-state function for likelihood of freeze-thaw failure around a spherical air void can be written as a function of half NND,  $\varphi_i$ , for an air void with radius  $R_i$ . It is important to note that this equation, which will be used for the duration of the Chapter, does not consider osmotic effects based on criticisms presented in Chapter 2 of [89] (i.e., the theory has no way to quantitatively detail developed internal pressure or the role of the air voids).

Equation 4-6 presents the limit state function where damage initiation is assumed to occur once hydraulic pressures,  $D$ , are greater than the tensile strength,  $C$ , of the surrounding paste matrix. Table 4-1 gives definitions for the variables found in Equation 4-6 and values which are constant in the following results sections are detailed in the far column. Additionally, Equation 4-7 details how the intrinsic permeability,  $K$ , of the surround cementitious paste shell is modeled based the capillary porosity,  $C_p$ , in [13].

**Equation 4-6 - Limit-state function for hydraulic pressure evaluation in RSAA system.**

$$LSF = C - D = (0.057f_c - 100) - \frac{\eta}{3} \left( 1.09 - \frac{1}{S_{cp}} \right) \frac{UR}{K} \left( \frac{\varphi_i^3}{R_i} + \frac{3\varphi_i^2}{2} \right)$$

**Table 4-1 - Symbol definition and values retained as constant for analysis and results in Section 4.5 for Limit-state function, Equation 4-6.**

Symbol	Definition	Value (Units)
C	Capacity (i.e., tensile strength) of cementitious shell	N.A.
D	Demand (i.e., hydraulic pressure) placed on cementitious shell.	N.A.
$f_c$	Compressive strength of cementitious shell	Variable in Section 4.5
$\eta$	Viscosity of water near 0 deg. C.	0.019 (g/cm/s) [13]
$S_{cp}$	Degree of saturation of capillary porosity in the cement paste shell	1 (fully saturated)
U	Amount of freezable in the capillary porosity	0.232 (1/°C) [13]
R	Freezing Rate	$1.45 \times 10^{-3}$ (°C/sec) [41]
K	Intrinsic permeability of the cement paste	See Equation 4-7 [13] (cm <sup>2</sup> )

**Equation 4-7 - Intrinsic permeability estimation for cement paste as a function of the capillary porosity,  $C_p$ , developed in an experimental fit from [13].**

$$K = (3550C_p^2) \times 10^{-17}$$

At every saturation step and around each air-filled void, Equation 4-6 is evaluated. Based on the LSF result, a value of 0 is assigned to the air-void shell region if

damage initiation is not expected to occur (i.e., the hydraulic pressures expected in the system are below the tensile strength). For air-void shell systems where the pressures are greater than the tensile strength a value of 1 is assigned to the region, suggesting failure within that region of the cubic system is likely. Figure 4-9 displays how this system can be visualized in 2D with associated values of half NND,  $\varphi_i$ , and air voids which are still air filled, given by radii,  $R_i$ . A mean likelihood of damage initiation,  $L_{DI}$ , is computed for the survived/failed regions to understand the average behavior of the modeled specimen - similar to evaluations of damage evolution shown in Figure 1-2 as a function of saturation. The likelihood of damage initiation,  $L_{DI}$ , is simply found by the sum of the air void-shell systems which have failed at a given saturation state divided by the number of systems that are below an air-void saturation state of 91.7%.

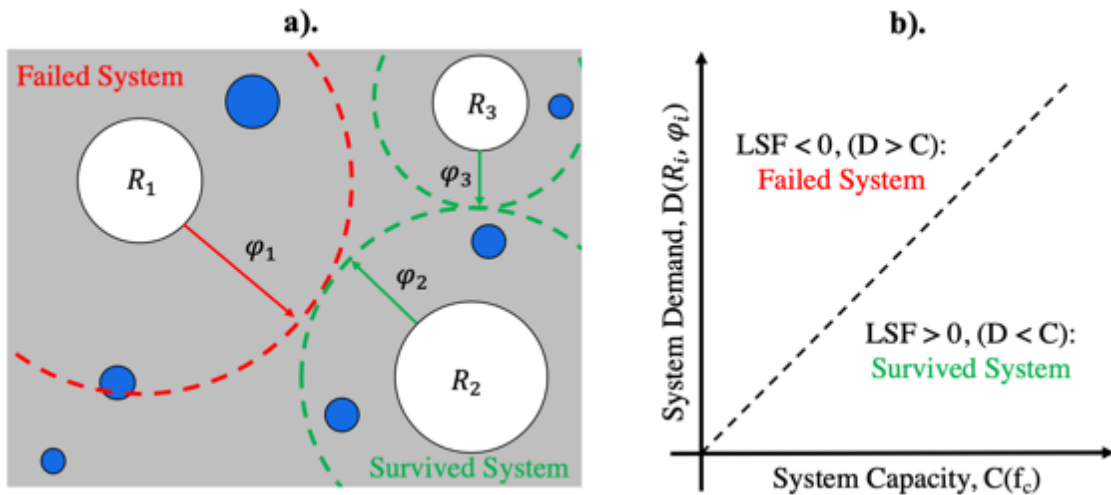


**Figure 4-9 - a). 2D example of half NNDs and surviving and failing regions of cubic system, b). limit-state visualization for Equation 4-6.**

It is important to note that the value of  $U$  (i.e., freezeable water content in the capillary porosity) was only obtainable for ordinary Portland cements with a  $w/c$  of 0.45 in

[13]. Additionally, the intrinsic permeability,  $K$ , is also limited in terms of its applicability and only accurately predicts the value for cement with capillary porosities with values less than 0.35 and greater than 0.10 [13]. As a result, an applicable, but condensed domain of  $w/c$  and  $\alpha$  can be evaluated with the derived limit-state function shown in Equation 4-6.

In the following results and parameter study, the mean half NND and likelihood of damage initiation at any given saturation for all simulated system are associated with a calculated  $2\sigma$  variance. The  $S_{cr}$  of the simulated systems can then be quantitatively assessed as the inflection point in the mean likelihood of damage initiation estimation for all simulations. Using this definition of  $S_{cr}$  estimation, the influence of various parameters, such as the regime in which the air void fill, the air void volume fraction and size distribution parameters, in addition to various solid matrix properties, can be evaluated to determine how it influences the  $S_{cr}$  predictions.

#### **4.5 Model Results and Discussion**

In line with the initial systems presented and assessed in the preceding sections, Figure 4-10 displays estimated likelihood of damage initiation,  $L_{DI}$ , values for the simulated cubic system with an air void volume fraction of 2% and the same size distribution information presented in Figure 4-5 as a function of air void filling regime. Corresponding with the evolution in NND as a function of air void saturation, shown in Figure 4-8, the  $L_{DI}$  curve for the smallest-to-largest regime initiates (i.e., becomes non-zero) first whereas the SVDK-behaviour regime begins to display damage for higher values of system, or macro-, saturation. Figure 4-10, in addition to the following images within this section, also displays two regions. The first region, defined as ‘Damage Initiation’,

occurs from 85% to 91.7% of the system saturation. Within this region, it is expected that the model should begin to register and develop damage. The second region, defined as ‘Damage Certainty’, occurs at and past 91.7% of the system saturation as any material with this level of water saturation should begin to display some level of tensile strain due to the expansion of ice upon freezing [16]. From Figure 4-10, it can be seen that the developed model predicts that damage should begin to occur in the material, irrespective of the air void filling regime, within the defined region of damage initiation – suggesting that the presented hypothesis of how air void saturation relates to the likelihood of damage initiation could be well-founded. To further investigate, the following section will evaluate the influence of the air void volume fraction, cubic system size, w/c ratio, degree of cement hydration, compressive strength, and lognormal air void size distribution parameters (i.e., the mean and standard deviation).

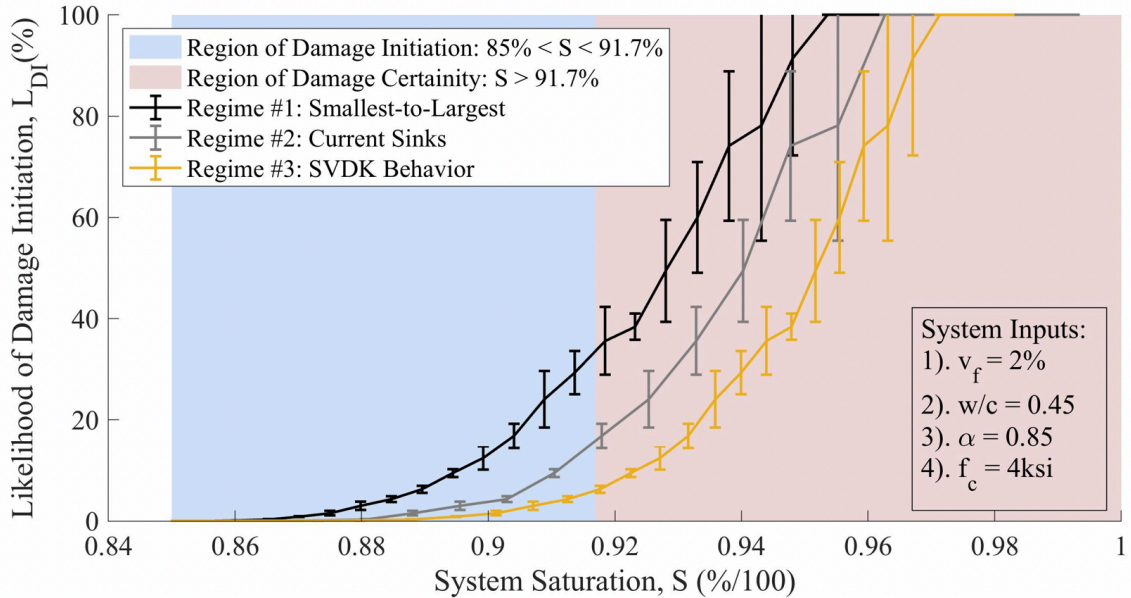


**Figure 4-10 - Initial outcome for likelihood of damage initiation given the detail system inputs and the air void size distribution shown in Figure 4-5a obtained from [50].**

A key aspect of the experimental  $S_{cr}$  phenomenon is that it is relatively invariant of the air void volume fraction in the material. Figure 1-2 clearly displays that irrespective of air content of the cementitious material, damage begins to initiate and propagate near a system saturation of 85%. Figure 4-11 evaluates the influence of air void volume fraction on  $L_{DI}$  and the three air void filling regimes. For filling regimes #2 and #3, similar to Figure 4-10, irrespective of the volume fraction,  $L_{DI}$  becomes non-zero and begins to exponentially grow within the expected region of ‘Damage Initiation’. For high volume fraction (i.e., 5% and 10%), Regime #1 predicts damage to initiate before 85% system saturation, but when considering the error-bars damage is unlikely initiate before 80%. All regimes display that as the volume fraction of air increases from 2% to 5%, there is a decrease in the system saturation at which  $L_{DI}$  begins to be non-zero. Interestingly, as the air void content increases from 5% to 10% very little to no change is seen in the  $L_{DI}$

predictions when considering the error bars – especially for Regime #3. This final finding supports that the developed model corresponds to the experimental trend (i.e.,  $S_{cr}$  is invariant of the total air content of the cementitious material).

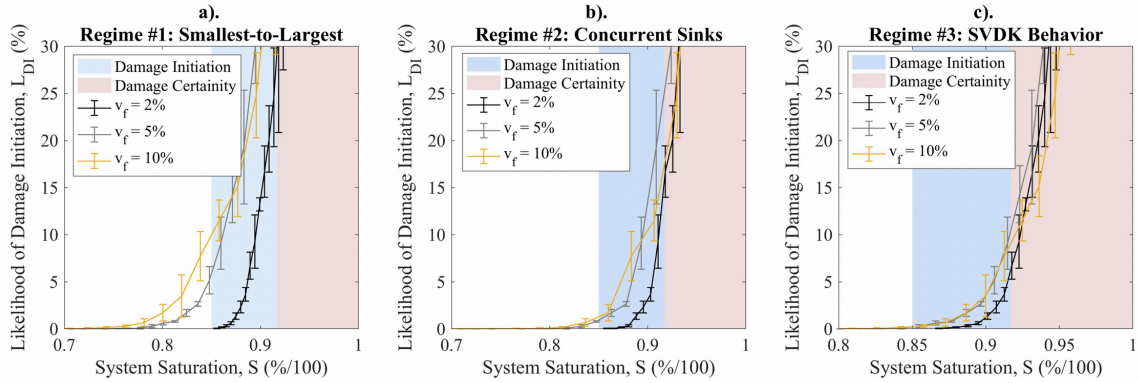


**Figure 4-11 - Estimations of likelihood of failure for filling regimes, a). smallest-to-largest, b). concurrent sinks, and c). SVDK behavior, using the same air void size distribution from Figure 4-5 and the system parameters shown in Figure 4-10.**

To further investigate why the model is invariant of air content, Figure 4-12a and 4-12b display how the evolution in NND evolves as a function of air void and system saturation, respectively, for various air contents. In Figure 4-12a the curves are distinct and follow intuition (i.e., as the volume fraction increases the air void saturation at which the nearest neighbor distance begins to exponentiate also increases). In Figure 4-12b, when the air void saturations and capillary porosity,  $C_p$ , are used to calculate the system saturation,  $S$ , the 5% and 10% nearest neighbor distances overlap. The reason why the model is invariant for large air contents (i.e., those greater than 5%) arises due to the scaling from the air void saturation to system saturation. For example, from Figure 4-12a the air void saturations,  $S_a$ , for each  $v_f$  (i.e., 2%, 5%, and 10%) at a mean NND of 1mm are approximately 0.575, 0.775, and 0.85. If the capillary porosity,  $C_p$ , is 10% of the cube, then the air void system saturations at this value of mean NND are 0.93, 0.925, 0.925 – there is

no difference between the 5% and 10% volume fractions. This displays that the invariance is a result of the fundamental behavior of the NND curves and how the air void saturations and then scaled to the system saturation.

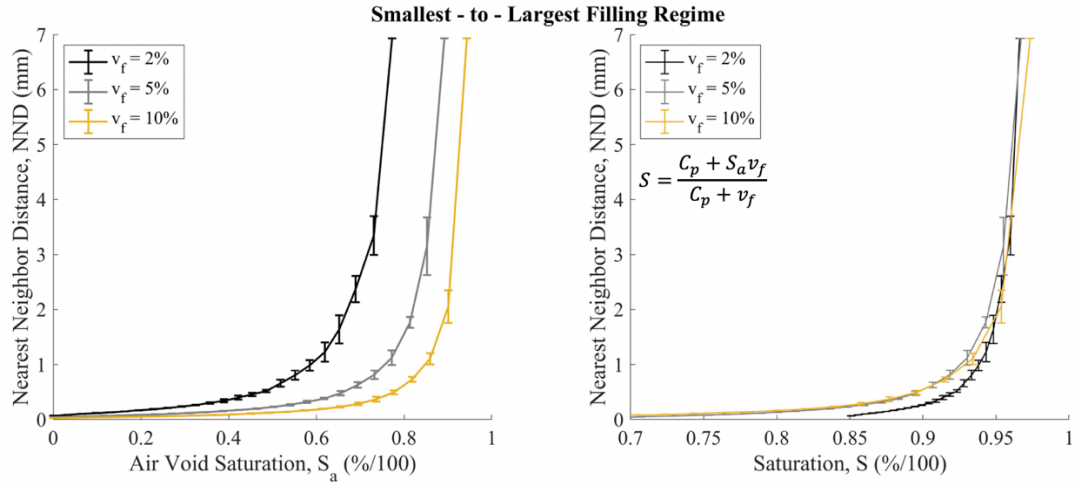


**Figure 4-12 - Evolution in NND as a function of total air void content,  $v_f$ , and a). air void saturation and b). system saturation.**

Figure 4-13 displays the influence of the cubic system size,  $l$ , on the  $L_{DI}$  for all of the air void filling regimes and air void volume fraction of 5%. For all regimes, as the  $l$  increases the  $L_{DI}$  behavior shifts right into the ‘Damage Initiation’ region. Similar trends are seen between the filling regimes as in Figure 4-11. An important note regarding the Figure 4-11 is that for the smallest value of  $l$  (i.e.,  $l = 3\text{mm}$ ) the error bars are significantly larger than for when  $l$  is set to 4mm or 5mm. This implies that the model system isn’t sufficiently representative and larger size length is needed – note that the error bars for the 4mm and 5mm curves are approximately equivalent and  $L_{DI}$  begins to be non-zero at the same value of system saturation for all filling regimes. Additionally, for  $l$  values of 4mm and 5mm, the initial  $L_{DI}$  development overlaps for all filling regimes - suggesting that damage initiation would be predicted for the same values of system saturation. Due to this,

cubic systems of 4mm are used for the remaining analysis as the number of air voids in the system scales by the cubic root of the system size, making calculation highly inefficient.

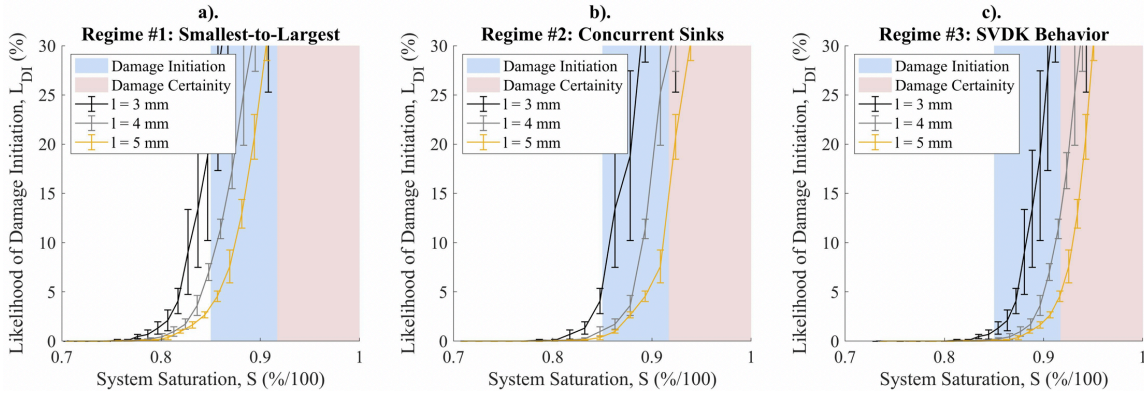


**Figure 4-13 - Influence of cubic system size on LSF results for various filling regimes. Same material parameters as for Figure 4-10 where the air void volume fraction is 5%.**

Knowing now that air void filling regime #1 predicts the fastest  $L_{DI}$  development as a function of system saturation, parameters which influence the cement paste shell surrounding the air void are evaluated. Figure 4-14a evaluates the influence of the degree of cement hydration,  $\alpha$ , on  $L_{DI}$  development where the water to cement ratio is held constant at 0.45. For  $\alpha$  values of 0.85 and 0.80 the  $L_{DI}$  predictions perform similarly as to the previous analyses, but for the  $\alpha$  value of 0.90 the  $L_{DI}$  prediction move significantly towards lower values of system saturation - this is an artifact of the capillary porosity estimation. Given a w/c of 0.45 and a  $\alpha$  of 0.90 (or 90%), the estimation  $C_p$  is  $\sim 0.08$ , which is outside the realm of applicability for Equation 4-7 and results in an intrinsic permeability that is unrealistically low, which gives higher estimations of the hydraulic pressure,  $D$ , and therefore in a higher damage likelihood at lower values of air void and macro-system saturation. Figure 4-14b displays a similar trend (i.e., when  $\alpha$  is set constant to 0.85, a w/c

of 0.425 gives a  $C_p$  of  $\sim .085$ ). These two plots, corresponding to the discussion made in Section 4.4, display the domains of material parameters where the derived model is applicable.

It is worthwhile to note that when the system is well conditioned (i.e., given values that are representative of the approximations made for the intrinsic permeability estimation) the general behavior of  $L_{DI}$  as a function of system saturation corresponds to experimental expectations as detailed in Section 2.2 and Figure 1-2 (i.e., for changes in material parameters, the same  $S_{cr}$  trend is found). Figure 4-15 displays the influence of fluctuations in compressive strength,  $f_c$ , on  $L_{DI}$  development. Clearly, significant changes in the parameter do not influence behavior in a significant manner - corresponding with why  $S_{cr}$  is seen in all forms of cementitious materials [16,18,45].

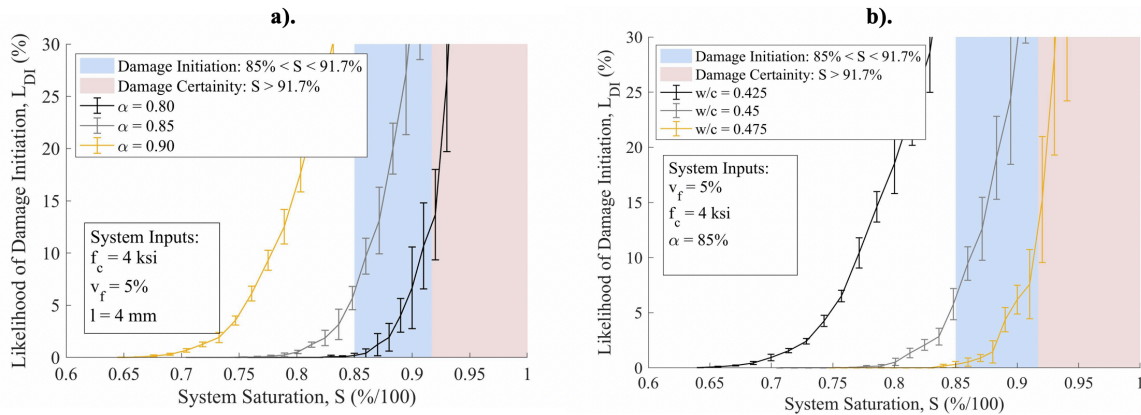


**Figure 4-14 - Influence of a). degree of cement hydration and b). water-to-cement ratio for the same air void size distribution from Figure 4-5. Smallest-to-largest filling regime.**

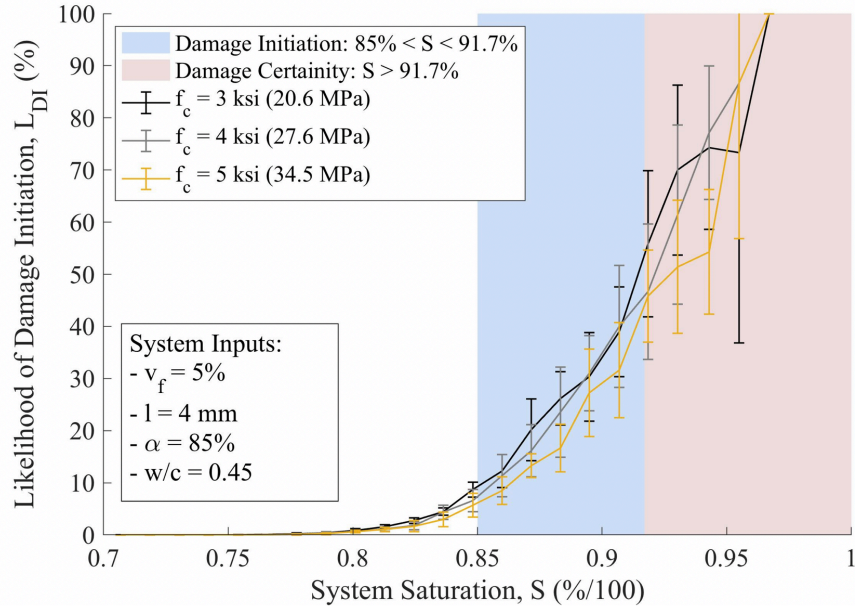


**Figure 4-15 - Influence of compressive strength on failure likelihood. Smallest-to-largest filling regime.**

Prior to this point, the air void size distribution used in the presented results has corresponded to the lognormal fit for the size distribution of air voids seen in a  $\mu$ CT experiment of cement pastes [50] displayed in Figure 4-5a. Figure 4-16a displays the influence of changes in the mean of the lognormal air void size distribution where the standard deviation,  $\sigma$ , is held constant at  $50\mu\text{m}$  for the smallest-to-largest filling regime. As the mean decreases from  $125\mu\text{m}$  to  $75\mu\text{m}$  the  $L_{DI}$  initiates (i.e., becomes non-zero) at progressively higher values of system saturation and approaches 85%. Figure 4-16b displays the influence of the standard deviation,  $\sigma$ , of the air void size distribution when the mean is held constant at  $100\mu\text{m}$ . Interestingly, the  $L_{DI}$  become non-zero at same value of system saturation for all values of  $\sigma$  but then the rates of development begin to differ past an  $L_{DI}$  value of approximately 5%. Figures 4-17a and 4-17b provide insight into the different behavior for variations in the mean and standard deviation in Figure 4-16,

respectively. Figure 4-17a suggests that increases in the mean of the air void size distribution initiates the air void system with higher mean values of void-to-void spacing- resulting in a more distanced air void system for the same system saturation. As a result, this yields higher values of  $L_{DI}$  that approach 85% as shown in Figure 4-16a, which corresponds to experimental trends detailed in [90]. Figure 4-17b shows that fluctuations in the standard deviation result in significant rate changes in NND evolution for high values of system saturation (i.e., greater than 87.5%) - no different than for  $L_{DI}$  at saturation values near 85% in Figure 4-16b. In summary, these results suggest that increases in the mean of the air void size distribution increases the initial void-to-void spacing effectively decreasing the expected value of  $S_{cr}$  and that increases in the size distribution's standard deviation results in increased rates of  $L_{DI}$  passed the inflection point of the  $L_{DI}$  curve.

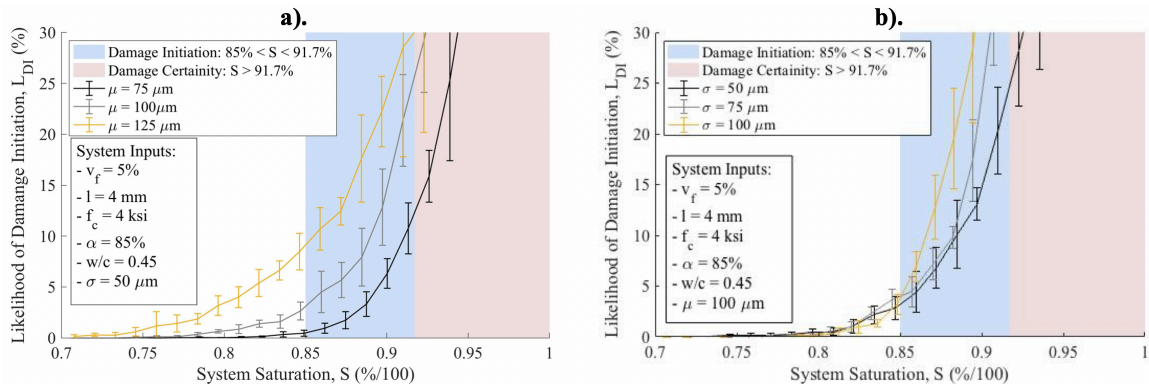


**Figure 4-16 - Influence of a). distribution mean and b). distribution standard deviation on model outcomes for the smallest-to-largest filling regimes.**

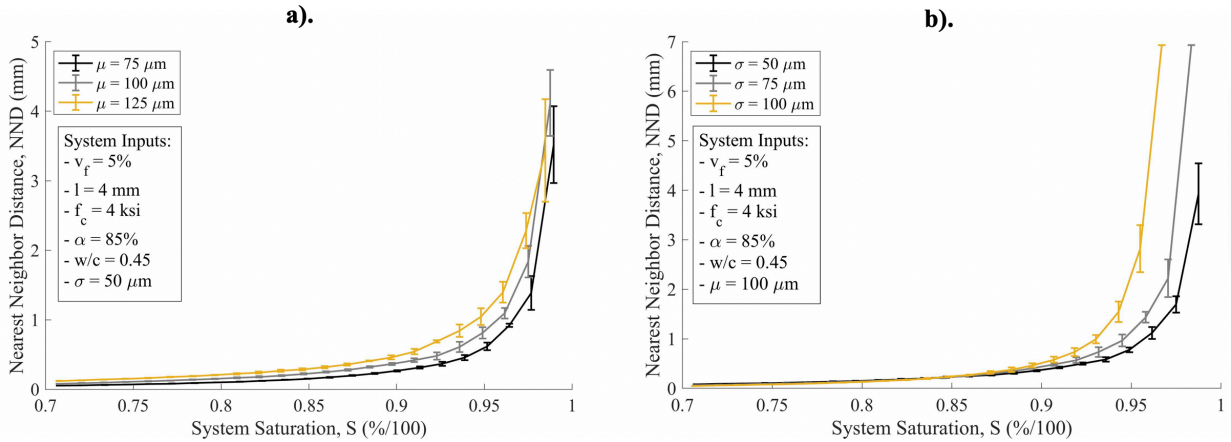


**Figure 4-17 - Influence of a). distribution mean and b). distribution standard deviation on NND for the smallest-to-largest filling regimes.**

#### 4.6 Conclusions

The results and discussion made in the preceding section detailed the influence of various air void system parameters, properties of the surrounding cementitious paste, and gross system size on the likelihood of damage initiation,  $L_{DI}$ , as a function of the macro-system saturation. Overall, it was displayed that the developed model can clearly predict the  $S_{cr}$  behaviour of cementitious materials as displayed in Figure 1-2 and how different air void filling regimes could influence the outcome. As discussed, critical saturation,  $S_{cr}$ , has been shown to be invariant of the cementitious material type (i.e., paste, mortar, or concrete), the total air content (i.e.,  $v_f$  in this model), and corresponding materials parameters such as the w/c, degree of cement hydration, and various air void distribution parameters. The work presented herein displays that the initial hypothesis (i.e., that  $S_{cr}$  occurs due to the increase in mean NND as the air voids saturate, which significantly influences the likelihood of failure at high values of system saturation) is very defensible.

Analysis of Figure 4-11 displayed that increases in the air void volume fraction from 5 to 10% made no significant statistical difference in the system saturation at which the model predicted damage to begin and exponentiate. Figures 4-14a and 4-14b, although limited in the domain of values for  $w/c$  and  $\alpha$  which would be analysed, displayed that for well-conditioned systems the  $L_{DI}$  aligned with findings in Figures 4-11 and 4-13. Figure 4-15 showed that the model is highly invariant to compressive strength (i.e., for large changes in  $f_c$  there is little to no change in  $L_{DI}$  behaviour). Figures 4-16 and 4-17 displayed that as the mean of the air void size distribution increases the  $L_{DI}$  estimations decrease in terms of system saturation, whereas increases to the standard deviation only increase the rate of  $L_{DI}$  development at high values of system saturation. The latter finding suggests that air void systems with broader size distributions could deteriorate faster in water-exposed and freeze-thaw prone regions. Lastly, it was shown that assuming the air voids fill in a regime of smallest-to-largest results in the most conservative  $L_{DI}$  estimations (i.e., it would be expected for the system to begin experiencing damage at lower values of system saturation as compared to filling regimes #2 and #3), but still yields agreeable results with regimes that better capture how air voids fill in a polydisperse system and always predict  $L_{DI}$  to initiate and begin to exponentially grow in the ‘Damage Initiation’ region.

Motivated in the introduction of this chapter, the intent of the presented work was to rigorously evaluate the previously detailed hypothesis for why  $S_{cr}$  is invariant across cementitious materials. The work presented here displays that the phenomena is strongly connected to the evolution in spacing between air voids as the system becomes increasingly saturated past the matrix point. It was displayed how air content, compressive strength, and air void filling regimes, slightly, or insignificantly, influence the likelihood of damage

initiation, suggesting that the model derived in Section 4.3 and 4.4 is robust and captures the governing physics of the phenomenon. Based on this work and the content presented in Chapter 3, the value of  $S_{cr}$  and long-term saturation from the matrix saturation to  $S_{cr}$  can now be understood by air void-scale physics which correspond to trends and outcomes from experiment and can be further adapted for use in design.

In terms of future work, it is of significant interest to apply the poromechanical model to the presented RSAA framework to evaluate if both the Powers'-based limit-state function developed and derived herein and the poromechanical method yields similar outcomes. It is also envisioned that the use of the poromechanical model would also for the prediction of specimen scale strains – analogous to [38]- that cementitious material undergo as a function of temperature depression. As mentioned in Section 4.2.2, the poromechanical model captures more of the physics of freezing in cementitious media (e.g., influence of crystallization forces in addition to hydraulic, fluctuations in intrinsic permeability as a function of temperature, and the cryo-suction effect of air voids). Despite this, the poromechanical model has also been shown to be strongly dependent on the size of the air void and the distance between air voids – see [39] – and would be expected to follow a similar trend to the NND evolution as a function of air void or system saturation, no different than the model within this chapter.

## **CHAPTER 5. RELATIVE INFLUENCE OF DESIGN PARAMETERS AND PERFORMANCE PREDICTION**

### **5.1 Introduction and Review**

As detailed in Section 2.2, the response and resistance of concrete mixtures to freeze-thaw (FT) cycles has been studied since the early 1940s with major contributions by T.C. Powers. In the mid 1950s, P. Klieger conducted three studies [10–12] relating the FT resistance of standard concrete mixtures to their respective 28-day compressive strength, water-to-cement ratio, and total air content. Despite significant advancements made in concrete technology (e.g., chemical admixtures, curing techniques, cement compositions), international durability requirements for concrete exposed to FT largely reflect the design variables and associated values measured by Klieger and decades of design experience. More recently, the problem of ‘joint-rot’ in rigid pavements, advancements in imaging and experimental technologies, and improved mechanistic models have produced new understanding of damage mechanisms associated with FT [18,21,39,50,62]. Results of recent studies have widened the gap between research and practice, necessitating an examination of current design provisions, as specified in American (ACI), Canadian (CSA) and European (BS EN), standards to ensure FT performance [8,26,91–93]. Within this chapter the current exposure categories and design criteria established for FT resistance are probabilistically examined using models developed by T.C. Powers [13,94] in a novel limit-state form – similar to that presented in the critical saturation ( $S_{cr}$ ) model developed and evaluated in Chapter 4.

Previous efforts to probabilistically evaluate or predict the FT resilience of concrete mixtures have utilized limited experimental datasets to inform ‘best-fit’ functions [95–98]. The utilization of Powers’ models advances previous work in two ways. First, the presented limit-state function is highly general (i.e., it can be utilized to assess mixtures across a broad range of physically relevant parameters). Second, the model’s limit-state form allows for the determination of reliability indices and sensitivity assessments familiar to the engineering community and germane to concrete design, production, and acceptance.

The intention of this chapter is to assess selected design variables – namely, compressive strength, total air content, and the ASTM C457 spacing factor - in the context of the developed limit-state function. Numerical findings are compared to published accelerated FT test results as in previous studies [39], where the use of the durability factor, DF, obtained from ASTM C666 [41] testing provides a quantitative basis of comparison to probability of failure calculations.

Using the developed limit-state function, derived in the following section, it is demonstrated how design variables can be quantitatively selected to ensure FT resistance. Additionally, analysis of the model allows for identification of model parameters that are not regularly considered, such as permeability and freezing rate, and examines their relative significance or importance. The presented model and findings encourage the movement away from the current prescriptive design criteria to performance-ensuring specifications based upon statistically informed and experimentally validated models, while furthering the field’s fundamental understand of what parameters influence freeze-thaw resistance for use in design.

## 5.2 Formulation and Theory:

### 5.2.1 General Formulation and System of Study

Limit-state (LS) models are composed of capacity and demand inputs that empirically generate regions of survival and failure for a system. Equation 5-1 and Figure 5-1 detail how LS functions are generally developed and conceptualized [99]. In Equation 5-1,  $C(\mathbf{x})$  and  $D(\mathbf{x})$  represent the capacity and demand functions where  $\mathbf{x}$  is a vector of explicit, random design variables. Figure 5-1 displays that failure occurs when the function,  $LSF(\mathbf{x})$ , is zero or negative, indicating the region where the demand,  $D(\mathbf{x})$ , placed on the system is equal to or exceeds the capacity,  $C(\mathbf{x})$  – similar to that found in Figure 4-9b.

#### Equation 5-1 - General limit-state model formulation.

$$LSF(\mathbf{x}) = C(\mathbf{x}) - D(\mathbf{x})$$

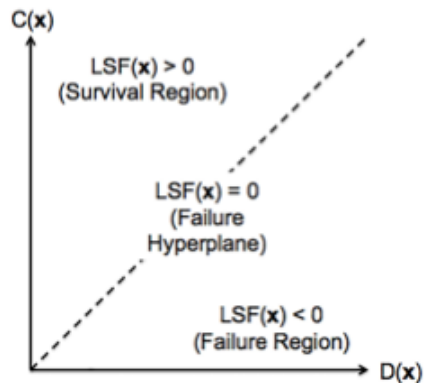


**Figure 5-1 - Limit-state function schematic where the LS function hyper-plane separates the survival and failure regions.**

The presented LS function implements Powers' models, detailed in subsequent sections, where the system under study is a single air void with a surrounding hardened

paste shell, as detailed by Figure 2-1 and reshown by Figure 5-2. Although simplified, this model has been used to represent the critical region of air-entrained concrete where failure initializes [7]. The functions  $C(x)$  and  $D(x)$  take the form of the tensile strength of the hardened paste shell and the internal hydraulic pressure developed during a FT cycle, respectively – no different than the  $S_{cr}$  model in Section 4.4. The air void system of the concrete and intrinsic properties of the hardened cement paste shell, such as the porosity and permeability, are modeled using Powers' models due to their familiarity in the industry and research field [89,100]. By using a physics-based model, the findings have inherent physical relevance and can be readily interpreted to inform the design, placement, and response of a concrete mixture exposed to FT conditions.

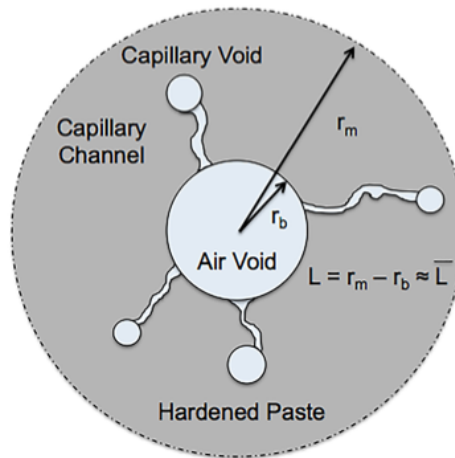


**Figure 5-2 - The system of study contains a spherical air void with radius,  $r_b$ , and hardened paste shell of thickness,  $L$ .**

### 5.2.2 Powers' Hydraulic Pressure Theory

Powers' hydraulic pressure theory states that pressures are developed within the hydrated cement paste from the forced movement of pore solution due to volumetric expansion of freezing water [13,89]. The authors recognize that multiple other theories

have been established since this time, such as those based upon Biot-Coussy theory [37–39]. For the purposes of this work, it is of interest to use the original model that describes the relationship between pressure development in the hardened cement paste and other environmental and material factors: freezing rate, distance between entrained air voids, and capillary saturation [89].

Powers' theory yields a closed form expression for the hydraulic pressure developed throughout the paste-shell surrounding an entrained air void of arbitrary size. Conservatively, the demand function,  $D(x)$ , is set to the maximal pressure developed over a distance,  $L$ , from the periphery of the air void and is displayed in Equation 5-2. The values of viscosity,  $\eta$ , at 0°C and the freezable water content per degree in the cement paste,  $U$ , are taken from Powers [13] as 1.9e-3 Pa\*s and 2.34e-4 kg\*°C<sup>-1</sup>.  $R$ , the freezing rate, is defined by an allowable range specified in ASTM C666 [41], the capillary pore network, is assumed to be saturated,  $S_{cp} = 1$ , and  $K$  is the permeability of the saturated hardened cement paste and is modeled as shown in Section 5.2.4 following [13,94].  $L$  and  $r_b$  represent the hardened cement paste shell thickness and the radius of the entrained air void shown in Figure 5-2.

**Equation 5-2 - Powers' maximal pressure**

$$D(x) = \frac{\eta}{3} \left( 1.09 - \frac{1}{S_{cp}} \right) \frac{UR}{K} \left( \frac{L^3}{r_b} + \frac{3L^2}{2} \right)$$

### 5.2.3 Air Void Systems

In addition to defining the hydraulic pressure theory in 1949, Powers also derived two spacing factor,  $\bar{L}$ , equations, which approximate half the distance between air voids, to ensure FT resistance for air-entrained concrete [13]. In his seminal work, the spacing factor is assumed to be an approximation of the thickness of the paste shell,  $L$ , displayed in Figure 5-2 and Equation 5-2. Powers' derivations are based upon approximations of the volumetric ratio of the cement paste,  $F_p$ , to the entrained air,  $A$ , where the radius of the air voids within the system is uniform. Within the original work, Powers states, "there is reason to believe that the factors obtained from either equation exceed the actual spacing [13]." Based upon this inclination, Powers substantiates the use of the lower value obtained from Equations 5-3 and 5-4, as shown in Figure 5-3, for a given cement paste to entrained air volume ratio ( $F_p/A$ ) and is reported as  $\bar{L}$  using standard ASTM C457 evaluation techniques.

Powers' first spacing factor,  $\bar{L}_1$ , displayed in Equation 5-3, is defined as the ratio of the volume of the cement paste to entrained air in the concrete multiplied by the quotient of the volume and the surface area for the uniform air void system.  $\bar{L}_1$  is the applicable spacing factor for concretes with paste to entrained air ( $F_p/A$ ) ratios less than 4.342 [13,41]. The second spacing factor,  $\bar{L}_h$ , displayed in Equation 5-4, assumes that each air void is at the center of an equivalent cube of cement paste and the spacing factor adopts a geometric sense by approximating the value of the nearest distance from a corner of the idealized cube to the surface of the air void.  $\bar{L}_h$  is used for concretes with paste to entrained air ( $F_p/A$ ) ratios greater than or equal to 4.342 [13,41].

**Equation 5-3 - Powers' spacing factor for cementitious materials will values of  $(F_p/A)$  less than 4.342 [13,41].**

$$\bar{L}_l = \frac{r_b}{3} \left( \frac{p_f}{A} \right)$$

**Equation 5-4 - Powers' spacing factor for cementitious materials will values of  $(F_p/A)$  greater than or equal to 4.342 [13,41].**

$$\bar{L}_h = r_b \left( 1.4 \left( \frac{p_f}{A} + 1 \right)^{1/3} - 1 \right)$$

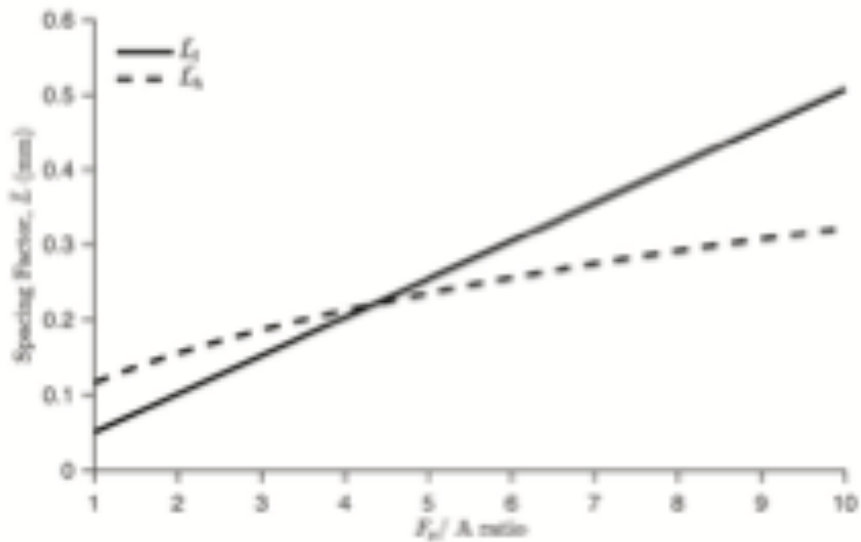


**Figure 5-3 - Comparison plot of Powers' spacing factors for an arbitrary radius of 0.15 mm (0.006in).**

For the final LS function formulation, the spacing factor  $\bar{L}_h$  is utilized as the value of the shell thickness,  $L$ , found in Equation 5-2. The use of  $\bar{L}_h$  is substantiated in two ways. First,  $\bar{L}_h$  is justified by its practicality in terms of concrete design (i.e., it is uncommon for  $(F_p/A)$  ratios to be less than 4.342 for mixtures that will be exposed to FT environments). For example, the mean  $(F_p/A)$  value for the concrete mixtures in the developed FT dataset,

discussed in Section 5.3.1, is 8.8, indicating that  $\bar{L}_h$  is the spacing factor most often reported. Second, for  $(F_p/A)$  ratios greater than or equal to 4.342,  $\bar{L}_h$  gives a lower spacing factor than  $\bar{L}_l$  yielding smaller values of hydraulic pressure during freezing. Although smaller values of hydraulic pressure imply a reduction in likelihood of failure, due to the fact that  $\bar{L}_h$  is understood as an upper-bound for the “actual spacing” factor [13], it will yield more realistic approximations of the influence of freezing on the hardened cement paste shell. For the remainder of this chapter,  $\bar{L}_h$  is assumed equivalent to  $L$ .

#### 5.2.4 *Intrinsic Properties: Porosity and Permeability*

Along with specifying a required compressive strength and total air content for a given FT exposure category, ACI, CSA, and BS EN codes limit the water-to-cement ratio ( $w/c$ ). The intent of the maximal limits placed on the  $w/c$  is to reduce the amount of freezable water at early ages [7] which influences the final porosity and permeability of the concrete [13,94]. Powers and Brownyard’s model [94] for a cement paste’s capillary porosity,  $C_p$ , which is a function of the  $w/c$  and degree of cement hydration, is employed to empirically model the permeability,  $K$ , found in Equation 4-4 and published by Powers [13]. Equations 4-4 and 4-7 display the models used to determine the capillary porosity and the permeability,  $K$ , of the hardened cement paste.

Although the  $w/c$  of a concrete mixture is specified under each provision for FT resistance, the value is maintained as a model input rather than a random design variable. The  $w/c$  is considered to be a mixture constant that has negligible variability as compared to parameters such as compressive strength, air content, and spacing factor. Additionally, the permeability of the hardened paste shell is considered to remain constant throughout

the freezing cycle based upon Powers' original discussion [13]. A future improvement of the presented model would consider the reduction in the hardened cement paste permeability as a function of the freezing temperature.

### 5.3 Final Limit-State Formulation and Solution Method

The final LS function is obtained by modeling the capacity function,  $C(\mathbf{x})$  or hardened paste tensile strength, on the order of 6% to 9% of the total compressive strength based upon an empirical fit [101]. To assess the exposure categories and design criteria, the LS function shown in Equation 5-5 is derived where the compressive strength,  $f_c$ , total entrained air content,  $A$ , and spacing factor,  $\bar{L}_h$ , are the random variables of interest. Figure 5-4 displays an analytic output for Equation 5-5, where the zero-value contour line defines the region of failure where  $D(\mathbf{x})$  exceeds  $C(\mathbf{x})$ .

**Equation 5-5 - LF model written as a function of compressive strength,  $f_c$ , spacing factor,  $\bar{L}_h$ , and total air content,  $A$ .**

$$\text{LSF}(f_c, \bar{L}_h, A) = 100 + 0.057(f_c) - 0.03\eta \frac{\text{UR}(\bar{L}_h)^2}{K} \left( 1.4 \left( \frac{P_f}{A} + 1 \right)^{1/3} + \frac{1}{2} \right)$$

With random distributions defined by ACI, CSA, and BS EN specifications for the design variables, a first-order reliability method (FORM) analysis implementing the improved HL-RF algorithm [99,102,103] is used to find the reliability index,  $\beta$ , and associated probability of failure,  $P_f$ , of the system. In terms of the presented model, failure can be defined as the likelihood that that the hydraulic pressure exceeds the tensile strength of the hardened cement paste. Using the information obtained within the FORM assessment, the relative importance of the selected design variables can be determined

along with the sensitivity of the LS function to the model parameters. Additionally, the results of the system are compared to performance-based measurements, such the durability factor (DF), to validate the model.

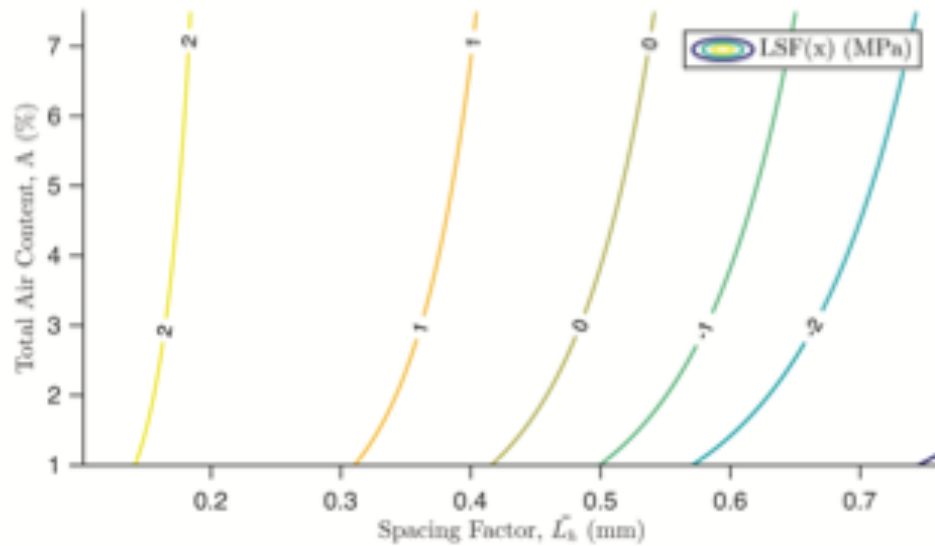


**Figure 5-4 - Analytic evaluation of the developed LS function where the compressive strength is assumed as 27.6MPa (4ksi), over a domain of A and  $\bar{L}_h$ .**

#### 5.4 Experimental Database of ASTM C666 Results

##### 5.4.1 Freeze-thaw Data

Similar to previous efforts [104,105], a dataset composed of 85 different ordinary Portland cement (OPC) concrete mixtures was developed from published literature [106–110] (where values of A,  $\bar{L}_h$ ,  $F_p$ , and DF, as determined by Procedure A of ASTM C666, were reported). Roughly 50% of the dataset reported the 28-day compressive strength,  $f_c$ , of the concrete; those that did not were assigned the mean value of  $f_c$ . The dataset represents w/c, total air content, and compressive strength ranging from 0.35 to 0.55, 0.2% to 8.5%, and 20 MPa to 80MPa, sufficiently bounding the range specified by ACI, CSA, and BS EN

for FT resistance. Figure 5-5 displays the collected data where a DF of 80% demarcates a passing or failing specimen at or before 300 cycles of FT per ASTM C666. In Figure 5-5, ranges of  $w/c$  are grouped to display that the subsets of the database are well distributed, from a practical standpoint, across  $A$  and  $\bar{L}_h$ . It is important to note that the freezing rate at which the specimens were tested, aggregate soundness, initial saturation conditions, and the specimen-curing period were not collectively reported.

Due to the fact that the studies represented in the FT database were conducted from 1981 to 2012, modifications to ASTM C666 were reviewed to ensure the data could be collectively evaluated. It was found that only minor changes were made to the test method since 1977 [41,111], so the data are comparable. The ranges of material parameters, such as for  $f_c$ ,  $A$ , and  $\bar{L}_h$ , from the respective studies (i.e., [106–110]) were found to represent the full domains of interest for each parameter for the presented limit-state model and analysis.

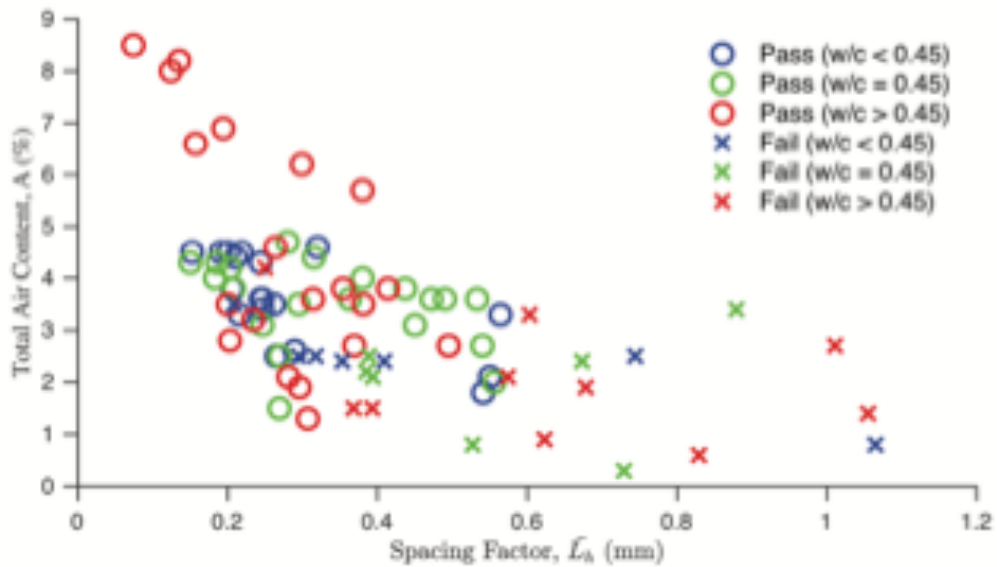


**Figure 5-5 - Cumulative ASTM C666 test results for concretes with w/c ranging from 0.35 to 0.55.**

#### 5.4.2 Random Variable Distributions and International Exposure Categories

For the purposes of exposure category and experimental assessment, the design variables are treated as statistically independent and each is assumed to have a lognormal distribution. Due to the fact that the hydraulic pressure theory singularly assesses the hardened cement paste shell matrix around an air void, the tensile strength of the paste is correlated with the gel-space ratio rather than the total air content [13]. Similarly, it has been experimentally displayed that the relationship between the spacing factor and the total entrained air content is too scattered to draw a meaningful conclusion in terms of correlation and is further complicated without knowledge of admixture combination [112,113]. For example, based upon Figure 5-5, a concrete mixture with a measured spacing factor of 0.4mm can have a measured total air content ranging from 1.5% to 6%.

Similar trends were found in [112] and also displayed that variations in total air content and spacing factor for the same mixture after re-tempering were uncorrelated.

Due to the fact that the lognormal distribution is skew-right or contains more probability content at greater values as compared to a normal distribution, the design specifications are either under- or over-estimated. For example, per ACI 201.2R-16 and under an F2 exposure, the concrete compressive strength is required to have a minimum average strength of 25MPa (3500psi) prior to initial exposure to freeze-thaw cycling [7]. The design strength would be higher than 25MPa, substantiating the lognormal distribution and resulting in an over-estimated reliability. The defined air content would have the same effect, whereas the skew-right nature of the spacing factor distribution would result in an under-estimation of the reliability of the system. Further justification of the use of a lognormal distribution for the spacing factor is obtained by the published distributions of air voids using standard ASTM C457 techniques in 2012 by Liu and Hansen [25].

With the distribution functions established, means and standard deviations can be obtained by the provisions for concrete FT resilience found in ACI, CSA, and BS EN codes and committee documents. Table 5-1 summarizes the exposure categories for each organization excluding the exposures for combined FT and deicing salt exposures. The values specified by ACI committee 201 are utilized for the exposure category assessment as the combination of the specified w/c and compressive strengths will provide the most conservative reliability calculation (i.e. as w/c decreases, permeability decreases causing an increase in the estimated hydraulic pressure, accompanied by a lower value of compressive strength).

Significant deviations occur not only in the recommended design values, but also in their definition, as detailed in the footnotes of Table 5-1. For example, ACI 201 suggests a minimal strength criterion prior to initial exposure to FT whereas ACI 318, CSA, and BS EN specify a minimal mean 28-day compressive strength. Additionally, the BS EN codes require a minimal air content, whereas CSA and ACI specify an allowable range for each exposure. Interestingly, CSA requires a minimal  $\bar{L}$  for severe exposures using standard ASTM C457 techniques, but ACI and BS EN codes do not adopt any form of required, or suggested, air void parameter.

**Table 5-1 - Summary of international design provisions for concrete exposed to FT [7,8,92,93].**

Severity (Units)	Exposure Category	Max. w/c	Min. $f'_c$ at 28 days		Total Air Content <sup>2</sup> (%)	Min. Cement Content		Air Void Parameter, $\bar{L}$	
			(MPa)	(ksi)		( $\text{kg}\cdot\text{m}^{-3}$ )	( $\text{lb}\cdot\text{cy}^{-1}$ )	(mm)	(in)
<b>Moderate</b>  (low chance of saturation)	ACI 318 – F1	0.55	24	3.5	5.0 <sup>3</sup>	-	-	-	-
	CSA – F2	0.55	25	3.6	4-7	-	-	-	-
	BS EN – XF1	0.55	30	4.4	-	300	500	-	-
	ACI 201 – F1	0.50	25 <sup>1</sup>	3.6	6.5 <sup>3</sup>	-	-	-	-
<b>Severe</b>  (high chance of saturation)	ACI 318 – F2	0.45	31	4.5	6.0 <sup>3</sup>	-	-	-	-
	CSA – F1	0.50	30	4.4	5-8	-	-	0.23 <sup>5</sup>	0.09 <sup>5</sup>
	BS EN – XF3	0.50	30	4.4	$\geq 4.0$ <sup>4</sup>	320	540	-	-
	ACI 201 – F2	0.45	25 <sup>1</sup>	3.6	7.0 <sup>3</sup>	-	-	-	-

1. ACI 201 specifies their min.  $f'_c$  as the average compressive strength value prior to exposed to a single FT cycle.

2. Total air content values for concrete mixtures with a maximum aggregate size near 19.1mm (0.75in).

3. ACI 318 and 201 allow a  $\pm 1.5\%$  departure on of the specified air content.

4. BS EN air content is a minimum.

5. Minimum allowable value from the average of three measurements measured per ASTM C457.

For purposes of exposure category assessment, a value of 3.4 MPa (500 psi) is adopted for the  $2\sigma$  value based upon the largest allowable departure in compressive cylinder testing specified in ASTM C39 [114]. ACI 318 [8] and 201 [7] documents allow a 1.5% tolerance for total air content tested on a job site, which is adopted as the  $2\sigma$  value. It is important to note that design guidelines provide a total air content and the developed model assesses entrained air content. For the remainder of the paper and calculations, the value of the entrained air content is set equal to the specified total, or fresh, air volume.

Within Chapter 4 of ACI 201.2R-16, it is stated that concrete mixtures with a spacing factor of less than 0.20mm (0.008in) perform well in service and under ASTM C666. The chapter further notes that multiple studies have found that mixtures with spacing factors up to 0.36mm (0.014in) and as low as 0.10mm (0.004in) display high FT resistance. A  $2\sigma$  deviation of 0.10mm is selected to accompany the 0.20mm (0.008in) mean.

## **5.5 Results and Experimental Comparison**

### *5.5.1 Exposure Category Assessments*

The values in Table 5-1 for the ACI 201 F1 and F2 exposure specifications are used as the respective means of the design variable distributions. The degree of cement hydration,  $\alpha_H$ , for the 0.5 w/c is set to 0.85 and the 0.45 w/c is set to 0.75 based upon the simple model provided by Bentz in 2005 for sealed curing conditions at 28 days [115]. Paste fractions, established by standard design procedure [116], of either mixture are set to 30% and 31%, respectively. Table 5-2 details the calculated probability of failure,  $P_f$ , for each mixture across the range of allowable freezing rates per ASTM C666 [41].

**Table 5-2 - Probability of failure values for various freezing rates.**

<b>Exposure Category</b>	<b>R = 11 (°C*hr<sup>-1</sup>)</b>	<b>R = 5 (°C*hr<sup>-1</sup>)</b>	<b>R = 4.4 (°C*hr<sup>-1</sup>)</b>
P <sub>f,F1</sub> (%)	1.22	0.0060	0.0020
P <sub>f,F2</sub> (%)	1.15	0.0055	0.0018

As displayed, the P<sub>f</sub> values for the F1 exposure category are slightly larger than those found for the F2 exposure for each freezing rate. This finding is expected due to the reductions in mean air content and estimated permeability associated with the F1 exposure category, which effectively increase the hydraulic pressures on the solid matrix during freezing while keeping the distribution of spacing factor and compressive strength the same. Interestingly, the values in Table 5-2 display a three order of magnitude difference in probability of failure from the largest to smallest allowable freezing rate. As most, if not all, experimental studies do not publish the freezing rate used in their experiments, significant variability is introduced when validating the LS function with ASTM C666 data as displayed by the results of the reliability assessment in Table 5-2. For the remaining calculations, a freezing rate, R, of 5 °C\*hr<sup>-1</sup> is used following [39], but could be changed to evaluate the resistance of a concrete placement if the freezing rate of the site condition is known.

### 5.5.2 Importance and Sensitivity Study

Order of importance and sensitivity analyses enable assessment of the influence of the design variables and LS function model parameters on system reliability. The standard

importance vector for the F2 exposure variable distributions and explicit inputs is shown in Table 5-3. The importance vector measures the respective contribution of the design variable to variance in the LS function, providing a relative measure of variable importance. Comparing the importance values for each random variable in Table 5-3, the value for the spacing factor is over an order of magnitude larger than the compressive strength and entrained air content values. This result indicates that  $\bar{L}_h$  dictates the response of the system undergoing FT. From the signs of the importance values, increasing compressive strength and air content increases reliability as expected, while increasing the spacing factor decreases reliability. Based on the importance values, it is concluded that the probability of failure contours are governed by the spacing factor. Figure 5-6 shows the relationship – the probability of failure is strongly dependent upon the spacing factor for values of 0.25mm (0.010in) and greater.

**Table 5-3 - Standard Importance Vector.**

<b>Random Variable Importance Values</b>		
<b><math>f_c</math></b>	<b><math>\bar{L}_h</math></b>	<b>A</b>
-0.0378	0.9991	-0.0193

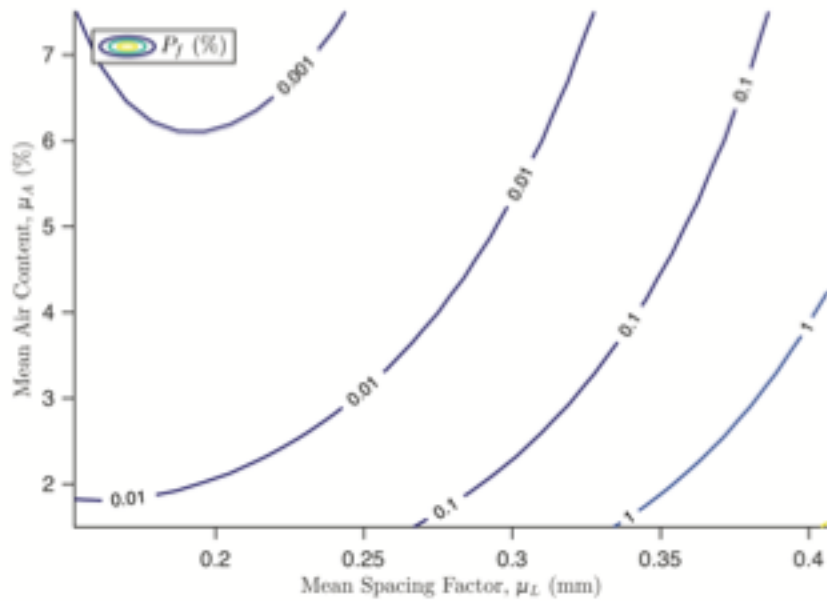


**Figure 5-6 - Probability of failure assessment for variable means of A and  $\bar{L}_h$  within allowable range specified by ACI provision 201.16-2R.**

The scaled importance vectors,  $\bar{\delta}$  and  $\bar{\eta}$ , describe sensitivities of the reliability index,  $\beta$ , with respect to the variable means and standard deviations, respectively. Scaling enables comparison of the random variables across distributions, units, and scales, with the sensitivities quantifying the effect of changes in the means or standard deviations on the reliability. Table 5-4 details the scaled importance vectors. Again, it was found for both scaled importance vectors that the spacing factor,  $\bar{L}_h$ , influences  $\beta$  the most followed by the compressive strength. From Table 5-4, decreasing the mean of the spacing factor distribution will increase the overall reliability of the system.

**Table 5-4 - Scaled Importance Vectors.**

Importance  Vector	Random Variable Importance Values		
	$f_c$	$\bar{L}_h$	A
$\bar{\delta}$ (means)	0.0384	-0.1376	0.0198
$\bar{\eta}$ (deviations)	-0.0082	-3.5072	-0.0035

Sensitivities for the LS function model parameters are also investigated to gain a better physical understanding of the influence of components of the model on the reliability of the system. Table 5-5 provides the sensitivities for the seven parameters, where  $\nabla\beta$  indicates the change in reliability index,  $\beta$ , given a unit change in the parameter. The last row of Table 5-5,  $\Delta\beta$ , displays the expected change in  $\beta$  for a 5% reduction in the initial value used in the F2 exposure category assessment calculation for parameters  $S_{fc}$ ,  $\eta$ ,  $S_{cp}$ ,  $U$ , and  $p_f$ . The  $\Delta\beta$  values shown for R and K were resolved from a reduction in the freezing rate by 1°C per hour and an increase in the degree of cement hydration by 5%.

Considering the value of capillary saturation in Powers' model,  $S_{cp}$ , is bound from 0.917 to 1, the influence it has on the outcome of  $\beta$  is substantial. The only other factors that influence the paste-void system on the same order of magnitude are the permeability, K, and freezing rate, R. Clearly, small changes in the inputs for K, which is written as a function of the w/c and  $\alpha_H$ , results in a substantial change in the reliability of the system. Similarly, the influence of the model with respect to change in freezing rate, R, as demonstrated by the exposure category assessment, is substantial.

**Table 5-5 - LS function model parameter  $\beta$  sensitivities.**

Sensitivity	LS Function Parameter						
	$S_{fc}^1$	$\eta$	$S_{cp}$	U	R	K	$p_f$
<b>Initial Value</b>	0.057	0.019	1	0.232	1.39e-3	6.94e-17	31.0
<b><math>\nabla\beta</math></b>	9.294	-42.040	-8.875	-3.443	-575.480	1.15e16	-0.006
<b><math>\Delta\beta</math></b>	-0.026	0.040	0.444	0.0399	0.1599	-0.3616	0.009

1.  $S_{fc}$  denotes the slope of the tensile strength capacity function,  $D(x)$ .

### 5.5.3 Experimental Comparison and Validation

To assess the model, a comparison with experimental data is conducted. Average values of design variables and model parameters are determined from the FT dataset values and used to find the probability of failure,  $P_f$ , over the same domain of total air content and spacing factor shown in Figure 5-5. Figure 5-7 shows the total FT dataset overlaid on the calculated database-mean  $P_f$  contour lines. In the figure, the model and experimental data follow a comparable trend – as air content decreases and spacing factor increases, failure is more likely to occur. It is important to note that Figure 5-7 only directly displays the influence of two variables (i.e., A and L) on the mean  $P_f$  contour and therefore provides a limited perspective on the overall utility of the derived limit-state function. For example, it can be clearly seen that a cluster of failing specimens is within the 0.001 and 0.01 mean  $P_f$  contours – this is attributed to the fact that the mean  $P_f$  here is not representative for those specific mixtures as it does not consider their respective values of  $f_c$ ,  $w/c$ , or  $F_p$ .

To validate the model, each value of design variable and model parameter associated with a test specimen is analyzed using FORM and the developed LS function to determine an associated  $P_f$ . Figure 5-8 displays the linear trend found between the calculated values of  $P_f$  and their reported DF using a bisquare weighting method that deletes extreme outliers and down-weights mid-outliers. Figure 5-9 shows the relationship between the  $P_f$  of each test specimen and its reported spacing factor, compressive strength, and total air content, while contrasting the ability for ACI 201 design guidance and the probabilistic model to predict performance under ASTM C666. It is clear that the relationship between spacing factor and reliability is strongest and that the total air content and compressive strength, despite being specified design variables, displays significant scatter when compared to  $P_f$ . Furthermore, Figure 5-9 shows that the probabilistic model can easily discriminate between passing and failing ATSM C666 specimens, whereas ACI 201 design guidance cannot.

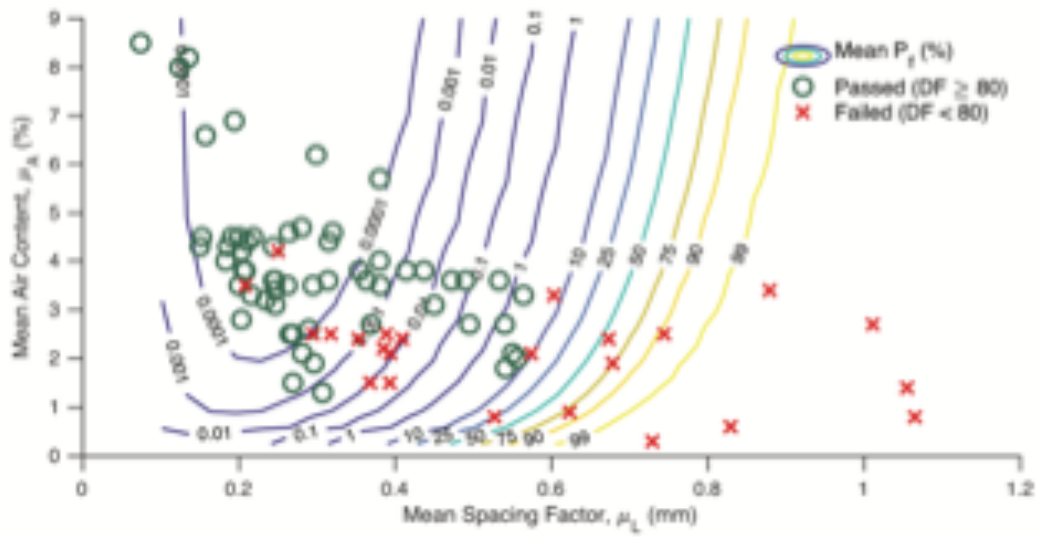


Figure 5-7 - Cumulative FT data overlaid on the  $P_f$  contour for average values from the FT database.

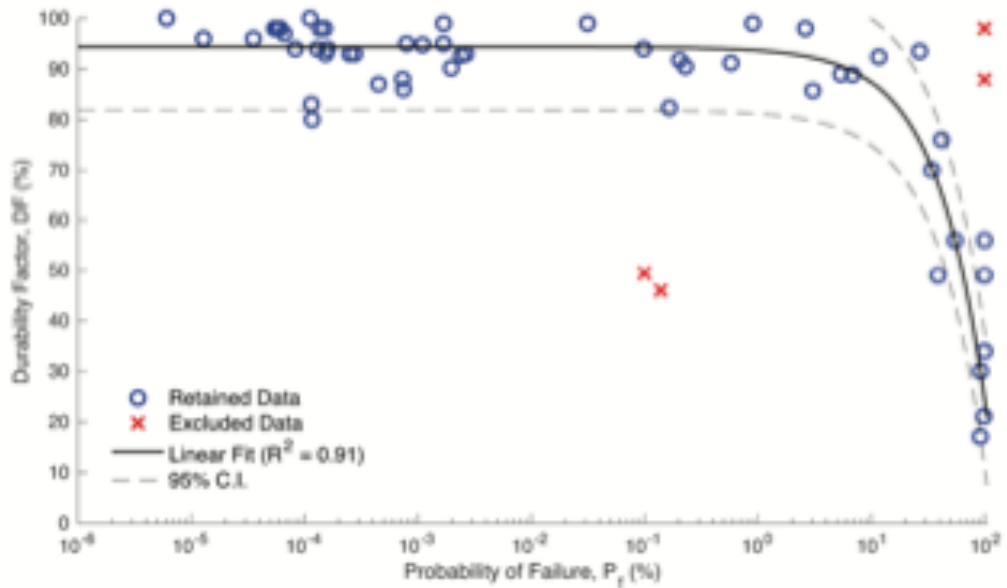
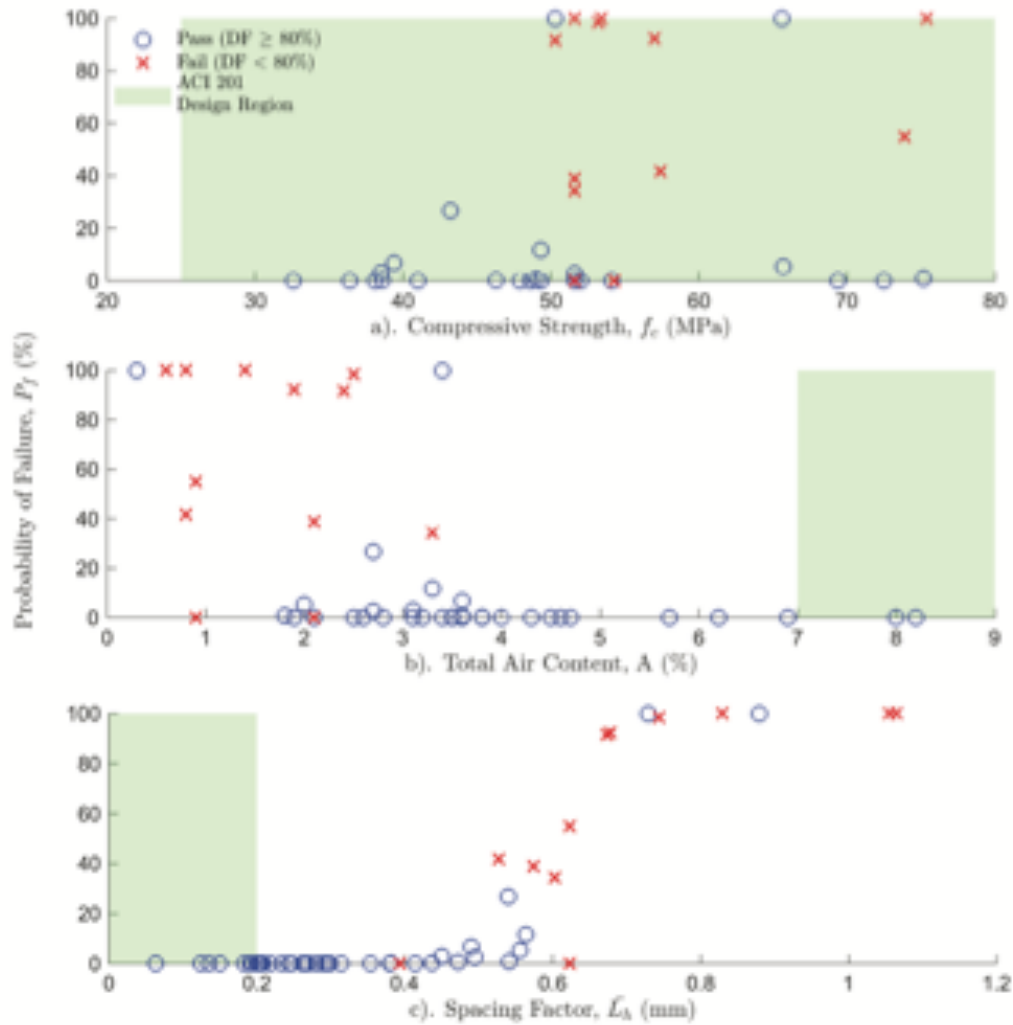


Figure 5-8 - Cumulative analysis of developed LS function to predict performance by experimental assessment.



**Figure 5-9 - Comparison of design variables  $\bar{L}_h$ ,  $A$ , and  $f_c$  to  $P_f$  for cumulative FT dataset [106–110].**

To find the relationship between  $\bar{L}_h$  and  $P_f$ , a simple exponential equation with the form  $P_f(\bar{L}_h) = C_1 e^{C_2 \bar{L}_h}$ , where  $C_1$  and  $C_2$  are constants, is fit to the data using the same bisquare weighting method and least squares. Equation 5-8 provides the exponential function found and Figure 5-10 shows the curve overlaid on the FT data. An exponential equation was selected, rather than cubic root, to capture the initial exponential gain in probability of failure with increasing spacing factor. Figure 10 also depicts two exponential

fits where the values of Equation 5-8 have been multiplied by 2 and 5, representing factors of safety to be used for design purposes. Both the experimental data and  $P_f(\bar{L}_h)$  equation show the range of spacing factors that is known to perform well under FT exposure during ASTM C666 testing (i.e., ranging from 0.10mm (0.004in) to 0.36mm (0.014in)). For  $\bar{L}_h$  greater than 0.36mm (0.014in), the probability of failure begins to significantly increase. These equations enable the design of concrete to meet the desired performance-based specifications for FT resistance.

**Equation 5-6 - Probability of failure fit as a function of spacing factor.**

$$P_f(\bar{L}_h) = 1.44 \times 10^{-4} e^{19.5 \bar{L}_h}$$

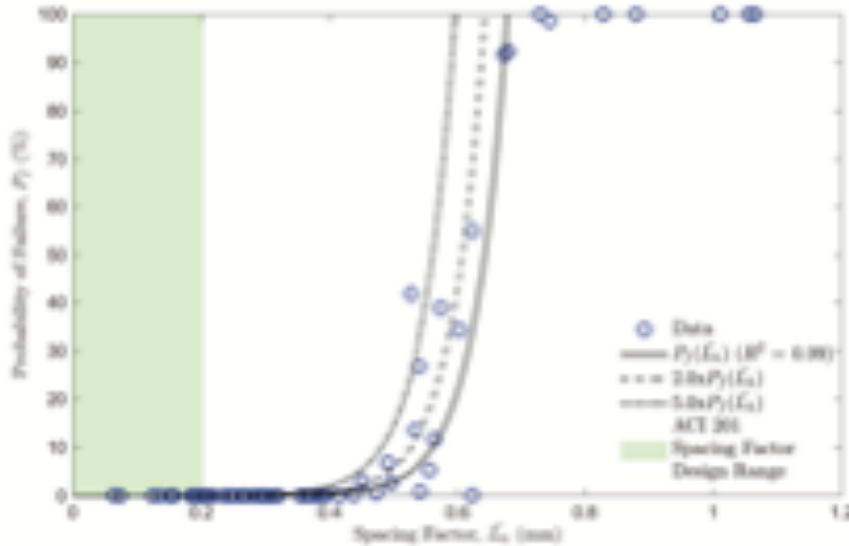


**Figure 5-10 - Exponential function development for probabilistic design of air-entrained concrete.**

## 5.6 Conclusions

Through the use of the developed LS function, a collection of conclusions can be drawn. First, The spacing factor,  $\overline{L}_h$ , has the largest influence on concrete FT performance, as assessed through accelerated testing. Although the probability of failure values for the ACI 201 FT exposure categories were reasonably low, even for the highest freezing rate considered, spacing factor is not currently specified within ACI or BS EN codes. It should be recalled that the spacing factor distribution used in the exposure category assessment was based on values that have been shown to perform well under controlled laboratory testing.

Second, the saturation state, freezing rate, and permeability significantly influence the concrete FT response, as shown by the sensitivity assessment. Despite the fact that the freezing rate in the field cannot be directly controlled, the permeability of the concrete can be designed through selection of an appropriate w/c, inclusion of supplementary cementitious materials, and ensuring adequate curing periods. Third, a critical saturation state, where exposure to a single FT cycle results in measurable loss in modulus, likely corresponds to a value of Powers' spacing factor near, or above, 0.5mm (0.020in) where the probability of failure asymptotically increases. This finding displays that the resistance of concrete to FT is significantly dependent upon the initial geometry of the entrained air void system.

Lastly, a key contribution of the developed LS function is a simple exponential equation that can be used to inform air-entrained concrete mixture design or to carry out predictive reliability assessments of in-place concrete. The functions shows that as the

spacing factor increases past a value of 0.5mm there is an exponential increase in probability of failure of the concrete. It should be noted that the presented work does not analyze or consider the influence of deicing salts, which categorizes the very severe exposures for FT in ACI, CSA, and BS EN codes, and only considers OPC concretes. The presented within this chapter displays that the spacing of the air voids is more important than the total volume of the entrained air through the presentation of a probabilistic model that can be readily used by design engineers and manufacturers.

# **CHAPTER 6. A DATA SCIENCE APPROACH FOR PROCESS-STRUCTURE-PROPERTY LINKAGES IN HYDRATING CEMENT PASTES**

## **6.1 Introduction**

Despite the ubiquitous use and study of cementitious materials, failures and unexpected deterioration still occur [3–5]. A major challenge in the field of cement sciences stems from the amorphous nature of the hydration products that yield pore structures which exist across multiple orders of magnitude (1nm to 1mm), have varying morphologies, and evolve as a function of time and environmental exposure [36]. Decades of previous research has shown that specific types of porosity (e.g., interlayer space in C-S-H sheets or capillary pores) govern different engineering-related properties of the material (e.g., permeability or diffusivity) [36,70]. Despite this knowledge, the majority of research in the field of cement sciences has largely neglected the structural link between the hydration process of cement grains and their engineering properties [117–120]. For the purposes of the presented work, it is of interest to develop a full set of process-structure-property linkages in hydrating cement pastes using a data science, or a material informatics, approach [121] and display how they can be directly input into engineering science models, such as the SVDK model developed within Chapter 3.

Leveraging a large database of simulated cements, a framework is developed to display how common process parameters, such as water-to-cement ratio and total hydration time, can be used to accurately predict the diffusivity transport property by incorporating

reduced-order statistical information of how the microstructure of CCRL cement 133 evolves while undergoing hydration. As displayed in Sections 3.3 and 3.4, the diffusivity property of cement pastes, as compared to other properties, such as the intrinsic permeability, governs the total time to critical saturation - making it a critical property to be able to predict as a function of controllable parameters. Within this study, the hydration of cement pastes is carried out using the Virtual Cement and Concrete Technology Laboratory (VCCTL) software, called CemHyd3D [122], developed by the National Institute of Standards and Technology (NIST). Additionally, a set of microCT results from the VisibleCement Library [123] is evaluated and current challenges for distinguishing general phases (i.e., hydration products, anhydrous cement grains, and porosity or water) in real hydrating cement paste are highlighted. It is displayed that until a large set of CT images is made available at much higher resolutions ( $<0.95\mu\text{m}/\text{voxel}$ ) and better segmentation algorithms are developed to distinguish between chemical phases found within hydrating cement pastes, information provided by hydration models, such as CEMHYD3D and  $\mu\text{ic}$  [124], can provide state-of-the-art information to be used in data-driven process-structure-property (PSP) linkages.

The approach developed within this chapter displays how voxelated cement pastes that are undergoing hydration can be: 1). segmented into three ‘phases’ (i.e., hydration products, anhydrous cement grains, and water-filled porosity), 2). evaluated using 2-point statistics, 3). distinguished by their principle components, and lastly, 4). used to develop reduced order models for PSP linkages. Figure 6-1 displays a general framework for how this information is incorporated to result in the PSP linkage developed within this chapter. Section 6.2 serves as a brief review for cement hydration kinetics, primarily focusing on

hydration reactions which will be used to distinguish between the cement grains and hydration products within CEMHYD3D and also outlines the material informatics approach to PSP linkage development. Section 6.3 details the databases of hydrating cement pastes developed using CEMHYD3D or obtained from NIST's Visible Cement dataset and how they are segmented into 3-phases (i.e. water/porosity, hydration products, or anhydrous cement grains). Using the CEMHYD3D database, Section 6.4 then applies the material informatics approach to developing PSP linkages and displays its outcomes – highlighting the importance of including the structural component in the prediction the diffusivity property. Additionally, Section 6.4 will leverage the developed PSP linkage and display how it can be used with the single void dissolution kinetics (SVDK) model derived in Section 3.3, allowing for the engineering design of a material based upon common process parameters.

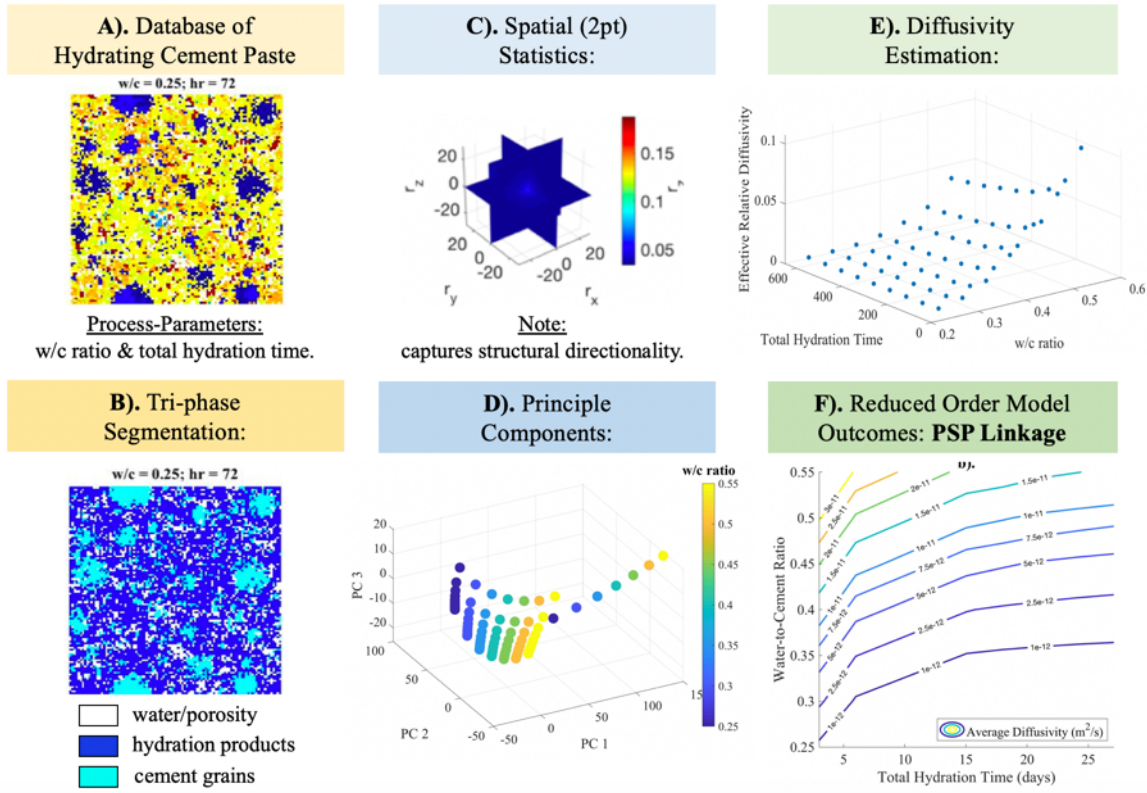


**Figure 6-1 - Generalized framework for PSP linkage development displayed within this chapter.**

As motivated in Chapters 1 and 2, in order to move toward the service life design of cementitious material in freeze-thaw environments, it is necessary to understand how cementitious materials become water-saturated over long time frames when exposed to fluids and why the critical saturation phenomena exists across such as broad range of cementitious materials. Chapters 3 and 4 developed hypotheses and tested novel models which can predict the long-term saturation rate and also explain why the critical saturation phenomena is seen experimentally. Both of these models, most centrally the SVDK and MVDK models, are dependent upon material parameters, such as the diffusivity or intrinsic permeability, of the hardened cement paste that surrounds spherical air voids. The work within this chapter effectively ‘closes-the-loop’ by displaying how the diffusivity material

parameter can be predicted as a function of simple parameters such as water-to-cement ratio and total hydration time and then put back into the aforementioned physics-based models to predict total time to critical saturation – effectively allowing for the design of a minimal total service life.

## **6.2 Literature Review**

Within this section, the material informatics approach to PSP linkage development is first reviewed followed by the fundamentals of cement hydration in order to promote the accurate segmentation of the various chemical compounds and phases into three general categories (i.e., hydration products, anhydrous cement grains, and water/porosity). Specific attention within Section 6.2.2 is given to primary cement hydration products and the complications that arise when trying to distinguish various hydration products from non-hydrated cement grains in grey-scaled microCT images. It is important to note that neither of these sections are intended to be exhaustive, and readers should direct their attention to [121] and [36,125] for further details on the fields of material informatics and the science of cement hydration kinetics, respectively.

### *6.2.1 Hierarchical Material Informatics:*

It is well-established that salient aspects of a material’s microstructure govern their macroscopic properties (e.g., imperfections such as slips and dislocations in the chemical structure of crystalline materials result in lower values of elastic modulus than stiffnesses found at the atomic level [126]). Hierarchical material informatics is aimed at capturing the most important multi-length-scale structural features that control a material’s final engineering properties. The informatics component is incorporated by tracking a large

quantity of statistical features of a material as a function of its process parameters and developing reduced order models to predict the structural features or final material properties. By doing so, process-structure property (PSP) linkages can be rapidly developed whereas historically, they have been experimentally laborious to generate [117–120] (e.g., Powers and Brownyard’s model for intrinsic permeability [94] of cement pastes as a function of capillary porosity and therefore, degree of cement hydration and water-to-cement ratio took place over half a decade). Furthermore, material informatics is aimed at using a data science approach to incorporate the massive amount of information that can be now obtained through experiments, such as micro- and nano-CT or SEM/EBS images, which provide quantitative information that can be correlated with the engineering property of the material [121].

A material informatics approach to PSP linkages effectively requires: 1). A quantitative evaluation of the microstructure of the material, 2). Statistical representation of the microstructure to capture the high-dimensional aspects of the structure, 3). A reduced order assessment to identify the most salient discriminatory features between a set of microstructures, 4). A quantitative measure of the material property of interest, and 5). Regression based models to ‘learn’ quantitative process-structure and structure-property relationships [121]. As mentioned in the introduction of this section, a full treatment of the theory and manifold methods in material informatics is outside of the scope of this review section. Rather, a brief description of the critical components is described in the following paragraphs and then implemented in Sections 6.3 and 6.4 as a case-study for the field of cement sciences.

As detailed in Chapter 2 of [121], the digital fabrication or evaluation of a real material microstructure is the first critical component in the informatics approach. Whether a material is being evaluated using nanoCT or developed within a microstructural design software, such as dream3D, it is essential to ensure that resolution of the material be below that of the critical length-scale of the material that either governs the property of interest or allows for the statistical discrimination of various samples. The concepts of resolution and sampling of a material allows for the formation of a material microstructure function which quantifies the spatial- and temporal-distributions of potential states (e.g., phase or orientations) of a material at each discretized point, area, or volume of the material. With the establishment of such a function, the material can be conveniently expressed and re-created in a statistically meaningful way. Practically, this results in a segmented material in which critical phases, orientations, and structures can be faithfully established. As a result, these ‘segmented’ microstructures can be evaluated using variations of n-point statistics, which provides a high-dimensional statistical assessment of the material. A 1-point statistic can be understood simply as the volume fraction assessment of a phase in a material, whereas a 2- and 3-point statistic captures the likelihood of various phases present to one another and can additionally provide information on the texture or orientation of the material’s phases in a quantitative manner [121].

The n-point statistical quantification of the material effectively results in a data management problem in which principal component analyses can be used to identify the most essential statistical descriptors of a set of material microstructures. The principal components of a collection of microstructures are found by maximizing the variance between the statistical correlations of each microstructure of interest – see Chapter 4 of

[121] - pending that they are sufficiently statistically dissimilar. As a result, the most essential features of a set of microstructures are now represented in a reduced order form and can be used to create high-fidelity linkages with material properties - which are often determined from experiment or numerical techniques such as using homogenization [127] or composite theories [128]. With known process parameters, a reduced order form of the salient structural features, and expected engineering properties, regression-model models can be developed to create process-structure, structure-property, or full PSP linkages - encapsulating a material informatics approach to PSP linkages.

It is important to note that to-date an approach of this kind has been yet to be leveraged to assess hydrating cement pastes or concrete. Previous efforts have used statistical homogenization of segmented microCT images of cement hydrating to predict the evolution in properties such as the elasticity [127] or diffusivity [70], but have neglected the rigorous evaluation and representation of the material microstructure [129] which is central to material informatics. Lastly, the establishment of high-fidelity PSP linkages can then be used predict material outcomes under specific loading or environmental scenarios, providing a direct way to design the response of a material by controllable process parameters – a strategic opportunity for the field of cement and concrete sciences.

### *6.2.2 Cement Hydration and Challenges for Phase Segmentation from CT images:*

Cement grains are composed of various chemical compounds with large trace quantities of calcium, silica, aluminum, and iron [36,126]. Due to the various compounds found in cement grains (e.g.,  $C_3S$ ,  $C_2S$ ,  $C_3A$ , and  $C_4AF$ ), different portions of a single cement particle can hydrate faster or slower when mixed with water [36]. A seminal review

of cement hydration can be found in [125]. Herein germane portions of the cement hydration process are discussed for domain-driven image segmentation of the CEMHYD3D and NIST Visible Cement databases found in Section 6.3. A visualization of the concurrent formation of hydration products can be found in Figure 6-2 where dissolution, diffusion, nucleation, complexation, and adsorption are taking place [130].

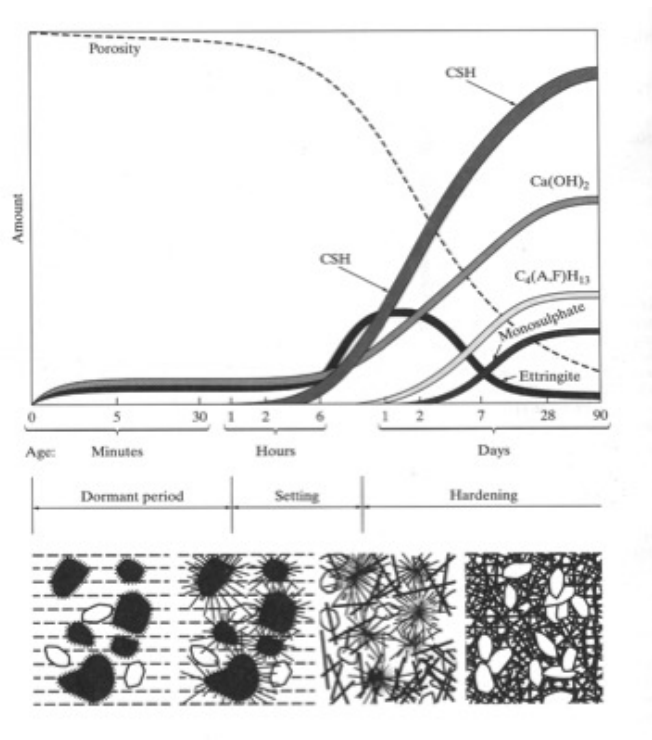


**Figure 6-2 - Evolution in various hydration products and porosity as a function of time [130].**

As shown in Figure 6-2, as cement hydration occurs over time, the water-/vapor-filled pore space decreases as hydration products (i.e., C-S-H, Ca(OH)<sub>2</sub>, Ettringite, etc.) increase. C-S-H, or calcium-silicate-hydrate, is the primary hydration product that is known for yielding strength to cementitious materials. A comprehensible review of the structure of C-S-H can found in [36]. Generally, all of the hydration products with the exception of Ca(OH)<sub>2</sub> are seen as grey in SEM and microCT experiments [123]. The reason

for this is due to the fact that significant amounts of water are complexed onto C-S-H, Ettringite, and Monosulfoaluminate.  $\text{Ca}(\text{OH})_2$ , or free-lime, is seen as very white due to its crystallinity [123]. As cement hydration occurs, the hydration products should develop along the surface of the cement grains and continue until little of the original product is remaining. As detailed in [123,130,131] it is uncommon for cement hydration to go to 100%. Figure 6-3 displays a series of SEM images taken from [131] and shows how the volume of cement grains and water-filled pores decrease as a function of hydration time and the hydration products increase, leading to a progressively greyer image.

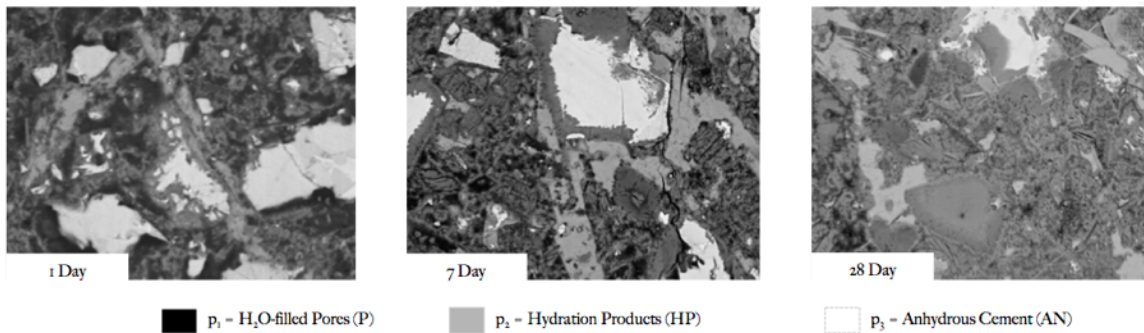


**Figure 6-3 - Evolution of grey-scaled seem images from [131] that with a black, grey, white color bar which can general distinguish present phases of water-filled pores, hydration products, and anhydrous cement, respectively.**

By analyzing Figure 6-3 the following conclusion can be made and used to inform segmentation outcomes: a). the dark/black space (i.e., water-filled pores) decreases as a function of hydration time, b). grey pixels (i.e., hydration products) tend to develop at the surface of the bright white cement grains and increase in volume as a function of hydration time, and c). the bright white cement grains tend to decrease but not completely disappear. These conclusions are primarily used to ensure the segmentation of the microCT data is supported by fundamental understanding of how cement hydration occurs. It is important

to note that due to the different types of hydration products formed during the cement hydration process, segmenting the material system in a manner similar to [127] – shown in Figure 6-4 - where a single threshold is defined to distinguish hydration products and anhydrous cement was not expected to accurately separate the hydration products and anhydrous cement grains. As shown in Figure 6-5, the partially reacted grains have the same greyscale value as ettringite and lime – hydrations product [123]. Therefore, a single threshold value cannot holistically discriminate between the diversity of hydration products formed in a cement paste. Additionally, as will be discussed in the segmentation portion of Section 6.3, the compaction errors made during sample preparation make it exceedingly difficult to extract meaningful reduced order representations of the  $\mu$ CT subvolumes despite different process parameters (i.e., w/c and total hydration time).

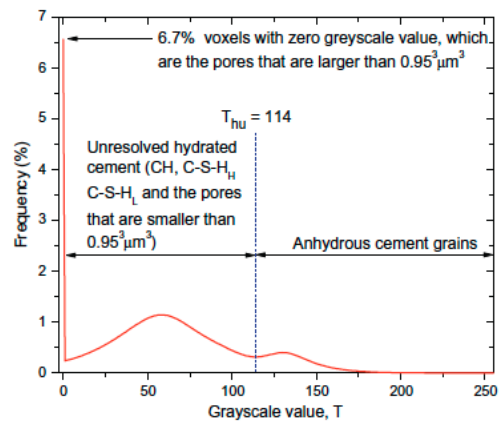


**Figure 6-4 - Threshold methodology used in [127] to distinguish between porosity, hydration products, and anhydrous cement grains.**

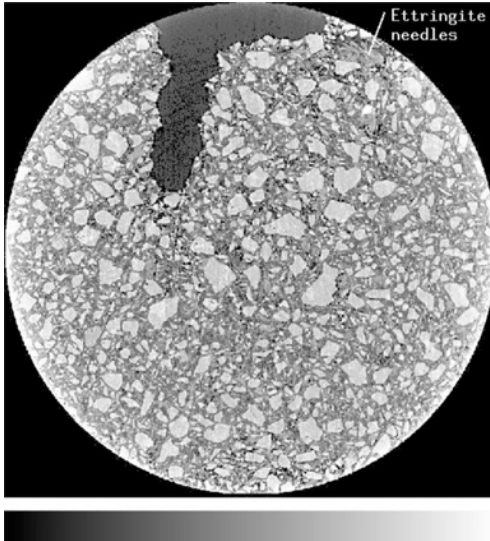


**Figure 6-5 - Slice of CCRL cement 133 with a w/c of 0.35 at 16 total hours of hydration [123].**

Due to the identified complications, literature that had previously attempted to segment various images of hydrating cements into water/porosity, hydration products, and anhydrous cement grain was reviewed [70,123,127,129,132–136]. It was found that due to the resolution limit of the Visible cement database (i.e.,  $0.95\mu\text{m}/\text{voxel}$ ) and other material complexities – such as how certain hydration products are crystalline and are seen near the same greyscale value as the anhydrate cement- it is likely only feasible to confidently distinguish large-capillaries (i.e.,  $> 0.95\mu\text{m}$ ), regions of hydration products, and bulk anhydrous cement grains. Of the segmentation techniques used, the method developed in [70] and used in [129,136] is first evaluated for the Visible Cement Database presented in Section 6.3.1 and employs a simple Ostu’s multi-thresholding technique [137].

### **6.3 Database Development of Hydrating Cement Pastes**

To ensure consistency across the Visible Cement and CemHyd3D databases, the most common cement evaluated in the  $\mu\text{CT}$  experiments in [123] is exclusively considered

and are presented in Sections 6.3.1 and 6.3.2. Figure 6-6 shows a 2D color image of standard CCRL cement 133 used in the formation of the Visible Cement Database and the CemHyrd3D database developed for the data science to PSP linkages presented herein. Within Figure 6-7, red, aqua, green, and yellow represent the primary clinker phases (i.e.,  $C_3S$ ,  $C_2S$ ,  $C_3A$ , and  $C_4AF$ ) and constitute 89% of the volume of the anhydrous cement or 62.2%, 11.7%, 7.3%, and 7.5%, respectively. Reflecting the Visible Cement dataset, the CemHyd3D database maintains the same process parameters (i.e., total hydration time and water-to-cement ratio).

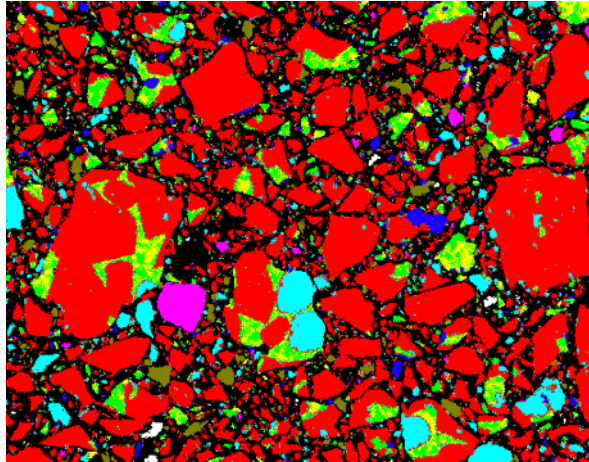


**Figure 6-6 - 2D color image of cement 133 exposed to synchrotron light source in Grenoble, France. Image magnification is 500x with dimensions 256 $\mu$ m by 200 $\mu$ m. Red is  $C_3S$ , aqua is  $C_2S$ , green is  $C_3A$ , yellow is  $C_4AF$ , pale green is gypsum, white is free lime, dark blue is potassium sulfate, magenta is the magnesium-calcium phase, and orange is an aluminosilicate (kaolin) phase [123].**

### *6.3.1 NIST's Visible Cement Database Development and Segmentation*

The  $\mu$ CT evaluations from [123] were conducted at various water-to-cement weight ratios (w/c) ranging from 0.28 to 0.45 and were evaluated at hydration times ranging from 0 hours to 175 hours (i.e.,  $\sim$ 7.25 days). Outcomes of the entire experiments include grey-

scaled 512x1024x1025 voxel volumes each voxel dimension is 0.95 $\mu$ m. A 2D section of the cylindrical specimen is displayed in Figure 6-5 and a single pane from one of the 3D subvolumes of the grey-scaled raw data is shown in Figure 6-7. The data made publicly available for each specimen from [123] are 300x300x300 voxel sub-volumes taken from the top or bottom half of the specimen. This implies that at every evaluation time, there are 600 distinct grey-scaled 2D panes when considering the top and bottom specimens. Table 6-1 displays the 6 specimens that were evaluated and their respective process parameters: water-to-cement ratio and total hydration time. For different experiments, there are as many as 8 distinct temporal evaluations and as few as 4.

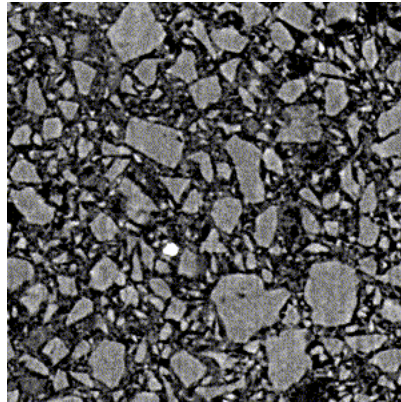


**Figure 6-7 - 300x300pixel image of a 0.30 w/c cement paste at 162 of total hydration time from [123].**

**Table 6-1 - Various experiments made on CCRL cement 133 for different w/c and total hydration time in [123].**

Water-to-Cement Ratio (w/c)	Experiment #	Total Hydration Time(s): (hours)
0.3	1	24, 27, 29, 48, 52, 162
0.35	1	4, 8, 12, 16, 20, 25, 34, 40
	2	5, 9, 15, 23
	3	6, 17, 136
0.45	1	3, 8, 11, 128
	2	5, 8, 11, 124

The top and bottom sub-volumes for all of the experiments were obtained and using the segmentation protocols reviewed in Section 6.2.2 were evaluated based upon what could be expected from ideal cement hydration and trends seen in Figure 6-3. Similar to the previous efforts, the images were segmented into three phase: water/porosity, anhydrous cement, and hydration products. It is important to note that due to the small difference in linear attenuations [62] distinguishing between water and porosity within a hydrating cement paste is not feasible at resolutions of  $0.95\mu\text{m}/\text{voxel}$  [138].

Following [66,121,128], 2 different thresholds were established based on the entire greyscale distribution of the  $300\times 300\times 300$  subvolumes as shown in Figure 6-8. Figure 6-9 displays a visual outcome of the global thresholding methodology proposed in [70]. Upon

close examination of many of the segmented panes using the global and multi-thresholding technique, it was found that within the cement grain particles, hydration products would be present and often in significant quantities. Due to this complication, a local multi-thresholding technique was applied for every 2D pane within a given subvolume and the thresholds were computed such that the phases could be segmented. This resulted in a similar problem (i.e., hydration products were present within the cement grains), when it is well-established that cement hydration is primarily a surface reaction [132], as shown in Figure 6-10.

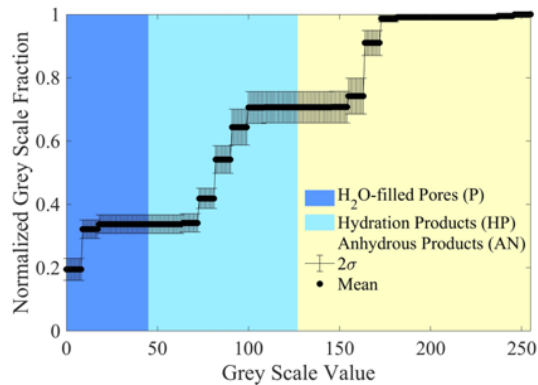


**Figure 6-8 - Global Otsu's multi-threshold segmentation methodology following [66,121,128] to distinguish between water-filled pores, hydration products, and anhydrous products.**

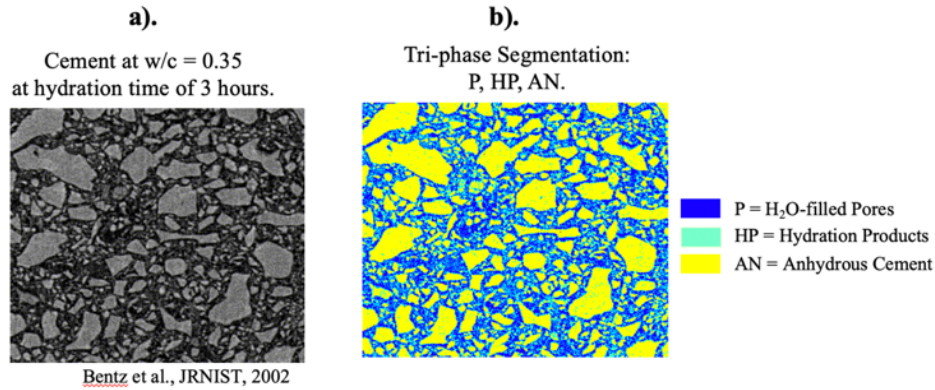


**Figure 6-9 - Example outcome of global segmentation methodology where a). is the original grey-scaled image and b). is the same tri-phase segmented area.**

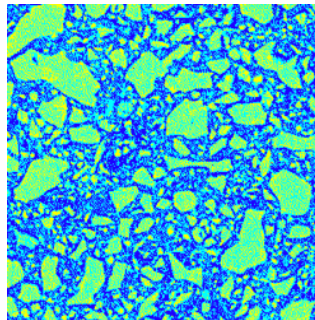


**Figure 6-10 - Example problem with global and local multi-thresholding approach (i.e., cyan hydration products are found well-within the yellow cement grains). Note that the image color bar is the same as that provided in Figure 6-9b.**

In order to solve the detailed segmentation problem, which would result in over-estimations of the cement hydration product volume, a novel thresholding scheme was developed. From Figures 6-9b and 6-10 it is clear that the initial multi-threshold method can establish the visual boundary of the anhydrous cement grains. Recognizing this, the same local multi-thresholding technique was used and a segmentation algorithm was developed to identify the boundaries of the cement grains and fill them entirely with the anhydrous product. From the initial multi-threshold calculation, the water-filled porosity was identified and distributed into the modified image in the previous step. Lastly, any of

the unidentified pixels within a given 2D pane were labeled as the hydration product phase. Figure 6-11 displays this methodology removed previous problems of having hydration products existing within the cement grains and also displays how cement hydration undergoes largely a surface reaction. Additionally, the outcome is visually similar to the evolution proposed in Figure 6-3 for various SEM images.

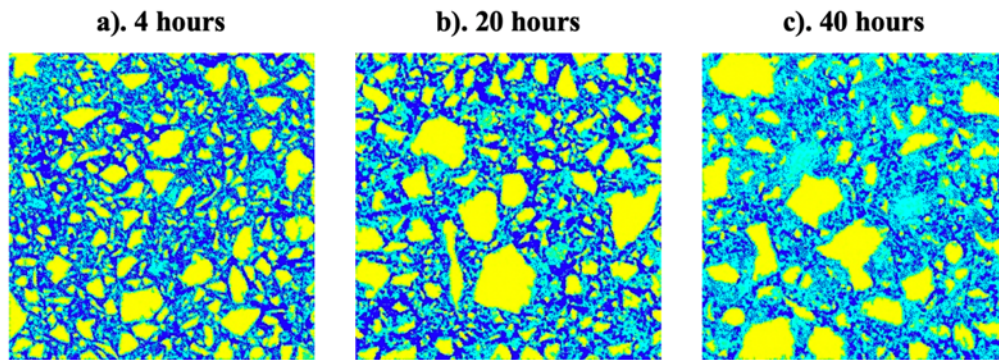


**Figure 6-11 - Improved segmentation outcomes using an updated phases-detection algorithm for cement paste with a w/c of 0.35.**

Despite the successes with the improved algorithm, two primary challenges existed. The first related to the large sample imperfections as shown in Figure 6-12. These voids were a result of poor sample preparation and result in the threshold classifying them as large water-filled pores. The second challenge related to the formation of crystalline hydration products such as  $\text{Ca}(\text{OH})_2$  or lime. By misclassifying these products and having large compaction voids, it is unlikely the phase volume fraction estimations could be accurate. Due to the poor resolution and inability to remove clear errors in the Visible Cement data source, it did not serve as an immediately viable way to develop PSP linkages – leading to the use of NIST’s CemHyd3D software to provide ‘cleaner’ datasets that could

be confidently segmented. Despite this, the progress made on segmented hydrating cement pastes is worthwhile and could inform future study.

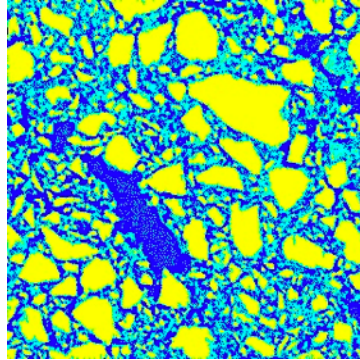


**Figure 6-12 - Example compaction or sample imperfection found a cement paste with a w/c of 0.30 at 162 total hours of hydration.**

### 6.3.2 VCCTL Cement Database Development and Segmentation

NIST's Virtual Cement and Concrete Testing Laboratory (VCCTL) provides users the ability to simulate the hydration of cements, concretes, and mortars using CemHyd3D, an inbuilt software. Using SEM and EBS inputs, CemHyd3D relies on kinetic models to predict the formation of hydration products and the resulting changes in the material microstructure [122]. Additionally, it can be used to predict material properties: elastic modulus and diffusivity; the latter of which is of interest and obtained for this database.

The process-parameter inputs in to the CemHyd3D software are w/c ratio, total hydration time, and CCRL cement 133 – in line with the parameters available in the Visible Cement dataset [123]. CemHyd3D allows for the user to request when microstructures are output from the kinetic-hydration model using time steps or based upon the total degree of cement hydration. For the developed database, a total of 28-days of cement hydration was assessed with microstructure outputs every 72 hours - resulting in 10 microstructures for

each w/c ratio. 7 different w/c ratios (i.e., 0.25, 0.30, 0.35, 0.40, 0.45, 0.50, and 0.55) were simulated 5 times each, resulting in a total of 349 100x100x100 voxel microstructures, where each voxel is 1 micron in length - analogous to the Visible Cement Database - and associated with a specific phase. Figure 6-13a displays a single 2D plane where the different colors represent phases present at a given voxel. Analogous to the previous section, the phases are then binned into water/porosity, hydration products, or anhydrous cement grains based upon known reactions [36,125,130], as shown in Figure 6-13b.

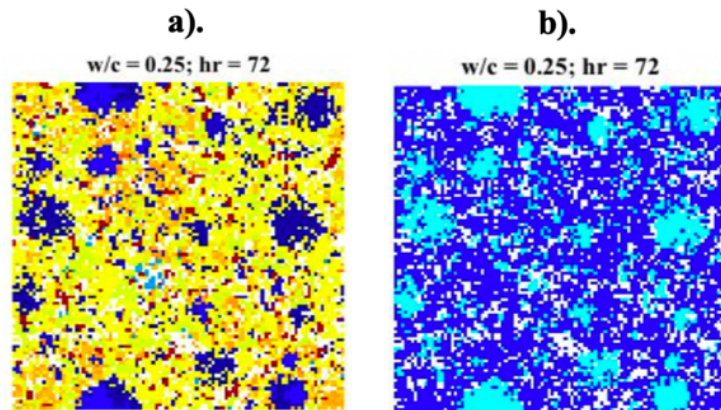


**Figure 6-13 - Example a). CemHyd3D output where each pixel/voxel represents a different phase and b). segmentation of the CemHyd3D image where white is water/pores, cyan is anhydrous cement grains, and blue is hydration products.**

Figure 6-14 displays a 2D pane from the center of 9 different microstructures of hydrating CCRL cement 133. It can clearly be seen that the influence of w/c and total hydration time has a significant influence on the microstructure. As the w/c increases the amount of water/porosity increases and the total amount of cement grains decreases. For each microstructure pane, the total amount of hydration products increases as a function of time.

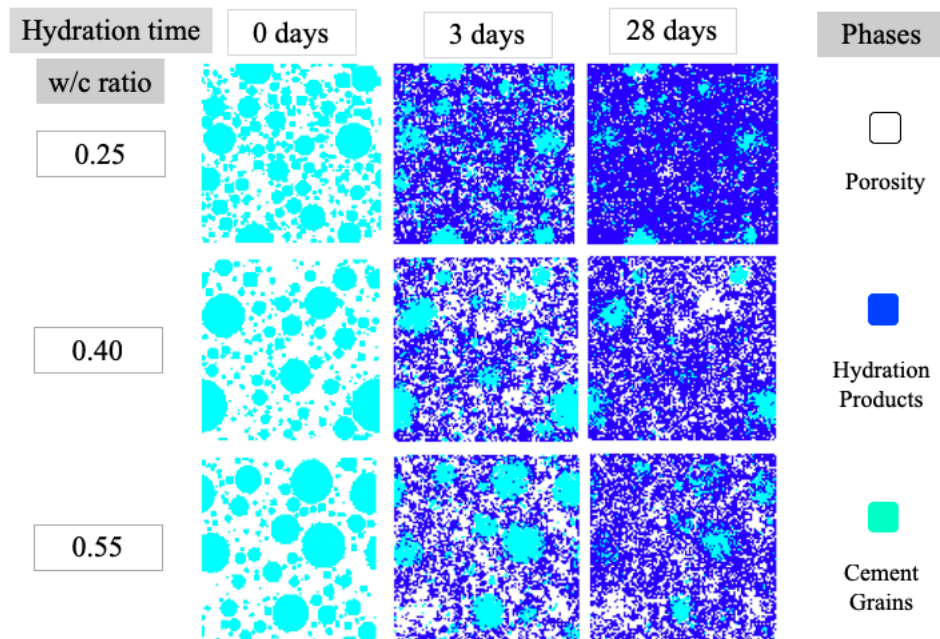


**Figure 6-14 - Generalized outcome of CemHyd3D database that has been segmented porosity, hydration products, and cement grains.**

#### 6.4 Materials Informatics Framework

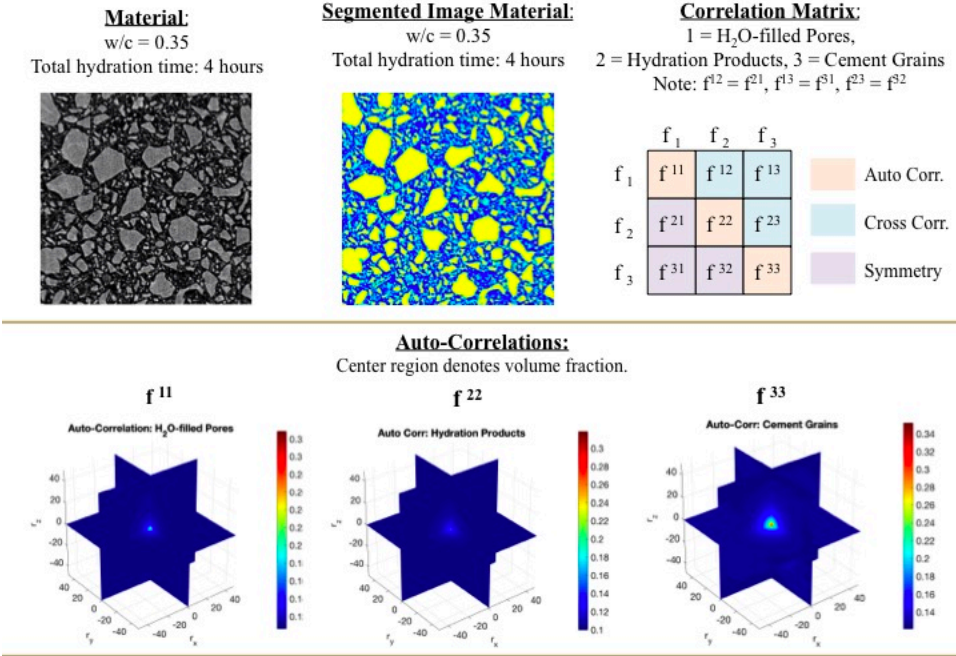
As mentioned in Section 6.3.1, due to challenges of segmenting the raw microCT data of hydrating cement in the Visible Cement database, the entire material informatics framework is only applied to CemHyd3D database described and developed in Section 6.3.2. Within this section, the workflow and framework for spatial statistics is first applied, followed by principle component analysis and how machine learning techniques are applied to develop reduced-order and high-fidelity process-structure, structure-property, and full PSP linkages. Additionally, how the diffusivity of the hydrating cement pastes is determined with CemHyd3D is detailed in Section 6.4.3.

### 6.4.1 Spatial Statistics

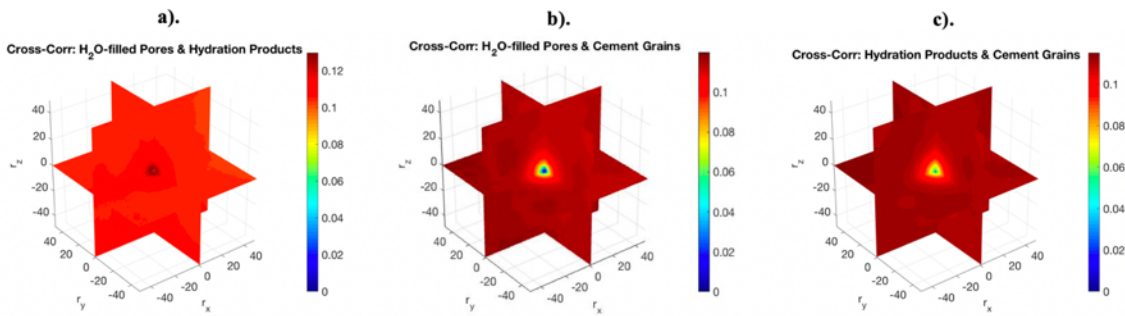
Spatial statistics provide a direct way to quantify salient structural features of a material. 2-point statistics, a subset of n-point statistics, evaluates the probability of phase  $i$  being a vector  $r$  away from phase  $j$  [121]. As mentioned in Section 6.2.1, 2-point statistics are of particular interest as they provide a sufficiently complete and quantitative representation of the segmented cement paste microstructures. Due to the three-phase nature of the segmented cement paste microstructures there a total of six different potential statistical evaluations of interest. Figure 6-15 displays the general workflow for carrying out 2-point statistics on the segmented repository of structures, where autocorrelations,  $f^{ii}$ , represent the probability of the same phase present in both evaluated voxels and cross-correlations,  $f^{ij}$ , assessing the probability of the evaluated voxels being composed of different phases. Figures 6-16a to 6-16c display the cross-correlations that can also be calculated for the same cement paste microstructure shown in Figure 6-15.

2-point statistics were calculated on the segmented CemHyd3D microstructures using the same methodology presented in the workflow shown in Figure 6-15. It is important to note that 2-point statistics were selected to capture any level of anisotropy in the hydrating cement paste microstructure that might exist. Furthermore, seeing as how the diffusivity of a material a direction property [70], a statistical representation of the microstructures that captures directionality is necessary. Figure 6-17 displays autocorrelations for the three segmented phases for 3 different w/c ratios at a total hydration time of 72 hours were  $f^{00}$ ,  $f^{11}$ , and  $f^{22}$  are autocorrelations for the water-porosity, hydration products, and anhydrous cement grain phases, respectively.

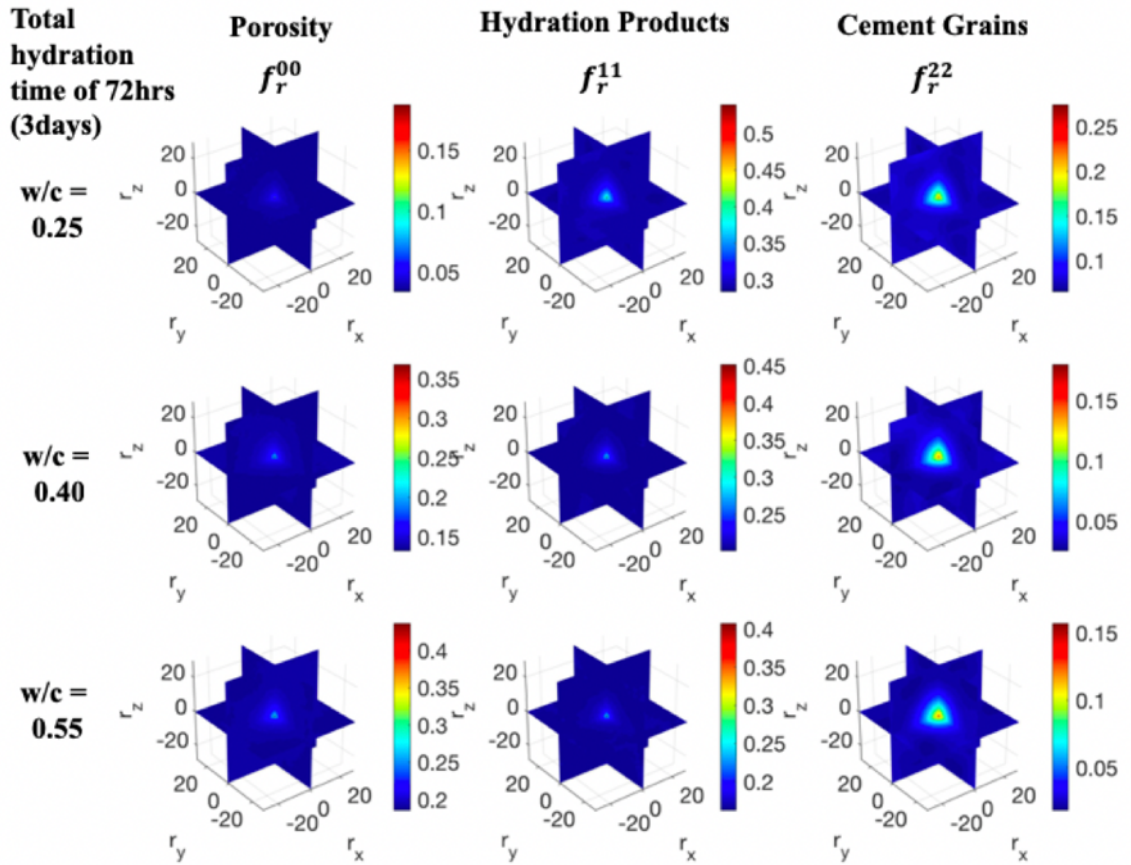
**Example 2-Point Statistics Spaces:** cut-off set to 50



**Figure 6-15 - General workflow for 2-point statistics evaluations for the Visible Cement and CemHyd3D segmented databases.**

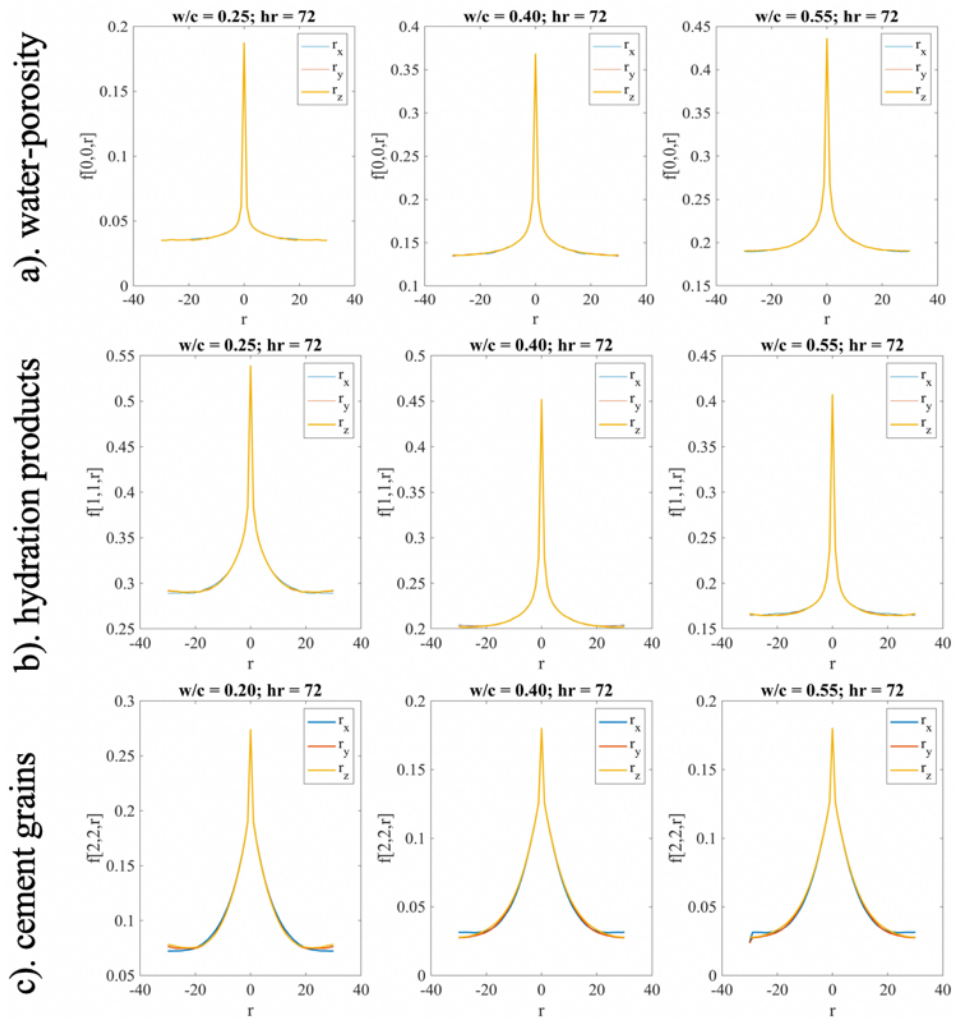


**Figure 6-16 - Cross correlations a).  $f^{12}$  - H<sub>2</sub>O-filled pores and hydration products, b).  $f^{13}$  - H<sub>2</sub>O-filled pores and cement grains, and c).  $f^{23}$  - hydration products and cement grains.**



**Figure 6-17 - 3D representation of autocorrelation outcomes for the CemHyd3D database.**

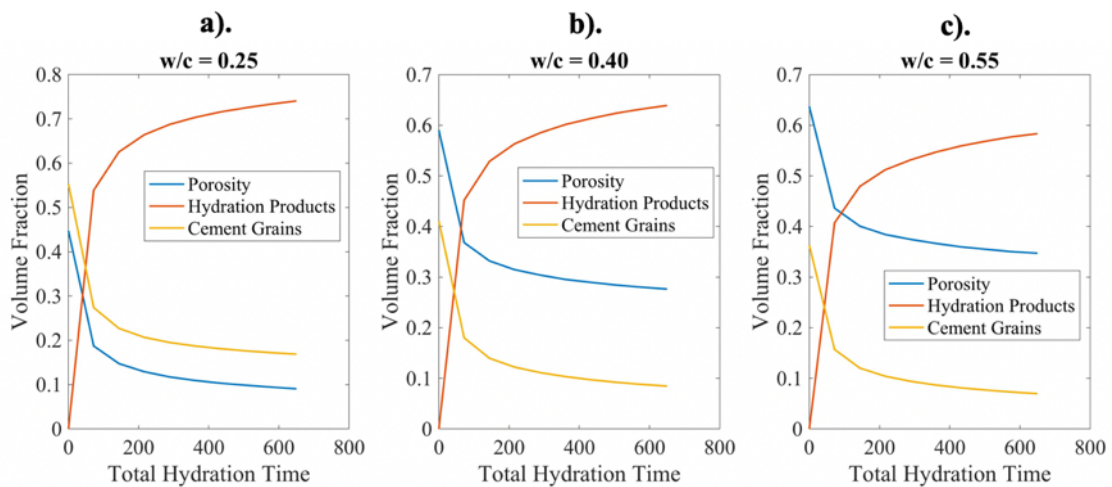
In order to ensure that the 2-point statistics calculations of the CemHyd3D database was capturing the full microstructure, Figures 6-18a to 6-18c were developed. The plots display that a cutoff (i.e., the maximal size of 2-point statistic vector  $r$ ) of 30 sufficiently represents the hydrating structures. Similar to Figure 6-17 the plots represent structures at a single hydration time of 72 hours or 3 days.



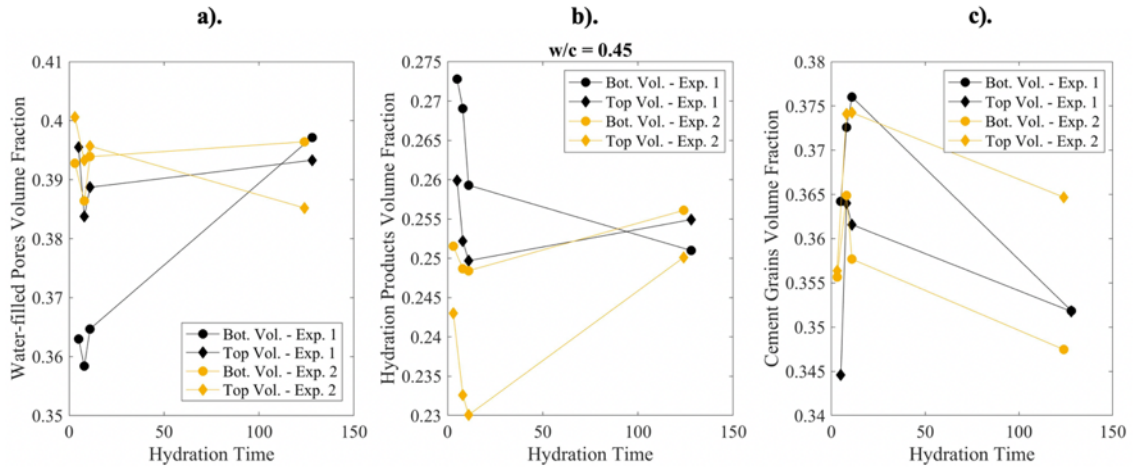
**Figure 6-18 - Cut evaluation of various w/c cement pastes at a total hydration time of 72 hours using autocorrelations of a). water-porosity, b). hydration product, and c). cement grain phases where  $r$  has units of voxel length (i.e.,  $\sim 1$ micron).**

Using the autocorrelation assessments, the respective volume fractions of the three phases can be plotted as a function of the process parameters to ensure they intuitively agree with the general hydration kinetics discussed and displayed in Section 6.2.2. Figure 6-19 displays the evolution in volume fraction history. Clearly, in the first 3 days (i.e., from 0 to 72 hours) there is the most significant evolution in respective volume fractions. This corresponds to the theory presented in Section 6.2.2. For the purposes of

this assessment, it is of interest to understand later hydration time (i.e., the prediction of late-age diffusivity parameters can be used to inform service-life models that would consider well-hydrated cementitious materials). In order to further motivate why it was necessary to use the CemHyd3D database rather than the Visible Cement Database, Figure 6-20 shows the predicted evolution in volume fractions from the 2-point statistic evaluations for the segmented microCT datasets for a w/c of 0.45 over all available total hydration times – clearly there is no readily identifiable trend as compared to Figure 6-20. Due to this, any reduced order assessment of the high-order spatial statistics carried out on these structures will not yield meaningful results and also disagrees with domain knowledge of cement hydration kinetics. Although Figure 6-20 only displays results for one w/c and two others were available, they both displayed equally chaotic results and served as the pivot towards building and using the CemHyd3D database for the PSP linkage development.



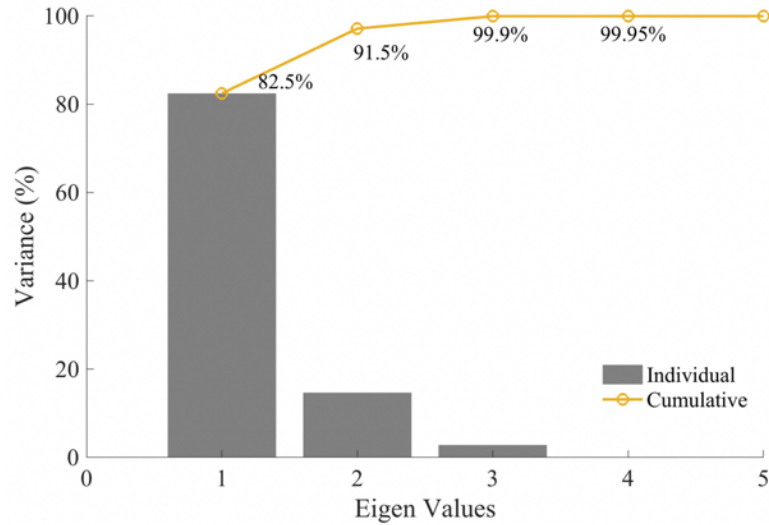
**Figure 6-19 - Evolution in phase volume fraction evolution as a function of total hydration time in hours for w/c of a). 0.25, b). 0.40, and c). 0.55.**



**Figure 6-20 - Evolution in volume fractions a). water-porosity, b). hydration products, and c). cement grains as a function of total hydration time in hours for a w/c cement paste of 0.45.**

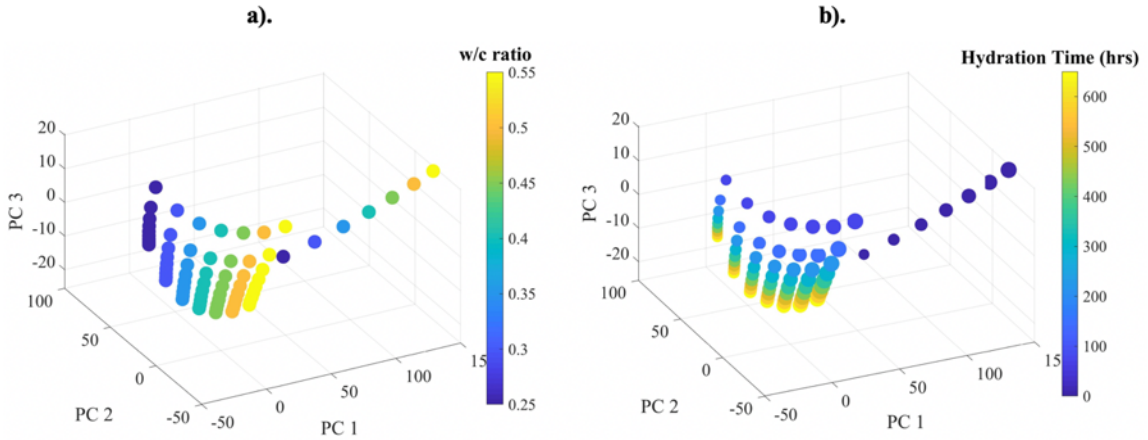
#### 6.4.2 Principal Component Analysis

Due to the statistical symmetries present in the 2-point statistics matrix shown in Figure 6-15, a data matrix was populated with the auto-correlation of the water/porosity and cement grains and the cross-correlations of water/porosity and cement grains to fully represent the statistical variability of each segmented structure for the CemHyd3D database. The data matrix is composed of the combination of these 3 2-point statistic outcomes for each of the 349 microstructures. Figure 6-21 displays the scree plot which describes the total variance captured by each respective eigenvalue index of the data matrix following the principle component (PC) analysis. Based on the results and following representations, the first 3 PC scores (i.e., eigenvalue indices) capture a sufficient amount of the variance from the outcomes of the 2-point statistics calculations.



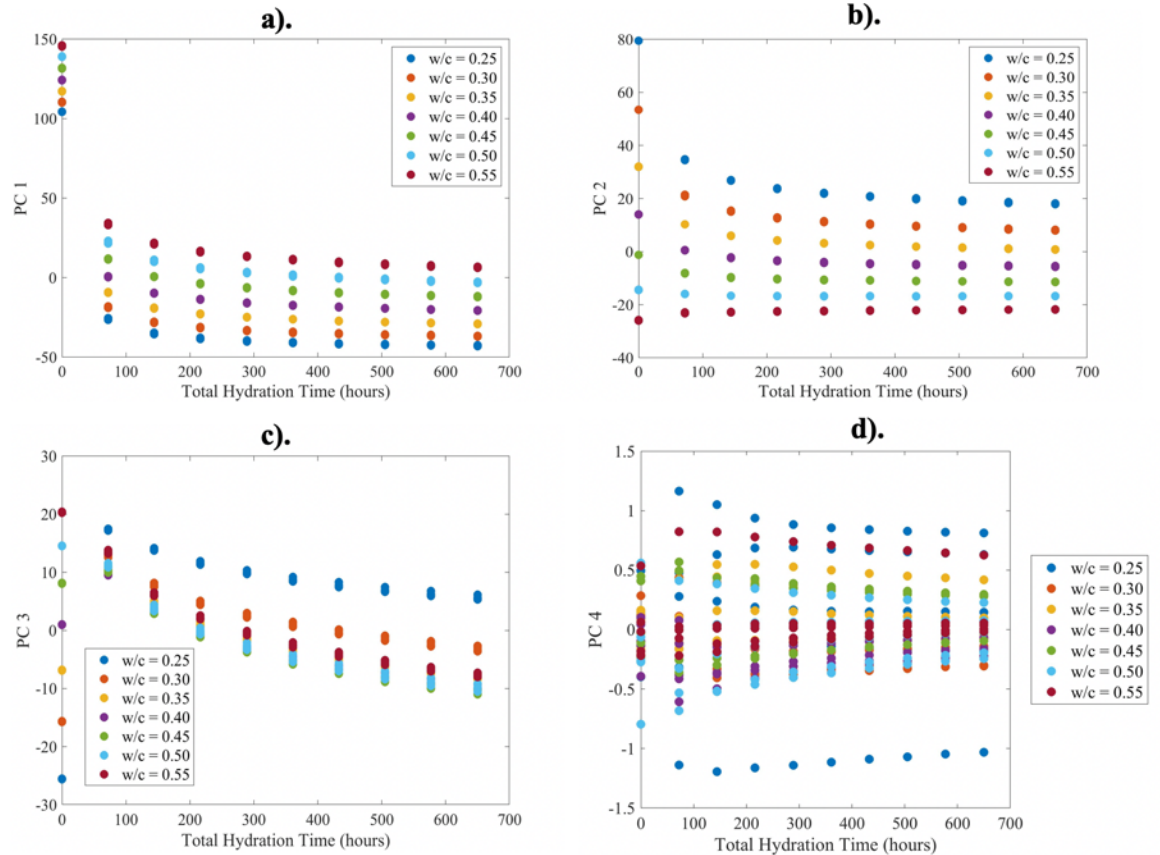
**Figure 6-21 - Scree plot of first five principal components (i.e., eigenvalues) of the data matrix which contains 2-point statistic information for each microstructure class.**

Figure 6-22a and 6-22b display the ability for the new structures to be easily distinguished by their first 3 PC scores and process parameters. It is important to note that there are 70 plotted points in these plots where the average PC score is plotted for the same w/c and total hydration time microstructures. Although 3D plots are difficult to visually analyse, it is clear that the PC analysis was able to clearly distinguish between the various classes of segmented microstructures using the high-order 2-point statistic evaluation. Figure 6-22 represents the ‘reduce-order’ form of the spatial statistics, which will be used to form process-structure and structure-property linkages in the following section.



**Figure 6-22 - 3D visualization of primary principal components to distinguish between process parameters a). w/c and b). total hydration time.**

Prior to PS, SP, or PSP model development, visual trends between the respective PC scores and process parameters are evaluated. Figures 6-23a to 6-23d show the trends for PC scores 1-4 as a function of w/c ratio and total hydration time for all 349 microstructures. It can be readily concluded that there is little variance between the replicate microstructures (i.e. those with the same w/c ratio and total hydration time) despite that they have initial random structures. This suggests that the REV is representative. Figures 6-23a to 6-23c display clear trends with the process parameters. Figure 6-23d does not show any clear trends, further suggesting that it is not needed to represent the hydrating microstructures. It is important to note that trends are not entirely clear from total hydration times of 0 hours to 72 hours in Figure 6-23c. Due to the fact that a significant portion of the hydration process takes place during this time, these departures from the other microstructures are logical. Future studies of interest are evaluating early hydration times.



**Figure 6-23 - Visualization of w/c and total hydration time to form trends between a). PC1, b). PC2, c). PC3, and d). PC4 for all 349 microstructures.**

It is often of interest to investigate what the respective PC scores represent (i.e., volume fraction, spacing, orientation, etc.). Figure 6-24 displays the basis vectors for the first three PC scores from the PCA analysis. The first two rows display auto-correlation information and suggest that PC 1 is dominated by volume fraction information and PC 2 contains information about the distribution of the porosity and cement grain phases. Furthermore, the PC2 plots suggest that the microstructure is highly isotropic, displaying little variance in any direction.

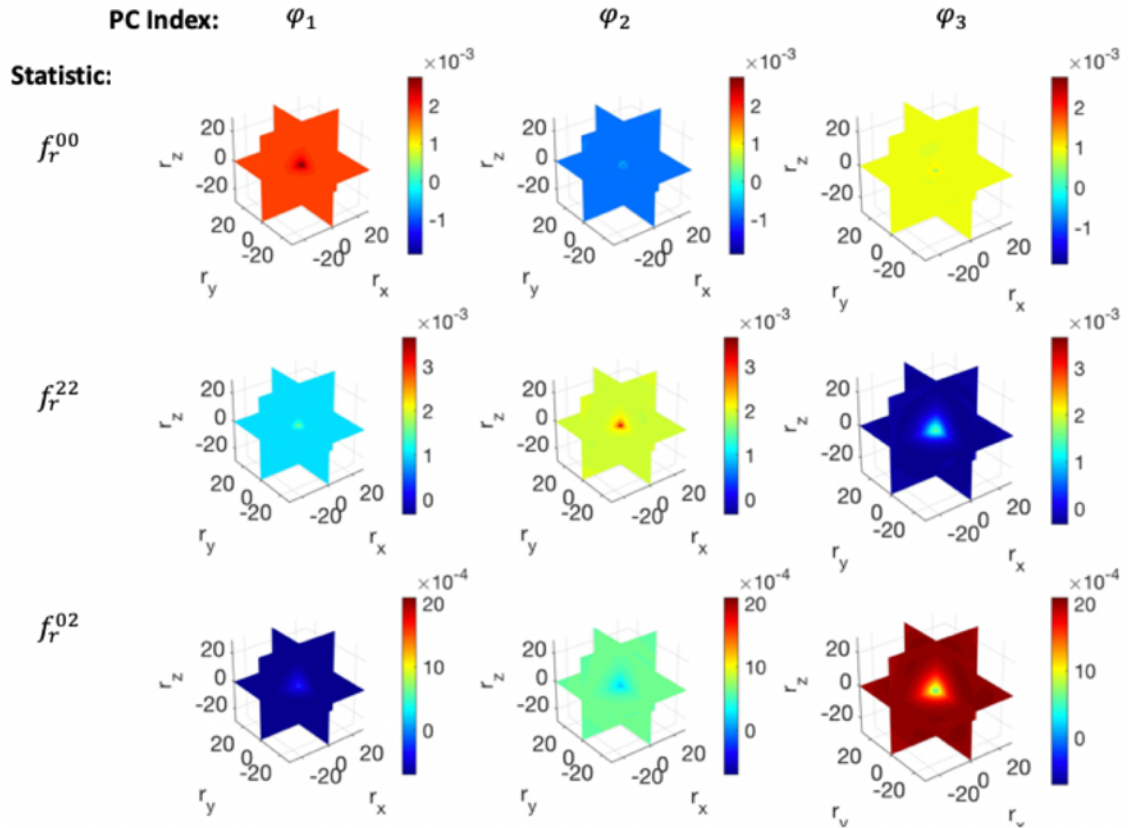


**Figure 6-24 - Basis vector plot for statistical assessment of the 349 microstructures and various principal components.**

### 6.4.3 Machine Learning and Diffusivity Determination

#### 6.4.3.1 Gaussian Processes for Machine Learning Applications

A Gaussian Process (GP) regression model was selected for fitting the process-parameters to PC scores shown in the preceding section based upon: an initially unknown model form, a small dataset once PC scores with the same parameters were averaged, and the lack of interest in using prior time series information to inform the model. For the purposes of this project and general interest of the field, it is of high utility to use controllable parameters (i.e., w/c ratio and total curing time, which is analogous to

hydration time) to predict the structure. Figure 6-25 summarizes the theory needed to understand GP models and detailed information can be found in [139,140].

### Gaussian Process Modeling Summary:

---

A gaussian process (GP) is composed of a set of random variables (RVs) where any collection of RVs have a joint gaussian distribution. Furthermore, a GP can be described by mean,  $m(x)$ , and covariance,  $k(x,x')$ , functions and is inherently non-parametric and kernel-based.

Take the model,  $h(x)^T \beta + f(x)$ , where  $h(x)$  are basis functions,  $\beta$  is a vector of coefficients, and  $f(x)$  describes latent variables with a covariance function of  $k(x,x')$ . A response,  $y_i$ , can then be predicted as  $P(y_i|f(x_i), x_i) \approx N(y_i|h(x_i)^T \beta + f(x_i), \sigma^2)$ .

Generally, it is expected that similar predictors,  $x_i$ , have similar response values,  $y_i$ . The covariance function captures this in GP models because it provides information between latent variables,  $f(x_i)$  and  $f(x_j)$  where  $i \neq j$ . This implies the covariance function describes how a response at one point is affected by responses at other points.

For the purposes of the fitted models, the standard squared exponential kernel function is used to describe  $k(x,x')$ , the covariance function and is written as:  $k(x_i, x_j|\theta) =$

$\sigma_f^2 \exp \left[ -\frac{1}{2} \frac{(x_i - x_j)^T (x_i - x_j)}{\sigma_l^2} \right]$ , where  $\sigma_l$  is the length scale parameter and  $\sigma_f$  is the signal deviation.

Lastly, the parameters of the GP model can be estimated by maximizing the log likelihood  $P(y|X)$  as a function of  $\beta$ ,  $\theta$ , and  $\sigma^2$ .

Simplified from: <https://www.mathworks.com/help/stats/gaussian-process-regression.html>

### Figure 6-25 - Summary of theory for gaussian process models for applications in machine learning [139,140].

MATLAB's GPR suite [139] was used to fit 3 different process-structure models where the parameters are approximated by minimizing the loss (mean squared error between predictions) due to cross-validation, which is the objective function shown in Figure 6-26a and steps taken to convergence in Figure 6-26b. A k-fold cross-validation was implemented with 10 folds and 90 percent of the dataset that contained all of the cement paste structures at time  $t = 0$ , leaving a minimum of 7 test responses. The structures

at time  $t = 0$  were not used as test variables to ensure the late-age prediction of the PC scores or diffusivity value was improved.

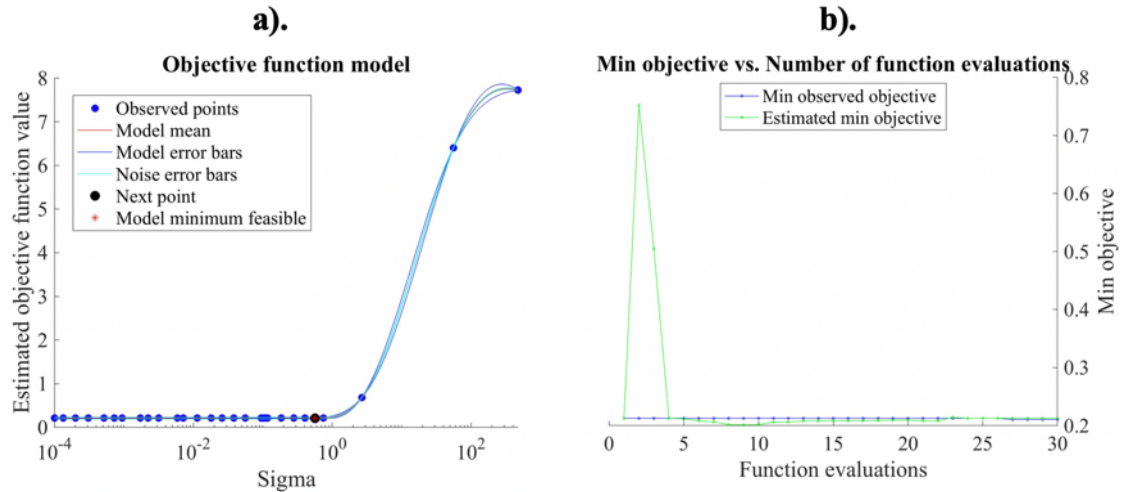


**Figure 6-26 - Outcomes of objective function determination: a). value and b). minimization.**

#### 6.4.3.2 Diffusivity Estimation Using CemHyd3D

In addition to the process-structure (PS) linkage, estimating the relative diffusivity of hydrating cement pastes is also needed to form a full PSP linkage. This section details how the relative diffusivity of the cement pastes was predicted using CemHyd3D, detailing the theory behind the calculation and showing the ability of the PC scores to correlate with the determined values.

CemHyd3D allows for users to predict the relative diffusivity of cement, mortar, and concrete microstructures that have hydrated past time  $t = 0$ hrs. The calculation is made by converting all of the available pore-space and CSH (a porous hydration product) into a network of conductors, as shown in Figure 6-27a [122,141]. The relative conductivity of cement paste is then calculated in a single direction as the series

combination where the porosity has a conductance of 1 and the CSH has a conductance of 0.005. The relative conductivity is then related to the relative diffusivity by the Nernst-Einstein relation as shown in Figure 6-27b [122,141].

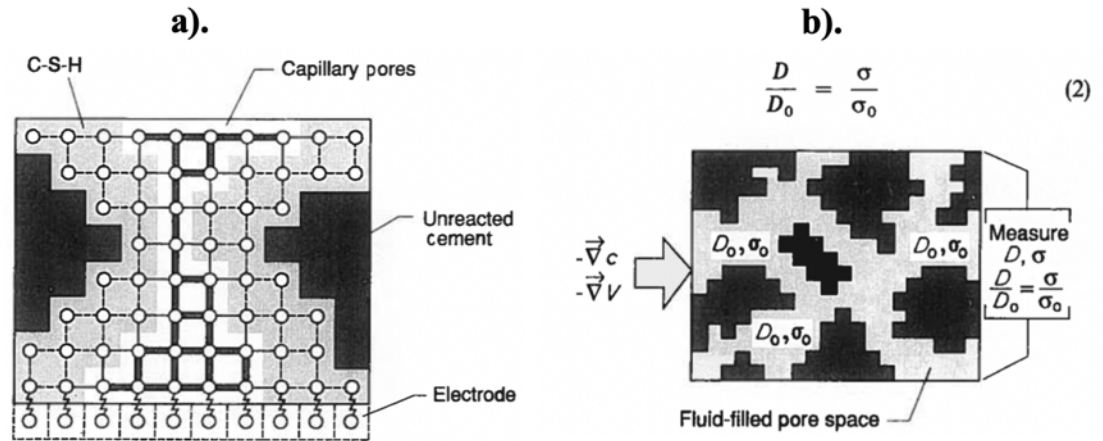


**Figure 6-27 - a). Network model of pores and CSH and b). Nernst-Einstein relation used to predict the diffusivity of the 349 CemHyd3D microstructures [122,141].**

Using this approach, the relative diffusivity in the x, y, and z directions was calculated for each microstructure. Similar to the PC scores, the values were averaged for microstructures with the same process parameters due to their lack of variance. For the purposes of visualization and future linkage development, the average relative diffusivity for each microstructure class (i.e., same w/c ratio and total hydration time) is retained (i.e.,  $D/D_0$  as shown in Figure 6-28b). Figure 6-28a shows the relationship between the PC scores and the average relative diffusivity. Figure 6-28b shows the relationship between the process parameters and the average relative diffusivity.

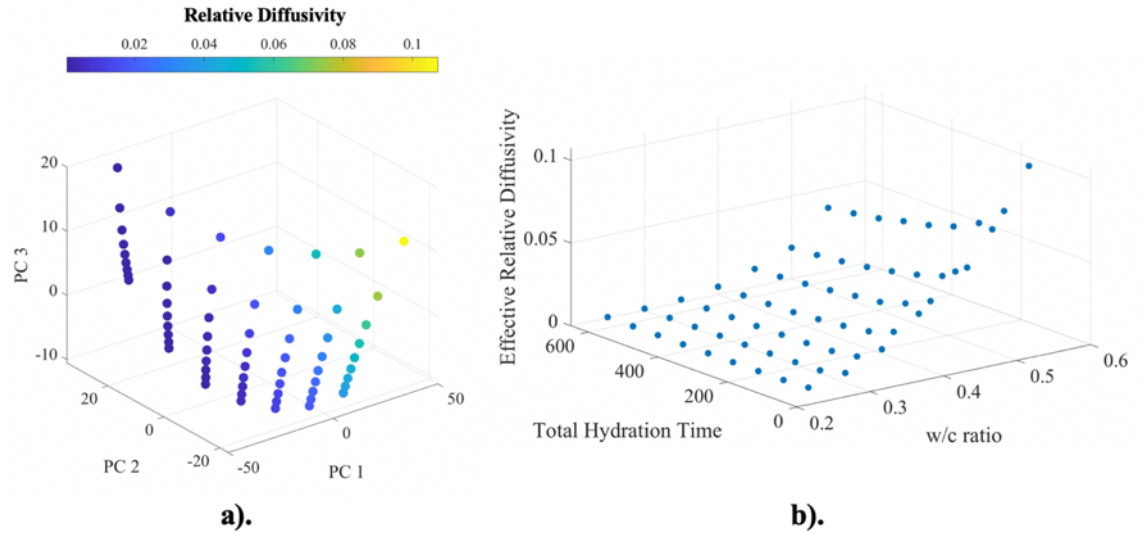


**Figure 6-28 - Average (effective) relative diffusivity as a function of a). PC scores and b). process parameters of the cement paste microstructures.**

#### 6.4.4 Process-Structure, Structure-Property, PSP Linkages

##### 6.4.4.1 Process-Structure Linkages

Using the gaussian process (GP) methodology presented in the preceding section, with a squared exponential kernel function, 3 distinct cross-validated models were created. Figure 6-29a shows the ability for the cross-validated GP model to predict the first principle component scores as a function of the process parameters. Figure 6-29b display the train-test parity plot for the developed PC1 GP model – it is clearly very accurate and precise. Figures 6-30a and 6-30c show the developed GP surfaces for PC scores 2 and 3 and Figures 6-30b and 6-30d display the corresponding parity plots, analogous to Figure 6-29b. The outcome of these plots is a full process-structure linkage which can confidently represent 99.9% of the variance in the CemHyd3D microstructure database – effectively allowing for the immediate prediction of the cement paste structure as a function of the process parameters and can be reproduced with the kernel model parameters given in Table 6-2.

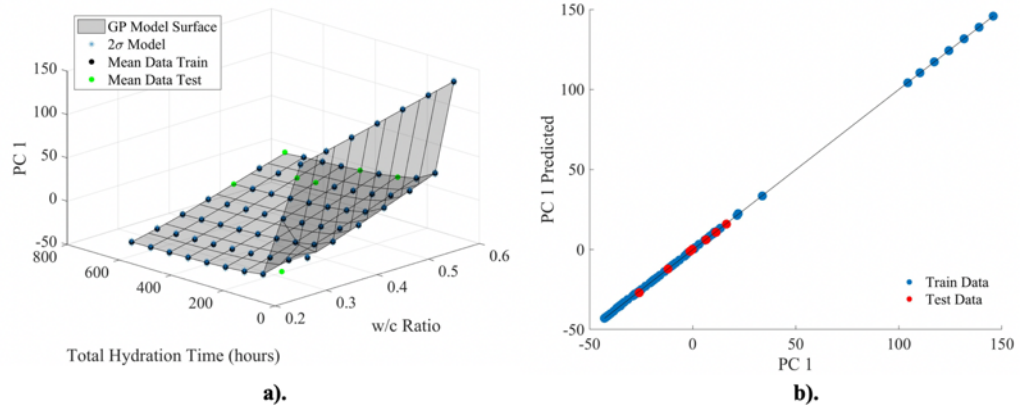


**Figure 6-29 - a). GP model outcome and b). parity plot of known PC1 versus Predicted PC1 using the GP model and an 80-20 train-test split.**

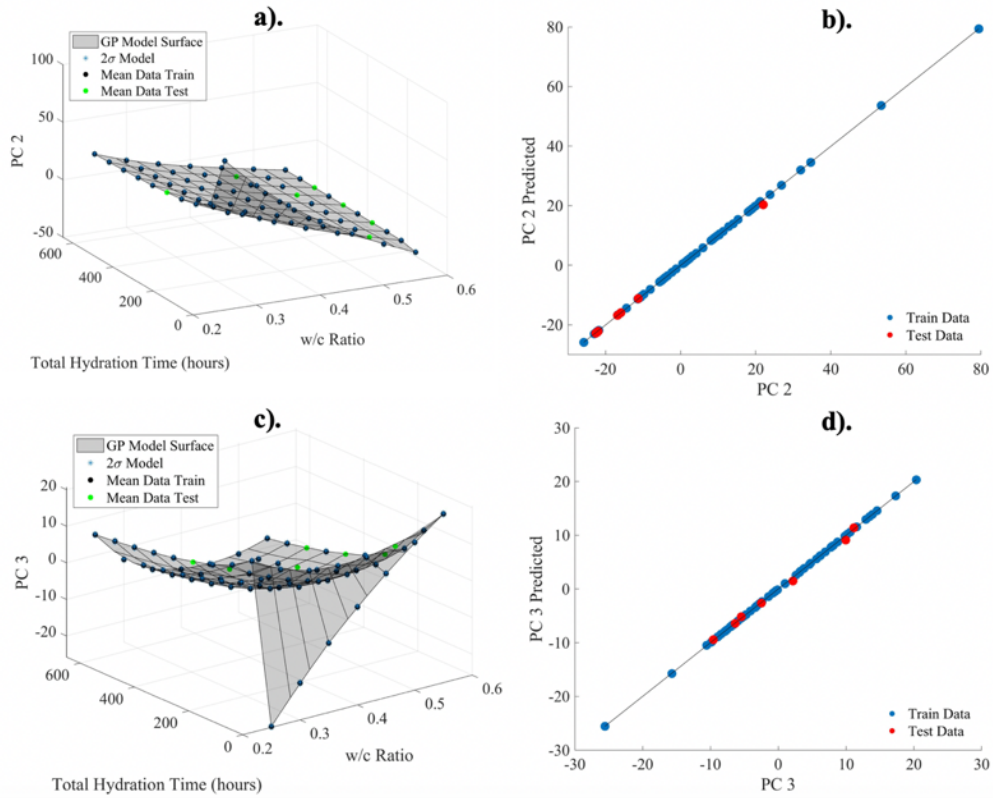


**Figure 6-30 - a). and c). represent the fit GP model surface (i.e., process-structure linkage) for PC scores 2 and 3 whereas b). and d). represent the parity plots for each PC score.**

**Table 6-2 - GPR model parameters for fit squared exponential kernel functions.**

GPR Model Parameter	PC 1	PC 2	PC 3
$\sigma_f$	69.2	59.5	19.3
$\sigma_l$	0.58	0.27	0.16
$\sigma_n$	0.47	0.19	0.09

Following the same methodology for the process-structure linkages, cross-validated GPR models were developed using PC scores and process-parameters, respectively, to predict effective, or averaged, relative diffusivity (ERD). Figures 6-31a and 6-31b display the outcome parity plots. The results suggest that the structural (PC score) predictors are better than process-parameters. In Figure 6-31a all of the test data falls within the natural variance of train data, whereas it does not in Figure 6-31b - there are numerous negative predictions for ERD which is highly un-physical. These results suggest that the structural link is essential for full property predictions from initial process parameters. By using the GP models presented in Figures 6-29 and 6-30 and connecting it to structures-property linkage shown in Figure 6-31a a full PSP linkage for hydrating cement pastes is formed.

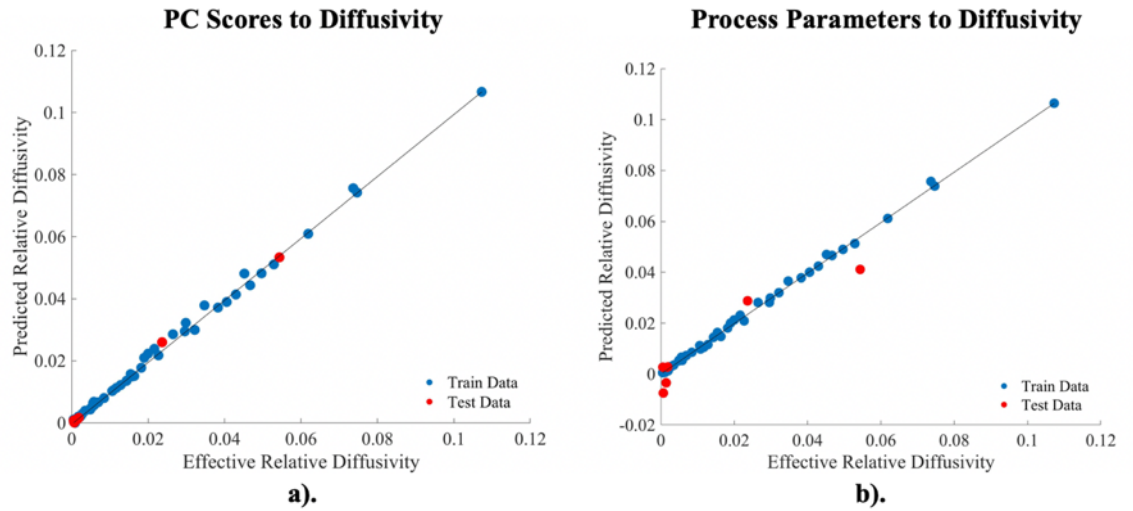


**Figure 6-31 - Parity plots for a). PC scores to diffusivity and d). process parameter top diffusivity GP models.**

#### 6.4.5 Extension of Results to the SVDK Model

Using the fit gaussian process regression models displayed in the preceding section, a PSP linkage can be established. Figure 6-32a displays the mean predicted effective diffusivity of the cement microstructures as a function of the process parameters where the PC scores of the structures were used link the parameters to the properties. Figure 6-32b shows values of diffusivity obtained from the previous plot assuming that the smallest value of predicted effective diffusivity had a value of  $10^{-13}$  m<sup>2</sup>/s (i.e., the absolute low-bound of experimental outcomes detailed in Section 3.3) and scaling the remaining values accordingly. Figure 6-33b displays a direct PSP linkage where the structure component is imbedded into the final property prediction. Using the outcome of Figure 6-32b, the diffusivity values are directly entered into the SVDK model developed in Section 3.3 to show how the time to full dissolution, or saturation, of single air voids can be expected to vary as a function of w/c and total hydration time – the outcome is shown in Figure 6-33.

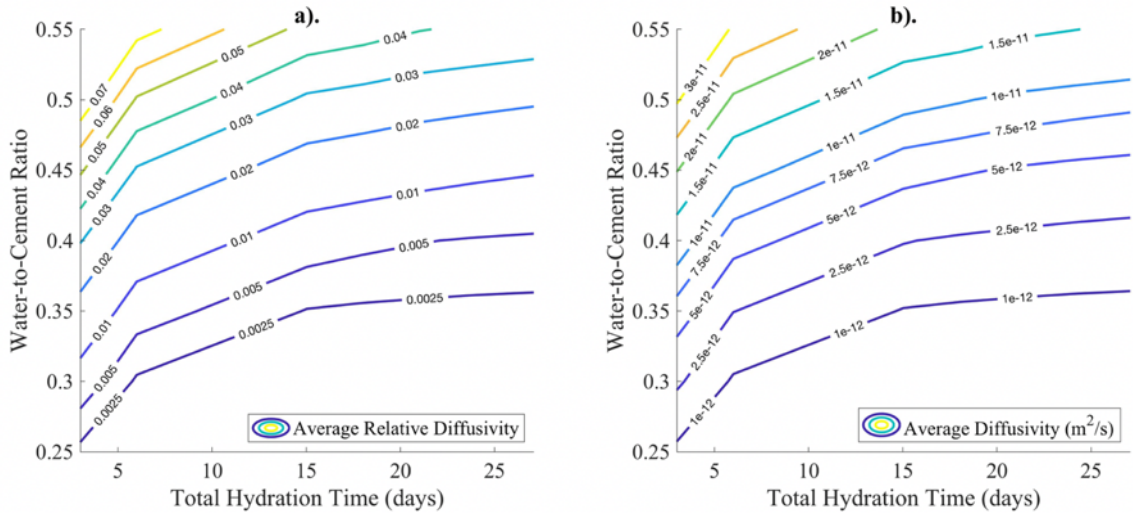


**Figure 6-32 - Influence of process parameters on a). mean effective diffusivity and b). average diffusivity.**

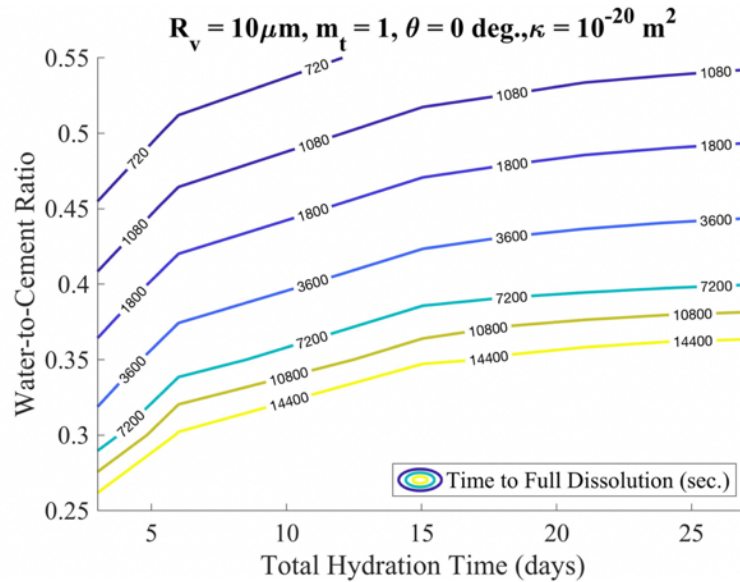


**Figure 6-33 - Influence of process parameters on time to full dissolution using the SVDK model.**

Figure 6-33 shows how the engineering science and material informatics framework developed and displayed herein can be used to progress the field toward service-life design. Figure 6-33 suggests that time to full dissolution, or saturation of the

air voids, for cements that have been allowed to sufficiently cure (i.e., for greater than 15 days) is only dependent on the w/c of the cement paste. Additionally, the image shows that a 0.05 decrease in w/c ratio effectively doubles the time to full dissolution. This finding may allow for the tailoring of the minimal service-life of the material in freeze-thaw environments to be controlled by the most common parameter in concrete mixture design as the saturation of the air void system is of significant concern as displayed in Chapter 4. Connecting properties to performance, when this PSP linkage is coupled with the MVDK model the influence of cement properties (i.e., w/c ratio, total hydration time, porosity, etc.) could be used to predict the long-term saturation rate,  $S_2$ .

## **6.5 Conclusions**

The efforts presented within this chapter clearly display that a materials informatics framework to develop PSP linkages for cement pastes is not only feasible, but necessary. As shown in Figure 6-31, incorporating a reduce order representation of segmented cement pastes structures is essential to accurately predicting the evolution in material properties like the diffusivity and allows for the development of high-fidelity PSP linkages, as displayed in Figure 6-32. Using the PSP linkages, process-parameters can then be connected to engineering phenomena, using the predicted material properties to predict performance. Figure 6-33 displays how the averaged diffusivity values can be input into the SVDK model and used to predict time to full dissolution of trapped air within a single spherical air void.

Key outcomes from Figure 6-33 include the independence of time to full dissolution on total hydration of the cement paste past 15 days and for well-hydrated systems a

reduction in w/c of 0.05 doubles the time to complete liquid saturation. It is important to note that the CemHyd3D database of microstructures was developed with intentions to evaluate and predict late-age diffusivity properties but could be improved by including additional data points between 0 and 72 days of total hydration when the bulk amount of cement hydration occurs. Additionally, to ensure a level of compatibility with the Visible Cement dataset only CCRL cement 133 was evaluated. By using various cements, the influence of difference cement chemistries could be evaluated and included within the PSP framework.

Additional improvements of the presented data science approach for PSP linkages in cement pastes could include the use of a multi-output gaussian process model to simultaneously predict the principal components scores rather than having three separate models as displayed in Section 6.4.4 and Table 6-2. Using this approach, multiple properties could also be predicted along with the diffusivity. Overall, this work displayed how a data science framework can be beneficially used in the field of cement sciences and could be leveraged to rapidly prototype and identify process-parameters that would result in a material with high saturation resistance and therefore significant freeze-thaw durability.

# **CHAPTER 7. UNIFICATIONS AND MODERNIZATION OF THE AMERICAN CONCRETE INSTITUTE'S FREEZE-THAW DESIGN SPECIFICATIONS**

## **7.1 Introduction, Contracted Efforts, General Methodology**

In order to ensure the service-life of placed concrete, the design and construction industries need uniform guidance on durability recommendations across American Concrete Institute (ACI) documents. As detailed by Figure 1-1 and motivated in the first chapter, the translation of understanding from the state-of-the-art in engineering sciences to specifications is essential to progress the field toward service-life design. Within this chapter, three ACI documents where discrepancies exist were examined: ACI 201.2R-16, 318-14, and 350-06 [7–9]. These three documents contain the main guidance that informs the current concrete design and building practice regarding durability requirements and exposure category descriptions set for freeze-thaw environments. Unfortunately, there is considerable disagreement between these documents in providing clear values of water to cementitious material ratio (w/cm), strength requirements, and air content (volume %) that guarantee durability. Further complicating matters, there is no standard language to define the various exposure category descriptions for each deterioration mechanism. A systematic and rigorous analysis of existing freeze-thaw durability data is conducted herein to provide an evidence-based resource to establish unified guidance by the aforementioned ACI Committees.

It is important to note that these efforts were conducted alongside three other universities: Oregon State University (OSU), the University of Texas at Austin (UTA), and the University of New Brunswick (UNB) and the efforts were solicited and reviewed by ACI's Concrete Research Council. Specifically, OSU evaluated current limits and specifications on high-sulfate exposures whereas UTA and UNB jointly investigated current chloride limits and exposure categories. For the purposes of the research presented in this chapter, the work conducted on freeze-thaw will exclusively be discussed but it is important to note that these efforts fit within a larger effort to modernize and unify ACI durability documents.

To thoroughly evaluate the current code, existing freeze-thaw durability data for concrete from field exposure sites, published literature, and Army Corps of Engineers infrastructure evaluations were analyzed. For the freeze-thaw portion of the project outcomes include: 1) Recommendations to ACI Committees 201, 318, and 350 on unified durability limits and exposure category descriptions; 2) Identification of knowledge gaps and future studies to address deficiencies in existing data sets; and 3) A detailed research methodology that leverages modern field performance and lab testing to inform the development of performance-based standards. Furthermore, the completed work details the need for improved test methods to further validate the reliability of specified mixture proportions and material parameters for durability – in line with Figure 1-1 for advancing the field toward service life design.

## 7.2 Literature Review

### 7.2.1 *Summary of Freeze-Thaw Exposure Categories, Specifications, and Recommendations*

There are four general exposure categories found in ACI documents [7–9] that are concerned with concrete design for freeze-thaw (FT) durability. Tables 7-1 and 7-2 display design requirements and recommendations for minimum compressive strength, maximal water-to-cementitious-materials (w/cm) ratio, and total air content as a function of maximum aggregate size (MSA) as established by ACI committees 201, 318, and 350 [7–9]. For all ACI documents, the F0 exposure category refers to no exposure to FT cycling. The remaining exposure categories (i.e., F1-F3) are distinguished by the expected saturation state of the concrete and potential exposure to deicing chemicals. The F1 exposure category refers to concrete placements in regions with low likelihood of saturation and exposure to FT cycling. The F2 and F3 exposure categories apply to concrete placements in regions with high likelihood of saturation and exposure to FT cycling, where F3 is distinguished by additional exposure to deicing chemicals. It is important to note that ACI 201.2R-2016 has two F3 categories (a and b) that are delineated by the method in which the surface of the concrete is finished. F3a is hand-finished concrete whereas F3b is formed and machine-finished (1). As detailed in R26.4.3.1(a) of ACI 318-14, ACI 318 does not address differences in surface finishes throughout the document. Considering Table 7-1, it is apparent that ACI 350 has a singular design recommendation for FT durability, differing drastically from ACI 201's recommendations and ACI 318's specifications.

**Table 7-1 - Minimum design strengths and maximum water to cementitious materials ratio based on freeze-thaw exposure category from different ACI documents (1,4-6).**

Exposure Category	ACI 201.2R-2016		ACI 318-14		ACI 350-06	
	Min $\bar{f}_c$ # ksi (MPa)	Max w/cm	Min $f'_c$ ** ksi (MPa)	Max w/cm	Min $f'_c$ ksi (MPa)	Max w/cm
<b>F0</b>	None	None	2.5 (17)	N/A	-	-
<b>F1</b>	3.5 (25)	0.5	3.5 (25)	0.55	-	-
<b>F2</b>	3.5 (25)	0.45	4.5 (32)	0.45	4.5 (32)	0.42
<b>F3 (a/b)*</b>	4.5 (32)	0.45§	5.0‡ (35)	0.40‡	-	-

\* ACI 201.2R-2016 delineates exposure class F3 based on surface finish. F3a is hand-finished concrete with maximal limits on the total amount of allowable supplementary cementitious materials content. F3b is concrete that is formed and machine-finished.

# Min  $\bar{f}_c$  is defined in ACI 201.2R-2016 as the minimum average compressive strength that should be achieved before initial exposure to freezing and thawing [7].

§ A lower w/cm may be needed when corrosion is of concern (ACI 201.2R-2016) [7].

\*\* Min  $f'_c$  is defined by ACI 318-14 as the minimum specified compressive strength of concrete [8].

‡ For plain concrete (i.e., non-reinforced concrete), the maximum w/cm shall be 0.45 and the minimum  $f'_c$  shall be 4.5ksi [8].

To date, the definitions for the minimal strength requirement associated with ACI 318 and ACI 201 are fundamentally different. Exact definitions of the respective minimal strength requirements can be found in the footnotes of Table 7-1. The intent of ACI 201's recommended minimum  $\bar{f}_c$  is to ensure a minimal compressive strength prior to initial exposure to FT cycling [7]. The values found in ACI 201.2R-2016 for min  $\bar{f}_c$  are based upon findings from a study conducted by P. Klieger in 1957 that evaluated the minimum required curing time to impart scaling resistance [10]. As detailed in Section R19.3 of ACI 318-14 [8], the minimal  $f'_c$  values are established to be consistent with the specified maximum w/cm, which is selected to ensure sufficient resistance to fluid penetration. Furthermore, Section R26.4.3.1(a) of ACI 318-14 states that, "the Code does not include provisions for...temporary freezing-and-thawing conditions during construction..." – identifying the fundamental departure between the ACI 201 and ACI 318 strength provisions [8]. Despite the difference in definition of  $f'_c$  and  $\bar{f}_c$ , when the ACI 318's min  $f'_c$  and max w/cm values for the F3 exposure category are relaxed to consider non-reinforced concrete the ACI 318 and ACI 201 design requires are in agreement in terms of value.

As shown in Table 7-2, ACI 201 recommends higher values for the total air content than those specified by ACI 318 [7,8]. ACI 201 obtains the design values, as shown in Table 7-2, by requiring 18% air content in the paste fraction of the concrete mixture with the associated maximal w/cm for each exposure category. The values recommended for total air content in ACI 201.2R-2016 are based upon two studies [11,12] conducted by P. Klieger in 1952 and 1956 that evaluated the influence of MSA and total air content in the paste fraction on net expansion after 300 FT cycles. Although

the technical basis for which ACI 318 establishes their target air content values was not identified, the values are similar to those recommended in ACI 201.2R-2016 and are likely informed by decades of design experience. Interestingly, Section R26.4.3 of ACI 318-14 clearly states, “it is not the responsibility of the licensed design professional to proportion concrete mixtures,” despite that a requirement for total air content directly influences volumetric proportioning [8]. This finding, although non-technical, establishes the extent to which durability requirements can be developed. Lastly, restrictions on the use of supplementary cementitious materials (SCMs) are only required for F3a exposures per ACI 201.2R-2016, whereas ACI 318-14 places restrictions on SCM use for its F3 exposure category. Allowable cementitious material replacement percentages, which are equivalent in definition and value amongst ACI 318 and ACI 201 documents, are shown in Table 7-3.

**Table 7-2 - Air content limits based on freeze-thaw exposure category from different ACI documents [7,8].**

MSA in (mm)	Air Content (%)			
	Exposure Category: F1		Exposure Category: F2 and F3	
	ACI 201.2R-2016*	ACI 318-14	ACI 201.2R-2016	ACI 318-14
3/8 (9.5)	7.0	6.0	7.5	7.5
1/2 (13)	7.0	5.5	7.0	7.0
3/4 (19)	6.5	5.0	7.0	6.0
1 (25)	6.5	4.5	6.5	6.0
1.5 (38)	6.0	4.5	6.5	5.5
2 (50)	6.0	4.0	6.0	5.0
3 (76)	5.0	3.5	5.5	4.5

\* ACI 201.2R-2016 and ACI 318-14 allow for a field tolerance of air content of  $\pm 1.5\%$ .

**Table 7-3 - Allowable cementitious replacement percentages for ACI 318 F3 and ACI 201 F3a exposure categories [7,8].**

<b>Cementitious Materials</b>	<b>Maximum Percent of Total Cementitious Materials by Mass*</b>
Fly ash or other pozzolans conforming to ASTM C618	25
Slag conforming to ASTM C989/C989M	50
Silica fume to ASTM C1240	10
Total of fly ash or other pozzolans, slag, and silica fume	50
Total of fly ash or other pozzolans and silica fume	35**

\* The total cementitious materials also include ASTM C150/C150M, ASTM C595/C595M, ASTM C845/C845M, and ASTM C1157/C1157M cements.

The maximum percentage should include:

- (a) Fly ash or other pozzolans in ASTM C595/C595M blended cement or ASTM C1157/C1157M cement
- (b) Slag used in the manufacture of an ASTM C595/C595M blended cement, or ASTM C1157/C1157M cement
- (c) Silica fume, ASTM C1240, or present in a ASTM C595/C595M blended cement ASTM C1157/C1157M cement

\*\*Fly ash or other pozzolans and silica fume shall constitute no more than 25 and 10 percent, respectively, or total mass of the cementitious materials.

### 7.2.2 *Background and Critical Review of Freeze-Thaw ACI Provisions*

Due to the difference in strength requirement definitions, comparing the ability for one set of design requirements to yield more durable concrete is challenging. In terms of definition alone, it could be concluded that ACI 201's  $\min \bar{f}_c$  recommendation is more conservative than ACI 318's  $\min f'_c$  requirement as it provides assurance that a sufficient strength is achieved prior to FT cycling. Such a conclusion does not consider that ACI 318-14 places the responsibility of cold-weather concreting on the contractor. Furthermore, current compliance requirements, found in Section R26.4.2 of ACI 318-14, only require that 28-day strength evaluations be met in addition to the required maximal w/cm, target air content, and potential SCM replacement limits [7].

As detailed in Section 7.2.1, the maximal w/cm values for F2 and F3 categories associated with ACI 318 and ACI 201 are equivalent but differ in value for the F1 category. As will be shown in Section 7.3, the w/cm of a concrete mixture is not correlated with its FT durability as assessed by the ASTM C666 durability factor (DF). Despite the difficulty in comparing which set of strength and max w/cm recommendations will ensure performance, it is well established that increased total air content, when properly distributed, improves FT durability [13,39,104], suggesting that ACI 201's total air content requirement would yield more durable concrete mixtures for F2 and F3 FT environments based upon the values shown in Tables 7-1 and Table 7-2. When this conclusion is evaluated in terms of mixture design, a net increase in total air content has implications for achievable compressive strength, which is critical for mixture compliance.

In addition to reviewing the history of the current recommendations and specifications for FT durability, data and results from published literature, long-term exposure sites, and dam inspections were collected and assessed [108–110,142–147]. It was found that long-term exposure sites and dam inspections provided primarily qualitative data that was not supported with information regarding the design of the mixture [142–144]. Due to this finding, results from published studies that evaluated both the freeze-thaw performance (ASTM C666 [41]) and microstructural characteristics (ASTM C457 [14]) were invaluable to critically assessing and providing evidence-based recommendations to unify the current FT provisions [108–110,145–147].

The state-of-the-art in terms of FT experiment and simulation was also reviewed to provide a holistic basis upon which to inform the unification of current FT recommendations and specifications. Since 1949, it has been known that the mean half-distance between entrained air voids, measured by Powers' spacing factor ( $\bar{L}$ ), is critical to FT resistance [13]. Decades of laboratory testing have confirmed that the spacing factor is a strong predictor for FT durability [13,39,104] but is not currently specified by any ACI committee. Despite advancements in testing, the measurement of a mixture's spacing factor  $\bar{L}$  per ASTM C457 requires a trained petrographer, making the assessment time-consuming and costly. Furthermore, because  $\bar{L}$  is often conducted on concrete cores of hardened placements, it is recommended that  $\bar{L}$  be used as a means of mixture pre- or post-qualification [100].

In light of the complications associated with  $\bar{L}$  testing and specification, Section 4.2.3.2.4 of ACI 201.2R-2016 suggests that total air content is a stand-in for direct

specification of the spacing factor – i.e., it is assumed that the required air content will impart the necessary value of  $\bar{L}$  to ensure a FT resistant concrete mixture [7]. ACI 201's conclusion does not coincide with decades of research and hundreds of concrete mixtures have shown that total air content does not guarantee a quality air void system and can be influenced by the combination of different admixtures [43,105,112]. The findings of these studies suggest that total air content does not fully represent the spacing of the entrained air void system. In effort to unify the current FT specifications and recommendations from ACI committees, it was apparent that current design variables needed to be quantitatively compared in terms of their ability to predict FT performance.

### **7.3 Database Development and Durability Analysis**

A database composed of 157 different ordinary Portland cement (OPC) concrete mixtures containing no SCMs that were subjected to ASTM C666 Procedure A accelerated FT testing was assembled to assess the influence of mixture proportions and properties on FT performance [108–110,145–147]. Mixtures with SCMs were excluded because the current design provisions for allowable SCM replacement are equivalent in value within ACI 201.2R-2016 [7] and ACI 318-14 [8]. As detailed in Section 7.2.1 and 7.2.2, common design parameters for FT durability include: w/cm, compressive strength, total air content, air content in the paste fraction, specific surface, and spacing factor. When reported, these parameters were retained for each mixture in the database for comparison to the DF obtained by ASTM C666 testing. The comparison plots shown in Figures 7-1 to 7-3 visually evaluate the ability for two variables to correlate with FT durability, as measured by the DF. Following [39,109], passing regions (i.e., regions where the DF is greater than 80) have been filled to display where design parameters can

ensure FT performance. It is important to note that Figures 7-1 to 7-3 collectively evaluate all possible combinations of the identified design parameters to predict performance and are representative of OPC concrete mixtures with MAS ranging from ½” to 1”. Furthermore, the design parameters associated with the 157 mixtures are representative of standard design space, where values of w/c, 28-day compressive strength, total air content, air content in the paste fraction, and spacing factor range from 0.2 to 0.7, 2ksi to 14ksi, 1% to 9%, 2% to 35%, and 0.004” to 0.05” respectively.

Since both ACI 318 and ACI 201 directly attribute concrete durability to resistance to fluid penetration, Figure 7-1 compares the ability for the water-to-cement (w/c) ratio for the 157 mixtures to predict FT performance as a function of the other design variables. Figure 7-1a clearly shows that w/c and 28-day compressive strength show no correlation for FT performance, with the exception of one region for very high compressive strengths (i.e. greater than 9ksi) and low w/c (i.e., less than 0.35). Figures 7-1b and 1c display that concrete mixtures with total air contents and total air content in the paste fraction greater than 4% and 14%, respectively, ensure FT performance – much lower values than currently specified by ACI 318 or ACI 201. Findings from Figure 7-1d align with commentary found in Chapter 4 of ACI 201.2R-2016 (i.e., concrete mixtures with values of spacing factor less than 0.009” ensure FT performance) [7].

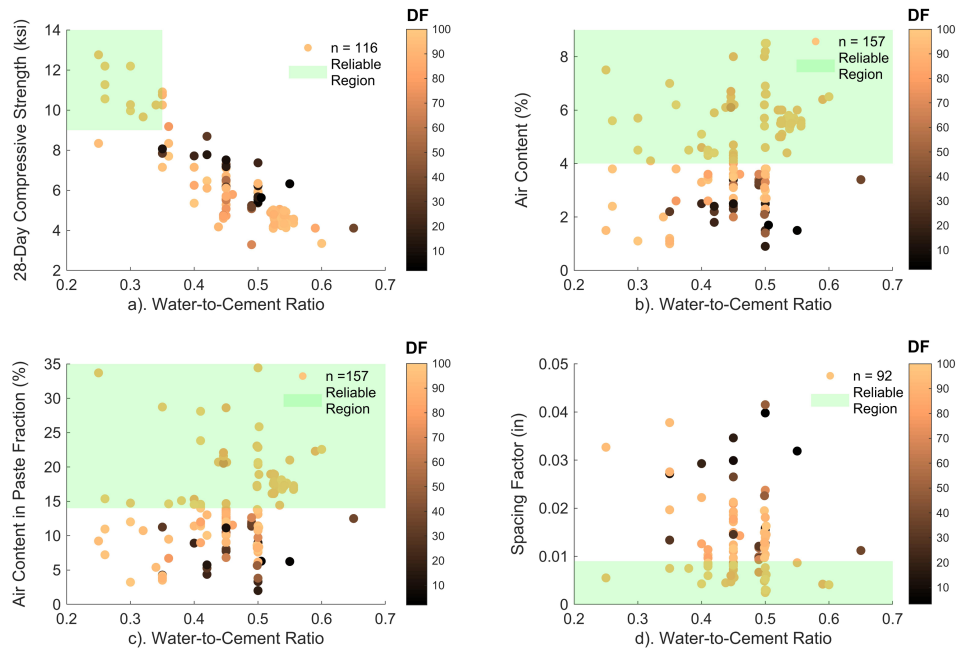


**Figure 7-1 - Comparison plot for water-to-cement ratio and a). 28-day compressive strength b). total air content c). total air content in paste fraction and d). spacing factor to ensure FT performance [108–110,145–147].**

In terms of durability-based design, required compressive strength is discussed in ACI 318 and ACI 201 documents to ensure FT performance following resistance to fluid penetration [7,8]. ACI 318 views the compressive strength specification exclusively as a means through which an appropriate w/cm (or w/c) can be ensured [8]. ACI 201 sees compressive strength specification in terms of available tensile strength to resist the hydraulic and crystallization pressures subjected to the solid phase of concrete during a freezing event [7]. Figure 7-2, in addition to Figure 7-1a, compare the ability for 28-day compressive strength and other design variables to ensure FT performance. Similar to Figures 7-1a and 7-1b, Figures 7-2a and 2-2b, show that concretes with total air content and total air concrete in the paste fraction greater than 4.0% and 14% display high FT

resistance. Furthermore, Figure 7-1a and 7-2b show that concretes with 28-day compressive strength values greater than 9ksi are highly resistant to FT.

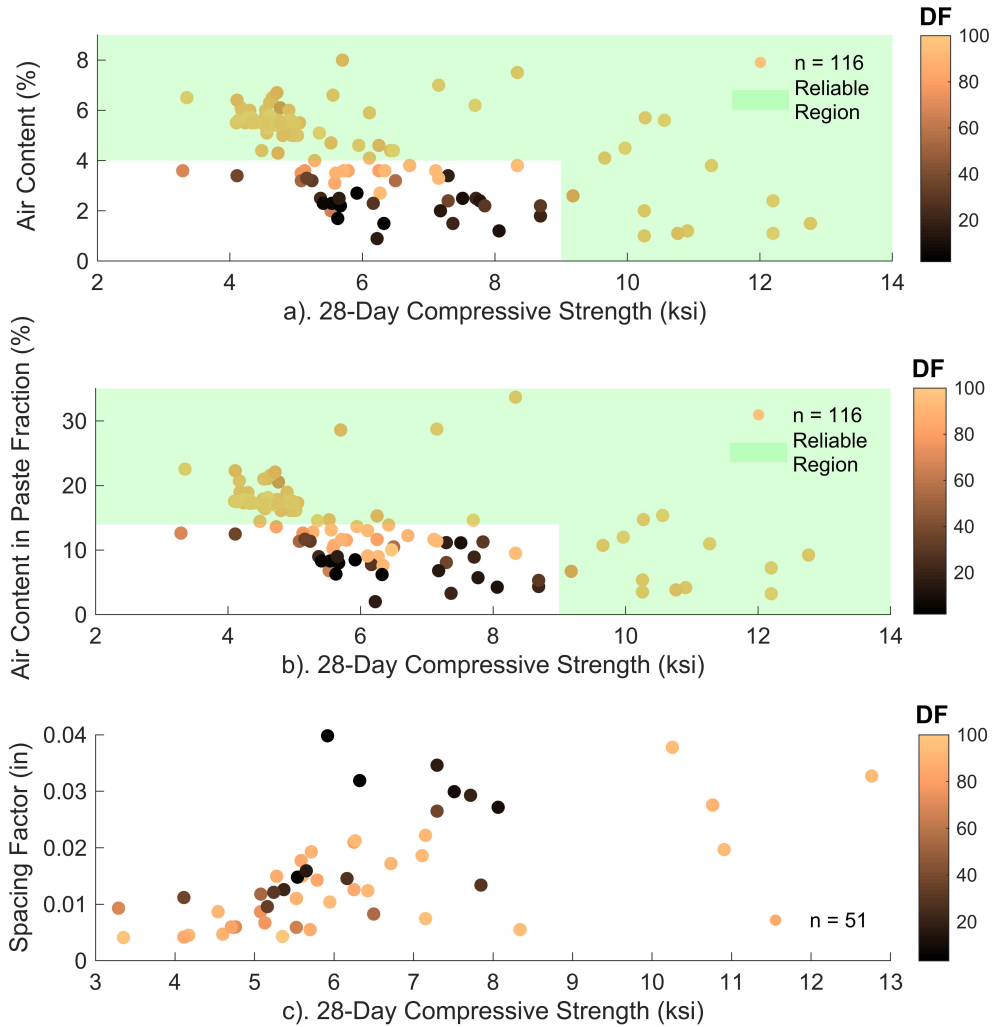


**Figure 7-2 - Comparison plot for 28-day compressive strength and a). total air content b). total air content in paste fraction and c). spacing factor to ensure FT performance [108–110,145–147].**

Figure 7-3 evaluates the ability for different measures of the entrained and entrapped air void system to correlate with FT durability. Within the commentary found within ACI 201.2R-2016 [7], it is clear that the committee sees the quantity (volume) and quality (spacing) of the air void system as the primary means of ensuring long-term FT

performance. Figure 7-3a displays a linear relationship where values of the total air content and total air content in the paste fraction greater than 3.5% and 14% ensure FT durability. Figure 8-3b shows that concretes mixtures with spacing factors less than 0.02” with total air content values greater that 3.5% perform well. Similarly, Figure 7-3c shows that concrete mixtures with spacing factors less than 0.015” with total air content values in the paste fraction greater than 13% are highly FT resistant.

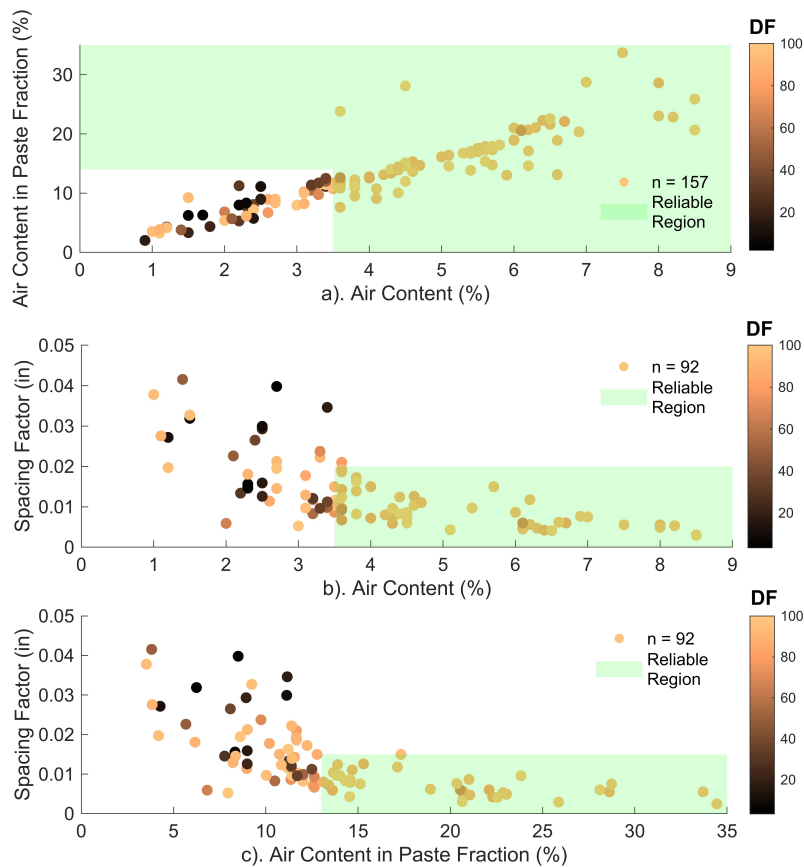


**Figure 7-3 - Comparison plot for various measurements to ensure FT performance: a). total air content and total air content in the paste fraction; b). total air content and spacing factor; c). total air content in the paste fraction and spacing factor [108–110,145–147].**

Based upon the preceding multi-parameter assessment the following conclusion can be derived:

a). Despite ACI 318 and ACI 201's reference to w/cm and w/c as a primary way to control the FT durability of a concrete mixture, the data does not support such a claim. Based upon the comparison showed in Figure 7-1, total air content, total air content in the paste fraction, and spacing factor govern FT resistance.

b). The compressive strength of concrete does not ensure FT performance, unless greater than 9ksi.

c). ACI 201's practice of designing total air content by requiring 18% air content in the paste fraction is much larger than the 14% threshold found in the preceding assessment, yielding overly conservative recommended total air content values in ACI 201.2R-2016.

d). Figure 7-3b further suggests that total air content and spacing factor are not directly correlated (e.g., a spacing factor of 0.009", which imparts reliable FT resistance, can be obtained through total air content measurements ranging from 3.0% to 7.0%).

#### **7.4 Suggested Modifications to ACI Code**

From the results of this investigation, the recommended unified design recommendations for FT performance are shown in Tables 7-4 to 7-7. Based on the completed work, the authors suggest the adoption of ACI 318-14's exposure category descriptions, maximal w/cm values, and min  $f'_c$  definition and values. Additionally, the use of the minimal total air content values, shown in Table 7-6, are suggested in comparison to the allowable ranges specified in ACI 201.2R-2016 and ACI 318-14. Furthermore, pending the criticality of the concrete mixture, the authors see a need to

clearly detail to licensed design professionals additional laboratory-based testing options for either pre-qualifying or post-validating that a concrete mixture will perform reliably in a FT environment.

The proposed guidance on the unification of FT durability specifications are detailed and justified as follows:

- Upon considering the commentary found in R19.3 of ACI 318-14, the FT exposure category definitions established by ACI 318 and ACI 201 are similar. The major difference is the discrepancy between exposure category F3 where ACI 201 distinguishes between the surface finish type, which has implications for allowable SCM replacement. Due to the fact that ACI 318-14 does not distinguish between surface-finish, as detailed in R26.4.3.1(a) of ACI 318-14, and all concrete mixtures must comply with the compliance requirements established by ACI 318, the SCM exemption established for exposure category F3b by ACI 201 is currently irrelevant to practice.
- The proposed adoption of ACI 318-14 maximal w/cm values is substantiated by the findings in Section 7.3 (i.e., w/cm and w/c were not found to substantially influence FT performance). Due to these findings adopting the lower values of w/cm would be unfounded.
- The design variable  $\min f'_c$ , defined by ACI committee document 318-14, is adopted in comparison to the minimum average compressive strength prior to initial exposure,  $\min \bar{f}_c$ , to ensure uniformity within design code (i.e., ACI 318-14 does not consider potential freezing-and-thawing conditions during construction). The suggested values of  $\min f'_c$  shown in Table 7-1 are also retained. The authors

additionally encourage the removal of the allowable reduction in air content for concretes with compressive strengths greater than 5ksi – in terms of the analysis conducted, this value is too low.

- It is proposed that the total air content values be expressed as a *minimum* (rather than an average with an allowable 1.5% tolerance, as is current practice). The values found in Table 7-6 are based upon 14% and 15% total air content in the paste fraction of the concrete mixture for F1 and F2/F3 exposure categories, respectively, where the absolute minimum total air content for any MSA is 3.5%. The intent of establishing the air content specification as a minimum is justified in two ways. First, the presented analysis displayed that concrete mixtures with greater than 14% air content in paste fraction and more than 3.5% total air content renders the concrete highly FT resistant. Secondly, the new values also yield total air contents near, or below, that were already required considering the tolerance – implying the minimum specification relaxes the current requirements, especially those recommended in ACI 201.2R-2016.

While reviewing the current design provisions and carrying out the presented analysis, it was identified that there is a significant need for improved on-site evaluation techniques of the quality of the entrained air void system and further assessments on the correlated influence of surface finish and SCM replacement on FT durability. To date, various gravimetric metrics are used to quantify the volume of entrapped and entrained air on construction sites, but do not accurately evaluate the quality (i.e., the size and spacing) of the air void system. Recent advancements in variable pressure [43], ultrasonic [148,149], and shock physics techniques have been

shown to better quantify the quality of the air void system, but need further testing and evaluation by the construction industry prior to establishment within durability specification. Figure 7-4 displays that the specific surface of the air void system could serve as a direct way to ensure a sufficiently low value of spacing factor, pending its ability to be accurately predicted using the aforementioned techniques underdevelopment. Additionally, Figure 7-4 supports that concretes with air contents greater than 3.5% and a specific surface greater than  $500 \text{ in}^2/\text{in}^3$  yields air void systems with spacing factors  $< 0.015''$  and are therefore highly FT resistant. As on-site evaluation technologies are improved and the material parameters that dictate the response of concrete to FT are better understood, the presented unified durability specifications can become increasingly performance-based, allowing for furthered service life assurance in FT environments.

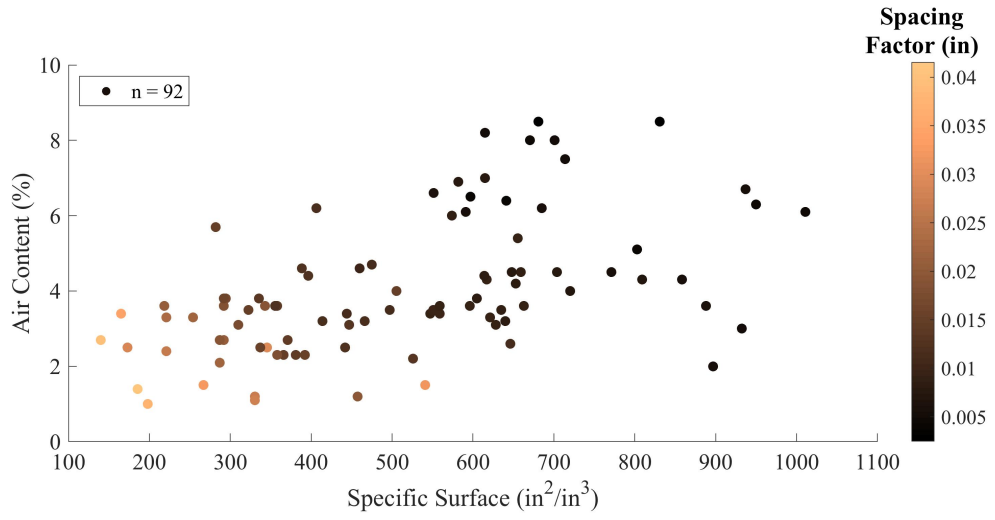


**Figure 7-4 - Influence of specific surface and total air content on spacing factor,  $\bar{L}$ .**

**Table 7-4 - Unified exposure category descriptions for FT attack.**

<b>Exposure Category</b>	<b>Severity</b>	<b>Condition</b>
F0	Not applicable	Concrete not exposed to freezing-and-thawing conditions
F1	Moderate	Concrete exposed to freezing-and-thawing cycles with limited exposure to water
F2	Severe	Concrete exposed to freezing-and-thawing cycles with frequent exposure to water
F3	Very Severe	Concrete exposed to freezing-and-thawing cycles with frequent exposure to water and exposure to deicing chemicals

**Table 7-5 - Unified design recommendations for FT performance.**

<b>Exposure Category</b>	<b>Min <math>f'_c</math></b> (psi)	<b>Max w/cm</b>	<b>Min Total Air Content</b> (%)	<b>Limits on Cementitious Replacement</b>
F0	None	None	None	None
F1	3500	0.55	See Table 6	None
F2	4500	0.45	See Table 6	None
F3	5000*	0.40*	See Table 6	See Table 3

\* For plain concrete (i.e., non-reinforced concrete), the maximum w/cm shall be 0.45 and the minimum  $f'_c$  shall be 4500 psi (4).

**Table 7-6 - Unified minimum total air content recommendations for FT performance.**

MSA in	Minimum Air Content (%)*	
	Exposure Category: F1	Exposure Category: F2 and F3
3/8	5.0	6.0
1/2	5.0	6.0
3/4	4.5	5.5
1	4.5	5.5
1-1/2	4.0	5.0
2	4.0	5.0
3	3.5	4.5

\* Determined by an average of three assessments at the point of placement where no value is less than 0.5% of the required minimum.

**Table 7-7 - Complementary durability assessment test methods recommended for mixture pre-qualification or post-assessment for critical concrete placements.**

<b>Exposure Category</b>	<b>Min Specific Surface*, (in<sup>2</sup>/in<sup>3</sup>)</b>	<b>Max Spacing Factor*, (in)*</b>	<b>Min Durability Factor<sup>#</sup></b>
F0	None	None	None
F1	500	0.015	85
F2/F3	650	0.009	90

\* Requiring that the air content is greater than or equal to 3.5% and measured by ASTM standard C457, or some other experimentally validated means, as the average of three assessments, where no assessment has a value is less than 20% of the mean of the samples.

\*\* Measured by ASTM standard C457 as the average of three assessments, where no assessment has a spacing factor greater than 0.018” or 0.012” for the F1 and F2/F3 categories, respectively.

# Measured by ASTM standard C666 as an average of three separate specimens representative of the same concrete mixture.

## **CHAPTER 8. CONTRIBUTIONS, APPLICATIONS , REMAINING KNOWLEDGE GAPS, AND FUTURE WORK**

### **8.1 Contributions and Applications**

As formulated in Section 1.3, the paradigm presented and evaluated within this dissertation is centered around making contributions to the domains of the engineering sciences, applications of data analytics, and international durability specifications to advance the capacity to design the service-life of cementitious materials in freeze-thaw environments. Sections 8.1.1 through 8.1.3 highlight the contributions made in these domains and discusses their immediate and potential applications.

#### *8.1.1 Engineering Sciences*

Within Chapters 3 and 4, evidence-based hypotheses for how air-entrained cementitious materials become progressively saturated when immersed in water which in turn results in an increased likelihood of damage initiation were investigated. In Chapter 3, two models were developed. The first model, named the single-void dissolution kinetics (SVDK) model, described and evaluated how a single spherical air void becomes fully water saturated over time due to the dissolution and transport of trapped gaseous air. The second model, name the multi-void dissolution kinetics (MVDK) model, built upon the void-scale saturation phenomena understood by the SVDK model and incorporated it into a realistic 3D polydisperse system. Both models were compared to existing experimental data and showed strong agreement. The major contributions of these models are physics-based descriptions of how entrained and entrapped air voids become saturated over time at

the air void and specimen scales which progresses cementitious materials toward critical saturation. The central application of the work within Chapter 3 is the ability to accurately predict the evolution in macro-system saturation and the time it would take to arrive at the critical saturation as a function of air void system and cementitious material parameters (e.g., air void size distribution, air void volume fraction, the intrinsic permeability, and diffusivity, etc.). Additionally, as noted in the SVDK model, tailoring the contact angle of the water in the voids could be used to reduce the long-term saturation rate or cause trapped air within a void to remain indefinitely air-filled.

With improved understanding of how air voids become saturated over time, Chapter 4 displayed how the saturation of air voids and the corresponding increased spacing between non-water-filled voids could be used to predict the critical saturation value,  $S_{cr}$ , in a large, simulated domain of cementitious materials. Within Chapter 4 a limit-state model was derived and used to evaluate an air entrained cement paste whose air voids saturated under various filling regimes. It was displayed that the air void volume fraction, compressive strength, and various other material properties did not significantly influence the predict critical saturation. Rather, as hypothesized in Chapter 2, it was shown that the systematic saturation of the air voids results in an increased mean distance between unsaturated air voids (i.e., those with a saturation less than 91.7%) that controls the likelihood of damage initiation of the material upon freezing. Although the major application in service-life design is the determination of the time it takes for the material to reach critical saturation, without understanding why the critical saturation phenomenon fundamentally occurs its use as a service-life design metric is not fully satisfactory. Within Chapter 4, a defensible reason for why the same value of critical saturation is seen for such

a broad range of cementitious materials was formulated, evaluated, and found to be able to replicate experimental critical saturation behavior.

### *8.1.2 Data, Modelling, and Analytics*

Chapters 5 and 6 complemented the efforts undertaken in Chapters 3 and 4 by probabilistically evaluating the damage initiation model for  $S_{cr}$  prediction derived in Chapter 4 and developing a process-structure-property (PSP) linkage that could be used to predict the saturation of air voids as a function of controllable parameters, such as water-to-cement ratio and total hydration time. Centrally, Chapter 5 displayed the sensitivities of the derived limit state model for critical saturation prediction and displayed how changes in design variables such as spacing factor, total air content, and material strength influence the overall probability of failure of concrete. Additionally, the probabilistic approach leveraged in Chapter 5 allowed for the evaluation of ACI, CSA, and BS EN design requirements to ensure long-term freeze-thaw durability. It was found that a measure of the distance between air voids was the most critical parameter to ensure freeze-thaw durability and also validated the derived limit-state model with a large dataset of rapid freeze-thaw durability tests from the literature. In summary, Chapter 5 displayed that to what extent various design parameters and material properties influence freeze-thaw resistance.

In Chapter 6, a data-science framework for PSP linkage development in hydrating cement pastes was presented to accurately predict material properties from simple and highly controllable parameters, such as the w/c ratio. Although the primary contribution is the establishment of the data-science framework - and how to carry it out in an efficient manner - Chapter 6 also displayed how data-driven PSP linkages can be directly used to

predict the long-term saturation behavior of entrained and entrapped air voids when its outcomes are incorporated with the SVDK model. From this, it was concluded that past 15 days of total hydration time the w/c controls the saturation kinetics and that for every 0.05 reduction in w/c the total time to complete saturation of a single air void in increase by a factor of 2. Findings of these kind suggest that by combining the PSP framework presented in Chapter 6 with the contributions made to the engineering sciences the total service-life of the material can begin to be designed.

### *8.1.3 Durability Specifications*

Chapter 7 reviewed and rigorously evaluated the current discrepancies between ACI committees' recommendations for how engineers design and specify concrete for freeze-thaw durability. After developing a large database of long-term freeze-thaw tests on concrete and considering potential implications for changes in design requirements for the concrete industry at large, it was concluded that ACI 318's exposure conditions definitions, maximal w/c ratios, and design strengths should be adopted by ACI committees 318, 201, and 350. Based on the assessment of the freeze-thaw database, a minimum for total required air content was established by requiring 14% to 15% of air content in the paste fraction of any concrete mixture. This is a significant departure from the 18% air in the paste fraction that was used to establish the current air content values where fluctuations of 1.5% of total air content in the concrete were allowed at the point of placement. The established minimums are conservative while ensuring that freeze-thaw exposed concretes are guaranteed air contents which correspond with high freeze-thaw durability. Lastly, additional suggestions were made to designers on how to pre- or post-validate a concrete

mixture's freeze-thaw durability, pending their criticality, when no previous ACI codes or documents had done so.

## **8.2 Opportunities for Material Design**

The presented research has displayed that there is a strong synergism between the air void size distribution and material properties of the surrounding porous cementitious paste which could be designed to to ensure freeze-thaw service-life. Figure 8-1 displays key outcomes from Chapters 3, 4, and 6, for material design. A key outcome of the SVDK model was that the order of magnitude of time it takes for one of the spherical air voids to become completely water-filled, as shown in Figure 3-17d, is directly proportional to the volume of the trapped mass within the spherical void. Considering this, it could be concluded that larger air voids would be more favourable by ensuring a long time to critical saturation. However, the critical saturation prediction model displayed that as the mean of the air void size distribution increases the initial air void spacing also increases and results in damage at lower values of system saturation than for smaller air void systems. By tailoring the air void size distribution system appropriately, the value of critical saturation and the total time it takes to arrive at the critical saturation could be optimized.

## **Opportunities for Material Design for FT Service-Life:**

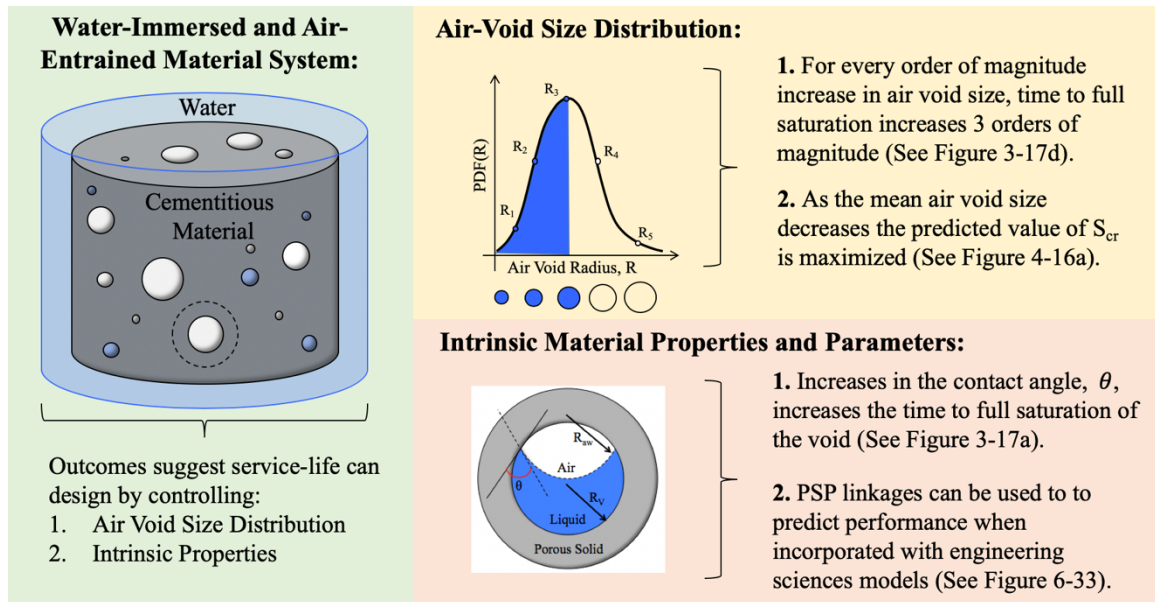


**Figure 8-1 - Summary of opportunities for material design based upon research outcomes in Chapters 3-6.**

Currently, deeper understanding of how intrinsic material properties, namely the solid-liquid contact angle,  $\theta$ , within the spherical air void and the diffusivity of the saturated cement paste are better understood. Figure 3-17a provides a ‘look-up’ chart for how the contact angle influence the time to full liquid saturation of the void. With improved admixture technologies that can cost the inside of a spherical air void with a hydrophobic surface, this knowledge could be directly manipulated to extend the saturation time of these air voids by a factor of 4. Additionally, within Chapter 6, it was displayed that for total hydration times of cement paste greater than 15 days, the w/c ratio controls the time to full saturation of the spherical voids and for every 0.05 decrease in w/c the total time to full saturation doubles. As a result, it is clear that air-entrained cementitious materials can be truly designed for freeze-thaw service-life by using the provided evidence of how the air void size distribution and intrinsic parameters (e.g., solid-liquid contact angle and intrinsic

permeability/diffusivity) effects the rates of saturation and overall freeze-thaw response. Section 8.3 details the future work and remaining knowledge gaps necessary to conduct and bridge to further progress the field toward service-life design.

### **8.3 Remaining Knowledge Gaps and Future Work**

As suggested by the title of this dissertation, the intention of the work presented was to move the field toward the capacity of service-life design. Within this final section, remaining knowledge gaps and future work are identified for the field to progress. It is the opinion of the author that the future challenges are largely centered at the interface of various fields including micro-fabrication, computational imaging, multi-phase transport, and parallel computing. By bringing experts together in these domains, the following knowledge gaps and future work can thoroughly be conducted and carried out – with the result being the capacity for concrete materials to be designed and constructed for a desired service-life in a freeze-thaw prone environment.

#### *8.3.1 Engineering Sciences*

The presented SVDK and MVDK models, although experimentally compared, would benefit from rigorous experimental validation. A series of nanoCT imaging studies on how single air voids become saturated over time could be directly used to validate the dissolution kinetics of trapped air in spherical air voids as predicted by the SVDK model. Following such an assessment, a series of microCT experiments would also be beneficial to further evaluate the MVDK model – currently 1 data point is available for how air voids in cementitious materials systematically saturate when fluid immersed. Additionally, ‘model systems’ could be fabricated to evaluate the SVDK and MVDK models, noting that

they are applicable to a much broader domain of material systems than only those which are cement-based. For example, a series of silicone foams, which have lower values of diffusivity, could be used so that imaging studies would not need to be conducted over 60 days.

In addition to experimental validation, open theoretical questions still exist. An open question of interest is which combination, or domain, of parameters for the SVDK model could result in trapped air within spherical air voids that are completely stable (i.e., the voids will never water saturate). Improved understanding of this phenomenon could have significant outcomes not only on the total time to critical saturation estimate but also on how critical saturation is estimated. Additionally, it is important to note that all saturation models assume that the material is completely liquid immersed whereas most infrastructure goes through cyclic wetting and drying depending on its environment. Based on this, the time to critical saturation prediction models serve as an absolute minimal service-life prediction, but fundamental insight could be obtained about the hysteretic saturation behavior of air-entrained cementitious materials which would more-accurately prediction their overall service life in a given environment.

Regarding the critical saturation model, presented in Chapter 4, it was assumed that all of the air voids fill in a systematic manner. The critical saturation prediction model is then limited by the way in which air voids are expected to fill. Additionally, the derived limit-state model makes various assumptions that could be removed by incorporation of the poromechanical method. Although it is expected that the likelihood of damage initiation using the poromechanical method to be very similar to that predict by the limit-state function - seeing as how both are strongly dependent on the distance of cement paste

surrounding non-saturated air voids - it would provide for additional validation and improved physical understanding of the simulated cubic systems.

An interesting insight gained from carefully considering the implications of the SVDK and critical saturation prediction model relates to the relative influence of the size of air voids on the saturation rate and ability to ensure freeze-thaw durability. Concerning material design and optimality, it would be of interest to increase the value of critical saturation of a cementitious material while minimizing the total time to critical saturation. Based on the model outcomes as the mean air void size decreases the critical saturation is maximized but the time to saturation is minimized. Due to this, it is feasible that an optimal air void size distribution exists which would manipulate this paradox and is strongly encouraged as future work.

### *8.3.2 Data, Modeling, and Analytics*

A significant next step in the formation of data-driven PSP linkages of cement pastes would be an expansion of the current CemHyd3D database developed in Chapter 6. The database presented within this dissertation considered one cement and did not evaluate total hydration times from 0 to 3 days. Although this was not the objective of the chapter and a detailed framework was provided on how to implement the material informatics techniques, expanding the dataset would provide a broader idea of how other parameters such as different volume/weight fraction of calcium-silicate and calcium-aluminate anhydrous products could influence final material properties. Additionally, within Chapter 6, it was shown that significant efforts need to be made towards the ability to accurately segment CT images of hydrating cement pastes. Advancing the field's ability to utilize real

cement images will require nanoCT evaluations and an interdisciplinary team of cement hydration and image segmentation experts.

### *8.3.3 Specifications and Evaluation Methods*

Although efforts in Chapters 3, 4, and 5 directly supported the conclusion that the quality of the air void system in cementitious materials strongly contributes to its freeze-thaw durability, the unification and modernization recommendations made for ACI committees, presented in Chapter 7, did not include suggested requirements for the measurement of air content quality (i.e., size distribution or spacing). An additional table and notes were provided to designers to specify hardened property testing to acquire this information but doing so remains time consuming and costly for the industry. A major need for the industry and the field of freeze-thaw durability is a tool that directly evaluates, or accurately predicts, the final air void system properties in hardened concretes and mortars based on evaluations in the fresh state. With a validated tool of this kind, and its acceptance and proliferation in the industry, air void parameters, which strongly correlate with long-term freeze-thaw durability and the long-term air void saturation rate, could be specified and used to further the field toward service-life design.

Lastly, left as on-going and future work, the same database of concrete specimens exposed to rapid FT cycling by ASTM C666 standards - used for the ACI unification recommendations in Chapter 7 - could be evaluated using statistical sensitivity assessments. Using these data analytics techniques will provide an additional way to identify to which degree various parameters of concrete mixtures influence the freeze-thaw durability factor (DF) without assumptions of the underlying physics used to determine the

relative influence of design parameters in Chapter 5. As a result, approaching the problem without an assumption of how the material behaves due to freezing effects would provide additional insight that can be used to further validate the recommendations made to the ACI Concrete Research Council. Lastly, it is suggested that revisions be made to ASTM C666 for specimen conditioning prior to durability evaluation. Currently, the initial saturation of the specimens are not controlled for – implying that the overall outcomes of the current testing procedure does give immediately comparable results if specimens with different air contents are being compared.

## REFERENCES

- [1] J. Spacey, Design Life vs. Service Life, Simplicable. (2017).
- [2] D. Kulash, Freeze-Thaw Resistance in Concrete - An Annotated Bibliography, Strateg. Highw. Res. Progr. - Natl. Res. Council. (1992).
- [3] A. Biolchini, What went wrong with M-6, the poster child for concrete failure, Mlive.Com. (2017). [www.mlive.com/news/grand-rapids/index.ssf/2017/07/what\\_went\\_wrong\\_on\\_m-6\\_the\\_pos.html](http://www.mlive.com/news/grand-rapids/index.ssf/2017/07/what_went_wrong_on_m-6_the_pos.html).
- [4] C. Llopis-Jensen, Capital city roads failing decades early, Topeka Official says, Topeka Cap. J. (2015).
- [5] C. McWilliams, Class-action suit filed on behalf of homeowners with failing foundations, Courant.Com. (2016).
- [6] J.S. Kim, J.S. Kug, S.J. Jeond, D.N. Huntzinger, A.M. Michalak, C.R. Schwalm, Y. Weis, K. Schafer, Reduced North American terrestrial primary productivity linked to anomalous Arctic warming, Nat. Geosci. 10 (2017) 572–577.
- [7] A. Committee 201, Guide to Durable Concrete (ACI 201.2R-16), Farmington Hills, MI, 2016.
- [8] A. Committee 318, Building Code Requirement for Structural Concrete (ACI 318-14), Farmington Hills, MI, 2014.
- [9] A. Committee 350, Code Requirements for Environmental Engineering Concrete

Structures (ACI 350-06) and Commentary, Farmington Hills, MI, 2016.

- [10] P. Klieger, Curing Requirements of Scale Resistance of Concrete, Highw. Res. Board Bull. 150 (1957) 18–31.
- [11] P. Klieger, Effect of Entrained Air on Strength and Durability of Concrete Made with Various Maximum Sizes of Aggregate, Highw. Res. Board Proc. 3 (1952) 177–201.
- [12] P. Klieger, Further Studies on the Effect of Entrained Air on Strength and Durability of Concrete with Various Sizes of Aggregate, Proc. Highw. Res. Board. 128 (1956) 1–21.
- [13] T.C. Powers, T.F. Willis, The Air Requirement of Frost-Resistant Concrete, Proc. Twenty-Ninth Annu. Meet. Highw. Res. Board. (1949).
- [14] ASTM C457/C457M - 16: Standard Test Method for Microscopical Determination of Parameters of the Air-Void System in Hardened Concrete, 2016.
- [15] K. Tuutti, Corrosion of steel in concrete, Swedish Cem. Concr. Res. Inst. (1982). doi:10.4324/9780203414606\_chapter\_2.
- [16] C. MacInnis, J. Beaudoin, Effect of Degree of Saturation on the Frost Resistance of Mortar Mixes, ACI J. Proc. (1968) 203–208.
- [17] G. Fagerlund, Significance of critical degrees of saturation at freezing of porous and brittle materials, Div. Build. Mater. Lund Univ. (1973).
- [18] W. Li, M. Pour-Ghaz, J. Castro, J. Weiss, Water Absorption and Critical Degree of

- Saturation Relating to Freeze-Thaw Damage in Concrete Pavement Joints, *J. Mater. Civ. Eng.* (2012). doi:10.1061/(ASCE)MT.1943-5533.0000383.
- [19] S.H. Smith, P. Suraneni, C. Qiao, K.E. Kurtis, W.J. Weiss, Service-life of Concrete in Freeze-Thaw Environments: Critical Degree of Saturation and Calcium Oxychloride Formation, *Cem. Concr. Res.* 122 (2019) 93–106.
- [20] H. Todak, C. Lucero, W.J. Weiss, Why is the air there? Thinking about freeze-thaw in terms of saturation, *Concr. InFocus*. Spring (2015) 27–33.
- [21] W.J. Weiss, Concrete Pavement Joint Durability: A Sorption-Based Model for Saturation, the Role of Distributed Cracking, and Calcium Oxychloride Formation, *CONCREEP-10*. (2015). doi:10.1061/9780784479346.025.
- [22] Z. Liu, W. Hansen, Moisture uptake in concrete under freezing-thawing exposure, *Mag. Concr. Res.* (2016). doi:10.1680/jmacr.15.00193.
- [23] H. Todak, Durability assessments of concrete using electrical properties and acoustic emission testing, 2015.
- [24] D. Eriksson, T. Gasch, R. Malm, A. Ansell, Freezing of partially saturated air-entrained concrete: A multiphase description of the hygro-thermo-mechanical behaviour, *Int. J. Solids Struct.* 152 (2018) 294–304. doi:https://doi.org/10.1016/j.ijsolstr.2018.07.004.
- [25] Z. Liu, W. Hansen, A geometrical model for void saturation in air-entrained concrete under continuous water exposure, *Constr. Build. Mater.* (2016).

doi:10.1016/j.conbuildmat.2016.07.113.

- [26] T.L. Cavalline, M.T. Ley, L.L. Sutter, W.J. Weiss, T. Van Dam, A Road Map for Research and Implementation for Freeze-Thaw Resistant Highway Concrete, 11th Int. Conf. Concr. Pavments. (2016).
- [27] J.J. Valenza, G.W. Scherer, J.J. Valenza II, Mechanism for salt scaling, J. Am. Ceram. Soc. (2006). doi:10.1111/j.1551-2916.2006.00913.x.
- [28] J. Weiss, C. Qiao, P. Suraneni, Synthesis: Accelerating the implementation of research findings to reduce the potential concrete pavement joint deterioration, 2018.
- [29] G. Fagerlund, The long time water absorption in the air-pore structure of concrete, Div. Build. Mater. Lund Univ. (1993).
- [30] J.C. McCormac, Structural Steel Design, 4th ed., Pearson Prentice Hall, Upper Saddle River, NJ, 2008.
- [31] S.H. Smith, K.E. Kurtis, I. Tien, Probabilistic evaluation of concrete freeze-thaw design guidance, Mater. Struct. Constr. (2018). doi:10.1617/s11527-018-1259-z.
- [32] C. Powers, T. A. Helmuth, R, THEORY OF VOLUME CHANGES IN HARDENED PORTLAND-CEMENT PASTE DURING FREEZING, in: Proc. Thirty-Second Annu. Meet. Highw. Res. Board, 1953.
- [33] D.P. Bentz, M. a Ehlen, C.F. Ferraris, E.J. Garboczi, Sorptivity-based service life predictions for concrete pavements, 7th Int. Conf. Concr. Pavements–Orlando,

Florida, USA, Sept. (2001).

- [34] J. Bentz, D P, Ferraris, C.F., Wingpigler, Service Life Prediction for Concrete Pavements and Bridge Decks Exposed to Sulfate Attack and Freeze-Thaw Deterioration, Volume II- Technical Basis for CONCLIFE- Sorptivity Testing and Computer Models, Building and Fire Research Laboratory, National Institute of Standards and Technology, 2001.
- [35] W. Jason Weiss, R.P. Spragg, O. Burkan Isgor, M. Tyler Ley, T. Van Dam, Toward performance specifications for concrete: Linking resistivity, RCPT and diffusion predictions using the formation factor for use in specifications, in: High Tech Concr. Where Technol. Eng. Meet - Proc. 2017 Fib Symp., 2017. doi:10.1007/978-3-319-59471-2\_235.
- [36] P.K. Mehta, P.J.M. Monteiro, Concrete: microstructure, properties, and materials, 2006. doi:10.1036/0071462899.
- [37] O. Coussy, P.J.M. Monteiro, Poroelastic model for concrete exposed to freezing temperatures, Cem. Concr. Res. (2008). doi:10.1016/j.cemconres.2007.06.006.
- [38] Q. Zeng, T. Fen-Chong, P. Dangla, K. Li, A study of freezing behavior of cementitious materials by poromechanical approach, Int. J. Solids Struct. (2011). doi:10.1016/j.ijsolstr.2011.07.018.
- [39] N.P. Mayeresik, M. Vandamme, K.E. Kurtis, Assessing the efficiency of entrained air voids for freeze-thaw durability through modeling, Cem. Concr. Res. (2016). doi:10.1016/j.cemconres.2016.06.004.

- [40] N.P. Mayercsik, R. Felice, M.T. Ley, K.E. Kurtis, A Probabilistic Technique for Entrained Air Void Analysis in Hardened Concrete, *Cem. Concr. Res.* 59 (2014) 16–23.
- [41] ASTM C666/C666M - 15: Standard Test Method for Resistance of Concrete to Rapid Freezing and Thawing, 2015.
- [42] P.C. Fonseca, G.W. Scherer, An Image Analysis Procedure to Quantify the Air Void System of Mortar and Concrete, *Mater. Struct. Constr.* 48 (2015) 3087–3098.
- [43] M.T. Ley, D. Welchel, J. Peery, S. Khatibmasjedi, J. LeFlore, Determining the Air-Void Size Distribution in Fresh Concrete with the Sequential Air Method, *Constr. Build. Mater.* 150 (2015) 723–737.
- [44] D. Eriksson, T. Gasch, A. Ansell, A Hygro-Thermo-Mechanical Multiphase Model for Long-Term Water Absorption into Air-Entrained Concrete, *Transp. Porous Media.* (2018). doi:<https://doi.org/10.1007/s11242-018-1182-3>.
- [45] G. Fagerlund, Critical degrees of saturation at freezing of porous and brittle materials, 1973. doi:10.14359/17604.
- [46] R.M. Ghantous, H. Madland, J. Kwong, W.J. Weiss, Examining the Influence of the Degree of Saturation on Length Change and Freeze-Thaw Damage, *Adv. Civ. Eng. Mater.* 8 (2019) 20190001. doi:10.1520/acem20190001.
- [47] AASHTO PP 84-18: Standard Practice for Developing Performance Engineered Concrete Pavement Mixtures, *Am. Assoc. State Highw. Transp. Off.* (2018).

- [48] C. Hall, W.D. Hoff, Topics in Water Transport, in: Water Transp. Brick, Stone Concr., 2009.
- [49] N.A. Sahloul, M.A. Ioannidis, I. Chatzis, Dissolution of residual non-aqueous phase liquids in porous media: Pore-scale mechanisms and mass transfer rates, *Adv. Water Resour.* 25 (2002) 33–49. doi:10.1016/S0309-1708(01)00025-2.
- [50] M. Khanzadeh Moradllo, Q. Hu, M.T. Ley, Using X-ray imaging to investigate in-situ ion diffusion in cementitious materials, *Constr. Build. Mater.* (2017). doi:10.1016/j.conbuildmat.2017.01.038.
- [51] T. Cubaud, M. Sauzade, R. Sun, CO<sub>2</sub> Dissolution in Water Using Long Serpentine Microchannels, *Biomicrofluidics*. 6 (2012).
- [52] M. Azmin, G. Mohamedi, M. Edirisinghe, E.P. Stride, Dissolution of coated microbubbles: The effect of nanoparticles and surfactant concentration, *Mater. Sci. Eng. C*. 32 (2012) 2654–2658.
- [53] V.A. Fry, J.S. Selker, S.M. Gorelick, Experimental investigations for trapping oxygen gas in saturated porous media for in situ bioremediation, *Water Resour. Res.* 33 (1997) 2687–2696. doi:10.1029/97WR02428.
- [54] P.B. Duncan, D. Needham, Test of the Epstein-Plesset Model for Gas Microparticle Dissolution in Aqueous Media: Effect of Surface Tension and Gas Undersaturation in Solution, *Langmuir*. 20 (2004) 2567–2578.
- [55] P.S. Epstein, M.S. Plesset, On the Stability of Gas Bubbles in Liquid-Gas Solutions,

Chem. Phys. 18 (1950) 1505–1509.

- [56] S. Sirivithayapakorn, A. Keller, Transport of colloids in unsaturated porous media: A pore-scale observation of processes during the dissolution of air-water interface, *Water Resour. Res.* 39 (2003). doi:10.1029/2003WR002487.
- [57] S. Kentish, J. Lee, M. Davidson, M. Ashokkumar, The dissolution of a stationary spherical bubble beneath a flat plate, *Chem. Eng. Sci.* 61 (2006) 7697–7705. doi:10.1016/j.ces.2006.08.071.
- [58] G. Kapodistrias, P.H. Dahl, Scattering measurements from a dissolving bubble, *Acoust. Soc. Am.* 131 (2018) 4243–4251. doi:10.1121/1.3703060.
- [59] J.I. Siddique, D.M. Anderson, A. Bondarev, Capillary rise of a liquid into a deformable porous material, *Phys. Fluids.* (2009). doi:10.1063/1.3068194.
- [60] K.M. Masoodi, R., Pillai, *Wicking in porous materials: traditional and modern modeling approaches*, Taylor and Francis Group, 2012.
- [61] X. Li, S. Chen, Q. Xu, Y. Xu, Modeling capillary water absorption in concrete with discrete crack network, *J. Mater. Civ. Eng.* 30 (2018) 04017263. doi:10.1061/(ASCE)MT.1943-5533.0002122.
- [62] C.L. Lucero, D.P. Bentz, D.S. Hussey, D.L. Jacobson, W.J. Weiss, Using Neutron Radiography to Quantify Water Transport and the Degree of Saturation in Entrained Air Cement Based Mortar, in: *Phys. Procedia*, 2015. doi:10.1016/j.phpro.2015.07.077.

- [63] X. Li, Y. Wang, B. Zeng, Y. Li, H. Tan, H.J.W. Zandvliet, X. Zhang, D. Lohse, Entrapment and Dissolution of Microbubbles Inside Microwells, *Langmuir*. 34 (2018) 10659–10667. doi:10.1021/acs.langmuir.8b02173.
- [64] M. Buchgraber, A.R. Kovescek, L.M. Castanier, A Study of Microscale Gas Trapping Using Etched Silicon Micromodels, *Transp. Porous Media*. 95 (2012) 647–668. doi:10.1007/s11242-012-0067-0.
- [65] O. Carrier, N. Shahidzadeh-Bonn, R. Zargar, M. Aytouna, M. Habibi, J. Eggers, D. Bonn, Evaporation of water: evaporation rate and collective effects, *J. Fluid Mech.* 798 (2016) 774–786. doi:10.1017/jfm.2016.356.
- [66] E. Jambon-Puillet, N. Shahidzadeh, D. Bonn, Singular sublimation of ice and snow crystals, *Nat. Commun.* 9 (2018) 1–6. doi:10.1038/s41467-018-06689-x.
- [67] P.B. Duncan, D. Needham, Microdroplet dissolution into a second-phase solvent using a micropipet technique: Test of the epstein-plesset model for an aniline-water system, *Langmuir*. 22 (2006) 4190–4197. doi:10.1021/la053314e.
- [68] E.W. Weisstein, Sphere-Sphere Intersection, *MathWorld - A Wolfram Web Resour.* (n.d.). <http://mathworld.wolfram.com/Sphere-SphereIntersection.html>.
- [69] D.N. Espinoza, J.C. Santamarina, CO<sub>2</sub> Breakthrough - Caprock Sealing Efficiency and Integrity for Carbon Geological Storage, *Greenh. Gas Control*. 66 (2017) 218–229.
- [70] M. Zhang, Y. He, G. Ye, D.A. Lange, K. Van Breugel, Computational Investigation

- on Mass Diffusivity in Portland Cement Paste Based on X-ray Computed Tomography, *Constr. Build. Mater.* 10 (2012) 472–481.
- [71] H. Derluyn, P. Moonen, J. Carmeliet, Modelling of Moisture and Salt Transport Incorporating Salt Crystallization in Porous Media, *Proc. CONMOD'08.* (2008).
- [72] N. Bignell, The Effect of Dissolved Air on the Density of Water, *Metrologia.* 19 (1983) 57–59.
- [73] J. Sercombe, R. Vidal, C. Gallé, F. Adenot, Experimental study of gas diffusion in cement paste, *Cem. Concr. Res.* 37 (2007) 579–588. doi:10.1016/j.cemconres.2006.12.003.
- [74] G. Ye, Percolation of capillary pores in hardening cement pastes, *Cem. Concr. Res.* 35 (2005) 167–176. doi:10.1016/j.cemconres.2004.07.033.
- [75] O. Coussy, *Mechanics and Physics of Porous Solid*, 1st ed., Wiley, 2010.
- [76] Z. Liu, W. Hansen, Effect of hydrophobic surface treatment on freeze-thaw durability of concrete, *Cem. Concr. Compos.* 69 (2016) 49–60.
- [77] M. Ostoja-Starzewski, Material spatial randomness: From statistical to representative volume element, *Probabilistic Eng. Mech.* 21 (2006) 112–132.
- [78] X. Yin, W. Chen, A. To, C. McVeigh, W. Liu, Statistical volume element method for predicting microstructure - constitutive property relations, *Comput. Methods Appl. Mech. Eng.* 197 (2008) 3516–3529.
- [79] J.J. Valenza, G.W. Scherer, A review of salt scaling: II. Mechanisms, *Cem. Concr.*

- Res. (2007). doi:10.1016/j.cemconres.2007.03.003.
- [80] J.J. Valenza, G.W. Scherer, A review of salt scaling: I. Phenomenology, *Cem. Concr. Res.* (2007). doi:10.1016/j.cemconres.2007.03.005.
- [81] T.C. Powers, The mechanism of frost action on concrete, *Stat. Walk. Lect. Ser. Nat. Sand Gravel Assoc.* (1965) 35.
- [82] H.S. Esmaeeli, Y. Farnam, D.P. Bentz, P.D. Zavattieri, W.J. Weiss, Numerical simulation of the freeze–thaw behavior of mortar containing deicing salt solution, *Mater. Struct. Constr.* (2017). doi:10.1617/s11527-016-0964-8.
- [83] Y. Farnam, D. Bentz, A. Sakulich, D. Flynn, J. Weiss, Measuring Freeze and Thaw Damage in Mortars Containing Deicing Salt Using a Low-Temperature Longitudinal Guarded Comparative Calorimeter and Acoustic Emission, *Adv. Civ. Eng. Mater.* (2014). doi:10.1520/ACEM20130095.
- [84] B. Widom, Random Sequential Addition of Hard Spheres to a Volume, *J. Chem. Phys.* (1966). doi:10.1063/1.1726548.
- [85] Z. Adamczyk, P. Weronki, Random sequential adsorption of spheroidal particles: Kinetics and jamming limit, *J. Chem. Phys.* 105 (1996) 5562–5573.
- [86] A. Tewari, A.M. Gokhale, Nearest-neighbor distances between particles of finite size in three-dimensional uniform random microstructures, *Mater. Sci. Eng. A.* (2004). doi:10.1016/j.msea.2004.06.049.
- [87] N. Metropolis, Metropolis-Et-Al-1953, *J. Chem. Phys.* (1953).

doi:10.1111/maps.12421.

- [88] S.N. Chiu, D. Stoyan, W.S. Kendall, J. Mecke, Stochastic Geometry and Its Applications: Third Edition, 2013. doi:10.1002/9781118658222.
- [89] M. Pigeon, R. Pleau, Theories of frost action and de-icer salt scaling mechanisms. In: Durability of Concrete In Cold Climates, 1995.
- [90] K. Bharadwaj, D. Glosser, M.K. Moradillo, O.B. Isgor, W.J. Weiss, Toward the prediction of pore volumes and freeze-thaw performance of concrete using thermodynamic modelling, Cem. Concr. Res. 124 (2019) 105820. doi:10.1016/j.cemconres.2019.105820.
- [91] P. Suraneni, J. Monical, E. Unal, Y. Farnam, J. Weiss, Calcium oxychloride formation potential in cementitious pastes exposed to blends of deicing salt, ACI Mater. J. (2017). doi:10.14359/51689607.
- [92] CSA, A23.1-14/A23.2-14: Concrete Materials and Methods of Concrete Construction/Testing Methods and Standard Practice for Concrete, Can. Stand. Assoc. (2014).
- [93] B. EN, Concrete – Part 1: Specification, performance, production and conformity, Br. Stand. Inst. (2000).
- [94] T.C. Powers, T.L. Brownyard, Studies of the Physical Properties of Hardened Portland Cement Paste, J. Am. Concr. Inst. 43 (1947).
- [95] T. Cho, Prediction of Cyclic Freeze-thaw Damage in Concrete Structure based on

- Response Surface Method, *Constr. Build. Mater.* 21 (2007) 2013–2040.
- [96] T. Cho, Prediction of Cyclic Freeze-thaw Damage in Concrete Structures Based on an Improved Response Surface Method, *Int. J. Railw.* 21 (2010) 7–13.
- [97] F. Chen, P. Qiao, Probabilistic Damage Modeling and Service-Life Prediction of Concrete Under Freeze-Thaw Action, *J. Mater. Struct.* 48 (2015) 2697–2711.
- [98] J. Wawrezenczyk, A. Molendowska, Evaluation of Concrete Resistance to Freeze-Thaw Based on Probabilistic Analysis of Damaged, *Procedia Eng.* 193 (2017) 35–41.
- [99] A.M. Hasofer, N.C. Lind, Exact and Invariant Second-Moment Code Format, *J. Eng. Mech. Div.* 100 (1975) 111–121.
- [100] K.C. Hover, J. Bickley, R.D. Hooten, Guide to Specifying Concrete Performance - Phase II Report of Preparation of a Performance-Based Specification for Cast-in-Place Concrete, *RMC Res. Educ. Cent.* (2008) 53.
- [101] H.F. Gonnerman, E.C. Shuman, Compression, Flexure, and Tension Tests of Plain Concrete, *Proc. Am. Soc. Test. Mater.* 28 (1928) 527.
- [102] R. Rackwitz, B. Fiessler, Structural Reliability Under Combined Random Load Sequence, *Comput. Struct.* 9 (1978) 489–494.
- [103] Y. Zhang, A. Der Kiureghian, Two Improved Algorithms for Reliability Analysis, *Proc. 6th IFIP WG 7.5 Work. Conf. Reliab. Optim. Struct. Syst.* (1994) 297–304.
- [104] E.K. Attiogbe, C.K. Nmai, F.T. Gay, Air-Void System Parameters and Freeze-Thaw

- Durability of Concrete Containing Superplasticizer, *ACI Concr. Int.* 88 (1992) 43–59.
- [105] P. Plante, M. Pigeon, F. Saucier, Air-Void Stability, Part II: Influence of Superplasticizers and Cement, *ACI Material, ACI Mater. J.* 86 (1989) 581–589.
- [106] T. Yamato, Y. Emoto, M. Soeda, Strength and Freezing-and-Thawing Resistance of Concrete Incorporating Condensed Silica Fume, *Am. Concr. Inst. Spec. Publ.* 91 (1986) 1095–1118.
- [107] E. Okada, M. Hisaka, Y. Kazama, K. Hattori, Freeze-Thaw Resistance of Superplasticized Concretes, *Am. Concr. Inst. Spec. Publ.* 68 (1981) 215–232.
- [108] M. Pigeon, R. Pleau, P. Aitcin, Freeze-Thaw Durability of Concrete with and without Silica Fume in ASTM C666 (Procedure A) Test Method: Internal Cracking vs. Scaling, *Cem. Concr. Aggregates.* 8 (1986) 76–85.
- [109] R. Felice, Frost resistance of modern air entrained concrete mixtures, Oklahoma State University, 2012.
- [110] J. Tansei, R. Meininger, Freeze-Thaw Resistance of Concrete With Marginal Air Content, *US Dep. Transp. Fed. Highw. Adm.* (2006) 1–96.
- [111] ASTM, ASTM C666 – 77 (Historical Version) Standard Test Method for Resistance of Concrete to Rapid Freezing and Thawing, *Am. Soc. Test. Mater. ASTM Int.* (1997).
- [112] F. Saucier, M. Pigeon, G. Cameron, Air Void Stability, Part V: Temperature,

- General Analysis and Performance Index, ACI Material, ACI Mater. J. 88 (1991) 25–36.
- [113] R. Felice, J.M. Freeman, M.T. Ley, Durable Concrete with modern Air-Entraining Admixtures, ACI Concr. Int. 36 (2014) 37–45.
- [114] ASTM, ASTM C39/C39M – 17 Standard Test Method for Compressive Strength of Cylindrical Concrete Specimens, Am. Soc. Test. Mater. ASTM Int. (2017).
- [115] D.P. Bentz, Influence of Water-to-Cement Ratio on Hydration Kinetics: Simple Models Based on Spatial Considerations, J. Cem. Concr. Res. 36 (2006) 238–244.
- [116] S.H. Kosmatka, M.L. Wilson, Design and Control of Concrete Mixtures: 16th Edition, Portl. Cem. Assoc. (2016).
- [117] Y.Y. Kim, K.M. Lee, J.W. Bang, S.J. Kwon, Effect of W/C Ratio on Durability and Porosity in Cement Mortar with Constant Cement Amount, Adv. Mater. Sci. Eng. (2014).
- [118] S. Tsivilis, J. Tsantilas, G. Kakali, E. Chaniotakis, A. Sakellariou, The permeability of Portland limestone cement concrete, Cem. Concr. Res. (2003). doi:10.1016/S0008-8846(03)00092-9.
- [119] B. Felekoğlu, S. Türkel, B. Baradan, Effect of water/cement ratio on the fresh and hardened properties of self-compacting concrete, Build. Environ. (2007). doi:10.1016/j.buildenv.2006.01.012.
- [120] A. Shamsai, S. Peroti, K. Rahmani, L. Rahemi, Effect of Water-Cement Ratio on

Abrasive Strength, Porosity and Permeability of Nano-Silica Concrete, *World Appl. Sci. J.* 8 (2012) 929–933.

- [121] S. Kalidindi, *Hierarchical Materials Informatics*, 2015. doi:10.1016/c2012-0-07337-1.
- [122] D.P. Bentz, *CEMHYD3D: A Three-Dimensional Cement Hydration and Microstructure Development Modelling Package. Version 2.0*, Natl. Inst. Stand. Technol. Interag. (2000).
- [123] D.P. Bentz, S. Mizell, S. Satterfield, J. Devaney, W. George, P. Ketcham, J. Graham, J. Porterfield, *The Visible Cement Data Set*, NIST. 107 (2002) 137–148.
- [124] S. Bishnoi, K.L. Scrivener, *mic: A New Platform for Modelling the Hydration of Cement*, *Cem. Concr. Res.* (n.d.) 266–274.
- [125] J.W. Bullard, H.M. Jennings, R.A. Livingston, A. Nonat, G.W. Scherer, J.S. Schweitzer, K.L. Scrivener, *Mechanisms of Cement Hydration*, *Cem. Concr. Res.* 41 (2011) 1208–1223.
- [126] Mamlouk, Zaniewski, *Materials for Civil and Construction Engineers: Chapter 2*, 2009.
- [127] J. Huang, K. Krabbenhoft, A.V. Lyamin, *Statistical Homogenization of Elastic Properties of Cement Paste Based on X-ray Microtomography Images*, *Int. J. Solids Struct.* 50 (2013) 699–709.
- [128] G.W. Milton, *The Theory of Composites*, 2002. doi:10.1017/cbo9780511613357.

- [129] T.S. Han, X. Zhang, J.S. Kim, S.Y. Chung, J.H. Lim, C. Linder, Area of Lineal-Path Function of Describing the Pore Microstructures of Cement Paste and their Relations to the Mechanical Properties Simulated from  $\mu$ -CT Microstructures, *Cem. Concr. Compos.* 88 (2018) 1–17.
- [130] K.E. Kurtis, Cement Hydration Lecture Notes, in: *Mater. Sci. Concr.*, 2017.
- [131] P. Stutzman, Magnification Progression 2000x, UIUC Concr. Microsc. Libr. (n.d.).
- [132] E. Gallucci, K.L. Scrivener, A. Groso, M. Stompanoni, G. Margaritondo, 3D Experimental Investigation of the Microstructure of Cement Pastes Using Synchrotron X-ray Microtomography ( $\mu$ CT), *Cem. Concr. Res.* 37 (2007) 360–368.
- [133] K.L. Scrivener, The Use of Backscattered Electron Microscop and Image Analysis To Study the Porosity of Cement Pastes, *Mater. Res. Symp. Proc.* 137 (1989) 129–140.
- [134] N. Bossa, P. Chaurand, J. Vicente, D. Borschneck, C. Levard, O. Aguerre-Chariol, Micro- and nano-X-ray Computed Tomography: A Step Forward in the Characterization of the Pore Network of a Leached Cement Paste, *Cem. Concr. Res.* 67 (2015) 138–147.
- [135] S.Y. Chung, T.S. Han, J.J. Kim, K.S. Youm, J.H. Lim, Evaluation of Effect of Glass Beads on Thermal Conductivity of Insulating Concrete Using Micro CT Images and Probability Functions, *Cem. Concr. Compos.* 65 (2016) 150–162.
- [136] M. and Structures, Characterization and Comparison of Capillary Pore Structures of

Digital Cement Pastes, Dong, H Giao, P Ye, G. 50 (2017) 154.

- [137] N. Otsu, THRESHOLD SELECTION METHOD FROM GRAY-LEVEL HISTOGRAMS., IEEE Trans Syst Man Cybern. (1979).
- [138] C. Ma, J. Seuntjens, Mass-energy absorption coefficient and backscatter factor ratios for kilovoltage x-ray beams, Phys. Med. Biol. 44 (1999) 131–143.
- [139] MathWorks, Gaussian Process Regression Models, MathWorks Doc. (2019).  
<https://www.mathworks.com/help/stats/gaussian-process-regression-models.html>.
- [140] C.E. Rasmussen, C.K. Williams, Gaussian Processes for Machine Learning, MIT Press, 2006.
- [141] E.J. Garboczi, D.P. Bentz, Computer Simulation of the Diffusivity of Cement-Based Materials, J. Mater. Sci. 27 (1992) 2083–2092.
- [142] U.A.C. o. E.S.. District, Lock and Dam No. 25 Mississippi River Winfield, Missouri: Period Inspection Report No. 8, Res. Libr. - US Army Eng. Waterw. Exp. Stn. (1995) 1–200.
- [143] U.A.C. o. E.S.. District, Lock and Dam No. 25 Mississippi River Winfield, Missouri: Period Inspection Report No. 9, Res. Libr. - US Army Eng. Waterw. Exp. Stn. (1997) 1–226.
- [144] U.A.C. o. E.S.. District, Lock and Dam No. 25 Mississippi River Winfield, Missouri: Period Inspection Report No. 10, Res. Libr. - US Army Eng. Waterw. Exp. Stn. (1999).

- [145] W.M. Hale, S.F. Freyne, B.W. Russell, Examining the Frost Resistance of High Performance Concrete, *Constr. Build. Mater.* 23 (2009) 878–888.
- [146] B.D. Neeley, W.E. McDonald, M.K. Lloyd, Air-entraining Admixtures to Produce Frost-Resistant Concrete with Low Air Content, *U.S. Army Waterw. Exp. Stn.* (1992) 50.
- [147] K. Wang, G. Lomboy, R. Steffes, Investigation into Freezing-Thawing Durability of Low Permeability Concrete With and Without Air Entraining Agent, *Natl. Concr. Pavement Technol. Cent. Inst. Transportation.* (2009) 50.
- [148] N.A. Darraugh, J.Y. Kim, K.E. Kurtis, L.J. Jacobs, Air void characterization through ultrasonic attenuation using an immersion procedure, in: *AIP Conf. Proc.*, 2010. doi:10.1063/1.3362161.
- [149] W. Punurai, L.J. Jacobs, K.E. Kurtis, J. Jarzynski, J. Qu, Characterization of entrained air voids using scattered ultrasound, in: *AIP Conf. Proc.*, 2006. doi:10.1063/1.2184679.